Taylor & Francis
Taylor & Francis Group

Journal of Vertebrate Paleontology

ISSN: (Print) (Online) Journal homepage: https://www.tandfonline.com/loi/ujvp20

Postcranial Morphology of *Adalatherium hui* (Mammalia, Gondwanatheria) from the Late Cretaceous of Madagascar

Simone Hoffmann , Yaoming Hu & David W. Krause

To cite this article: Simone Hoffmann , Yaoming Hu & David W. Krause (2020) Postcranial Morphology of *Adalatherium hui* (Mammalia, Gondwanatheria) from the Late Cretaceous of Madagascar, Journal of Vertebrate Paleontology, 40:sup1, 133-212, DOI: 10.1080/02724634.2020.1799818

To link to this article: https://doi.org/10.1080/02724634.2020.1799818

Society of Vertebrate Paleontology Memoir 21
Journal of Vertebrate Paleontology
Volume 40, Supplement to Number 2:133–212

MEMOIR ARTICLE

POSTCRANIAL MORPHOLOGY OF *ADALATHERIUM HUI* (MAMMALIA, GONDWANATHERIA) FROM THE LATE CRETACEOUS OF MADAGASCAR

SIMONE HOFFMANN, *[,1] YAOMING HU,[2,†] and DAVID W. KRAUSE [2,3]
[1]Department of Anatomy, New York Institute of Technology, College of Osteopathic Medicine, Old Westbury, New York 11568, U.S.A., shoffm04@nyit.edu;
[2]Department of Anatomical Sciences, Stony Brook University, Stony Brook, New York 11794-8081, U.S.A.;
[3]Department of Earth Sciences, Denver Museum of Nature & Science, Denver, Colorado 80205, U.S.A., David.Krause@dmns.org

ABSTRACT—The holotype and only known specimen of *Adalatherium hui* from the Late Cretaceous of Madagascar preserves the first postcranial skeleton for the Gondwanatheria. It represents only the fourth Mesozoic mammaliaform described from articulated postcranial material from Gondwana (the others being the morganucodontans *Megazostrodon* and *Erythrotherium* and the stem therian *Vincelestes*). The postcranial skeleton of *Adalatherium* is virtually complete, and its preservation is exceptional; even costal cartilages and manual and pedal sesamoids are preserved. *Adalatherium* exhibits a variety of derived and plesiomorphic traits, probably reflective of a long evolutionary history in geographic isolation on Madagascar. Among the bizarre features are a mediolaterally compressed and anteroposteriorly bowed tibia, an unusually high number of trunk vertebrae (at least 16 thoracic and 12 lumbar vertebrae), a short tail, and a trochleated navicular facet on the astragalus. Aside from these features, *Adalatherium* displays derived and plesiomorphic characteristics in its pectoral girdle: the coracoid is well developed and contributes to half of the glenoid fossa, a separate procoracoid is absent, and the sternoclavicular joint appears to have been mobile. A ventrally facing scapular glenoid and the well-developed humeral trochlea suggest a relatively parasagittal forelimb posture. Notable features of the hind limb and pelvic girdle include a large obturator foramen similar in size to that of therians, a large parafibula, and the presence of epipubic bones. Articulation between the pelvic girdle and hind limb is in contrast to that between the pectoral girdle and the forelimb in that it is indicative of a sprawling posture.

SUPPLEMENTAL DATA—Supplemental materials are available for this article for free at www.tandfonline.com/UJVP

Citation for this article: Hoffmann, S., Y. Hu, and D. W. Krause. 2020. Postcranial morphology of *Adalatherium hui* (Mammalia, Gondwanatheria) from the Late Cretaceous of Madagascar; pp. 133–212 in D. W. Krause and S. Hoffmann (eds.), *Adalatherium hui* (Mammalia, Gondwanatheria) from the Late Cretaceous of Madagascar. Society of Vertebrate Paleontology Memoir 21. Journal of Vertebrate Paleontology 40(2, Supplement). DOI: 10.1080/02724634.2020.1799818.

INTRODUCTION

The fossil record of Mesozoic mammaliaforms has benefited from a relatively recent increase in postcranial diversity, mainly driven by the discovery of complete skeletons from the Northern Hemisphere, in particular from Asia (see Meng [2014] for a review of the Chinese Mesozoic mammaliaform record). In contrast, associated postcranial specimens are extremely rare from the southern supercontinent Gondwana. To date, only five mammaliaform taxa that are represented by more than isolated elements have been described from the entire Mesozoic of Gondwana. Of these five taxa, only three are known from articulated postcranial material: the morganucodontans *Megazostrodon* and *Erythrotherium* from the Early Jurassic of southern Africa (Crompton and Jenkins, 1968; Crompton, 1974; Jenkins and Parrington, 1976) and the stem therian *Vincelestes* from the Early Cretaceous of Argentina (Bonaparte, 1986; Rougier et al., 1992; Rougier, 1993). In addition to these three taxa, a partial skeleton is known, but has yet to be described or figured, for the eutriconodontan *Argentoconodon* from the Jurassic of Argentina (Gaetano and Rougier, 2011).

The paucity of the Gondwanan fossil record is striking in at least two ways. First, relatively complete mammaliaform specimens are lacking for long geological time intervals. *Megazostrodon* and *Erythrotherium* are known from the Lower Jurassic Upper Member of the Elliot Formation (likely Hettangian–Sinemurian [201.3–190.8 Ma]; Kitching and Raath, 1984; Bordy et al., 2004; Bordy and Eriksson, 2015), whereas *Vincelestes* is known from the Lower Cretaceous La Amarga Formation (Hauterivian–Barremian [132.9–125.0 Ma]; Rougier et al., 2011). Not a single associated or articulated postcranial specimen of a mammaliaform is therefore known from the ~60 myr time interval of the Cretaceous after the occurrence of *Vincelestes*. Second, the preserved specimens come from distantly related clades. *Megazostrodon* and *Erythrotherium* belong to the basalmost mammaliaforms, the Morganucodonta, whereas *Vincelestes* is regarded as a stem therian (Kielan-Jaworowska et al., 2004). In stark contrast, the Mesozoic fossil record of the Northern Hemisphere preserves postcranial specimens from all major mammaliaform clades, including docodontans, eutriconodontans, multituberculates, shuotheriids, haramiyidans, euharamiyidans, spalacotherioids, and several stem and basal therians (see Krause, Groenke, et al., 2020, for a complete list of postcranial specimens). Based on more fragmentary evidence, at least some of these major clades—multituberculates, eutriconodontans, and haramiyidans—are also known to have been present on Gondwana (e.g., Kielan-Jaworowska et al., 2004, 2007; Anantharaman

*Corresponding author.
†Deceased April 12, 2008.

Published online 18 Dec 2020

et al., 2006; Rougier et al., 2011; Gaetano et al., 2013; Krause, 2013; Krause et al., 2017, 2019, and references therein).

The skeleton of *Adalatherium hui*, Université d'Antananarivo (UA) specimen number 9030, from the Anembalemba Member of the Maevarano Formation (uppermost Cretaceous, Maastrichtian), northwestern Madagascar, which was preliminary described and analyzed by Krause, Hoffmann, et al. (2020), fills some of these large gaps: (1) geographically, because it is the first associated or articulated skeleton for a mammaliaform from the Mesozoic of Madagascar; (2) temporally, because it is the first mammaliaform skeleton from the post-Barremian Cretaceous (~60 myr) of Gondwana; and (3) systematically, because it belongs to the Gondwanatheria, an extinct group that is neither particularly basal to nor deeply nested within Mammalia (Krause et al., 2014b; Hoffmann, Beck, et al., 2020; Krause, Hoffmann, et al., 2020). It is noteworthy that the skeleton of *Adalatherium* also represents the first postcranial evidence for the Gondwanatheria. The Late Cretaceous to Paleogene Gondwanatheria were, until recently, only known from isolated teeth and fragmentary lower jaws (see Gurovich, 2006, 2008; Krause, 2013; Krause et al., 2014a). The first cranial specimen, represented by *Vintana sertichi*, was only described in 2014 (Krause et al., 2014b). The skeleton of *A. hui* adds substantially to the fossil record of this enigmatic group of early mammals and offers new insights into the phylogenetic position and paleobiology of Gondwanatheria, as did the cranium of *Vintana* (Kirk et al., 2014; Krause et al., 2014b).

Lastly, the quality of preservation of UA 9030 is remarkable. The specimen is essentially complete, and the individual elements are preserved in three dimensions (Figs. 1–2; Krause, Groenke, et al., 2020). Within Mesozoic mammaliaforms, such exceptional preservation is rarely matched. Despite the fact that fairly complete skeletons are known for several Mesozoic mammaliaforms, in particular those from China (e.g., Ji et al., 2006, 2009; Li and Luo, 2006; Meng et al., 2006, 2011; Yuan et al., 2013; Zheng et al., 2013; Zhou et al., 2013, 2019; Bi et al., 2014, 2018; Meng et al., 2015, 2017; Han and Meng, 2016; Chen et al., 2017; Han et al., 2017; Luo et al., 2017; Mao and Meng, 2019; Wang et al., 2019), they are often strongly compressed and do not allow for observation of their skeletal morphology in multiple views. Postcrania that are largely three-dimensionally preserved and essentially complete are known for the following Mesozoic mammaliaforms: the morganucodontans *Erythrotherium*, *Megazostrodon*, and *Morganucodon* (Jenkins and Parrington, 1976); the docodontan *Haldanodon* (Martin, 2005); the eutriconodontans *Gobiconodon* (Jenkins and Schaff, 1988), *Repenomamus* (Hu, 2006), and *Spinolestes* (Martin et al., 2015); the basal mammaliaform *Fruitafossor* (Luo and Wible, 2005); the multituberculates *Catopsbaatar* (Kielan-Jaworowska et al., 2002; Hurum and Kielan-Jaworowska, 2008), *Chulsanbaatar* (Kielan-Jaworowska and Gambaryan, 1994), *Kryptobaatar* (Kielan-Jaworowska and Gambaryan, 1994; Sereno and McKenna, 1995; Sereno, 2006; Bolortsetseg, 2008), *Mangasbaatar* (originally referred to as the 'Udan multi'; Bolortsetseg, 2008), *Nemegtbaatar* (Kielan-Jaworowska and Gambaryan, 1994), and *Yubaatar* (Xu et al., 2015); the dryolestoid *Henkelotherium* (Krebs, 1991; Jäger et al., 2019); and the stem therian *Vincelestes* (Rougier, 1993). The postcranial skeleton of UA 9030, which preserves nearly every bone, is thus truly exceptional.

Here, we document the morphology of the postcranial skeleton of *Adalatherium* through detailed description and illustration and compare it with those of other Mesozoic mammaliaforms. The phylogenetic context of *Adalatherium* is provided in Hoffmann, Beck, et al. (2020) and Krause, Hoffmann, et al. (2020). The geological context and information on preservation and preparation, both mechanical and digital, are presented in Krause, Hoffmann, et al. (2020) and Krause, Groenke, et al. (2020). The cranium, inner ear, mandible, and dentition of UA 9030 are described in individual chapters in this volume. Functional interpretation of locomotor mode and posture of *Adalatherium* will be published separately.

Institutional Abbreviations—**BMNHC**, Beijing Museum of Natural History, Beijing, China; **CAGS**, Chinese Academy of Geological Science, Beijing, China; **GI PST** (= **GISPS PST)**, Paleontological and Stratigraphic Section of the Geological Institute, Mongolian Academy of Sciences, Ulaanbaatar, Mongolia; **HG-M**, Han Gang collection, housed in the Paleontology Center, Bohai University, Jinzhou, China; **IVPP**, Institute of Vertebrate Paleontology and Paleoanthropology, Chinese Academy of Sciences, Beijing, China; **JZT**, Jizantang Paleontological Museum, Chaoyang, China; **LDNHMF**, Lande Museum of Natural History, Tangshan, China; **NGMC** (**GMV** in Ji et al., 1999), National Geological Museum of China, Beijing, China; **NHMUK**, Natural History Museum, London, U.K.; **NIGAPS**, Nanjing Institute of Geology and Palaeontology, Academia Sinica, Nanjing, China; **NJU**, Nanjing University, Nanjing, China; **PM**, Paleontological Center of the Mongolian Academy of Sciences, Ulaanbaatar, Mongolia; **PMOL**, Paleontological Museum of Liaoning at Shenyang Normal University, Shenyang, China; **PSS-MAE**, Collections of Joint Paleontological and Stratigraphic Section of the Geological Institute, Mongolian Academy of Science, Ulaanbaatar, Mongolia–American Museum of Natural History, New York, New York, U.S.A.; **UA**, Université d'Antananarivo, Antananarivo, Madagascar; **URBAC**, Uzbek-Russian-British-American-Canadian Joint Paleontological Expedition (specimens currently housed at San Diego State University, San Diego, California, U.S.A.); **WGMV**, Museum of Wuyishan Mountain, Wuyishan, China; **ZPAL**, Institute of Palaeobiology, Polish Academy of Sciences, Warsaw, Poland.

Anatomical Abbreviations—**ace**, acetabulum; **acf**, anterior costal facet; **acn**, acetabular notch; **afi**, astragalofibular facet; **afo**, astragalar foramen; **anc**, anconeal process; **ar**, anterior ridge; **as**, astragalus; **av**, anticlinal vertebra; **C**, cervical vertebra; **Ca**, caudal vertebra; **ca**, calcaneus; **caa**, calcaneoastragalar facet; **cacu**, calcaneocuboid facet; **caf**, cranial articular facet for occipital condyle; **cafi**, calcaneofibular facet; **cap**, capitate; **capr**, calcaneal protuberance; **cas**, calcaneal sulcus; **CC**, costal cartilage; **ccap**, contact with capitate; **ce**, centrale; **cl**, clavicle; **cla**, clavicle acromial end; **cls**, clavicle sternal end; **cop**, coronoid process; **cor**, coracoid; **ctzd**, contact with trapezoid; **cu**, cuboid; **cus**, cuboid sulcus; **cvt**, ventral tubercle on caudal vertebra; **DMP**, distal manual phalanx; **dpc**, deltopectoral crest; **dpg**, distal phalangeal groove; **DPP**, distal pedal phalanx; **dr**, dorsal ridge of transverse process; **ect**, ectocuneiform; **ectp**, ectepicondyle; **ent**, entocuneiform; **entf**, entepicondylar foramen; **entp**, entepicondyle; **ents**, entocuneiform sulcus; **epb**, epipubic bone; **exp**, extensor process; **fai**, facet for intercentrum; **fas**, facet for astragalus; **fbr**, fossa for brachialis muscle; **fca**, facet for calcaneus; **fcap**, facet for capitate; **fce**, facet for centrale; **fcu**, facet for cuboid; **fdmp**, facet for distal manual phalanx; **fdpp**, facet for distal pedal phalanx; **fect**, facet for ectocuneiform; **fent**, facet for entocuneiform; **ffi**, facet for fibula; **ffid**, distal facet for fibula; **ffip**, proximal facet for fibula; **fh**, femoral head; **fhl**, facet articulating with humerus lateral to radial condyle; **fhm**, facet for hamate; **fhtr**, facet for humeral trochlea; **fi**, fibula; **fif**, fossa on proximal aspect of fibula; **fimp**, facet for intermediate manual phalanx; **fimr**, fibular medial ridge; **fios**, fibular oblique sulcus; **fipp**, facet for intermediate pedal phalanx; **flu**, facet for lunate; **flxt**, flexor tubercle; **fmc**, facet for metacarpal; **fmes**, facet for mesocuneiform; **fmt**, facet for metatarsal; **fn**, femoral neck; **fna**, facet for navicular; **foc**, fovea capitis; **fomc**, fossa on metacarpal; **fomt**, fossa on metatarsal; **fosd**, facet for os Daubentonii; **fpfi**, facet for parafibula; **fpi**, facet for pisiform; **fpmp**, facet for proximal manual phalanx; **fppp**, facet for proximal pedal phalanx; **fr**, facet for radius; **frc**, facet for radial condyle; **frd**, facet for distal radius; **fsca**, facet for scaphoid; **fses**, facet for sesamoid; **ft**, facet

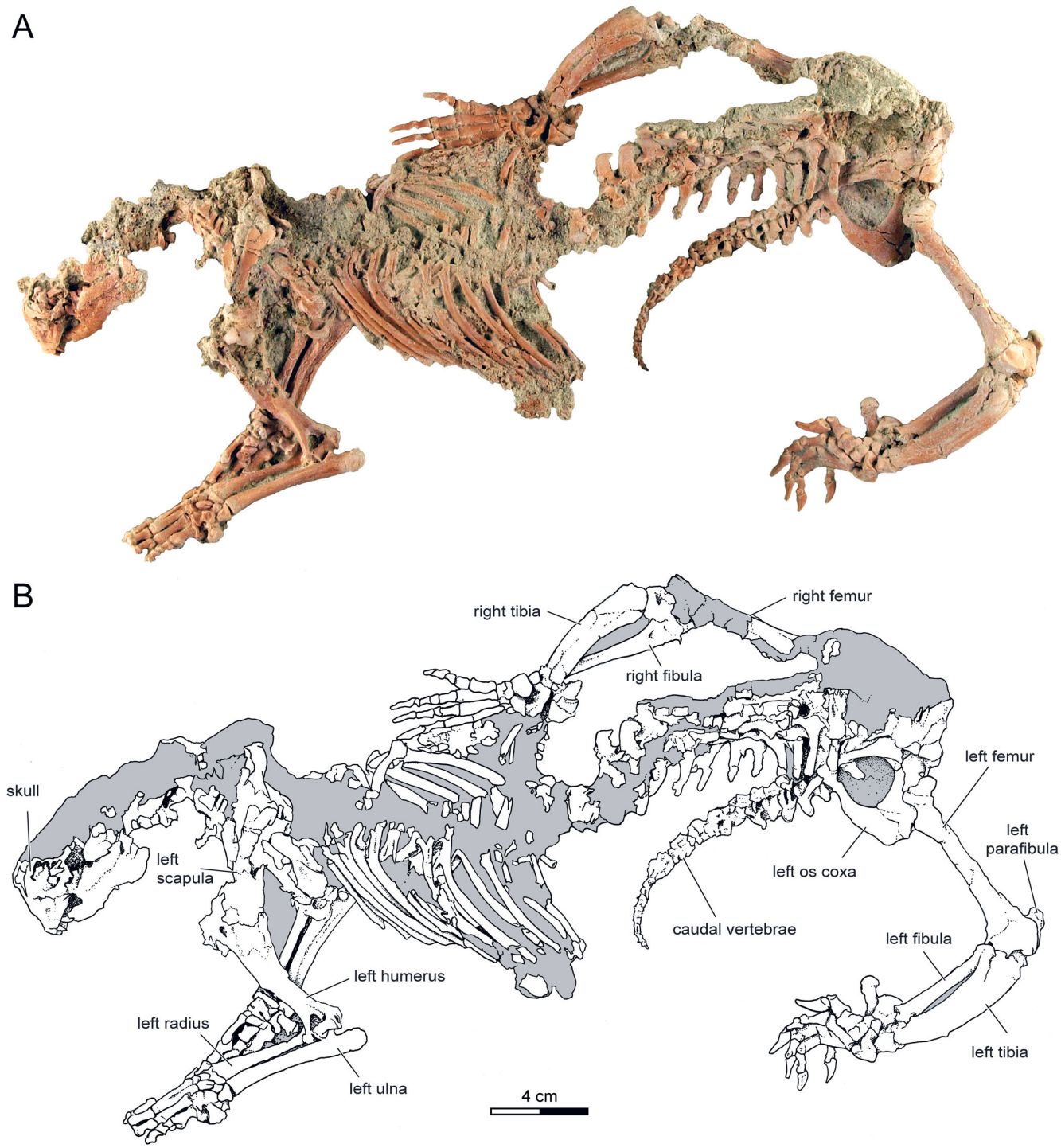

FIGURE 1. Skeleton of *Adalatherium hui*, holotype (UA 9030), in top view as preserved ('side A'), anterior is to left. **A**, photograph; **B**, interpretive drawing. Gray shading in interpretive drawing indicates matrix.

for tibia; **ftrq**, facet for triquetrum; **ftzd**, facet for trapezoid; **ftzm**, facet for trapezium; **fu**, facet for ulna; **glf**, glenoid fossa; **gluf**, gluteal fossa; **gra**, groove for radial artery; **gtr**, greater trochanter; **gtu**, greater tubercle; **hae**, hemal arch; **hh**, head of humerus; **hm**, hamate; **htr**, humeral trochlea; **htrr**, humeral trochlea radial condyle; **htru**, humeral trochlea ulnar condyle; **hu**, humerus; **icf**, intercondylar fossa; **icg**, intercondylar groove; **ifo**, infraspinous fossa; **il**, ilium; **ilf**, iliac fossa; **IMP**, intermediate manual phalanx; **ipe**, iliopubic eminence; **IPP**, intermediate pedal phalanx; **is**, ischium; **isd**, ischial dorsal margin; **isg**, ischial groove; **isr**, ischial ridge; **iss**, ischial spine; **ist**, ischial tuberosity; **itf**, intertubercular fossa; **itg**, intertubercular groove; **itrc**, intertrochanteric crest; **itrf**, intertrochanteric fossa; **L**, lumbar vertebra; **la**, lamina; **lac**, lateral astragalar condyle; **laf**, lateral astragalar facet; **lat**, lateral astragalotibial facet; **lep**, lateral epicondyle; **lfc**, lateral femoral condyle; **lml**, lateral malleolus; **ltc**, lateral tibial condyle;

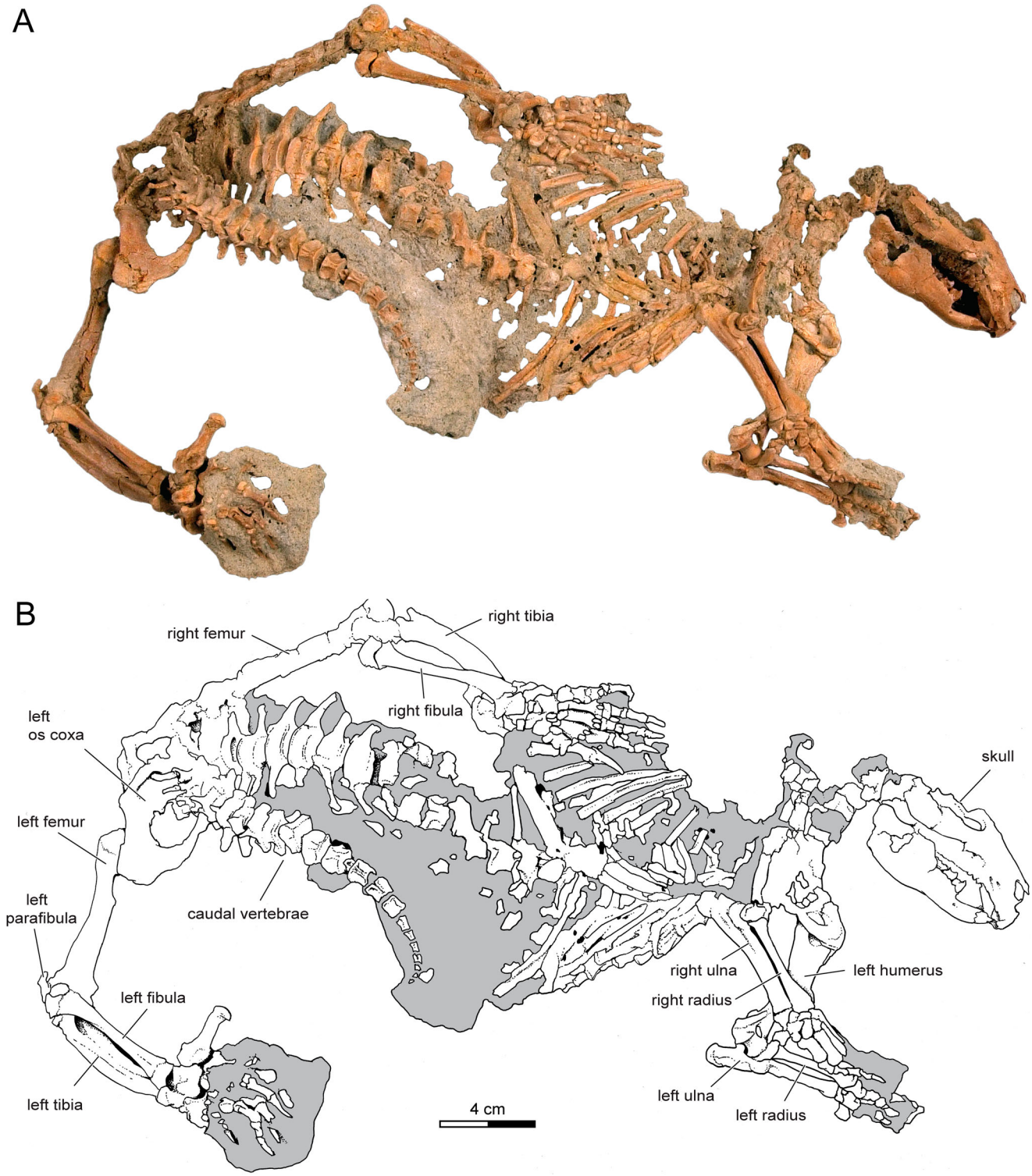

FIGURE 2. Skeleton of *Adalatherium hui*, holotype (UA 9030), in bottom view as preserved ('side B'), anterior is to right. **A**, photograph; **B**, interpretive drawing. Gray shading in interpretive drawing indicates matrix.

ltr, lesser trochanter; **ltu**, lesser tubercle; **lu**, lunate; **lus**, sulcus on lunate; **ma**, manubrium; **mac**, medial astragalar condyle; **maf**, medial astragalar facet; **mat**, medial astragalotibial facet; **Mc**, metacarpal; **mes**, mesocuneiform; **mfc**, medial femoral condyle; **mml**, medial malleolus; **mp**, mammillary process; **mr**, median ridge; **Mt**, metatarsal; **mtc**, medial tibial condyle; **na**, navicular; **nar**, navicular ridge; **nas**, navicular sulcus; **nat**, navicular tuberosity; **nc**, nuchal crest; **nf**, nutrient foramen; **obf**, obturator foramen; **odp**, odontoid process; **olp**, olecranon process; **osc**, os calcaris; **osd**, os Daubentonii; **paf**, posterior articular facet for axis; **pcf**,

posterior costal facet; **pe**, pedicle; **pfb**, parafibular base; **pfm**, parafibular muscular process; **pfn**, parafibular neck; **pfo**, palmar fossa; **pft**, parafibular tuberosity; **pg**, peroneal groove; **pi**, pisiform; **pib**, pisiform base; **pih**, pisiform head; **pin**, pisiform neck; **pir**, pisiform ridge; **pit**, pisiform tubercle; **pk**, palmar/plantar keel; **pli**, plantar lip; **PMP**, proximal manual phalanx; **poz**, postzygapophysis; **pp**, peroneal process; **PPP**, proximal pedal phalanx; **pr**, posterior ridge; **prz**, prezygapophysis; **ps**, pubis; **pss**, pubic symphysis; **pt**, palmar/plantar tuberosity; **ptg**, patellar groove; **R**, rib; **r**, radius; **rar**, radial anterior ridge; **rft**, rectus femoris tuberosity; **rh**, head of rib; **rmr**, radial median ridge; **rn**, neck of rib; **rnt**, radial notch; **rp**, posterior process of rib; **rt**, tubercle of rib; **s**, sulcus; **sc**, scapula; **sca**, scaphoid; **scag**, scaphoid groove; **scc**, scapular concavity; **scn**, scapular neck; **scs**, scapular spine; **ses**, sesamoid; **sfo**, supraspinous fossa; **sgt**, supraglenoid tubercle; **sp**, spinous process; **spf**, spinous process fossa; **spmc**, spinous process median crest; **spt**, spinous process table; **stb**, sternebrae; **stp**, styloid process; **strf**, supratrochlear foramen; **sua**, sustentacular facet; **suf**, subscapular fossa; **supcl**, lateral supracondylar crest (= supinator crest); **supcm**, medial supracondylar crest; **sut**, sustentaculum tali; **T**, thoracic vertebra; **tb**, tibia; **tc**, tuber calcanei; **tcr**, tibial crest; **tmt**, tubercle for teres major attachment; **trcf**, transverse costal facet; **trn**, trochlear notch; **trp**, transverse process; **trpf**, transverse process foramen; **trpn**, transverse process notch; **trq**, triquetrum; **trt**, transverse tubercle; **tt**, tibial tuberosity; **tzd**, trapezoid; **tzm**, trapezium; **uar**, ulnar anterior ridge; **uarm**, ulnar anterior ridge medial crest; **ul**, ulna; **ulc**, ulnar crest; **uls**, ulnar longitudinal sulcus; **vb**, vertebral body; **vfo**, vertebral foramen.

MATERIALS AND METHODS

A detailed account of the discovery, preparation, and computed tomography (CT) scanning of UA 9030 is given by Krause, Groenke, et al. (2020). Only aspects that specifically pertain to the description of the postcranial skeleton are discussed here.

Specimen

The postcranial skeleton of UA 9030 is in articulation, and most of it is exquisitely preserved (Figs. 1, 2); even the tiniest elements such as the distal-most caudal vertebrae and phalangeal sesamoids are present, as is nonosseous tissue (e.g., costal cartilages). However, some areas suffered damage during or after fossilization. The cervical vertebrae are only partly preserved; the anterior thoracic vertebrae are fragmented and disarticulated and were found in a block that was removed from posterior to the shoulder region during preparation. The right scapulocoracoid is entirely missing and might have eroded before discovery. The proximal aspect of the right humerus is preserved at the edge of the jacket; as such, it is possible, although unlikely, that the scapulacoracoid was not jacketed. Three distal phalanges of the left manus were not discovered in articulation due to modern erosion but were recovered from the surface during excavation. The left intermediate phalanx of digit IV and one left distal phalanx (probably also of digit IV) have not been recovered. Lastly, although the left hind limb is in articulation with the pelvis, the hind limbs and pelvis were contorted and are preserved twisted underneath the trunk so that the posterior part of the pelvis points anteriorly. This twisting appears to have contributed to severe damage of the sacral region. The sacral vertebrae and most of the left ilium are comminuted. In addition, the right epipubic bone and os coxa (aside from a possible fragment of the right ilium) are missing.

Mechanical Preparation

Both sides of UA 9030 were mechanically prepared in the Vertebrate Fossil Preparation Laboratory at Stony Brook University (SBU) and exposed for study (Figs. 1, 2). Photographic images of UA 9030 were taken at different stages of preparation. Figure 1 shows the 'top view' (as preserved) of the specimen at an early stage of preparation (note that a loose section of thoracic vertebrae between T5 and T16 was already removed from the specimen). The 'top view' will be referred to here as side A. The specimen was later flipped to prepare the 'bottom view' (side B) shown in Figure 2. The left forelimb (except the humerus) and left hind limb were later removed from the specimen and disarticulated for more detailed description and higher resolution scanning. The pelvis and all caudal vertebrae were also separated from the specimen but were kept partially articulated. In 2016, the articulated postcranium was deliberately separated into anterior and posterior portions to facilitate micro-CT (μCT) imaging.

Computed Tomography

The postcranial skeleton of UA 9030 was scanned at various facilities. The articulated specimen (excluding the left antebrachium, carpus, and manus; left hind limb; pelvis; and caudal vertebrae) was scanned at the GE Lightspeed VCT 64-source medical CT scanner in the Stony Brook University Department of Radiology (kV = 140; μA = 360; voxel size = 0.3457 mm × 0.3457 mm × 0.2 mm). The disarticulated left antebrachium, carpus, manus, and hind limb, as well as a partial series of thoracic vertebrae (T5–T16), the pelvis, and articulated caudal vertebral series were later scanned on the GE eXplore Locus in vivo μCT scanner at The Ohio University μCT Facility. The ulna, radius, femur, tibia, fibula, parafibula, calcaneus, and cuboid were scanned at 80 kV, 498 μA, and a voxel size of 0.089564 mm × 0.089564 mm × 0.089564 mm. The thoracic and caudal vertebrae, pelvis, metacarpals, metatarsals, remaining tarsals, all carpals, and pedal and manual proximal and intermediate phalanges were also scanned at 80 kV and 498 μA, but with a resultant voxel size of 0.044782 mm × 0.044782 mm × 0.044782 mm. Finally, the distal pedal and manual phalanges were scanned at kV = 70, μA = 114, and a voxel size of 0.019927 mm × 0.019927 mm × 0.019927 mm. The pelvis was rescanned at the New York Institute of Technology Visualization Center at kV = 130, μA = 61, and a voxel size of 0.071 mm × 0.071 mm × 0.071 mm. A small block that was removed posterior to the pectoral girdle during preparation and which contained fragments of thoracic vertebrae T1–T4 was scanned on the Nikon XTek XT H 225 μCT scanner at Yale University (voxel size = 0.02630699 mm × 0.02630699 mm × 0.02630699 mm). The separated anterior and posterior parts of the articulated specimen were scanned using the GE Phoenix V|tome|x s μCT scanner at the Microscopy and Imaging Facility at the American Museum of Natural History (anterior part at kV = 200, μA = 230, and voxel size = 0.10828451 mm × 0.10828451 mm × 0.10828451 mm; posterior part at kV = 200, μA = 230, and voxel size = 0.0890563 mm × 0.0890563 mm × 0.0890563 mm). In addition, a focused scan of the pectoral region (kV = 200; μA = 230; voxel size = 0.06523045 mm × 0.06523045 mm × 0.06523045 mm) was conducted at the same facility. The atlas was reconstructed based on a scan of the cranium at the High-Resolution X-ray Computed Tomography Facility in the Department of Geological Sciences at the University of Texas at Austin (kV = 190; μA = 250; voxel size = 0.0224 mm × 0.0224 mm × 0.0224 mm). A complete list of all scans of postcranial elements is included in Supplemental Data (Table S1).

Digital Preparation

Segmentation—DICOM and TIFF stacks were rendered into polygonal surface models using Avizo 8.1 and Amira 6.5 'Isosurface' and 'Volume Rendering' options, as well as through labeling individual voxels in the Label Field Editor and extracting polygon surface files of labeled materials. These surface files were used to digitally rearticulate the skeleton as well as virtually reconstruct fragmentary elements (e.g., atlas, thoracic vertebrae, astragalus). Surface files of all elements were saved as .obj files in Amira 6.5 and imported into Geomagic Wrap for postprocessing.

Surface Smoothing and Reconstruction—Surfaces were imported into Geomagic Wrap for smoothing and repair. In Geomagic Wrap, we first applied the 'Mesh Doctor' function. To smooth and further clean surfaces, we applied the 'Reduced Spikes' filter and the 'Reduce Noise' function. We deleted unconnected faces and wrapped the surface using the 'Rewrap' function. A final application of 'Mesh Doctor' was performed before saving the surface files. We generally used surface files from isolated elements of the left side that were scanned at higher resolution. In cases where left elements were missing (intermediate manual phalanx IV, distal manual phalanx IV) or incomplete (intermediate manual phalanx III, tibia, astragalus, calcaneus, entocuneiform, mesocuneiform, ectocuneiform, metacarpal III), we mirrored the surface files of the right elements in Geomagic Wrap and either used these files exclusively or substituted missing parts of individual bones. A similar protocol was used to reconstruct the atlas and selected thoracic and lumbar vertebrae. Preserved and sometimes displaced parts of each vertebra (e.g., vertebral body, transverse process, spinous process) were loaded into Geomagic Wrap and manually moved and assembled. The final surfaces were mirrored to substitute missing parts of each vertebra. High-resolution surface files of all elements were saved as .ply files and are available on MorphoSource.

Skeletal Reconstruction—Surface files that were used in the skeletal reconstruction needed to be further simplified in Geomagic Wrap using the 'Decimate Faces' function. We used a 90% reduction with subsequent smoothing through the 'Reduce Noise' function. Final files were saved in .stl format and imported into Autodesk 3ds Max. We first assembled the left forelimb and left hind limb and then mirrored the limbs to represent the right forelimb and right hind limb. Similarly, the left ribs, left clavicle, left scapulocoracoid, and left os coxa were mirrored to produce the rib cage, pectoral girdle, and pelvic girdle. Lastly, the left halves of the cervical vertebrae were mirrored to present more complete cervicals. The full skeletal reconstruction is available on MorphoSource.

Imaging

Images of isolated elements were taken in Amira 6.5 using the 'Snapshot' tool. Surface files were displayed in Amira using the following 'Surface View' options: 'Specular' off, 'Opaque,' 'Both Faces,' and either 'Vertex normals' or 'Triangle normal.' For isolated elements or the vertebral series, standard light and dark gray values were chosen. Photographic images of the specimen were taken at different stages of preparation.

Measurements

Linear measurements of skeletal elements were taken either on the original specimen using a handheld Mitutoyo CD-8″C digital caliper or on reconstructed surfaces using the Avizo 8.1 or Amira 6.5 '3D Length' tool. Angular measurements were extracted from digital surfaces using the Avizo 8.1 '3D Angle' tool. Humeral torsion was measured as the angle between the distal epicondyles and the deflection of the head following Kielan-Jaworowska and Gambaryan (1994). The latter is represented by a line that is orthogonal to a line through the middle of the intertubercular groove and the middle of the posterior surface of the head. In UA 9030, the intertubercular groove is damaged proximally on both sides. Its position was approximated by extending the intertubercular groove proximally to a point midway between the greater and lesser tubercles. Measurements and ratios of the postcranial skeletal elements of UA 9030 are provided in the data tables listed below.

Comparative Material

In addition to UA 9030, the following mammaliaform taxa (and specimens) were examined for comparison: *Agilodocodon scansorius* (BMNHC 001138), *Arboroharamiya allinhopsoni* (HG-M017, HG-M018), *Catopsbaatar catopsaloides* (PM 120/107), *Chulsanbaatar vulgaris* (ZPAL MgM-I/61, ZPAL MgM-I/83, ZPAL MgM-I/84, ZPAL MgM-I/85, ZPAL MgM- I/99b, ZPAL MgM-I/140, ZPAL MgM-I/151, ZPAL MgM-I/170a), *Docofossor brachydactylus* (BMNHC 131735), *Eomaia scansoria* (BMNHC 1140), *Juramaia sinensis* (BMNHC 1143), *Kryptobaatar dashzevegi* (ZPAL MgM-I/41, GI PST 8-2), *Liaoconodon hui* (IVPP 16051), *Maiopatagium furculiferum* (BMNHC 2940), *Megaconus mammaliaformis* (PMOL AM00007), *Megazostrodon rudnerae* (NHMUK M26407), *Morganucodon watsoni* (Welsh material in the collections of Cambridge University [*Eozostrodon* postcrania (*Eo*. PC) 1–100] and NHMUK), *Nemegtbaatar gobiensis* (ZPAL MgM-I/81, ZPAL MgM-I/82, ZPAL MgM-I/110), *Qishou jizantang* (JZT-D061), *Qishou* sp. (JZT-CK005), *Repenomamus giganticus* (IVPP 14155), *Repenomamus robustus* (IVPP 12728), *Rugosodon eurasiaticus* (BMNHC 1142), *Shenshou lui* (WGMV-001, LDNHMF 2001), *Sinobaatar lingyuanensis* (IVPP 12517), *Vilevolodon diplomylos* (BMNHC 2942), *Xianshou linglong* (IVPP 16707), *Xianshou songae* (BMNHC 003253), *Zhangheotherium quinquecuspidens* (IVPP 7466), and an unidentified taeniolabidoid multituberculate (ZPAL MgM-I/165; see Kielan-Jaworowska, 1989). In addition, casts of the following species were observed: *Akidolestes cifellii* (NIGAPS 139381), *Eomaia scansoria* (CAGS 01/G1), *Jeholodens jenkinsi* (GMV 2139), *Sinodelphys szalayi* (CAGS 00-IG-03), *Yanoconodon allini* (NJU-P06001), and *Zhangheotherium quinquecuspidens* (CAGS-IG99-07352). Only direct observations of specimens or casts are listed here. Specimens for which only published illustrations and descriptions were utilized are cited accordingly in the text. Taxa listed in the text without citation of the literature indicates personal observation of specimens.

DESCRIPTION

Postcranial Axial Skeleton

The postcranial axial skeleton comprises the vertebral column, ribs, and sternal apparatus, which are generally well preserved in UA 9030; only the cervical and sacral regions suffered considerable damage (Figs. 1, 2). Typical vertebrae from each of the four different regions (excluding the sacral) are easily distinguishable from one another. Transitions between neighboring regions (e.g., between cervical and thoracic, lumbar and sacral, or sacral and caudal vertebrae), however, with the exception of the thoracolumbar transition, are difficult to discern in UA 9030 due to damage. As will be discussed in the following sections, the vertebral formula for *Adalatherium* was likely as follows: seven cervical (C), at least 16 thoracic (T), at least 12 lumbar (L), an unknown number of sacral, and at least 24 caudal (Ca) vertebrae.

Atlas—Both halves of the atlantal neural arch are preserved in UA 9030 but are displaced and disarticulated. The better-preserved right half can be seen posterior to the nuchal crest

(Fig. 3A). The left half of the neural arch is fragmented into several pieces and obscured from view by sediment, but μCT images clearly reveal its presence (Fig. 3). Due to the fragmentary nature of this left half, the right half was mirrored for reconstruction of the atlas in Figure 4. The preserved portion of the atlas indicates that it is a robust element with an anteroposteriorly long lamina and a large vertebral foramen. In lateral view, the lamina of the neural arch is roughly triangular in shape, narrower ventrally and expanded dorsally. At its base, the lamina is robust and transversely wide but thins dorsomedially. The dorsal-most part of the lamina is damaged, leaving it uncertain whether the left and right halves of the neural arch were fused along the midline in life. The anterior and posterior edges of the lamina are smooth, and there is neither a facet for a proatlas on the anterior edge nor a postzygapophysis for the axis on the posterior edge, as is typical for mammals (Jenkins, 1970, 1971). The pedicle is completely preserved, as are the facet for the occipital condyle anteriorly and the facet for the axis posteriorly (Fig. 4). The cranial articular facet for the occipital condyle is large, concave, and elliptical in outline (with its long axis oriented in a ventrolateral to dorsomedial direction). Based on the reconstructed atlas, it appears that the occipital facet likely faced anteromedially, but the exact orientation of the facet is difficult to establish due to poor preservation of the atlas. The posterior articular facet for the axis is slightly concave and faces posteroventromedially. It has a stout base protruding posteromedially from the pedicle. The base of a ventrolaterally directed transverse process is preserved along the lateral aspect of the pedicle. Compared with the width of the lamina and pedicle, the base of the transverse process is relatively slender. It is unclear whether an atlantal rib articulated with this process in life. The intercentrum is not preserved in UA 9030; however, a flat but rough area on the ventral side of the pedicle indicates its presence (Figs. 3B′, 4E). The rough texture of the surface suggests that the intercentrum may not have been completely fused to the neural arch in life.

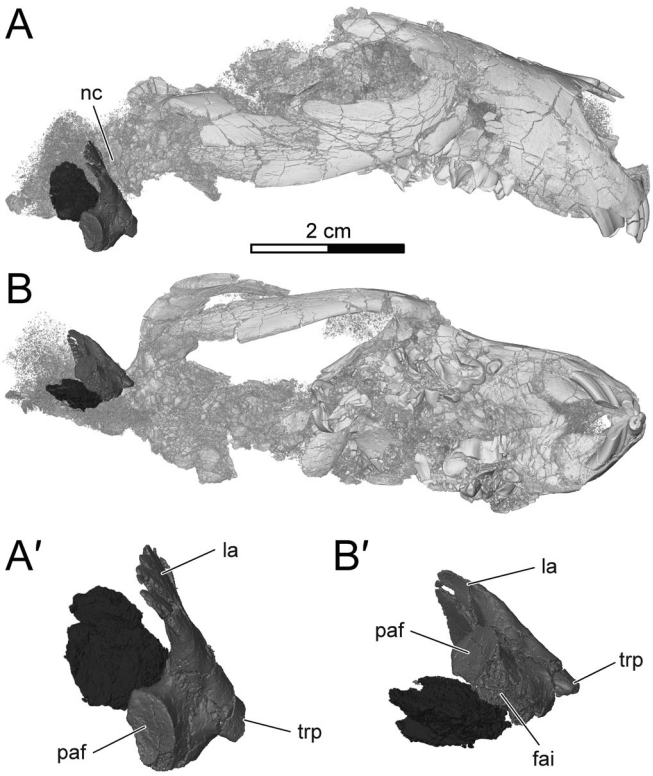

FIGURE 3. Atlas and cranium of *Adalatherium hui*, holotype (UA 9030), based on μCT reconstruction, in **A**, **A′**, right lateral; and **B**, **B′**, ventral views. **A**, **B**, cranium and atlas; **A′**, **B′**, isolated atlas (enlarged 2× size of **A** and **B**). Right neural half of atlas rendered in medium gray; left neural half of atlas rendered in dark gray. **Abbreviations**: **fai**, facet for intercentrum; **la**, lamina; **nc**, nuchal crest; **paf**, posterior articular facet for axis; **trp**, transverse process.

Axis—The right half of the neural arch, including part of the pedicle, and possibly part of the odontoid process (= dens) and postzygapophysis of the axis (C2) are preserved in UA 9030 (Fig. 5). The lamina is dorsoventrally tall and anteroposteriorly expanded. The anterior and posterior edges of the lamina are straight, and the lateral surface is almost flat. The preserved portion of the pedicle has a flat lateral surface and is anteroposteriorly much shorter than the lamina. A short and stout transverse process projects posteroventrally from the pedicle. The μCT images reveal a cylindrical structure deep and anterior to the lamina of the axis that resembles the shape of an odontoid process (Fig. 5).

Postaxial Cervical Vertebrae—The postaxial cervical vertebrae (C3–C7) are only partially preserved (Fig. 5). The transition between the cervical and thoracic vertebrae is not preserved in UA 9030. It therefore remains possible, although unlikely, that additional cervical vertebrae were present in *Adalatherium*. However, mammals are very conservative in the number of cervical vertebrae in that nearly all mammals have seven (Galis, 1999; Narita and Kuratani, 2005), as do most other synapsids

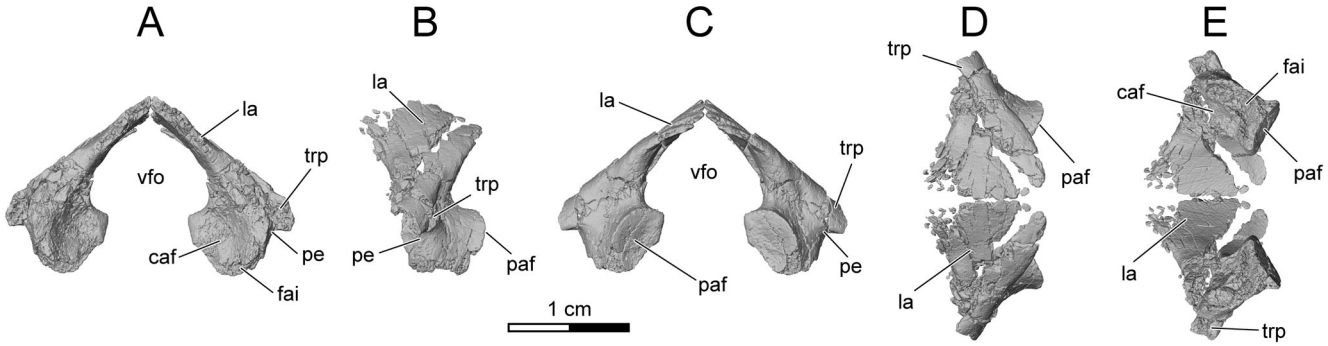

FIGURE 4. Atlas of *Adalatherium hui*, holotype (UA 9030), reconstruction based on μCT images, in **A**, anterior; **B**, left lateral; **C**, posterior; **D**, dorsal; and **E**, ventral views. Dorsal to top in **A, B**, **C**; anterior to left in **B**, **D**, **E**. Right neural arch mirrored from left side. **Abbreviations**: **caf**, cranial articular facet for occipital condyle; **fai**, facet for intercentrum; **la**, lamina; **paf**, posterior articular facet for axis; **pe**, pedicle; **trp**, transverse process, **vfo**, vertebral foramen.

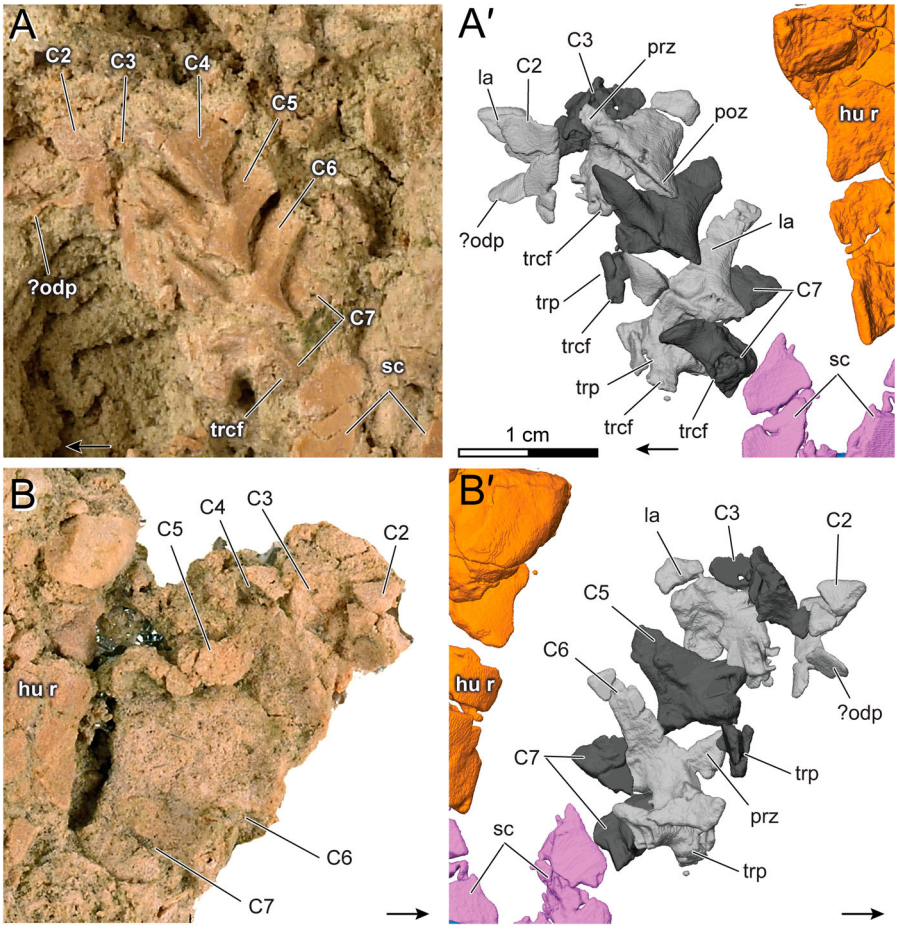

FIGURE 5. Cervical region of *Adalatherium hui*, holotype (UA 9030), in **A**, **A′**, top (side A); and **B**, **B′**, bottom (side B) views. **A**, **B**, photographs of original specimen; **A′**, **B′** reconstruction based on µCT images, with cervical vertebrae in gray tones, right humerus in orange, and left scapula in purple. Light and dark gray shades are used to distinguish between adjacent vertebrae, or parts thereof. Arrows point anteriorly. **Abbreviations**: **C**, cervical vertebra; **hu r**, right humerus; **la**, lamina; **odp**, odontoid process; **poz**, postzygapophysis; **prz**, prezygapophysis; **sc**, scapula; **trcf**, transverse costal facet; **trp**, transverse process.

(Crompton and Jenkins, 1973). It is likely that UA 9030 is no exception, and we assume a cervical vertebral count of seven for *Adalatherium* as well.

The preservation of the postaxial vertebrae is inconsistent across the cervical series. C3 preserves only part of the left lamina, whereas C4–C6 each preserves the left lamina, pre- and postzygapophyses, pedicle, and transverse process. C7 preserves only the left prezygapophysis and partial lamina. The laminae of the postaxial cervical vertebrae are anteroposteriorly short and dorsoventrally tall, indicative of large vertebral foramina. The bases of the laminae are anteroposteriorly expanded and gently narrow dorsally. The anteroventral parts of the laminae are deeply excavated on C5 and C6 to accommodate the postzygapophyses of preceding vertebrae. The prezygapophyses on these same vertebrae are large and protrude anteriorly beyond the anterior margins of the neural arches. The articular facets of the prezygapophyses on C5 and C6 are flat and face dorsally, almost in a horizontal plane (nearly perpendicular to the direction of the laminae), whereas the articular facet of the preserved prezygapophysis on C7 is rounded and its anterior tip gently bends ventrally. The postzygapophyses of C4–C6 extend posteriorly beyond the margin of the neural arch, but to a lesser degree than the prezygapophyses extend anteriorly (Fig. 5).

The left pedicles of C4–C6 are only partially preserved. The preserved dorsal portion of each pedicle is anteroposteriorly broad. The dorsal roots of the transverse processes emerge ventral to the posterior aspects of the prezygapophyses of C4–C6. They are slender and project ventrolaterally, each ending in a distinct, rounded costal facet for a cervical rib (Fig. 5). On C7, the dorsal root of the transverse process is much shorter and stouter, resulting in a costal facet for the cervical rib that is immediately ventral to the prezygapophysis. The costal facet for the cervical rib is larger in diameter on C7 than those on C4–C6. The ventral roots of the transverse processes as well as the vertebral bodies are not preserved on any of the postaxial cervical vertebrae. Together with the cervical rib, the dorsal and ventral roots of the transverse process of each vertebra would have enclosed a transverse foramen in life. The medial sides of the neural arches can be seen in the reconstructed surfaces (Fig. 5B′), but their poor preservation obscures considerable morphological detail. Additional unidentifiable fragments of cervical vertebrae are present next to the broken right humerus as well as surrounding the more intact parts of the cervical series.

Thoracic Vertebrae—In *Adalatherium*, we identify thoracic vertebrae as those dorsal vertebrae with free ribs, similar to the condition in extant mammals. This definition, however, is not applicable to all mammaliaforms. Several Mesozoic mammaliaforms retain mobile lumbar ribs and the thoracolumbar transition is defined by other morphological characteristics (e.g., orientation of zygapophyses, shape of vertebral body, shape and size of ribs). In *Adalatherium*, the orientation of the zygapophyses does not change much along the dorsal vertebral series and the shape of the vertebral bodies changes gradually; a clear transition is not noticeable in either zygapophyses or vertebral bodies. Of those characteristics used to distinguish thoracic and lumbar vertebrae in mammaliaforms, presence of mobile ribs can be most clearly recognized in *Adalatherium*.

The thoracic vertebral series of UA 9030 is mediolaterally compressed, and each individual vertebra suffered some damage, albeit to varying degrees. However, the preserved parts are sufficient to reconstruct the general morphology of the series and of most individual vertebrae (Figs. 6, 7). *Adalatherium* had at least 16 thoracic vertebrae (T). An already loose section of 12 articulated thoracic vertebrae (identified as T5–T16) was detached from the specimen during preparation, with the exception of the right halves of the four posterior-most vertebrae of this section, which remain in articulation with the rest of the specimen (Fig. 8). In addition to this articulated series of 12 vertebrae, there are parts of at least four thoracic vertebrae preserved in another block that was removed posterior to the shoulder region. The space between the last cervical and first articulated thoracic vertebra (T5) is large enough to accommodate at least these four thoracic vertebrae. Hence, we conclude that *Adalatherium* had at least 16 thoracic vertebrae. Because the cervicothoracic transition is not preserved in articulation in UA 9030, it is possible

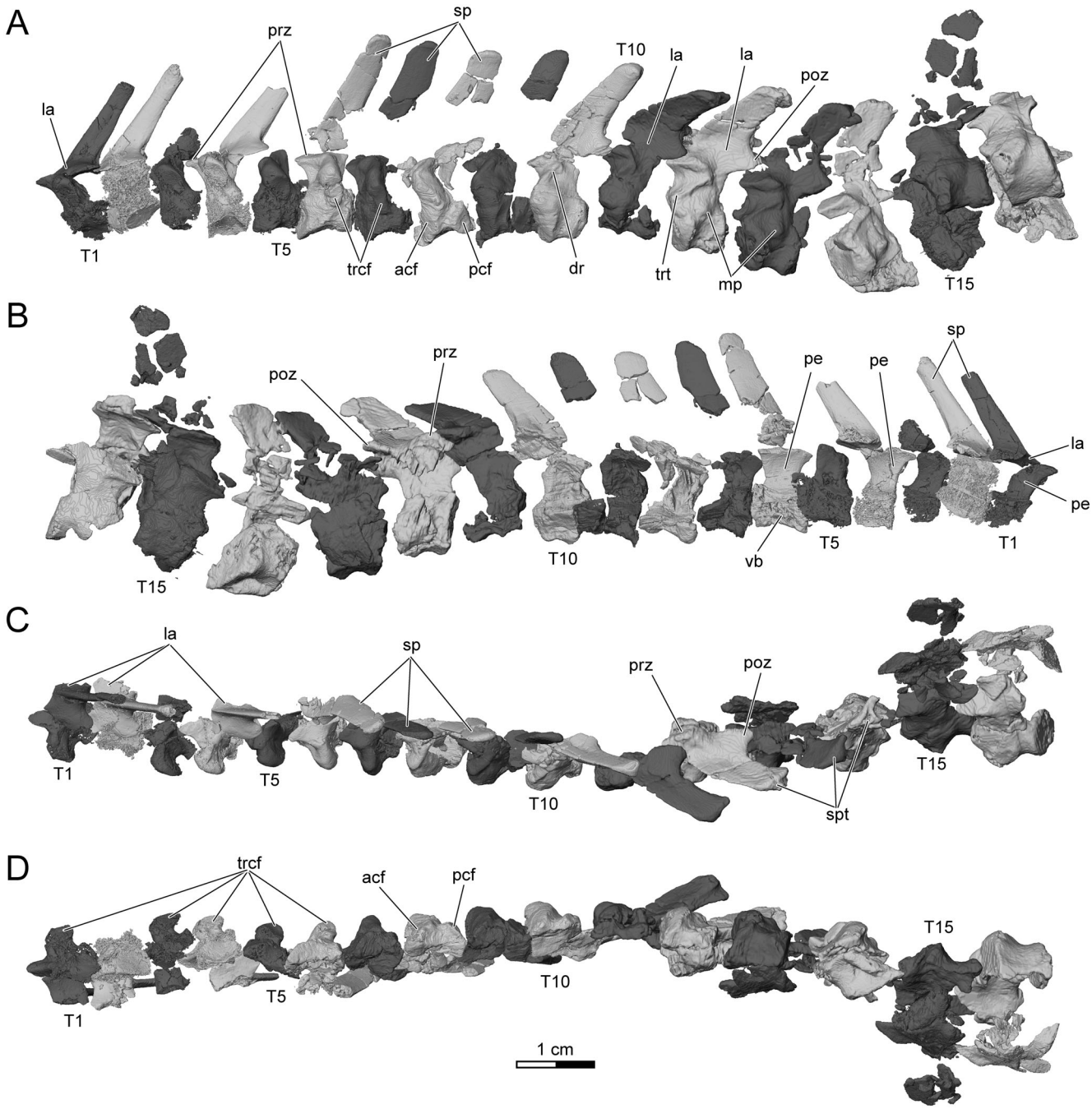

FIGURE 6. Thoracic vertebrae (T1–T16) of *Adalatherium hui*, holotype (UA 9030), in **A**, left lateral, **B**, right lateral, **C**, dorsal, and **D**, ventral views. Light and dark gray shades are used to distinguish between adjacent vertebrae, or parts thereof. **Abbreviations**: **acf**, anterior costal facet; **dr**, dorsal ridge of transverse process; **la**, lamina; **mp**, mammillary process; **pcf**, posterior costal facet; **pe**, pedicle; **poz**, postzygapophysis; **prz**, prezygapophysis; **sp**, spinous process; **spt**, spine process table; **T**, thoracic vertebra; **trcf**, transverse costal facet; **trt**, transverse tubercle; **vb**, vertebral body.

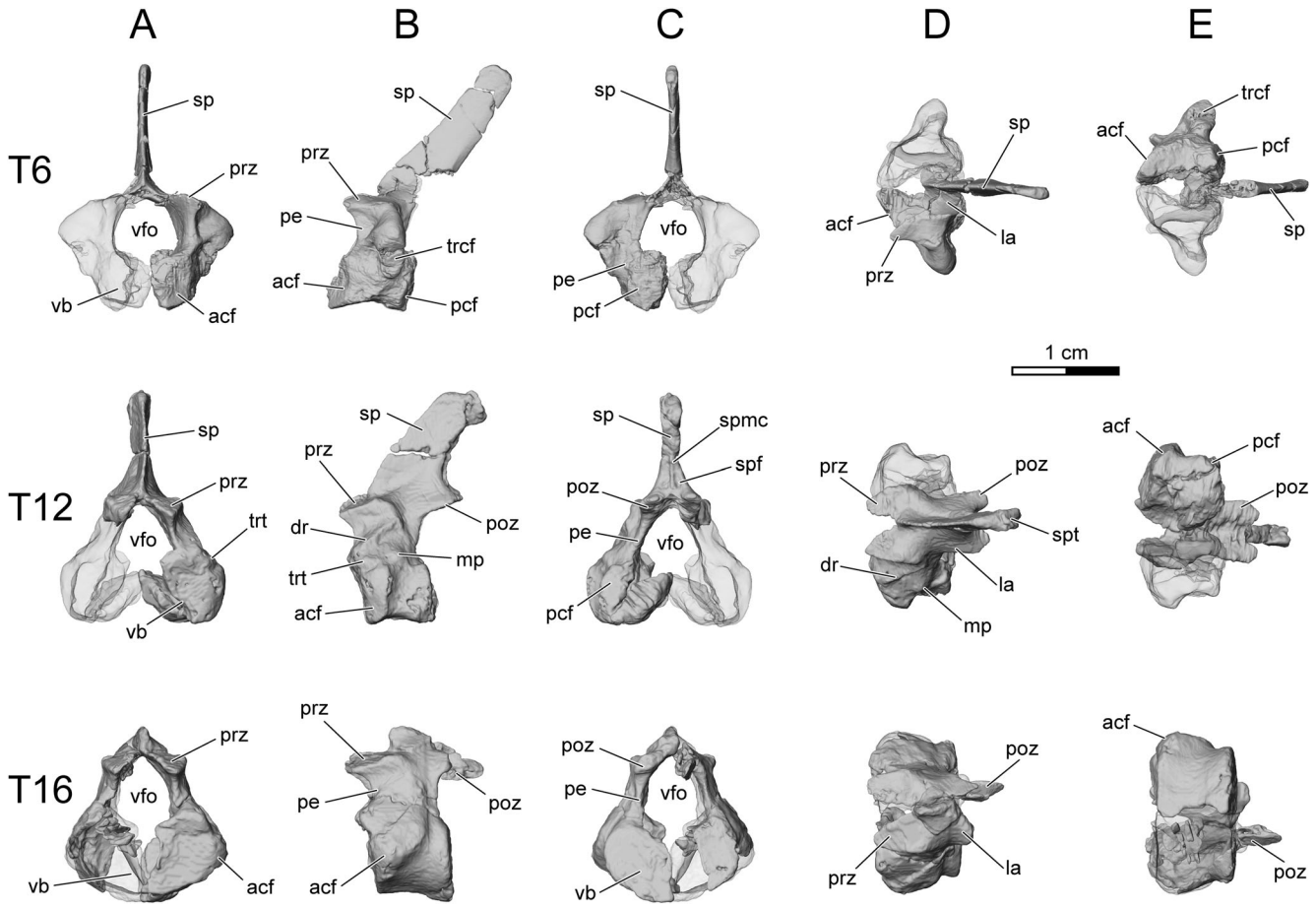

FIGURE 7. Reconstruction of selected thoracic vertebrae of *Adalatherium hui*, holotype (UA 9030), in **A**, anterior, **B**, left lateral, **C**, posterior, **D**, dorsal, and **E**, ventral views. Rows from top to bottom: T6, T12, and T16. Preserved elements are rendered as solid; mirrored elements are semitransparent. Dorsal to top in **A**, **B**, **C**; anterior to left in **B**, **D**, **E**. **Abbreviations**: **acf**, anterior costal facet; **dr**, dorsal ridge of transverse process; **la**, lamina; **mp**, mammillary process; **pcf**, posterior costal facet; **pe**, pedicle; **poz**, postzygapophysis; **prz**, prezygapophysis; **sp**, spinous process; **spf**, spinous process fossa; **spmc**, spinous process median crest; **spt**, spinous process table; **T**, thoracic vertebra; **trcf**, transverse costal facet; **trt**, transverse tubercle; **vb**, vertebral body; **vfo**, vertebral foramen.

that some anterior thoracic vertebrae are missing and that the number of thoracic vertebrae was even higher. However, based on the available space between the preserved cervicals and thoracics, we doubt that the number of thoracic vertebrae was much higher than 16. For the purposes of this study and to be able to refer to specific thoracic vertebrae, we will adopt the hypothesis that *Adalatherium* had 16 thoracic vertebrae: T1–T4 are disarticulated and preserved in a small block posterior to the scapula, T5–T12 as well as the left halves of T13–T16 were removed during preparation, and the right halves of T13–T16 remain in articulation anterior to the lumbar vertebrae (Figs. 8, 9).

Each thoracic vertebra has an anteroposteriorly stout body (centrum), which is platycoelous and roughly kidney-shaped in cross-section, mediolaterally wider than dorsoventrally deep (Fig. 7). In ventral view, the vertebral body is constricted at mid-length; it is concave transversely and anteroposteriorly. A mid-ventral keel along the ventral aspect of the vertebral body is absent in *Adalatherium*. The anteroventral corner of each vertebral body bears a concave anterior costal facet. The posterior costal facets are slightly smaller than the anterior costal facets and articulate with the heads of the following ribs. Both the anterior and posterior costal facets decrease in size relative to the vertebral body on more posterior vertebrae. Whereas the anterior costal facets are present on all thoracic vertebrae, the posterior costal facets are barely visible on T12–T15 and are absent on T16.

The pedicles contact the dorsolateral edges of each vertebral body and are obliquely oriented (anterodorsally to posteroventrally) in T1–T4 and almost vertically oriented from T5 on. They are indented both anteriorly and posteriorly, with the anterior margins being more concave than the posterior margins. The pedicles of neighboring vertebrae enclose a sizable intervertebral foramen. The lateral aspects of the pedicles in anterior thoracic vertebrae bear a distinct transverse process that is directed ventrolaterally (Fig. 6). On T1–T7, the transverse processes are prominent and arise along the full height of the pedicles. The facets for the tubercles of the ribs are large and concave and separated from the anterior costal facets on the body by distinct notches (Figs. 6, 7). On T8–T10, the transverse processes are more anteroposteriorly slender and mediolaterally shorter and gradually shift anteroventrally. The transverse costal facets are smaller and less separated from the anterior costal facets for the heads of the ribs (Fig. 6). From T11 on, the transverse processes are indistinct and the facets for the tubercle and head converge. A small ridge (dorsal ridge of transverse process) extends posterodorsally from each transverse process or tubercle and terminates posteroventral to the prezygapophysis in posterior thoracic vertebrae (Figs. 6, 7). On T1–T7, the dorsal

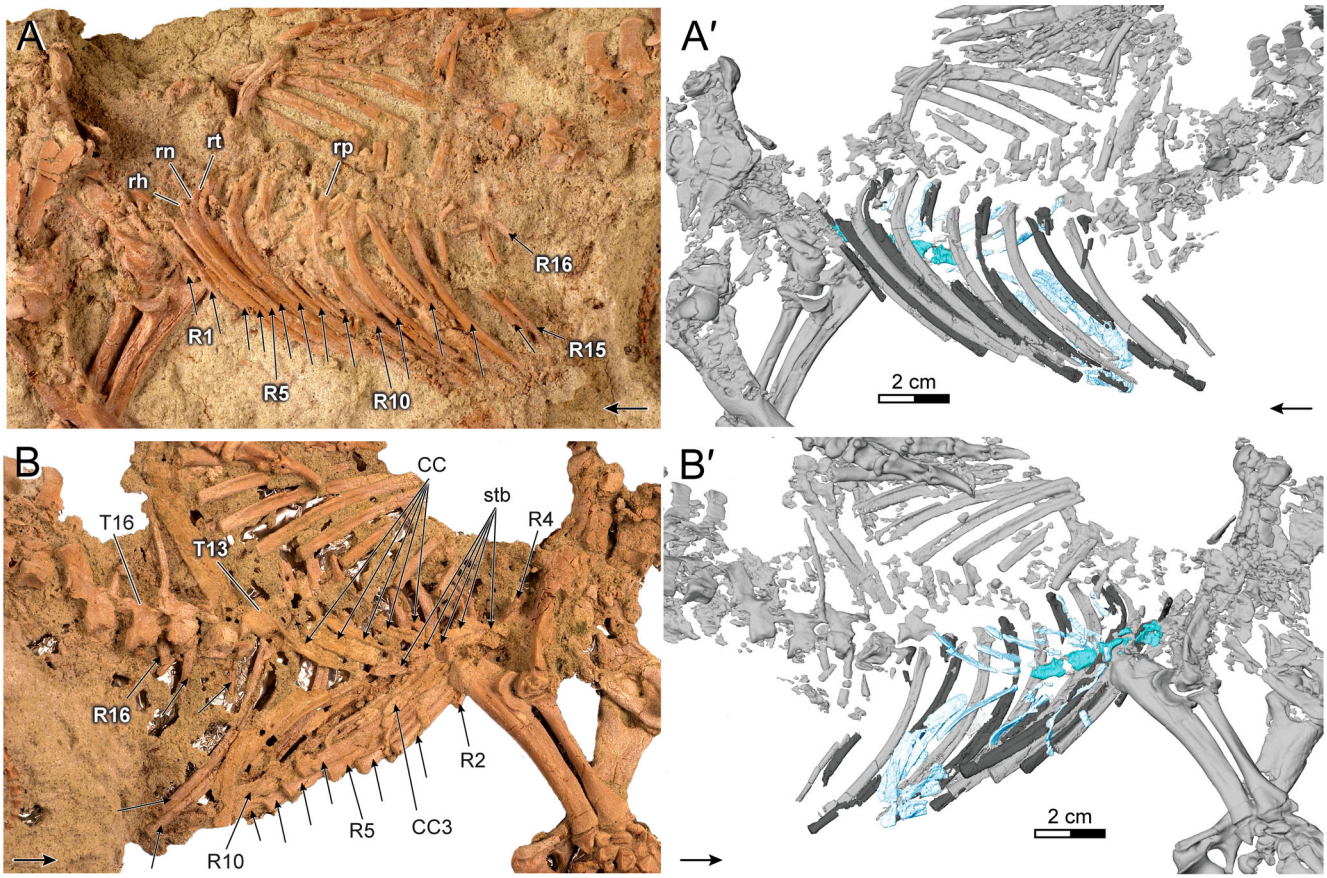

FIGURE 8. Ribs, costal cartilages, and sternebrae of *Adalatherium hui*, holotype (UA 9030), in **A**, **A′**, top (side A); and **B**, **B′**, bottom (side B) views. **A**, **B**, photographs of original specimen; **A′**, **B′**, rendering based on µCT images. All labeled ribs belong to left side, whereas costal cartilages belong to right side, except third costal cartilage (CC3), which is labeled on left side. Light and dark gray shades are used to distinguish between adjacent ribs, or parts thereof. Costal cartilages rendered in light blue; sternebrae rendered in turquoise. Arrows point anteriorly. **Abbreviations**: **CC**, costal cartilage; **R**, rib; **rh**, head of rib; **rn**, neck of rib; **rp**, posterior process of rib; **rt**, tubercle of rib; **stb**, sternebrae; **T**, thoracic vertebra.

ridges of the transverse processes are indistinct from the transverse processes. From T8 on, the dorsal ridges are slender and sharper (Fig. 6). The dorsal ridges gradually change direction from more vertical to oblique between T8 and T14. On T14 and T15, the dorsal ridges are fine crests extending from the transverse tubercles posterdorsally. The dorsal ridges appear indistinct on T16. Posteroventral to each dorsal ridge and posterior to each transverse tubercle on T12–T14 is a small but distinct mammillary process (Figs. 6, 7). The process is separated from the transverse tubercle by a shallow notch.

The pre- and postzygapophyses extend farther anteriorly and posteriorly, respectively, than the body or the pedicle. The articular facet of each prezygapophysis is flat, facing dorsally and slightly anterolaterally. Each postzygapophysis completely overhangs the posterior end of its corresponding vertebral body. Its articular surface faces ventrally and slightly posteromedially. There are no anapophyses below the postzygapophyses. Interestingly, the orientation of the pre- and postzygapophyses does not change much along the thoracic series.

The left and right laminae of each vertebra converge dorsomedially and support a dorsoventrally tall spinous process. The spinous processes of T1–T4 are separated from, but preserved in association with, the vertebral bodies of T1–T4 and are tentatively assigned to these vertebrae (Fig. 6). The dorsal half of the spinous process of T5 is preserved separate from the removed section. Spinous processes of T6–T15 are preserved in close association with their respective vertebrae. Each spinous process arises along the length of the laminae, is inclined posteriorly, and is nearly flat laterally (Fig. 6). The spinous processes of the anterior-most thoracic vertebrae (T1–T9) are slender and dorsoventrally tall. These processes are compressed transversely and not expanded posteriorly. The posterior margin is slightly blunter than the anterior margin. The apex of each process is convex in lateral view. A spinous process table or apical expansion is absent until at least T9. From T10 on, the spinous processes are relatively deep anteroposteriorly and dorsoventrally shorter and are triangular in cross-section, with sharp anterior margins and increasing in width posteriorly. Starting at T10, the apex of each spinous process is mediolaterally flat and expanded, forming a spinous process table (Fig. 6). The size of each table increases in more posterior vertebrae. Low ridges are present along the posterolateral margins of each spinous process. The left and right ridges diverge ventrolaterally toward the tips of the postzygapophyses. A fine median crest is present in the lower part of the spinous process. The median crest and the posterolateral ridges surround two small fossae along the posterior aspect of the spinous processes. The lateral ridges, median crest, and fossae are well preserved in T1, T2, T4, and T10–T12. They are most prominent on T11 and T12. This part of the spinous process is not preserved in T3 and T5–T9, but we suspect that the lateral ridges, median crest, and fossae were present in these vertebrae as well.

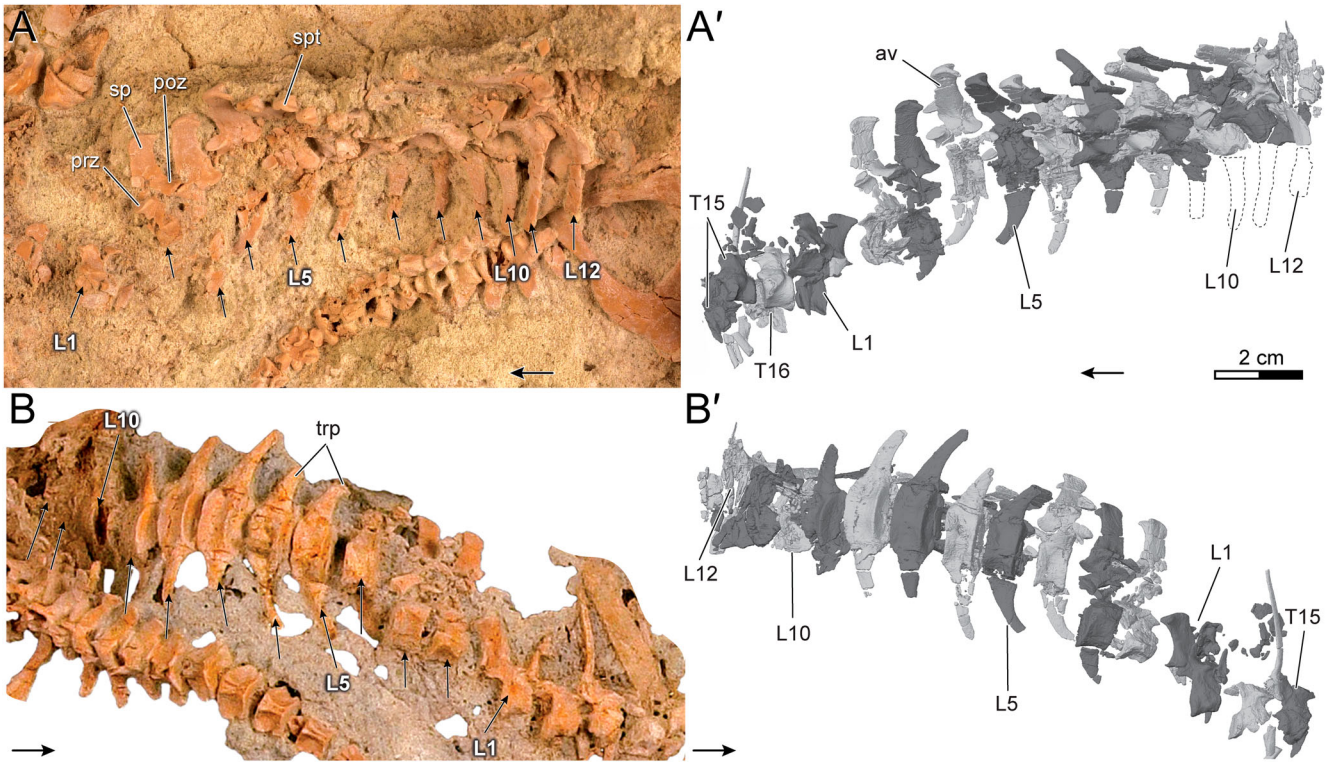

FIGURE 9. Posterior thoracic and anterior lumbar vertebrae (T15–L12) of *Adalatherium hui*, holotype (UA 9030), in **A**, **A′**, top (side A) and **B**, **B′**, bottom (side B) views. **A**, **B**, photographs of original specimen; **A′**, **B′**, reconstruction based on µCT images. Light and dark gray shades are used to distinguish between adjacent vertebrae, or parts thereof. Arrows point anteriorly. **Abbreviations**: **av**, anticlinal vertebra (L4); **L**, lumbar vertebra; **poz**, postzygapophysis; **prz**, prezygapophysis; **sp**, spinous process; **spt**, spinous process table; **T**, thoracic vertebra; **trp**, transverse process.

Thoracic Ribs (Including Costal Cartilages)—The ribs (R) are generally better preserved on the left side of UA 9030, whereas only ribs 3–10 are clearly visible on the right side (Fig. 8). Based on the better-preserved left side, 16 thoracic ribs, and therefore at least 16 thoracic vertebrae, are present. In addition, several fragments of ribs are present anterior to the first articulated rib in a block with the disarticulated T1–T4. At least one of the fragments is found in close association with T1 and likely represents the tubercle of the first rib. The other fragments likely belonged to R1–R4 but cannot be assigned with confidence.

A typical mammalian thoracic rib is composed of a dorsal osseous portion articulating with the vertebral column and a ventral cartilaginous portion articulating with the sternal apparatus (e.g., Evans, 1993). This is demonstrable for *Adalatherium* because both the osseous and cartilaginous parts of several ribs are preserved in UA 9030. The cartilaginous portion of the rib is rarely preserved in fossils; hence, the osseous portion alone is often referred to as the rib in the paleontological literature. Here, we follow this convention and call the dorsal osseous portion 'rib' and the fossilized cartilaginous portion 'costal cartilage.'

In general, the thoracic ribs of *Adalatherium* have an expanded proximal end that is divided into a tubercle and a head to articulate with the vertebrae (Fig. 8). The head of each rib is wedge-shaped, with two facets articulating with the costal foveae on the bodies of two successive vertebrae, whereas the tubercle articulates with the transverse process of the vertebra of the same number. The tubercles are larger in anterior ribs and gradually decrease in size between R5 and R9. The distal aspect of each tubercle is circular in cross-section on R6 and more anterior ribs (Fig. 8). The tubercles of R9–R11 are short and diverge from their corresponding heads dorsally and slightly posteriorly. An anteroposteriorly compressed neck separates the head from the tubercle. The dorsal margin of the neck has a rough texture that extends distally and ends at the junction between the neck and the shaft. The rough area marks the insertion of epaxial musculature. On more posterior ribs, the tubercles diminish in size and shift anteroventrally toward the heads. Starting at R12, the tubercles are confluent with the corresponding neck and head. Although the proximal ends of R13–R16 are not preserved in UA 9030, it is evident from the costal facets on the thoracic vertebrae that the heads each retain two articular facets for the bodies of successive vertebrae throughout the thoracic series. However, based on the facets on the thoracic vertebrae, the posterior facets, which articulate with the same vertebrae, are more developed than the anterior facets (which articulate with the preceding vertebrae). The last rib (R16) largely articulates with T16 and probably would have only slightly contacted the posterolateral margin of the body of T15 in life.

The anterior ribs (R5–R9) are more strongly curved than the posterior ribs. This might also be true for R1–R4, but the proximal aspects of those ribs are too fragmentary to estimate curvature. Ribs 10 and 11 are only gently curved. The shaft first curves ventrolaterally (and probably slightly posteriorly) for a short distance and then, for most of its length, is directed ventrally. Starting at R11, the curvature of the ribs is less pronounced and the angle between the neck and the shaft becomes indistinct. In all ribs, the main part of the shaft is moderately compressed anteroposteriorly and bears a longitudinal groove on its anterior and posterior aspects, resulting in a figure-eight cross-section at mid-length of the shaft. The distal-most portion of the shaft is elliptical in cross-section, (mediolaterally) wider than long. The distal extremity of the shaft bears a flat and elliptical facet for articulation with the corresponding costal cartilage. The ribs

articulate with their respective costal cartilages at least up to R13. The shaft of R14 is similar in size to that of more anterior ribs, but the distal end is not preserved and it remains uncertain whether it would have articulated with a costal cartilage in life. Ribs 15 and 16 are substantially more slender and shorter than more anterior ribs. It is likely that R15 and R16 were floating ribs that did not articulate with the sternum through costal cartilages.

Specimen UA 9030 is exceptional in having large and well-preserved costal cartilages (CC) of thoracic ribs. The fossilized cartilages in UA 9030 are distinctly different from osseous elements in surface texture (much rougher) and density (Fig. 8B, B′). On the right side, at least seven costal cartilages are clearly visible, six of which contact the sternum. The contact between these seven costal cartilages and ribs are not preserved but, based on proximity, they were likely associated with R3–R9. It appears that at least some posterior cartilages (possibly from CC8 on) were each fused with the preceding costal cartilages and did not individually articulate with the sternal elements directly, thus creating a costal margin.

Owing to its relatively good preservation, the left CC3 is singled out here for detailed description. The ventral part of the cartilage is dorsoventrally compressed and anteroposteriorly long, articulating with two adjacent sternal elements at their junction. Most of the shaft of CC3 remains dorsoventrally compressed and anteroposteriorly long. The shaft turns dorsolaterally to align with the distal end of the rib. Costal cartilages of the other true ribs probably retain a similar morphology, with a dorsoventrally compressed and anteroposteriorly long shaft that twists near the dorsolateral end. However, the lengths of the cartilages change greatly along the thoracic series; the posterior costal cartilages are almost twice as long as CC3.

Lumbar Vertebrae—There are at least 12 lumbar vertebrae (L1–L12) preserved in UA 9030 (Figs. 9, 10). The sacral region is damaged, and it is not possible to determine conclusively whether *Adalatherium* possessed more than 12 lumbar vertebrae. As mentioned above, the morphological transition from the thoracic to the lumbar series is gradual. We identify the transition between thoracic and lumbar vertebrae based on the absence of mobile ribs. The L1 has short and triangular transverse processes that are distinct from the mobile ribs of T16. In UA 9030, which represents a subadult individual, the suture between the transverse processes and the vertebral bodies of L1 and several other lumbars were still open and likely closed later in life. Nevertheless, the contact between the processes and the vertebral body was probably not mobile in life. On L1, a broad base of the transverse process is preserved along the lateral aspects of the vertebral body. The transverse processes of L1 taper distally and point anterolaterally. They are dorsoventrally compressed, with a convex anterior margin and a gently concave posterior margin. The transverse processes of L1 are much shorter than those of more posterior lumbar vertebrae. The lateral aspects of the vertebral body and pedicles are smooth and featureless. Each pedicle is indented both anteriorly and posteriorly, the posterior edge being more concave than the anterior edge. The morphology of the zygapophyses of L1 is quite similar to the condition in the posterior thoracic vertebrae. The articular facets of the zygapophyses do not change their orientation from those on the posterior thoracics; the prezygapophyseal facets face dorsally and slightly anterolaterally, whereas the postzygapophyseal facets face ventrally and slightly posteromedially (Fig. 9). The spinous process is also similar to those on posterior thoracics, but less inclined posteriorly.

Along the lumbar series, the vertebral morphology changes gradually. The vertebral bodies vary only slightly in length among L1–L9 (L10–L12 are not well enough preserved to accurately measure anteroposterior length of the vertebral bodies). The width of the vertebral bodies increases from L1 to L8 (Table 1). Starting at L1, the transverse processes increase in transverse width posteriorly. Maximum width is reached at L11. The transverse processes of L12 are slightly shorter than those on L11. The transverse processes are distally less pointed from L3 on. The orientation of the transverse process changes from lateral on L1–L2 to anterolateral on L3–L10 to lateral on L11 and L12. The pedicles do not change very much along the lumbar series; only their size increases posteriorly to some degree. There are no mammillary processes, nor anapophyses. Interestingly, the morphology and orientation of the zygapophyses are also relatively invariant. The spinous processes change gradually in orientation, size, and shape. The spinous processes of L1–L3 are posteriorly inclined, but the process is nearly vertical on L4, indicating that L4 is the anticlinal vertebra. Starting at L5, the spinous processes are more anteriorly inclined and slender. The spinous process tables appear to diminish in size, are less triangular in dorsal view, and are more rounded in lateral view from T7 on (Fig. 9A).

Sacral Vertebrae—There are many, finely comminuted fragments preserved posterior to L12, most of which are probably remains of the sacral series. However, none of the fragments is large enough or well enough preserved to be positively assigned to the sacral series and thereby to merit description.

Caudal Vertebrae—Specimen UA 9030 preserves 24 caudal vertebrae (Ca) largely in articulation, including the ultimate (i.e., distal-most) vertebra (Figs. 11, 12). Because the sacrum (including the transition between the sacral and caudal vertebrae) is crushed (Figs. 1, 2), it is unclear whether additional anterior caudal vertebrae were present. We estimate that if any anterior caudal vertebrae were missing at all, it is only one or two. For descriptive purposes, we will assume that *Adalatherium* had 24 caudal vertebrae and identify them as Ca1–Ca24.

A distinctive feature of the caudal series is that there is no lengthening of individual vertebrae in the middle of the series or at any other point along the caudal vertebral column (Fig. 11). Overall, the caudal series is short, being only about half as long as the thoracic and lumbar series combined (Figs. 1, 2; Table 1). The morphology of the caudal vertebrae gradually changes posteriorly. Vertebrae Ca1–Ca3 are only partially preserved and thus do not show the morphological gradient as well as the other vertebrae in the series. For that reason, they are described individually.

The Ca1 preserves only the right postzygapophysis, anterior to Ca2. Similar to Ca2, the postzygapophyseal facet appears to face ventrolaterally. The Ca2 preserves most of the left and right laminae, both postzygapophyses, the spinous process, and part of the right side of the vertebral body. The prezygapophyses are not preserved, but the postzygapophyses extend posterolaterally and slightly dorsally from the laminae. The postzygapophyseal facets face ventrolaterally. The spinous process is dorsoventrally tall and lenticular in cross-section. The Ca3 preserves the neural arch, the right prezygapophysis, left and right postzygapophyses, the left and right transverse processes, the base of the spinous process, and the right side of the vertebral body. The right aspect of Ca3 is better preserved than the left aspect; therefore, the description below focuses mainly on the right lamina, pedicle, and transverse process. The preserved part of the vertebral body does not provide much information about the morphology of the body itself, except (based on the position of the pedicles) that the body was large and probably elliptical in cross-section, as seen in more posterior vertebrae. The transverse process arises along the anterolateral aspect of the vertebral body. It is mediolaterally elongate, dorsoventrally compressed, anteroposteriorly broad, and slightly expanded distally. The process extends horizontally and points laterally and slightly anteriorly. The right pedicle arises from the anterior two-thirds of the dorsolateral edge of the body and is slightly inclined medially. It is anteroposteriorly narrower than the body and dorsoventrally short. The right lamina is about as broad (anteroposteriorly) as the

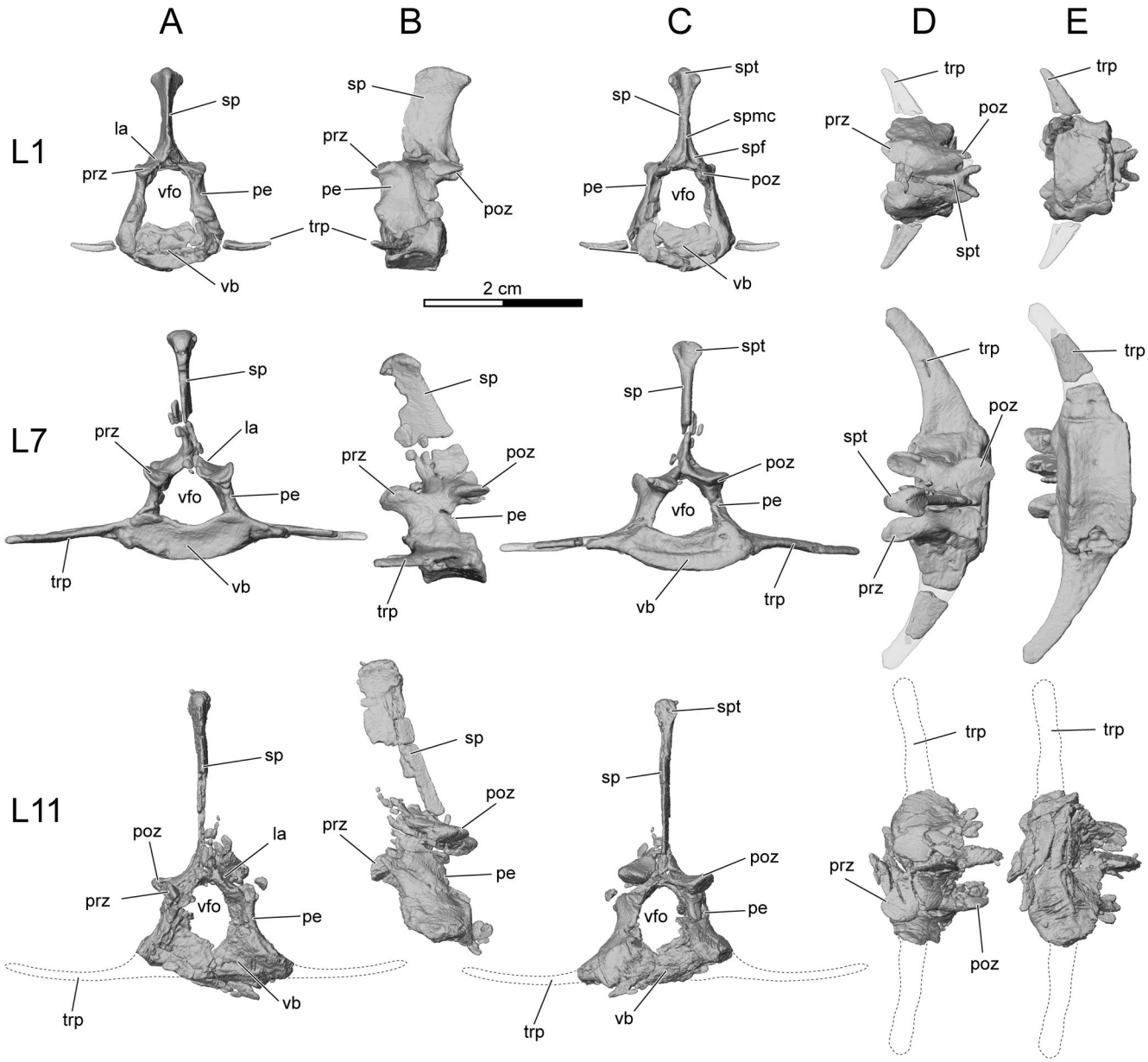

FIGURE 10. Reconstruction of selected lumbar vertebrae of *Adalatherium hui*, holotype (UA 9030), in **A**, anterior, **B**, left lateral, **C**, posterior, **D**, dorsal, and **E**, ventral views. Rows from top to bottom: L1, L7, and L11. Preserved elements are rendered as solid; mirrored elements are semitransparent. Dorsal to top in **A**, **B**, **C**; anterior to left in **B**, **D**, **E**. **Abbreviations**: **L**, lumbar vertebra; **la**, lamina; **pe**, pedicle; **poz**, postzygapophysis; **prz**, prezygapophysis; **sp**, spinous process; **spf**, spinous process fossa; **spmc**, spinous process median crest; **spt**, spinous process table; **trp**, transverse process; **vb**, vertebral body; **vfo**, vertebral foramen.

pedicle. The transverse width of the left and right laminae combined appears to be smaller than that of the vertebral body. The right prezygapophysis projects anteriorly well beyond the anterior edge of the neural arch and vertebral body. The right postzygapophysis extends posteriorly well beyond the posterior edge of the pedicle, and slightly over the edge of the vertebral body. The postzygapophyseal facet faces ventrolaterally. Judging by its preserved base, the spinous process is probably smaller than that on Ca2.

Vertebrae Ca4–Ca7 are better preserved than Ca1–Ca3; only the ventral portions of the vertebral bodies are missing. The transverse processes of Ca4–Ca7 are similar to that of Ca3 in orientation and size, but they arise from the lateral sides of the vertebral bodies rather than from the anterolateral aspect. On Ca8–Ca10, the transverse processes point posterolaterally rather than anterolaterally as in Ca4–Ca7. On Ca11, the transverse processes are small, posterolaterally directed projections that are separated from the posterior end of the vertebral body by a small notch. From Ca12 on, the transverse processes are reduced to thin lateral ridges along the vertebral bodies (Figs. 11, 12). On Ca15–Ca19, the notches posterior to the transverse processes are each enclosed and thus form a foramen (Fig. 12D).

The neural arches gradually diminish in size relative to the vertebral bodies. The spinous processes are short and posteriorly inclined in anterior caudal vertebrae (best seen in Ca 9). The spinous processes become smaller posteriorly but are still present until Ca10 (Fig. 11). Starting from Ca11, the neural arches fail to fully enclose vertebral foramina and the spinous

TABLE 1. Basic metrics of the vertebrae of *Adalatherium hui*, holotype (UA 9030).

Vertebra no.	VBL	VBW	VBH	TRPW	SPL	ZYGL
T1	—	—	—	—	~13	~8
T2	—	—	—	—	~15	~7
T3	~5.5	—	3.2	—	—	—
T4	~5.5	—	3.7	—	—	10.5
T5	5.3	—	4.1	—	—	—
T6	6.9	—	5.2	—	15.6	~7.0
T7	7.0	—	5.9	—	~16.0	—
T8	7.8	—	—	—	—	—
T9	7.2	—	4.6	—	—	—
T10	7.5	—	~5	—	14.0	11.1
T11	7.2	—	—	—	13.1	10.5
T12	6.8	—	~5	—	12.8	12.0
T13	6.9	—	~4.5	—	11.8	11.8
T14	6.8	—	4.6	—	~10	10.4
T15	6.9	—	5.0	—	—	11.5
T16	6.4	—	4.5	—	—	11.9
L1	6.4	~10.5	4.9	7.4	12.5	11.5
L2	7.3	~10.0	6.5	6.7	13.2	13.7
L3	7.2	~13.0	~6	8.5	15.1	~12.5
L4	7.1	13.9	5.6	11	14.9	13.8
L5	7.3	14.0	4.0	13.5	15.1	13.6
L6	~6.5	14.2	4.9	14.8	15.7	14.2
L7	7.6	15.6	4.8	15.4	~12.0	14.1
L8	7.9	15.8	4.7	~14.0	—	14.1
L9	~7.0	15.3	5.9	~13.0	—	14.1
L10	—	—	—	~14.0	—	~13.0
L11	—	~14.0	~3.5	15.8	20.4	~14.5
L12	—	—	—	13.2	14.7	15.8
Ca4	—	11.8	—	—	—	13.0
Ca5	7.2	—	—	—	—	—
Ca6	7.2	12.2	~10.5	9.5	—	12.1
Ca7	6.7	12.4	8.3	8.1	—	12.2
Ca8	7.4	11.6	8.1	7.8	6.1	11.9
Ca9	7.8	10.4	8.2	—	5.7	11.3
Ca10	7.5	12.2	7.7	6.5	—	8.8
Ca11	7.5	11.4	~8.5	5.6	—	—
Ca12	7.6	13.4	7.7	3.0	—	—
Ca13	7.4	11.9	7.1	1.8	—	—
Ca14	7.0	12.7	5.8	—	—	—
Ca15	6.6	10.1	5.2	—	—	—
Ca16	6.4	8.4	5.0	—	—	—
Ca17	6.5	7.2	3.0	—	—	—
Ca18	5.4	5.8	2.5	—	—	—
Ca19	4.7	4.9	2.6	—	—	—
Ca20	3.8	4.0	1.9	—	—	—
Ca21	3.2	3.3	1.9	—	—	—
Ca22	2.6	2.6	1.6	—	—	—
Ca23	2.4	2.0	1.1	—	—	—
Ca24	2.3	1.5	1.0	—	—	—

C1–C7, the sacral vertebrae, and Ca1–Ca3 were not included because they are too poorly preserved for measurement. '~' indicates estimates based on fragmentary elements. '—' indicates an accurate measurement could not be taken due to poor preservation. All linear measurements in mm.
Abbreviations: **Ca**, caudal vertebra, **L**, lumbar vertebra, **T**, thoracic vertebra; **SPL**, spinous process proximodistal length; **TRPW**, transverse process transverse (mediolateral) width; **VBH**, vertebral body dorsoventral height; **VBL**, vertebral body anteroposterior length; **VBW**, vertebral body transverse (mediolateral) width; **ZYGL**, zygapophyseal proximodistal length (measured from anterior end of prezygapophysis to posterior end of postzygapophysis).

processes are absent. The homologous area forms a longitudinal sulcus between the reduced left and right halves of each neural arch. This sulcus is present up to at least Ca16; unfortunately, the dorsal aspect of Ca17 is damaged. Starting from Ca18 (or 17), the longitudinal sulcus disappears; the remnant of the neural arch appears as a longitudinal ridge, which progressively diminishes in size on more posterior vertebrae and is absent on Ca22. The articular facets on the zygapophyses gradually change their orientation, from dorsomedial to medial for the prezygapophyses and from ventrolateral to lateral for the postzygapophyses in anterior caudal vertebrae. The transverse distance between the prezygapophyses, and even more so that between the postzygapophyses, diminishes progressively between Ca4 and Ca7. The pre- and postzygapophyses are gradually reduced between Ca8 and Ca10. The right postzygapophysis is absent in Ca8, the right prezygapophysis is reduced and the right postzygapophysis is absent in Ca9, and both the right pre- and postzygapophyses are absent in Ca10 (Fig. 12). The pre- and postzygapophyses are absent from Ca11 on.

The ventral aspects of the vertebral bodies of Ca8–Ca22 are deeply concave anteroposteriorly, with hypertrophic anterior and posterior lips. The ventral aspects of more anterior caudal vertebrae are not well enough preserved to describe the morphology. A longitudinal median sulcus separates both lips into left and right halves in Ca11–Ca19 (Fig. 12). The hemal arches are well developed on most caudal vertebrae with the exception of Ca4–Ca7, either because they are not preserved or because they were truly absent. Each hemal arch forms a deep, 'V'-shaped trough and articulates with the posterior lip of the vertebral body and anterior lip of the following vertebra. The hemal arches and vertebral bodies of Ca8–Ca12 together form a canal, which is progressively reduced in diameter posteriorly. The canal may extend anteriorly to include at least Ca7. Hemal arches on Ca13–Ca21 are 'U'-shaped, much smaller and shallower than the more anterior ones. Starting at Ca14, the size of the vertebrae is quickly reduced; the ultimate vertebra (Ca24) is a tiny bone tapering distally (Figs. 11, 12).

Manubrium—Several sternal elements are preserved and exposed on side B, including an anterior sternal element here identified as the manubrium (Figs. 13, 14). Several Mesozoic mammaliaforms have an additional element, the interclavicle, which is positioned between the two clavicles and connects the pectoral girdle to the manubrium. A separate interclavicle is retained in monotremes but lost in adult therians, where the manubrium contacts the left and right clavicles directly (Klima 1973, 1987; Vickaryous and Hall, 2006). As such, for our purposes here, it is crucial to outline the rationale for homologizing the interclavicle in fossil mammaliaforms.

In monotremes, the interclavicle and manubrium can be distinguished based on embryological as well as topographic relationships (e.g., Luo, 2015; see 'Comparisons' below for a broader discussion on identification of the interclavicle). In extinct mammaliaforms, the interclavicle and manubrium are primarily distinguished based on topographic relationships. First, the manubrium always contacts the first rib, whereas the interclavicle seldom does and, if so, only in conjunction with the manubrium. Second, the interclavicle can overlap the manubrium, as is the case in several extinct mammaliaforms (e.g., Luo, 2015).

In general, the area between the right humerus and the left scapulocoracoid, which contains the clavicles and manubrium, is poorly preserved in UA 9030 (Figs. 2, 13). The position of the first rib is uncertain; only two small fragments of the left first rib are preserved: one medial to the left ulna, the other a transverse tubercle and neck next to T1 (see 'Thoracic Ribs' above). The anterior sternal elements (including the possible manubrium) in UA 9030 are fragmented, crushed, and flattened and do not preserve their original topographic relationships (Fig. 13). In particular, the anterior-most sternal element is displaced and does not articulate with any other sternal element, although it is at least in association with both clavicles. The element in question is preserved anterior to the right humerus and is broken into several pieces (Fig. 13). Based on its shape, we tentatively identify this anterior-most element as the manubrium. Note that neither the contact relationship with the next sternal element nor the position of the first rib can aid in this identification. Therefore, it cannot be ruled out that the element represents an interclavicle. However, there is no additional bony element preserved in this

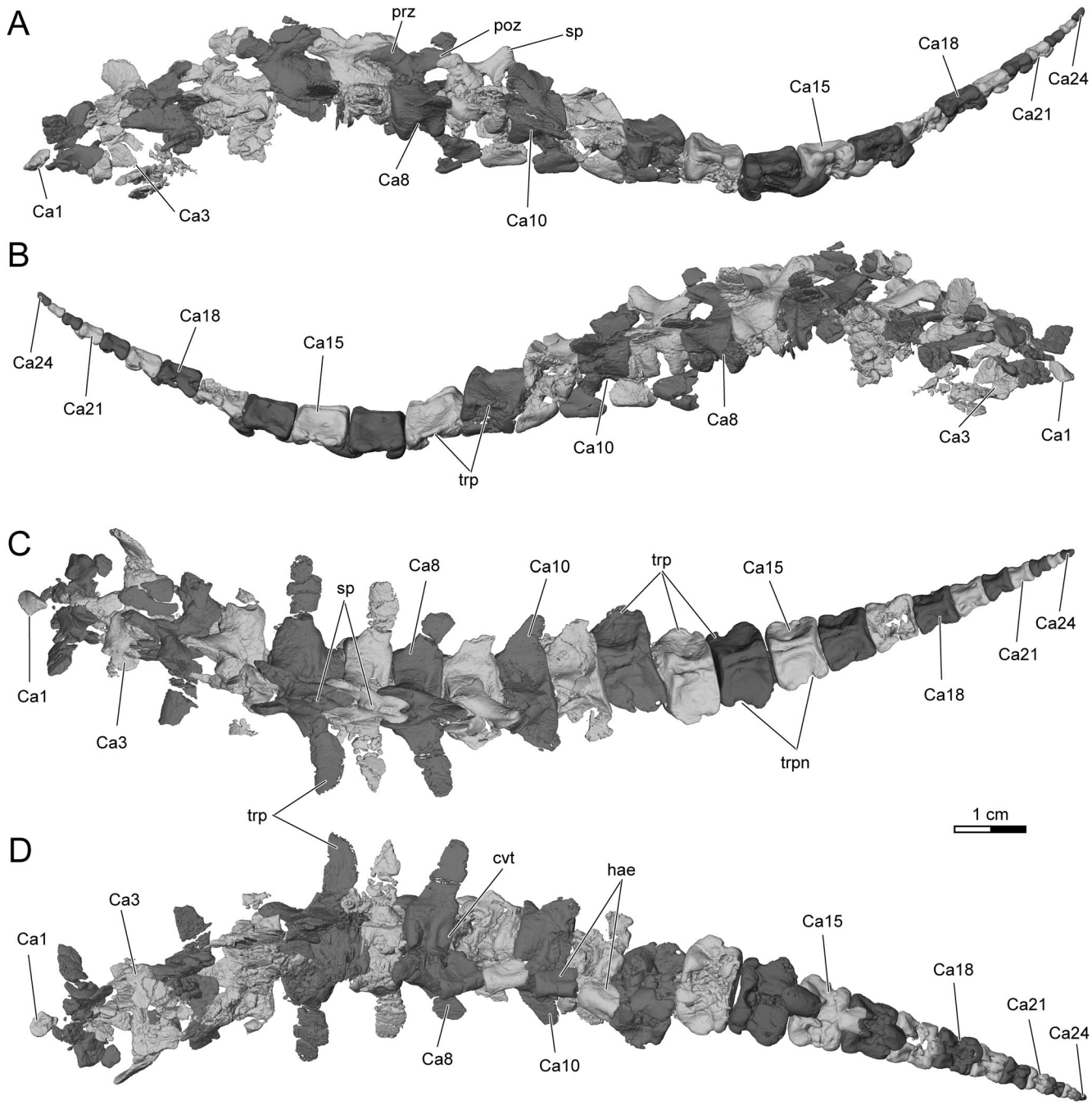

FIGURE 11. Caudal vertebrae of *Adalatherium hui*, holotype (UA 9030), in **A**, left lateral, **B**, right lateral, **C**, dorsal, and **D**, ventral views. Light and dark gray shades are used to distinguish between adjacent vertebrae, or parts thereof. **Abbreviations**: **Ca**, caudal vertebra; **cvt**, ventral tubercle on caudal vertebra; **hae**, hemal arch; **poz**, postzygapophysis; **prz**, prezygapophysis; **sp**, spinous process; **trp**, transverse process; **trpn**, transverse process notch.

region and the element in question generally resembles the winged manubrium of mammals; thus, we find identification as a manubrium to be the most plausible.

The tentatively identified manubrium is mediolaterally broad and anteroposteriorly short (Figs. 13, 14). It is mediolaterally wider anteriorly than posteriorly, with two broad lateral wings. The lateral wings are concave ventrally and would have received the proximal ends of the clavicles in life (Fig. 14D). The surface of the shallow ventral concavities is smooth. The anterior margin of the manubrium between the two wings is indented, whereas the posterior margin, for articulation with the first sternebra, is straight.

Sternebrae—Several sternebrae are preserved in articulation with the costal cartilages of R2–R8 posterior to the manubrium (Fig. 8). A typical sternebra is narrow, thick, and moderately long. The lateral margin of the bone bears a large costal facet on its posterior half, whereas the anterolateral corner of the element may contact the costal cartilage of the preceding rib. In other words, each costal cartilage articulates with two succeeding sternal elements. The ventral surface of the sternebra is concave. The individual sternal elements slightly increase in anteroposterior length and decrease in mediolateral width posteriorly. Overall, the sternum is much shorter than the thoracic series of vertebrae,

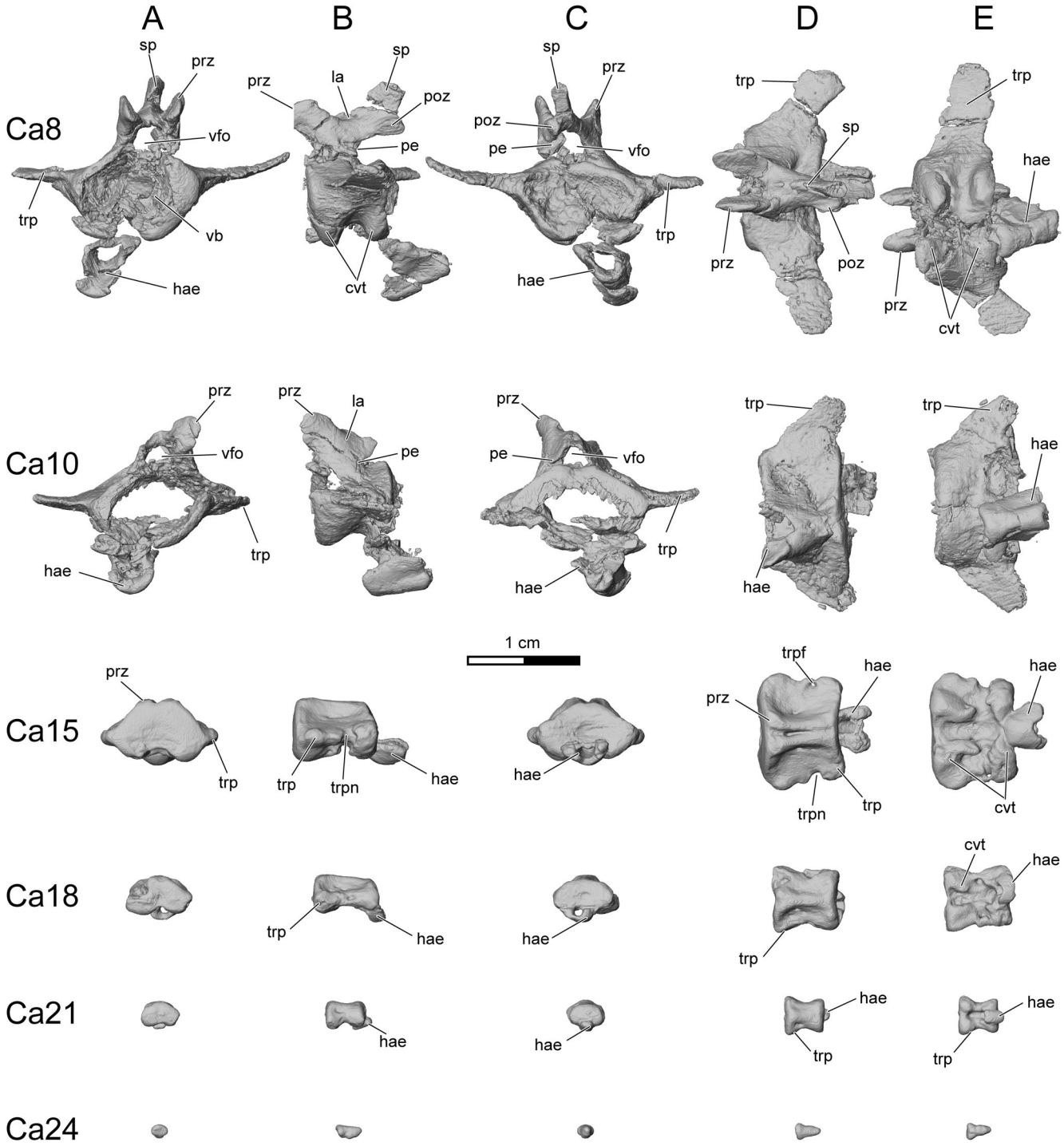

FIGURE 12. Selected caudal vertebrae of *Adalatherium hui*, holotype (UA 9030), in **A**, anterior; **B**, left lateral; **C**, posterior; **D**, dorsal; and **E**, ventral views. Rows from top to bottom: Ca8, Ca10, Ca15, Ca18, Ca21, and Ca24. Dorsal to top in **A**, **B**, **C**; anterior to left in **B**, **D**, **E**. **Abbreviations**: **Ca**, caudal vertebra; **cvt**, ventral tubercle on caudal vertebra; **hae**, hemal arch; **la**, lamina; **pe**, pedicle; **poz**, postzygapophysis; **prz**, prezygapophysis; **sp**, spinous process; **trp**, transverse process; **trpf**, transverse process foramen; **trpn**, transverse process notch; **vb**, vertebral body; **vfo**, vertebral foramen.

thus confirming the likely presence of floating ribs and a costal margin or arch that swept up in a posterolateral to anteromedial direction, as is typical of mammals (e.g., Evans, 1993).

Pectoral Girdle

The pectoral girdle comprises the scapulocoracoid and clavicle in *Adalatherium*. Only the left scapulocoracoid is preserved in UA 9030 (Figs. 13, 14). It is broken into a dorsal portion containing most of the scapular blade and a ventral portion containing the scapular neck, glenoid, and coracoid. The left clavicle is almost intact and well preserved, whereas the right clavicle is broken and folded on itself (Fig. 14).

Scapulocoracoid—Because the right scapulocoracoid is missing in UA 9030, this description is solely based on the left scapulocoracoid, which is fragmented but reasonably well preserved (Figs.

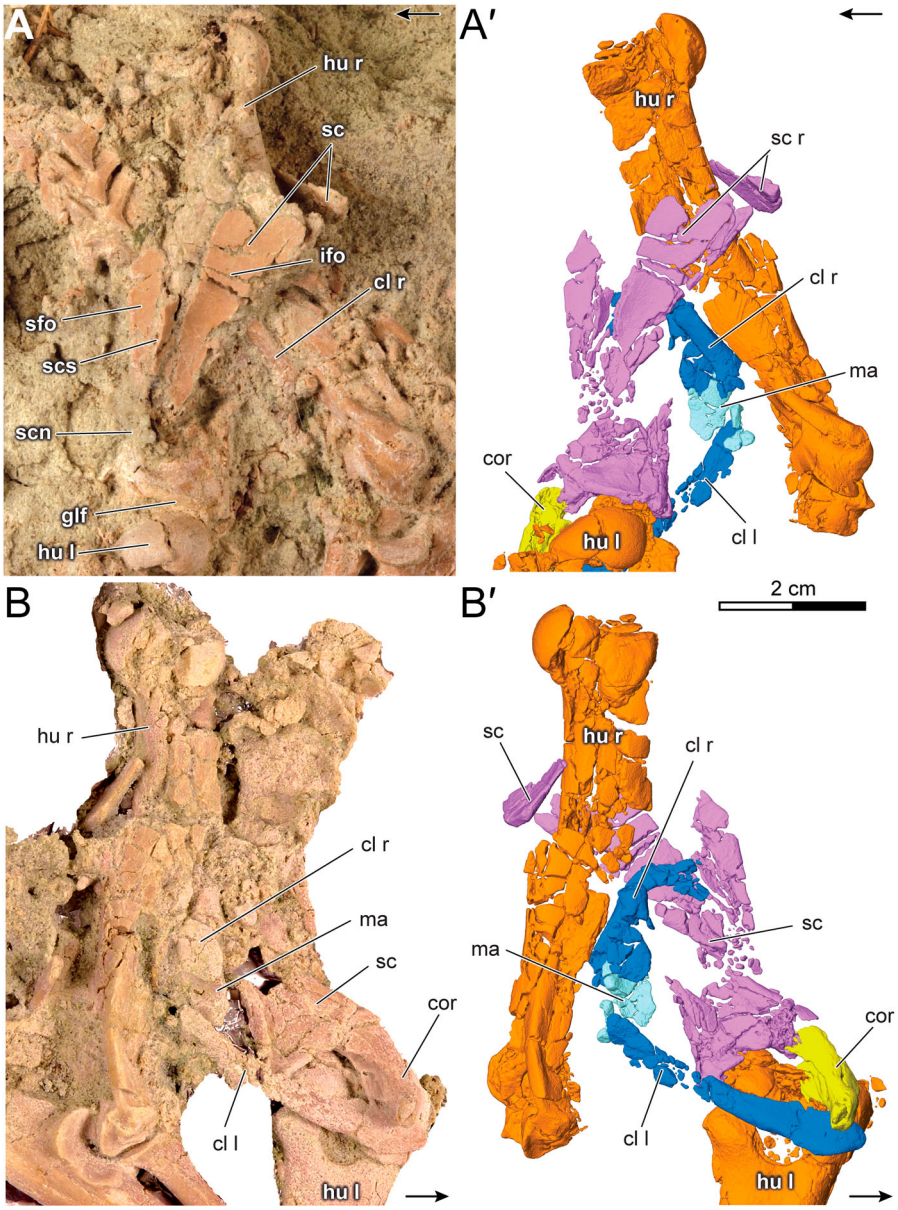

FIGURE 13. Pectoral region of *Adalatherium hui*, holotype (UA 9030), in **A**, **A′**, top (side A); and **B**, **B′**, bottom (side B) views. **A**, **B**, photographs of original specimen; **A′**, **B′**, reconstruction based on µCT images, with clavicles in dark blue, left coracoid in yellow, humeri in orange, manubrium in light blue, and left scapula in purple. Left and right humeri and clavicles indicated by letters 'l' and 'r'. Manubrium is displaced and rotated so that posterior end points anteriorly. Dorsal aspect of manubrium is visible in **A′**, ventral aspect in **B′**. Arrows point anteriorly. **Abbreviations**: **cl**, clavicle; **cor**, coracoid; **glf**, glenoid fossa; **hu**, humerus; **ifo**, infraspinous fossa; **ma**, manubrium; **sc**, scapula; **scn**, scapular neck; **scs**, scapular spine; **sfo**, supraspinous fossa.

13, 14). In addition to being broken into dorsal and ventral segments, the posterodorsal corner of the scapulocoracoid is separated from the rest of the dorsal portion and can be seen posterior to the right humerus (Fig. 13). The scapular blade is triangular in shape, expanding dorsally. The anterior border of the blade is straight, which is probably the case for the posterior border as well, but the latter is largely damaged. The preserved posterodorsal corner of the blade is rounded and not expanded. A small tuberosity along the posterodorsal aspect of the scapular blade probably represents the attachment site for the teres major muscle (Fig. 14). The preserved part of the dorsal margin of the scapulocoracoid suggests that it was straight and sharp. The µCT images reveal that the medial surface was smooth and gently concave, suggestive of a very shallow subscapular fossa (Fig. 14). The lateral aspect of the scapula presents a spine that we identify as the scapular spine. The ventral aspect of the spine is broken, and the acromion is not preserved. The acromion usually defines the position of the scapular spine in fossil mammals, either along the anterior border of the scapula (with a reduced supraspinous fossa) or in the center of the blade (with a sizable supraspinous fossa) (e.g., Luo, 2015). Although the acromion is not preserved in UA 9030, the anterior border of the scapula is reasonably well preserved and does not bear any indications of a broken acromion. The ventral aspect of the spine is clearly broken and could have extended into an acromion in life. The robust lateral end of the clavicle (see below) suggests the presence of a sizable acromion. Only a small section of the spine is present dorsal to the neck of the scapula. The preserved part of the spine is mediolaterally tall, indicating that the spine would have been prominent in life. The base of the spine divides the lateral aspect of the scapular blade almost evenly into a slightly more slender supraspinous fossa and a slightly wider infraspinous fossa. Both fossae are gently concave to almost flat in anteroposterior section. Despite the fact that the posterior margin of the scapular blade is poorly preserved, it seems unlikely that a prominent posterior crest ('inferior lateral crest' in Chen and Luo, 2013) was present. Although crushed, the scapular neck can be distinguished from the blade and

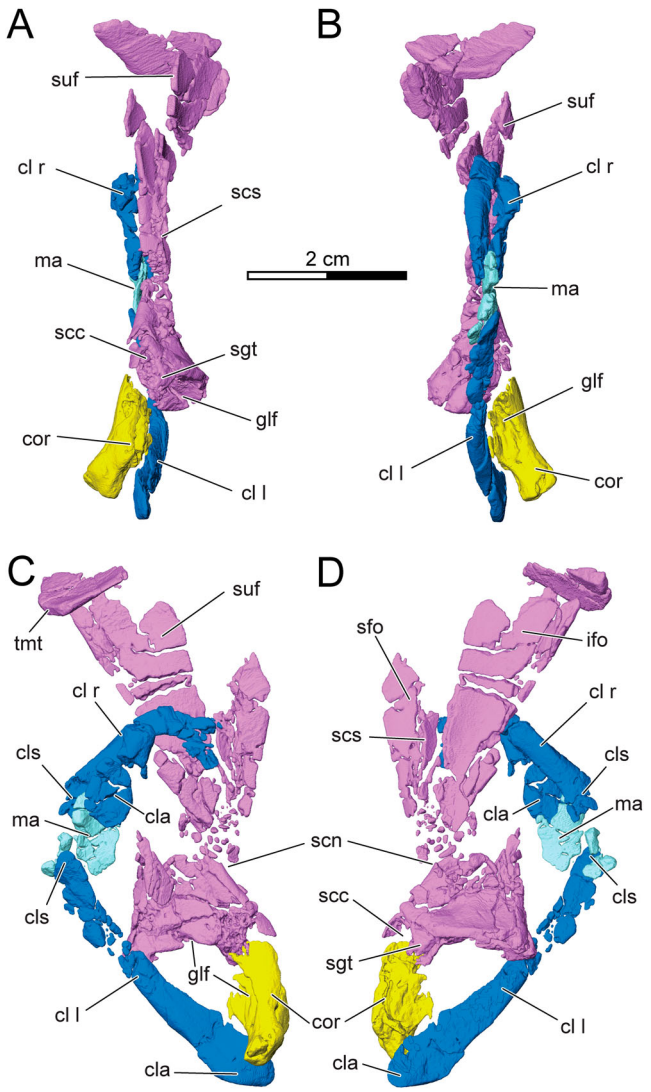

FIGURE 14. Pectoral girdle of *Adalatherium hui*, holotype (UA 9030), in **A**, anterior, **B**, posterior, **C**, medial, and **D**, lateral views based on reconstruction of µCT images, with clavicles in dark blue, left coracoid in yellow, manubrium in light blue, and left scapula in purple. Mainly showing elements from left side; left and right clavicles indicated by letters 'l' and 'r'. Note that manubrium is displaced and rotated so that posterior end points anteriorly. Ventral aspect of manubrium is visible in **C**, dorsal aspect in **D**. **Abbreviations**: **cl**, clavicle; **cla**, clavicle acromial end; **cls**, clavicle sternal end; **cor**, coracoid; **glf**, glenoid fossa; **ifo,** infraspinous fossa; **ma**, manubrium; **scc**, scapular concavity; **scn**, scapular neck; **scs**, scapular spine; **sfo**, supraspinous fossa; **sgt**, supraglenoid tubercle; **suf**, subscapular fossa; **tmt**, tubercle for teres major attachment.

forms the base for the glenoid fossa. The scapular neck is elliptical in cross-section, longer anteroposteriorly than mediolaterally wide.

The coracoid contacts the anteroventral margin of the scapula. The unfused suture between the scapula and the coracoid is recognizable in µCT images and extends along the anterior part of the glenoid fossa of the scapula to roughly mid-length (Fig. 14). The contact is broad anteroventrally and tapers posterodorsally. The coracoid is long, robust, and curved. It first extends ventrally and then recurves medially, with a blunt tip pointing ventromedially. Both the scapula and the coracoid contribute almost equally to the glenoid fossa. The scapular part of the glenoid is oriented roughly perpendicular to the long axis of the scapular blade, whereas the coracoid part of the glenoid fossa extends ventrally at a 100° angle. The coracoid part of the glenoid fossa is mediolaterally narrow and dorsoventrally deep, facing posteriorly and slightly laterally. A supraglenoid tubercle buttresses the glenoid, and a large concavity is present on its medial aspect, at the junction of the coracoid and scapula (Fig. 14).

Clavicle—The left clavicle of UA 9030 is completely preserved, whereas the right clavicle is broken at mid-length and folded on itself (Figs. 13, 14). The clavicle is long and gently expands laterally. The lateral end is dorsoventrally tall and slightly thinner anteroposteriorly than the shaft at mid-length. The exposed (nonarticular) ventrolateral surface of the lateral end is smooth. Generally, the shaft is gently curved rather than sigmoid or boomerang-shaped. The cross-section at mid-length is elliptical, dorsoventrally taller than mediolaterally wide. Overall, the medial end is small and less expanded than the lateral end. The small articular facet for the manubrium might indicate a mobile sternoclavicular joint (more similar to that of therians than to that of monotremes; Luo, 2015).

Humerus

The right humerus is fractured into numerous pieces and is relatively poorly preserved (Fig. 13). The left humerus is in much better condition, preserving most of its original morphology in three dimensions, and serves as the primary basis for the description below (Figs. 15, 16). In UA 9030, consistent with its subadult status, the humerus has a distinct proximal epiphysis, which is partially sutured to the diaphysis. In contrast, the suture between the distal epiphysis and the diaphysis is not discernible. The humerus is described with the intertubercular groove facing anteriorly.

The humerus of *Adalatherium* is a robust element that is substantially shorter (71.5 mm; see Table 2 for other measurements) than the femur (90.8 mm). The proximal and distal ends of the humerus are twisted relative to each other (~25°), but the exact extent is difficult to measure because the intertubercular groove is damaged proximally (see 'Materials and Methods'). The bulbous humeral head overhangs the shaft posteriorly. The articular surface of the head is hemispherical, facing dorsally and posteriorly. Its curvature is greater than that of the scapular glenoid fossa, in both mediolateral and anteroposterior directions. The humeral head is separated from the greater and lesser tubercles by shallow but distinct notches. Both tubercles are prominent, projecting proximally to just slightly beyond the proximal level of the humeral head (Fig. 16). The greater tubercle is large, anteroposteriorly longer than mediolaterally wide. The lesser tubercle is similar in size to the greater tubercle, equal in width, but probably slightly shorter anteroposteriorly. The deltopectoral crest extends distally from the greater tubercle. It is blunt and low at its origin and becomes more prominent as it extends distally. The length of the deltopectoral crest (35 mm) is about half that of the humerus (71.5 mm). The attachment site for the teres major muscle is not well developed. The intertubercular groove is very shallow and mediolaterally wide; it is well defined along and immediately lateral to the deltopectoral crest but fades laterally. As preserved, the proximal portion of the intertubercular groove presents a large concavity, here termed the intertubercular fossa. A shallow concave depression was probably present in life, but its size has been exaggerated by the displacement of the proximal epiphysis.

The proximal two-thirds of the humeral shaft gradually diminishes in diameter distally. The humerus reaches its narrowest point distal to the distal end of the deltopectoral crest, where the shaft is approximately circular in cross-section. The distal one-third of the humeral shaft expands mediolaterally. A medial

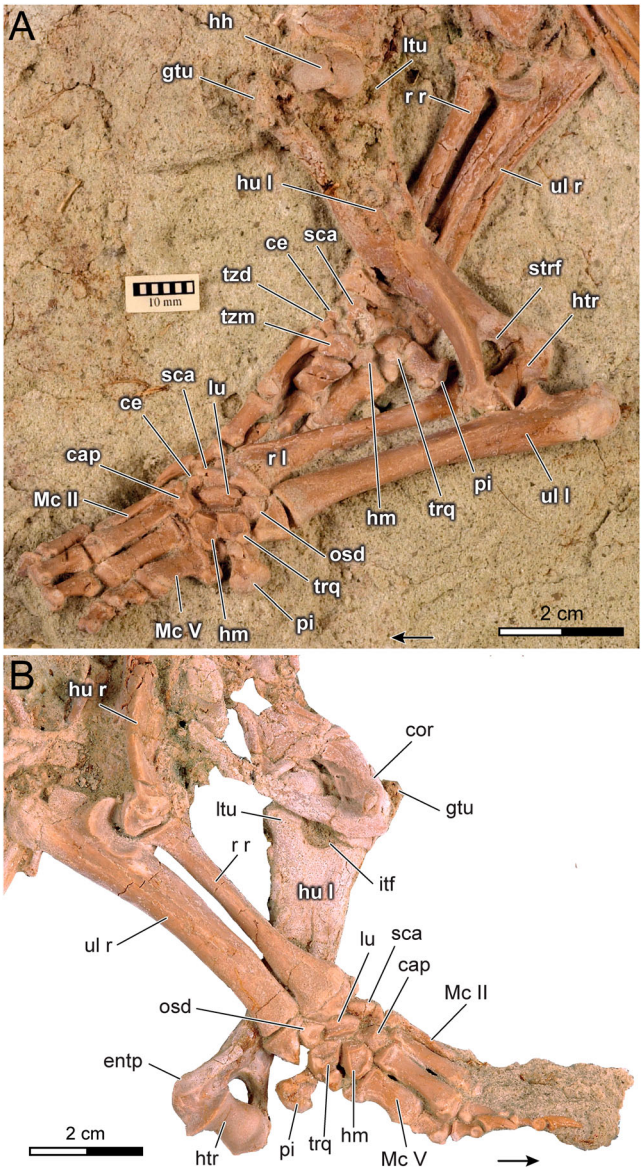

FIGURE 15. Forelimbs of *Adalatherium hui*, holotype (UA 9030), in **A**, top (side A) and **B**, bottom (side B) views. **A** is at early stage of mechanical preparation with both forelimbs in articulation; left side in foreground, right side deep to it. In **B**, left radius, ulna, and manus have been removed; right forelimb in foreground. Left and right humeri, radii, and ulnae indicated by letters 'l' and 'r'. Arrows point anteriorly. **Abbreviations**: **cap**, capitate; **ce**, centrale; **cor**, coracoid; **entp**, entepicondyle; **gtu**, greater tubercle; **hh**, head of humerus; **hm**, hamate; **htr**, humeral trochlea; **hu**, humerus; **itf**, intertubercular fossa; **ltu**, lesser tubercle; **lu**, lunate; **Mc**, metacarpal; **osd**, os Daubentonii; **pi**, pisiform; **r**, radius; **sca**, scaphoid; **strf**, supratrochlear foramen; **trq**, triquetrum; **tzd**, trapezoid; **tzm**, trapezium; **ul**, ulna.

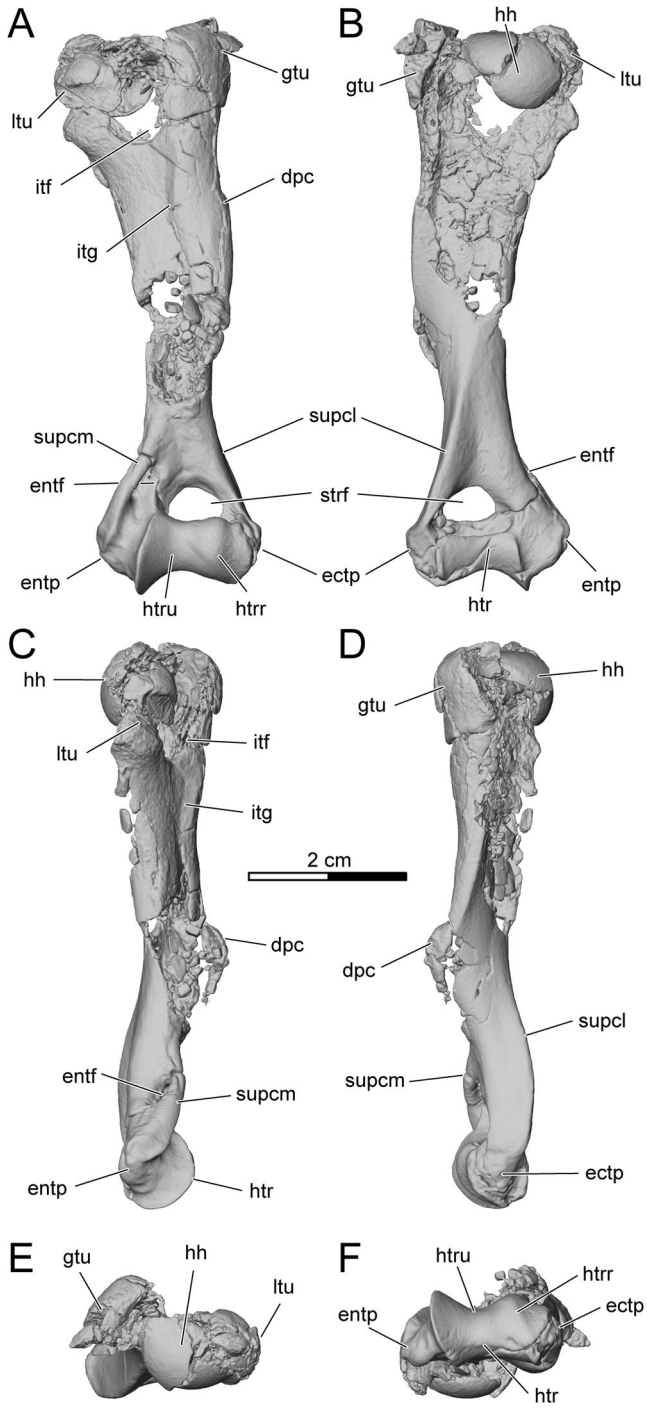

FIGURE 16. Left humerus of *Adalatherium hui*, holotype (UA 9030), in **A**, anterior, **B**, posterior, **C**, medial, **D**, lateral, **E**, proximal, and **F**, distal views based on µCT images. **Abbreviations**: **dpc**, deltopectoral crest; **ectp**, ectepicondyle; **entf**, entepicondylar foramen; **entp**, entepicondyle; **gtu**, greater tubercle; **hh**, head of humerus; **htr**, humeral trochlea; **htrr**, humeral trochlea radial condyle; **htru**, humeral trochlea ulnar condyle; **itf**, intertubercular fossa; **itg**, intertubercular groove; **ltu**, lesser tubercle; **strf**, supratrochlear foramen; **supcl**, lateral supracondylar crest (= supinator crest); **supcm**, medial supracondylar crest.

supracondylar crest is present as an extension of the oblique ridge from the distal end of the deltopectoral crest. It encloses a moderately large, elliptical entepicondylar foramen before terminating lateral to the entepicondyle. A more prominent lateral supracondylar crest (= supinator crest) is developed along the posterolateral edge of the shaft. The crest arises roughly at midlength of the shaft along the midline of the posterior aspect and ends proximal to the ectepicondyle. The posteromedial margin of the distal shaft is low and rounded, much less prominent than the lateral supracondylar crest along the posterolateral margin or the medial supracondylar crest along the anteromedial margin (Fig. 16). An ectepicondylar foramen is not present.

TABLE 2. Basic metrics of the left forelimb elements of *Adalatherium hui*, holotype (UA 9030).

Humerus	
Length	71.5
Midshaft width	13.2
Deltopectoral crest length	35.0
Trochlea width	14.9
Epicondylar width	20.9
Humeral torsion	25°
Radius	
Length	46.4
Midshaft depth	4.6
Midshaft width	3.9
Ulna	
Length	69.5
Midshaft depth	7.2
Midshaft width	4.8
Olecranon length	16.5

Length measured in proximodistal direction, width in mediolateral direction, and depth in anteroposterior direction. All linear measurements in mm.

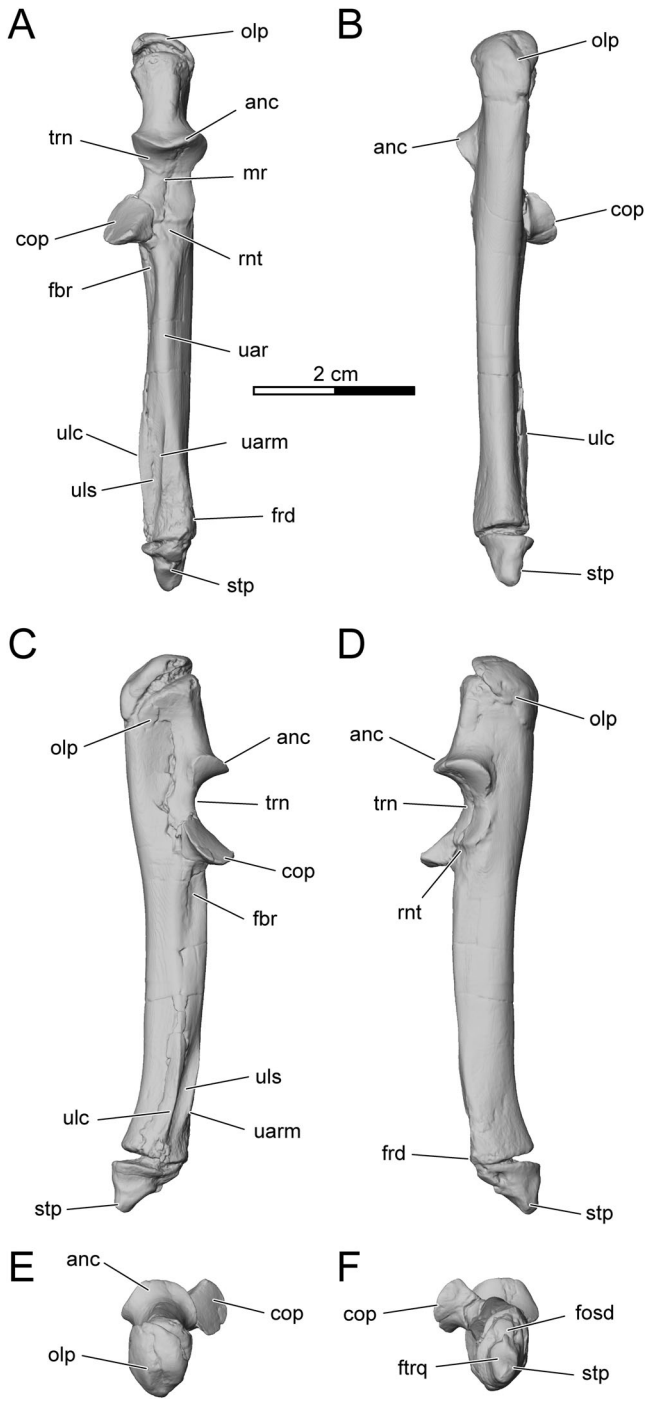

FIGURE 17. Left ulna of *Adalatherium hui*, holotype (UA 9030), in **A**, anterior, **B**, posterior, **C**, medial, **D**, lateral, **E**, proximal, and **F**, distal views. **Abbreviations**: **anc**, anconeal process; **cop**, coronoid process; **fbr**, fossa for brachialis muscle; **fosd**, facet for os Daubentonii; **frd**, facet for distal radius; **ftrq**, facet for triquetrum; **mr**, median ridge; **olp**, olecranon process; **rnt**, radial notch; **stp**, styloid process; **trn**, trochlear notch; **uar**, ulnar anterior ridge; **uarm**, ulnar anterior ridge medial crest; **ulc**, ulnar crest; **uls**, ulnar longitudinal sulcus.

The distal end of the humerus is approximately as mediolaterally wide as the proximal end. The articular area occupies more than half the mediolateral width of the distal epiphysis. It comprises a shallow radial condyle (= capitulum) and a deep trochlea. The gently convex radial condyle is more prominently developed along the anterior aspect of the distal articular facet but does not extend onto the posterior surface. A smooth and concave area between the radial condyle and the ectepicondyle articulates with the external lip of the head of the radius. Anteriorly, the radial condyle forms the lateral wall of the trochlea. The ulnar condyle and intercondylar groove are modified to form a trochlea. The trochlea is well developed and wraps around the distal end of the humerus onto the posterior aspect of the epiphysis. Posteriorly, the trochlea occupies the whole width of the articular facet, with sharp medial and lateral borders. The lateral border becomes less distinct anteriorly as it wraps around the distal end of the trochlea. The medial border of the trochlea maintains its sharpness all around the distal end.

The entepicondyle is distinct and protuberant. It is less than half as mediolaterally wide as the distal articular surface. On the anterior aspect of the entepicondyle, a well-defined groove extends distally from the entepicondylar foramen. The ectepicondyle is much smaller than the entepicondyle. It is a rugose protuberance lateral to the distal articular surface. A large fossa is visible on the anterior aspect proximal to the trochlea that probably encompassed the radial fossa, which accommodates the radial head, and the coronoid fossa, which accommodates the coronoid process of the ulna. In posterior view, a large and prominent olecranon fossa is present. The supratrochlear septum between the olecranon fossa (posteriorly) and the combined radial and coronoid fossae (anteriorly) is perforated, thus forming a large supratrochlear foramen.

Ulna

The ulna is a robust element in *Adalatherium* that is well preserved on both sides (Fig. 15); that from the left side was physically separated from the rest of the skeleton for study (Fig. 17). The proximal and distal epiphyses of the ulna are attached to, but not fully fused with, the diaphysis. The ulna is described with its trochlear notch facing anteriorly.

The ulna is only slightly shorter than the humerus (Table 2). It is only gently sigmoid in anterior view and bowed (convex anteriorly) in side view. The proximal epiphysis is large, covering the entire proximal end. Its surface is rough and faces dorsolaterally in anterior or posterior view and posterodorsally in medial or lateral view. The olecranon process is massive, occupying the proximal one-fourth of the bone. The process is rectangular in

cross-section, being anteroposteriorly longer than mediolaterally wide. It projects proximally and slightly posteriorly and is not curved anteriorly (Fig. 17C, D). In anterior view, the olecranon is nearly symmetrical (the medial edge is slightly more elevated than the lateral edge) but there is no sign of medial deflection. The anterior aspect of the olecranon is proximodistally flat and gently convex transversely. A distinct anconeal process arises along the anterior aspect of the olecranon process. The medial aspect of the olecranon process presents a large and shallow longitudinal fossa that extends distally to the level of the coronoid process (Fig. 17C). A round but robust posteromedial edge separates the medial aspect of the olecranon from its flat posterior aspect. The lateral side of the olecranon process is slightly concave (Fig. 17A, D). The posterolateral edge, which separates the lateral and posterior sides of the olecranon, is slightly less distinct than the posteromedial edge. It forms a fine edge extending distally from the proximal edge of the olecranon.

The trochlear notch is anteroposteriorly deep and proximodistally long. Both the anconeal and coronoid processes are prominent (Fig. 17). The anconeal process forms the proximal lip of the trochlear notch, which protrudes farther laterally than medially. In anterior view, the process is thus slightly asymmetrical, with the lateral edge being slightly longer and extending nearly horizontally, whereas the medial edge is shorter and extends proximomedially. The trochlear notch is overall saddle-shaped, concave anteroposteriorly and convex transversely. In anterior view, the trochlear notch is constricted in the middle and expands transversely at its proximal and distal ends. The median ridge of the trochlear notch (the ulnar guiding ridge of Szalay and Sargis, 2001), which fits into the deepest part of the trochlea on the humerus, is low and indistinct. The median ridge begins (proximally) at the tip of the anconeal process, extending distally and slightly medially. The distal portion of the ridge does not continue onto the coronoid process. The median ridge divides the trochlear notch into medial and lateral portions (Fig. 17A). A fine crest delimits the distal extension of the lateral portion. The facet on the medial portion continues distally onto the coronoid process. The humeral articular facet on the coronoid process faces proximomedially, sloping about 40° from a plane perpendicular to the long axis of the ulna. In medial or lateral view, the coronoid process protrudes farther anteriorly than the anconeal process. It has a semicircular outline, being convex medially and straight laterally. The lateral aspect of the coronoid process faces laterally and slightly anteriorly. It bears a shallowly concave and roughly triangular facet for the radial head. The facet extends laterally into a narrow, convex radial notch that is positioned just distal to the lateral portion of the trochlear notch and would have articulated with the radius in life. The trochlear and radial facets on the coronoid process form an angle of about 90°.

The ulnar shaft distal to the trochlear and radial notches gently curves posteriorly. A rounded ridge arises distal to the radial notch and extends toward the distal end of the ulna and defines the anterior border of the ulnar shaft, here termed the ulnar anterior ridge (Fig. 17A). The distal one-third of the ridge gradually expands mediolaterally and forms a longitudinal triangular area. The area has a posteriorly recurved medial border and a blunt lateral border. The lateral border is rounded and smoothly turns into the lateral aspect of the shaft, whereas the medial border is a well-defined crest (termed ulnar anterior ridge medial crest in Fig. 17). The distal-most portion of the triangular area articulates with the distal end of the radius. The articular facet is small and barely distinguishable (Fig. 17D).

The ulnar shaft just medial to the ulnar anterior ridge and distal to the coronoid process bears a longitudinal fossa, which probably represents the fossa for the brachialis muscle, as seen in extant therian mammals (Fig. 17A). The length of the fossa is about one-sixth of the ulnar length. The medial border of the fossa is much less salient than the ulnar anterior ridge. Nevertheless, the bone that demarcates the medial border of the brachialis fossa extends distally well beyond the fossa and forms a sharp crest along the distomedial aspect of the ulna (ulnar crest). The ulnar crest and the ulnar anterior ridge, particularly the fine medial crest of the ulnar anterior ridge, define a deep longitudinal sulcus (ulnar longitudinal sulcus). The sulcus and the crests diminish just proximal to the distal epiphysis (Fig. 17A). This morphology is suggestive of a well-developed interosseous ligament. The medial aspect of the ulnar shaft is smooth and flat. The posterior aspect of the ulnar shaft is gently convex and narrows distally only to expand again toward the epiphysis. The distal third of the ulnar shaft is roughly triangular in cross-section.

The distal epiphysis of the ulna has an elliptical base. The styloid process is prominent, arising posterolaterally from the base (Fig. 17). In lateral view, the distal epiphysis is triangular in shape, with proximal, posterior, and anteroventral sides, and a blunt apex that is directed posterodistally. There are two articular facets along the anteromedial edge of the process: a proximal one for the os Daubentonii (see below) and a distal one for the triquetrum (Fig. 17F). The facet for the os Daubentonii is smaller, gently convex, and almost square in outline. The facet for the triquetrum is larger, elliptical, and gently convex.

Radius

The radius is well preserved on both sides (Fig. 15), and, as for the ulna, the one from the left side was physically isolated for study (Fig. 18). The radius is described in the same orientation as the ulna, with its head fitting anterolaterally into the radial notch of the ulna.

The radius of *Adalatherium* is much shorter than the ulna, taking up two-thirds of the length of the ulna. Its proximal part is more slender than the ulnar shaft at the same level (Figs. 15, 17, 18). The radius gradually expands distally and, at the distal end, becomes more robust than the ulna. The radius is gently sigmoid in anterior view, with the proximal end slightly curved laterally and the distal end slightly curved medially. In UA 9030, the distal epiphysis of the radius is incompletely sutured with the diaphysis, whereas the proximal epiphysis is completely fused to the shaft.

In proximal view, the radial head is elliptical, mediolaterally wider than anteroposteriorly long. Both the medial and lateral ends gently taper transversely (Fig. 18E). The proximal articular facet is much larger than the proximal part of the radial shaft, overhanging the shaft in all directions, most prominently medially and laterally and less pronounced anteriorly. The proximal articular surface can be roughly divided into three parts (Fig. 18E). A large and almost circular concavity occupies the center. This portion articulates with the radial condyle of the humerus. The facet for the radial condyle is moderately deep, slightly longer in an anteromedial to posterolateral direction than transversely wide. A low and rounded ridge separates the radial condyle facet medially from a gently sloping facet for the humeral trochlea. The ridge and the facet for the humeral trochlea occupy the medial third of the articular surface. The humeral trochlea facet is flat and faces proximomedially and slightly posteriorly. When in articulation the facet is continuous, with the articular surface on the coronoid process of the ulna. Together they articulate with the medial aspect of the humeral trochlea. The low ridge is aligned with the median ridge of the ulnar trochlear notch. Lateral to the radial condyle facet is another convex area, which occupies the lateral fifth of the whole articular surface. In life, this area would have probably articulated with a concave facet lateral to the radial condyle on the distal humerus. The ulnar facet (articulating with the radial notch of the ulna) is well developed along the posterior aspect of the radial head

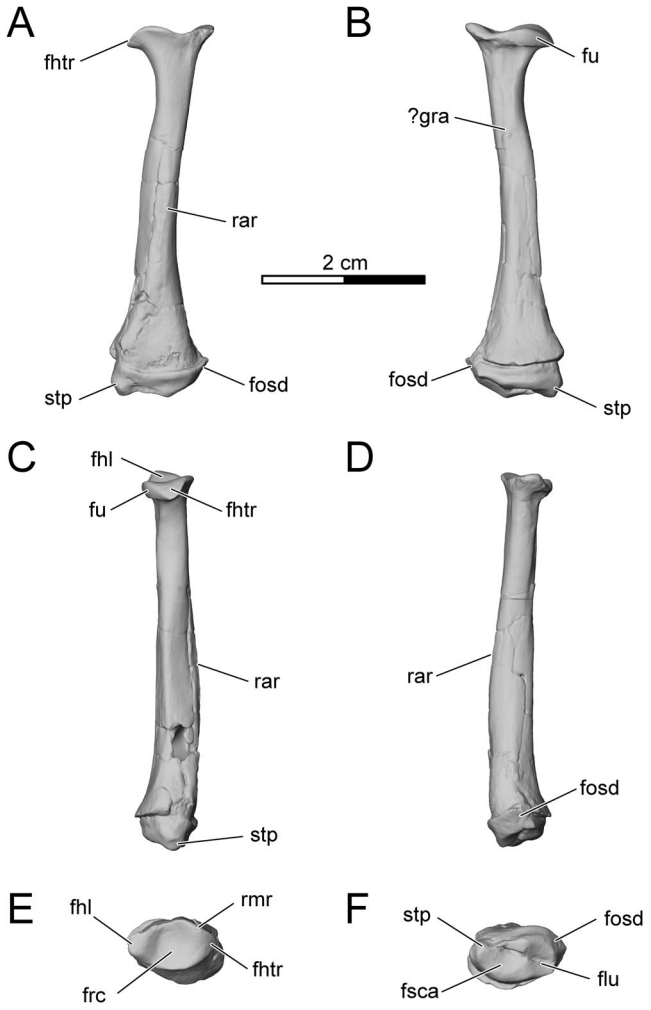

FIGURE 18. Left radius of *Adalatherium hui*, holotype (UA 9030), in **A**, anterior; **B**, posterior; **C**, medial; **D**, lateral; **E**, proximal; and **F**, distal views. **Abbreviations**: **fhl**, facet articulating with humerus lateral to radial condyle; **fhtr**, facet for humeral trochlea; **flu**, facet for lunate; **fosd**, facet for os Daubentonii; **frc**, facet for radial condyle; **fsca**, facet for scaphoid; **fu**, facet for ulna; **gra**, groove for radial artery; **rar**, radial anterior ridge; **rmr**, radial median ridge; **stp**, styloid process.

(Fig. 18B). The facet is lenticular; tapering medially and laterally, with the widest portion being located posterior to a low ridge.

The shaft of the radius gradually expands its diameter and changes its shape distally. The shaft can be roughly divided into three segments based on cross-sectional shape. The proximal one-third of the radial shaft is elliptical in cross-section and narrows distally to an almost circular outline. The anterior aspect is smooth and does not bear a distinct bicipital tuberosity. The middle third of the radial shaft is roughly triangular in cross-section. A conspicuous ridge is present along the anterior edge, dividing the anterior aspect into featureless anteromedial and anterolateral sides (Fig. 18A). The anterolateral side is gently convex, whereas the anteromedial side is flat. The posterior aspect of the middle part of the shaft is flat and narrower than the anteromedial aspect. A shallow groove is visible, traversing the shaft from proximomedial to distolateral, possibly tracking the path of the radial artery in life (Fig. 18B). A fine posteromedial ridge separates the posterior and anteromedial sides. The distal third of the shaft greatly expands mediolaterally and slightly posteriorly, leading to a roughly quadrangular cross-section. The anterior ridge and anteromedial aspect of the middle third of the shaft shift medially and become the anteromedial edge and medial aspect in the distal third of the shaft, respectively. The anterior aspect of the distal shaft is flat, whereas the lateral and posterior aspects are gently convex. The borders between the anterior, lateral, and posterior sides are indistinct.

The distal epiphysis is robust and has an elliptical outline, being transversely wide and anteroposteriorly short (Fig. 18F). The posterolateral corner of the epiphysis probably contacted the ulna in life, but a clear articular facet is not visible. The anteromedial corner bears a small styloid process, which is much less prominent than that of the ulna. The distal articular facet of the radius is slightly smaller than the distal epiphysis and not strictly perpendicular to the long axis of the radius. Instead, it faces distally and slightly posteriorly. The anterior lip of the articular facet is raised and more prominent than the posterior edge. The distal surface comprises the articular facets for the scaphoid medially and the lunate laterally (Fig. 18F). In addition, the radius articulated with the os Daubentonii along the lateral aspect of the epiphysis. The large facet for the scaphoid occupies the medial half of the distal surface. It is triangular and concave. The posteromedial border of the facet is convex and forms a blunt ridge. The facet for the lunate is positioned lateral to the scaphoid facet. It is smaller than the scaphoid facet, elliptical, concave, and surrounded by fine crests (Fig. 18F). A small tubercle in the middle of the anterior border of the distal surface marks the boundary between two facets. The facet for the os Daubentonii, on the lateral side of the distal epiphysis, faces distolaterally, is triangular in outline, and is about half as wide mediolaterally as the lunate facet.

Manus

Both manus are exceptionally well preserved. The right manus of UA 9030 is completely preserved in articulation (Fig. 15), whereas the left manus is missing several phalanges. Of these, three distal phalanges were recovered from the surface during excavation but the intermediate phalanx of digit IV and one distal phalanx were not found. The left manus was disarticulated for study and forms the basis for this description unless otherwise stated.

The carpus of UA 9030 comprises 10 elements (Fig. 19; Table 3): four proximal carpals (scaphoid, lunate, triquetrum, pisiform), one centrale, four distal carpals (trapezium, trapezoid, capitate, hamate), and an additional sesamoid bone called the os Daubentonii (Lessertisseur and Saban, 1967, in Kielan-Jaworowska, 1978). In life, the os Daubentonii would have fit into the gap between the distal epiphyses of the radius and ulna and the triquetrum; it may have also contacted the lunate. The individual carpal elements will be described in an order that is generally from proximal to distal and from medial to lateral (scaphoid, lunate, os Daubentonii, triquetrum, pisiform, centrale, trapezium, trapezoid, capitate, hamate) and illustrated in six views: dorsal, palmar (ventral), lateral (ulnar), medial (radial), proximal, and distal.

Scaphoid—The scaphoid is mediopalmarly to dorsolaterally long and proximodistally short (Figs. 15, 19, 20). In proximal view, the scaphoid forms an arch that is convex medially (Fig. 20E). A deep groove, termed scaphoid groove here (Fig. 20), separates the dorsolateral end, which articulates with the radius, from the mediopalmar end, which bears a robust palmar tuberosity. The scaphoid groove extends in a dorsomedial to lateropalmar direction and is visible on the medial aspect of the scaphoid as a sizable notch. The convex radial facet is triangular in shape and extends onto the dorsal aspect of the scaphoid. The dorsal and medial aspects of the bone are convex. A nutrient foramen is present just distal to the radial facet (Fig. 20A). The medial aspect is uneven and bears several pits and notches. Most prominently, a deeply incised notch is present along the

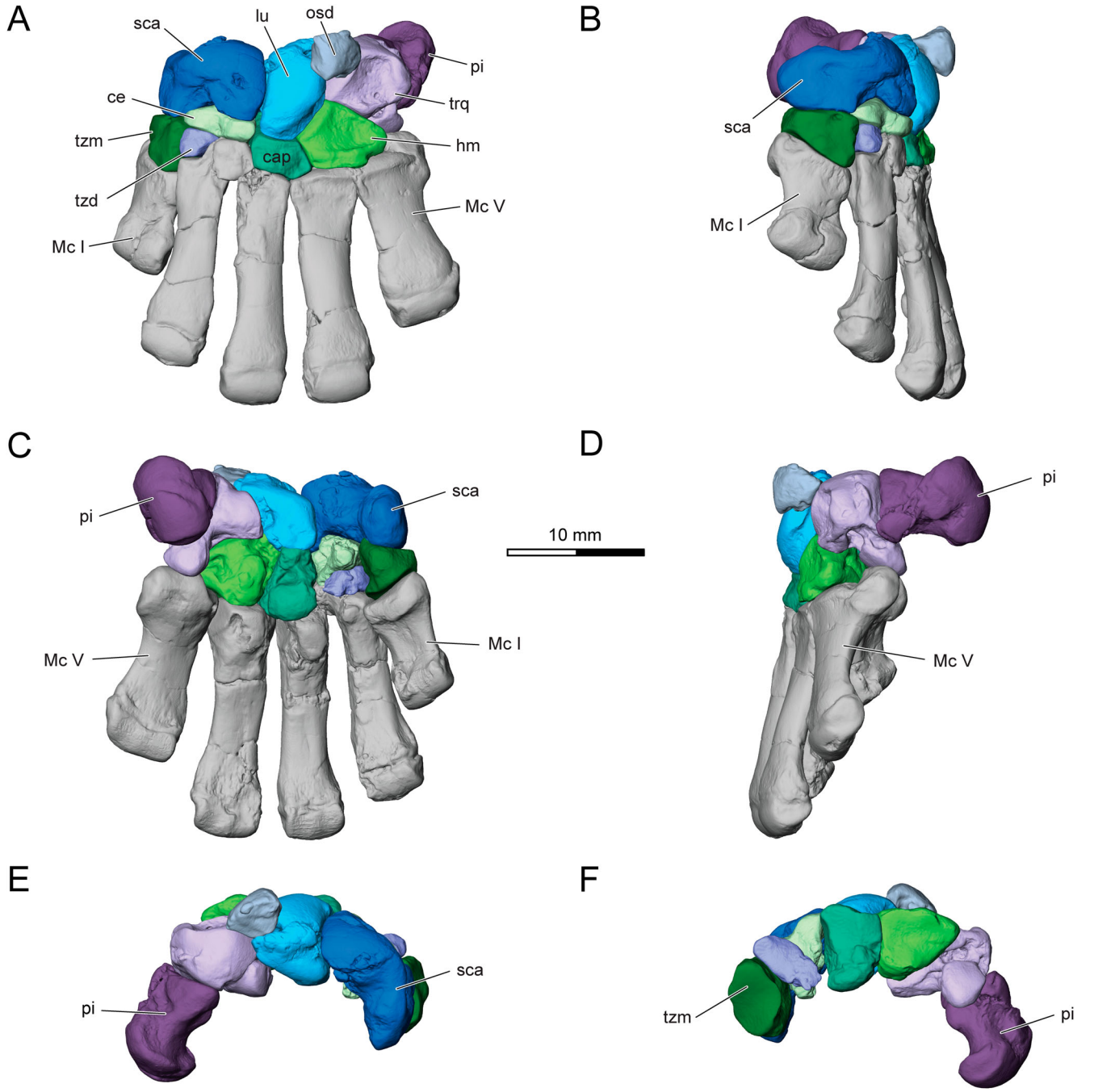

FIGURE 19. Reconstruction of left carpals and metacarpals of *Adalatherium hui*, holotype (UA 9030), based on µCT images, in **A**, dorsal, **B**, medial, **C**, palmar (= ventral), **D**, lateral **E**, proximal, and **F**, distal views. **Abbreviations**: **cap**, capitate; **ce**, centrale; **hm**, hamate; **lu**, lunate; **Mc**, metacarpal; **osd**, os Daubentonii; **pi**, pisiform; **sca**, scaphoid; **trq**, triquetrum; **tzd**, trapezoid; **tzm**, trapezium.

distal edge of the scaphoid. Laterally, the scaphoid articulates with the lunate (Fig. 19). The lunate facet is flat, elliptical, and faces lateropalmarly (Fig. 20D). The distal aspect bears articular facets for the trapezium and centrale (Fig. 20F). The trapezium facet is located on the palmar tuberosity; it is convex and elliptical in outline. The centrale facet occupies the dorsal aspect of the distal portion of the scaphoid. The facet is triangular in outline, concave medially, and flat laterally.

Lunate—The lunate is a proximodistally long, dorsopalmarly deep, and mediolaterally narrow bone (Figs. 15, 19, 21). The longitudinal axis of the bone was oriented in a proximolateral to distomedial direction in life. The lunate is centrally positioned in the manus and articulates with the radius dorsoproximally, the scaphoid medially, the capitate distally, the hamate distolaterally, the triquetrum laterally, and possibly the os Daubentonii proximolaterally (Figs. 15, 19). The radial facet is large and occupies the dorsoproximal aspect of the lunate. The convex facet is elliptical, extending in a proximolateral to distomedial direction. A small facet is present proximolateral to the radial facet, which might have contacted the os Daubentonii in life (Fig. 21A). In

TABLE 3. Basic metrics of the left carpals of *Adalatherium hui*, holotype (UA 9030).

Element	Length	Width	Depth
Scaphoid	6.5	4.6	10.4
Lunate	7.4	4.5	7.0
Os Daubentonii	4.6	5.0	3.8
Triquetrum	9.0	7.3	5.6
Pisiform	8.4	7.1	6.3
Centrale	3.2	5.9	5.1
Trapezium	4.2	4.5	6.1
Trapezoid	2.2	2.4	5.4
Capitate	5.8	4.5	6.0
Hamate	5.9	6.9	5.0

Length measured in proximodistal direction, width in mediolateral direction, and depth in dorsopalmar direction. All linear measurements in mm.

dorsal view, a prominent, narrow sulcus bounds the distolateral aspect of the radial facet. This sulcus separates the facets for the radius (and possibly the facet for the os Daubentonii) from the facets for the hamate and triquetrum distolaterally (Fig. 21A). A small nutrient foramen opens at the proximal terminus of the sulcus. The medial aspect of the lunate is triangular in outline, with convex proximodorsal and proximopalmar sides and a concave distal side. Two small facets, dorsal and palmar, indicate articulation with the scaphoid. The dorsal facet is proximodistally tall and dorsopalmarly narrow. The smaller palmar facet is rectangular in outline. Both facets are flat and, rather than strictly facing medially, are slightly tilted toward the center of the scaphoid, thereby somewhat facing each other (Fig. 21B). A convex and 'U'-shaped nonarticular area is located between the two facets. The lateral aspect bears the articular facets for the triquetrum proximally and the hamate distally (Fig. 21D). The facets for the hamate and triquetrum are nearly continuous. Only a swelling at the middle of the dorsolateral edge of the bone and a slight change in orientation of the facets mark the boundary between them. The facet for the triquetrum is rather small, triangular in outline, and flat. The proximopalmar aspect of the lunate, however, is not as well preserved, and it is entirely possible that the facet continued farther palmarly. The facet for the hamate is much larger, flat, and faces distolaterally. The distal aspect is not strictly perpendicular to the longitudinal axis of the bone but rather faces mediodistally. The facet for the capitate is convex and somewhat hourglass-shaped, expanded dorsally and palmarly but constricted in the middle.

Os Daubentonii—The os Daubentonii is a small carpal sesamoid bone rarely found in the mammalian skeleton

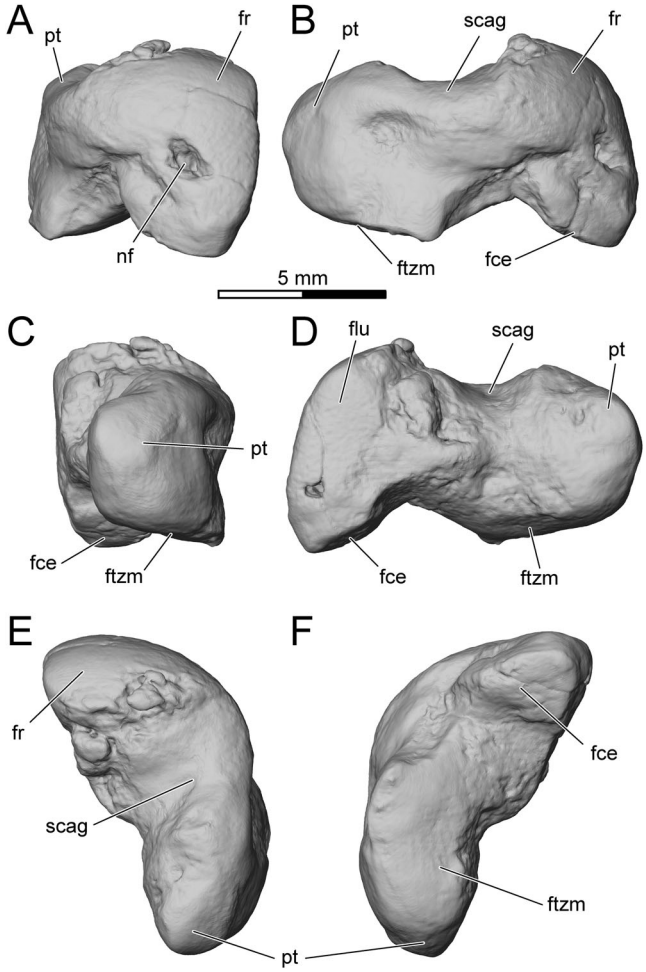

FIGURE 20. Left scaphoid of *Adalatherium hui*, holotype (UA 9030), in **A**, dorsal, **B**, medial, **C**, palmar (= ventral), **D**, lateral, **E**, proximal, and **F**, distal views. **Abbreviations**: **fce**, facet for centrale; **flu**, facet for lunate; **fr**, facet for radius; **ftzm**, facet for trapezium; **nf**, nutrient foramen; **pt**, palmar tuberosity; **scag**, scaphoid groove.

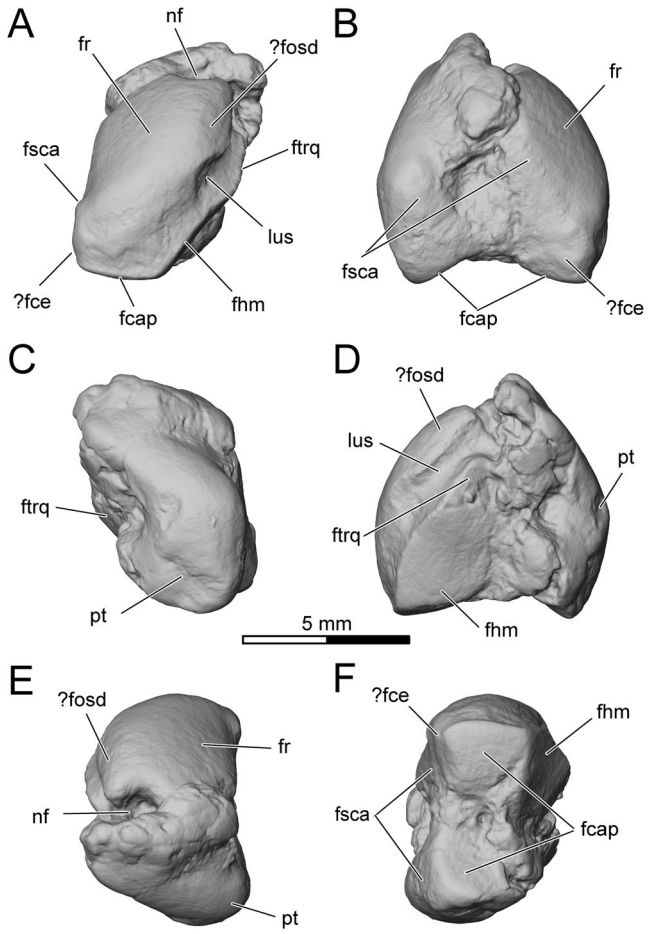

FIGURE 21. Left lunate of *Adalatherium hui*, holotype (UA 9030), in **A**, dorsal, **B**, medial, **C**, palmar (= ventral), **D**, lateral, **E**, proximal, and **F**, distal views. **Abbreviations**: **fcap**, facet for capitate; **fce**, facet for centrale; **fhm**, facet for hamate; **fosd**, facet for os Daubentonii; **fr**, facet for radius; **fsca**, facet for scaphoid; **ftrq**, facet for triquetrum; **lus**, sulcus on lunate; **nf**, nutrient foramen; **pt**, palmar tuberosity.

(Lessertisseur and Saban, 1967, in Kielan-Jaworowska, 1978). In *Adalatherium*, the sesamoid is tetrahedral in shape, with dorsal, proximomedial, proximolateral, and distolateral sides (Figs. 15, 19, 22). The os Daubentonii fits into the gap between the distal epiphyses of the radius and ulna (Fig. 15), with facets for those elements on the proximomedial and proximolateral aspects, respectively (Fig. 22E). The radial facet is gently convex, and the ulnar facet is triangular in outline and flat. A deep sulcus is developed at the intersection of the proximomedial and distolateral aspects (Fig. 22C, F). It opens as a notch at the distodorsomedial corner, where the bone may have contacted the lunate in life. The sulcus appears to be aligned with that on the dorsal aspect of the lunate (see above). The distolateral aspect bears a small and gently concave facet for the triquetrum (Fig. 22).

Triquetrum—The triquetrum is roughly pentagonal in outline in dorsal view, with proximolateral, proximomedial, distomedial, distal, and lateral margins (Figs. 15, 19, 23). The margins form elevated ridges that surround the concave dorsal surface. The triquetrum articulates with the ulna proximolaterally, the lunate and os Daubentonii proximomedially, the hamate distomedially, the pisiform palmarly, and metacarpal V distally. The proximomedial aspect of the bone is gently convex and bears a large and continuous facet for the lunate and os Daubentonii. In medial view, a small sulcus divides the lunate facet into a dorsally and palmarly positioned facet (Fig. 23B). This palmar facet is elliptical and gently convex. The proximolateral aspect of the triquetrum comprises a convex facet for the ulna (Fig. 23D, E). The distomedial aspect bears a large concave facet for the hamate (Fig. 23F). A sturdy process protrudes distally from the distolateral part of the triquetrum. The process is gently convex dorsally and bears a facet for metacarpal V (Fig. 23A, F). A deep and sizable fossa is present at the junction of the distal process and the body of the triquetrum. The distinct feature on the palmar aspect is a slightly raised facet for the pisiform (Fig. 23C). The facet is proximally located and extends distally onto the palmar side of the distal process. The surface of the facet is slightly convex and, overall, faces palmarly and slightly laterally.

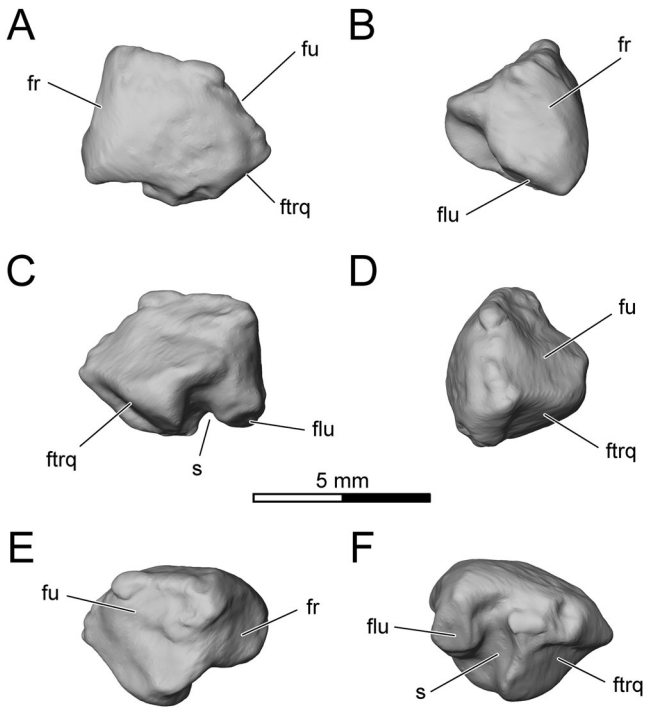

FIGURE 22. Left os Daubentonii of *Adalatherium hui*, holotype (UA 9030), in **A**, dorsal, **B**, medial, **C**, palmar (= ventral), **D**, lateral, **E**, proximal, and **F**, distal views. **Abbreviations**: **flu**, facet for lunate; **fr**, facet for radius; **ftrq**, facet for triquetrum; **fu**, facet for ulna; **s**, sulcus.

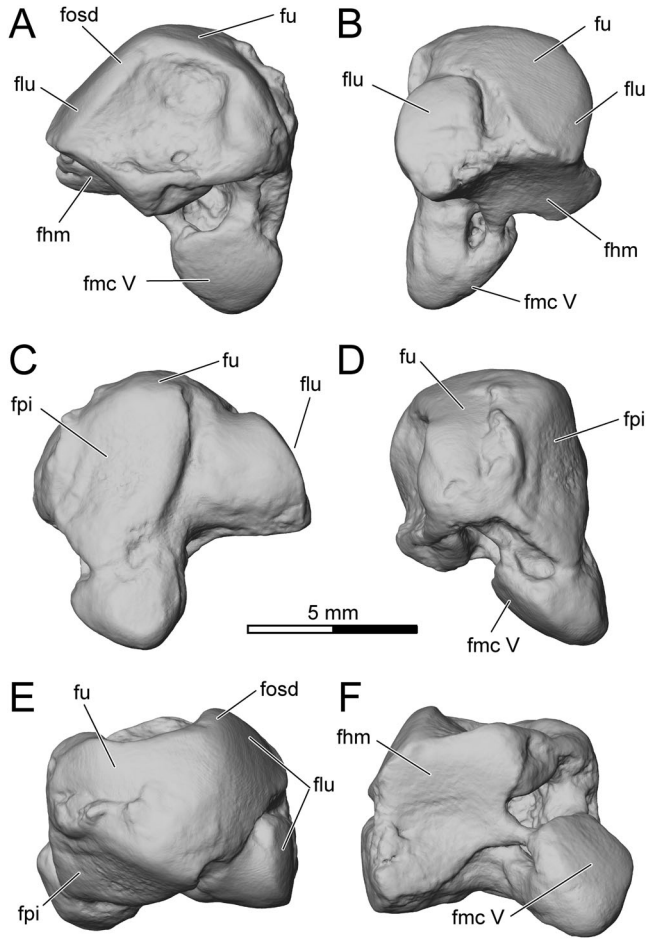

FIGURE 23. Left triquetrum of *Adalatherium hui*, holotype (UA 9030), in **A**, dorsal, **B**, medial, **C**, palmar (= ventral), **D**, lateral, **E**, proximal, and **F**, distal views. **Abbreviations**: **fhm**, facet for hamate; **flu**, facet for lunate; **fmc**, facet for metacarpal; **fosd**, facet for os Daubentonii; **fpi**, facet for pisiform; **fu**, facet for ulna.

Pisiform—The pisiform is a robust element equivalent in height and length to the triquetrum (Figs. 15, 19, 24). It contacts only the triquetrum and would have pointed palmarly and slightly laterally in life. The pisiform can be divided into a proximal base and a distal head, with a constricted neck between them (Fig. 24). Both the base and head are elongated, but in opposite directions. The base extends in a proximomedial to distolateral direction, whereas the head is expanded transversely. The base gently tapers dorsally, with an elliptical and concave facet for the triquetrum (Fig. 24B, D, E). A distinct tubercle is present just distal to the facet for the triquetrum on the medial aspect of the pisiform (Fig. 24B). The head is bigger than the base in dorsal and palmar views; it is bulbous in shape and curved medially. A sharp crest surrounds the head and separates it from the neck.

Centrale—The centrale is a small and plate-like bone (Figs. 15, 19, 25). The proximal aspect has a heart-shaped outline (Fig. 25E) and bears a gently convex medial facet and a smaller and flat lateral facet, matching the distal aspect of the scaphoid. In dorsal view, the centrale is proximodistally slender, tapering toward the medial and lateral ends (Fig. 25A). It has a rugose surface with a distinct depression in the middle. The lateral surface of the centrale bears a large and flat to slightly concave

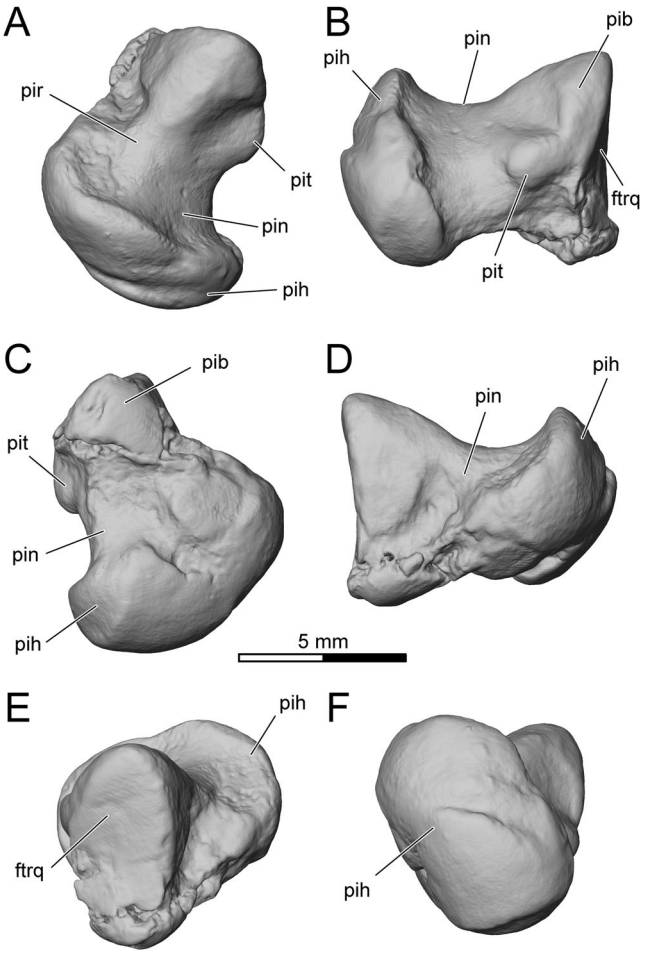

FIGURE 24. Left pisiform of *Adalatherium hui*, holotype (UA 9030), in **A**, dorsal, **B**, medial, **C**, palmar (= ventral), **D**, lateral, **E**, proximal, and **F**, distal views. **Abbreviations**: **ftrq**, facet for triquetrum; **pib**, pisiform base; **pih**, pisiform head; **pin**, pisiform neck; **pir**, pisiform ridge; **pit**, pisiform tubercle.

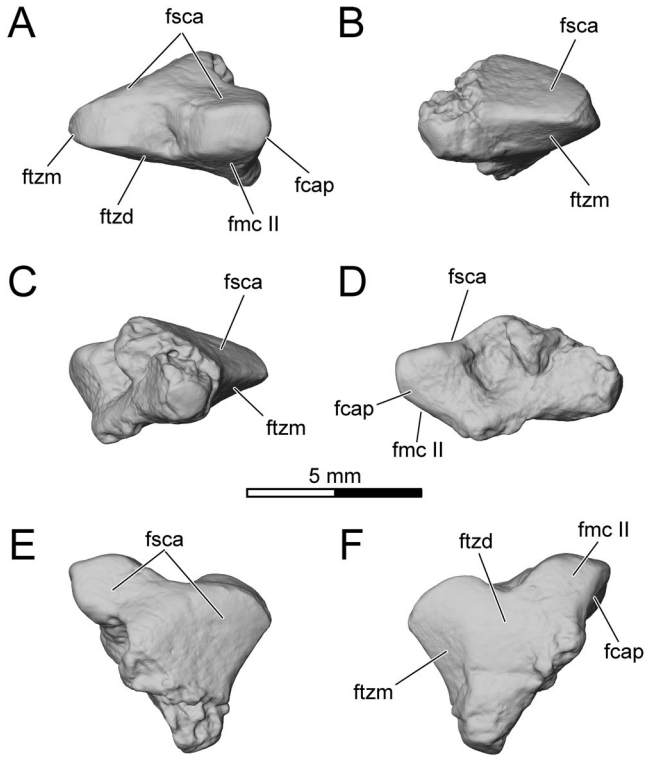

FIGURE 25. Left centrale of *Adalatherium hui*, holotype (UA 9030), in **A**, dorsal, **B**, medial, **C**, palmar (= ventral), **D**, lateral, **E**, proximal, and **F**, distal views. **Abbreviations**: **fcap**, facet for capitate; **fmc**, facet for metacarpal; **fsca**, facet for scaphoid; **ftzd**, facet for trapezoid; **ftzm**, facet for trapezium.

facet for the capitate (Fig. 25D). The surface is broken, and only the dorsal aspect of the facet is preserved. Medially, the facet for the scaphoid and trapezium converge such that the medial aspect of the centrale forms a wedge (Fig. 25B, C). The medial edge of the centrale is concave, which is best seen in proximal or distal view (Fig. 25E, F). Distally, the centrale articulates with the trapezium, trapezoid, and metacarpal II. The facet for the trapezium is narrow and concave and extends along the medial margin of the distal part of the centrale. The trapezoid facet is likewise narrow and extends along the midline of the centrale. The metacarpal II facet is restricted to the dorsolateral aspect of the distal centrale. Most of the flat metacarpal II facet is preserved on the left centrale; only the palmar-most aspect is missing (Fig. 25F).

Trapezium—The trapezium articulates with the scaphoid proximally, the centrale proximolaterally, the trapezoid and metacarpal II laterally, and metacarpal I distally (Figs. 15, 19, 26). In proximal view, the facets for the scaphoid and centrale meet at an obtuse angle, thereby forming a low ridge that extends in a dorsopalmar direction (Fig. 26E). The scaphoid facet is large, elliptical, and concave. The flat facet for the centrale is dorsopalmarly long and mediolaterally compressed. The dorsal aspect of the bone has a rugose texture and is triangular in outline, with its proximal and distal aspects converging medially (Fig. 26A). In lateral view, a small semilunar facet for the trapezoid is visible along the proximodorsal border (Fig. 26D). The facet is gently convex and slightly raised. The distal surface is fully occupied by the facet for metacarpal I (Fig. 26F). The facet is elliptical and saddle-shaped, concave dorsopalmarly and slightly convex mediolaterally. The trapezium does not possess a distinct palmar tubercle; the palmar aspect is convex with a smooth surface (Fig. 26C). A sizable sesamoid bone articulated with the trapezium palmarly (Fig. 26C).

Trapezoid—The trapezoid is the smallest of the carpal bones (Figs. 15, 19, 27). It is dorsopalmarly deep, and equal in length and width in dorsal view. The distal and lateral sides of the trapezoid form one continuous surface palmarly, and the cross-section of the bone changes from quadrangular dorsally to triangular palmarly (Fig. 27). In life, this distolateral surface would have perfectly fit into the notch at the proximomedial corner of metacarpal II. In proximal view, the trapezoid bears a flat facet for the centrale (Fig. 27E). The medial aspect is slightly concave and articulates with the trapezium. The palmar aspect of the trapezoid is poorly preserved in the disarticulated left forefoot and blocked from view by the trapezium in the right forefoot (Fig. 15). In the left forefoot, the trapezoid is pushed against the capitate palmarly. The contact area is not well preserved; therefore, the boundary between the two elements is unclear and cannot be traced in the scans of the left carpals. The µCT images of the right forefoot, however, reveal the morphology of the trapezoid deep to the trapezium. The trapezoid gently tapers palmarly and, if at all, only contacted the capitate along its palmar-most aspect.

Capitate—The capitate articulates with the hamate, the lunate, the centrale, and metacarpals II, III, and IV (Figs. 15, 19, 28). In

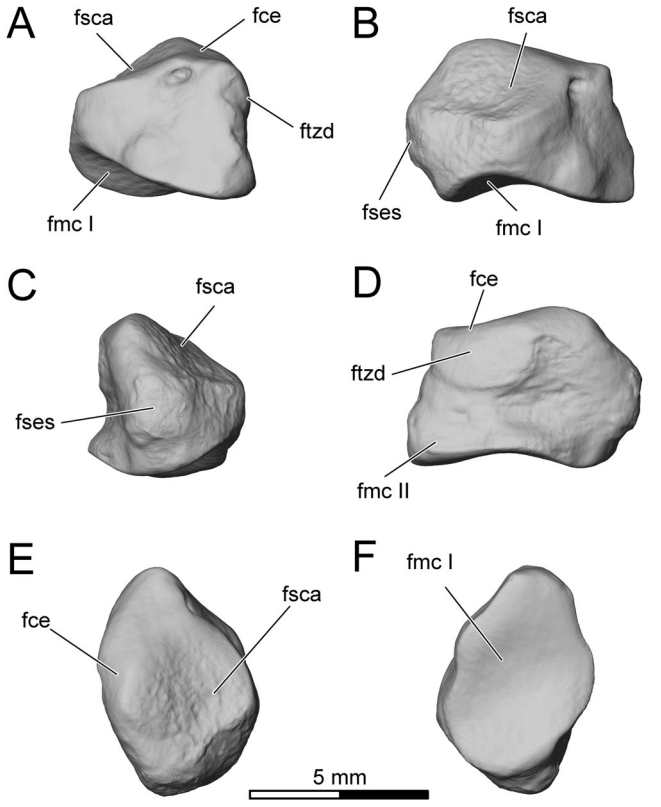

FIGURE 26. Left trapezium of *Adalatherium hui*, holotype (UA 9030), in **A**, dorsal, **B**, medial, **C**, palmar (= ventral), **D**, lateral, **E**, proximal, and **F**, distal views. **Abbreviations**: **fce**, facet for centrale; **fmc**, facet for metacarpal; **fsca**, facet for scaphoid; **fses**, facet for sesamoid; **ftzd**, facet for trapezoid.

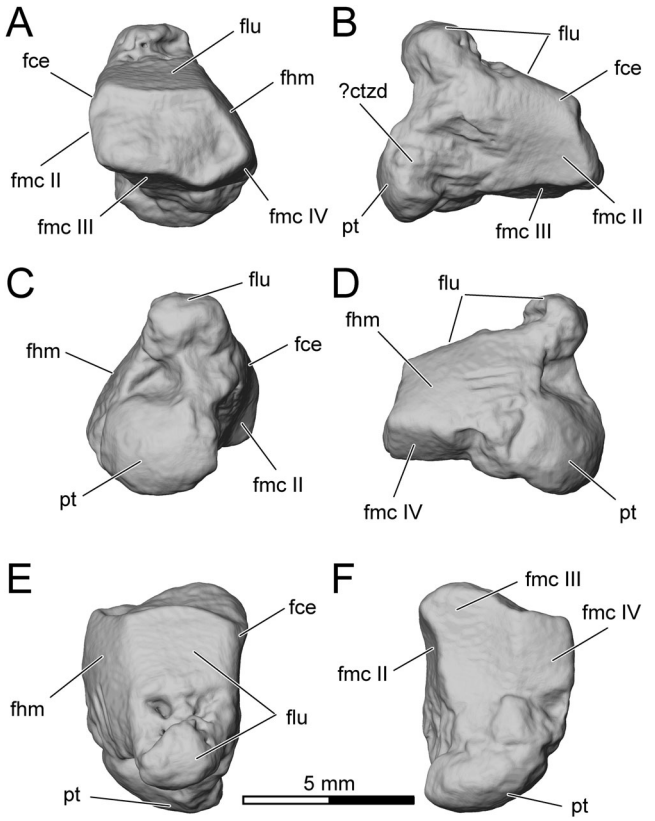

FIGURE 28. Left capitate of *Adalatherium hui*, holotype (UA 9030), in **A**, dorsal, **B**, medial, **C**, palmar (= ventral), **D**, lateral, **E**, proximal, and **F**, distal views. **Abbreviations**: **ctzd**, contact with trapezoid; **fce**, facet for centrale; **fhm**, facet for hamate; **flu**, facet for lunate; **fmc**, facet for metacarpal; **pt**, palmar tuberosity.

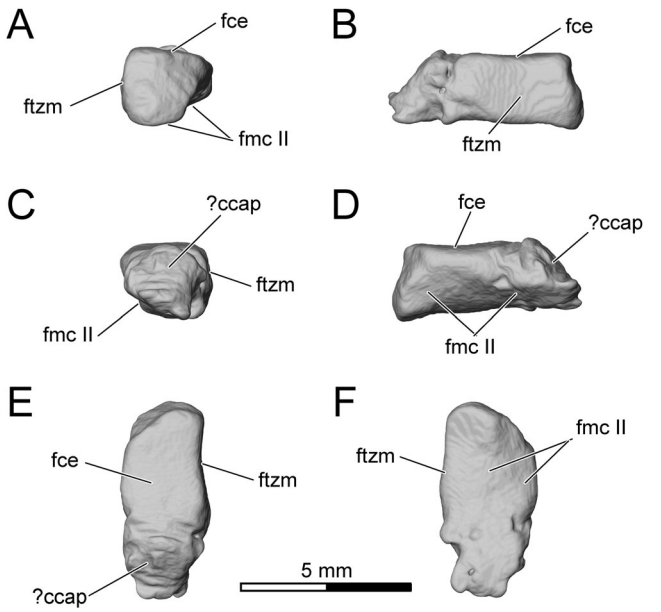

FIGURE 27. Left trapezoid of *Adalatherium hui*, holotype (UA 9030), in **A**, dorsal, **B**, medial, **C**, palmar (= ventral), **D**, lateral, **E**, proximal, and **F**, distal views. **Abbreviations**: **ccap**, contact with capitate; **fce**, facet for centrale; **fmc**, facet for metacarpal; **ftzm**, facet for trapezium.

dorsal view, the capitate has the shape of a mediolaterally elongate hexagon with proximomedial, proximal, proximolateral, distomedial, distal, and distolateral sides (Fig. 28A). Each side corresponds to an articular facet for its neighboring bones. The proximal aspect is flat and slopes proximopalmarly, ending in a small and bulbous proximal tubercle. The facet for the lunate extends to the proximal palmar tubercle. Given the convex articular facet on the lunate, both bones probably would have articulated along the dorsal and palmar aspects (Fig. 28B). The proximolateral surface bears a gently convex facet for the hamate. A narrow facet for the proximomedial aspect of metacarpal IV is present distolaterally (Fig. 28E). Distally, the concave facet for metacarpal III slightly narrows palmarly. Most of the medial aspect of the capitate is occupied by the gently concave facet for metacarpal II (Fig. 28B). A narrow proximomedial portion bears a gently convex facet for the centrale. The palmar aspect is dominated by a rounded tuberosity. The proximal tubercle is only about half the size of the distal tuberosity (Fig. 28C).

Hamate—The hamate articulates with the lunate proximomedially, the triquetrum proximolaterally, the capitate medially, and metacarpals IV and V distally (Figs. 15, 19, 29). The dorsal aspect is pentagonal in outline, with medial, proximomedial, proximolateral, distolateral, and distal sides that are surrounded by sharp edges (Fig. 29A). The proximomedial aspect of the bone slopes proximopalmarly and bears a gently convex facet for the lunate. The facet is dorsopalmarly deeper than mediolaterally wide and narrows palmarly. The facet for the triquetrum is gently convex and occupies the dorsal portion of the proximolateral aspect (Fig. 29A, E). The facet is triangular in outline,

tapering distolaterally. The medial aspect of the bone bears the facet for the capitate, which is gently concave and slightly widens palmarly (Fig. 29B). The distal aspect of the bone is trapezoidal in outline, with a long dorsal margin, a straight medial margin, a proximally curved lateropalmar margin, and a small palmar margin (Fig. 29F). The facet for metacarpal IV occupies the medial portion, whereas the facet for metacarpal V occupies the lateral portion of the distal surface. Both facets are concave dorsopalmarly; a low ridge and a swelling in the middle of the dorsal margin mark the boundary between the two facets. The palmar aspect of the bone is irregular, bearing several pits and grooves along the proximal and lateral margins (Fig. 29C). The most prominent feature of the palmar surface is an elliptical, slightly raised palmar tuberosity located in the distomedial corner (Fig. 29B–E).

Metacarpals—The metacarpals (Mc) of both manus in UA 9030 are well preserved (Fig. 15). Mc I–Mc V of the left manus, which provide the focus for the description below (Figs. 19, 30), form a gentle arch, convex dorsally. They also form an arch, in dorsal or ventral view, distally as well as proximally, although Mc II is displaced proximally compared with the other metacarpals and Mc I is shifted distally. The metacarpals are more slender and proximodistally shorter than their corresponding metatarsals. The first metacarpal is the most robust and shortest of the metacarpals. The robustness (ratio of midshaft mediolateral width/proximodistal length) decreases in the order Mc I > Mc V > Mc IV > Mc II = Mc III, whereas the length increases in the order Mc I < Mc V < Mc II < Mc III ≈ Mc IV (Table 4).

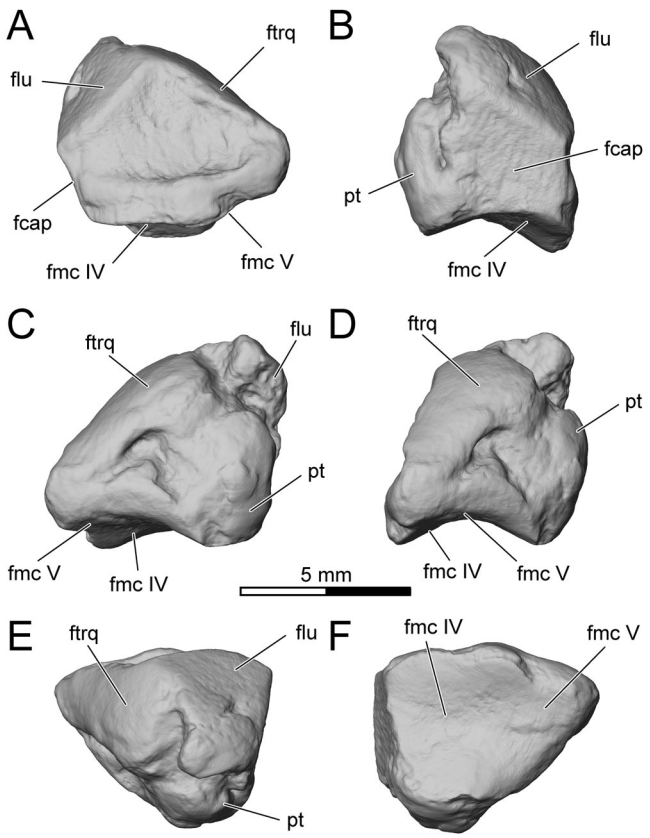

FIGURE 29. Left hamate of *Adalatherium hui*, holotype (UA 9030), in **A**, dorsal, **B**, medial **C**, palmar (= ventral), **D**, lateral, **E**, proximal, and **F**, distal views. **Abbreviations**: **fcap**, facet for capitate; **flu**, facet for lunate; **fmc**, facet for metacarpal; **ftrq**, facet for triquetrum; **pt**, palmar tuberosity.

The first metacarpal is short and robust and slightly constricted at mid-length (Figs. 19, 30A). The proximal margin of Mc I lies oblique to the shaft such that the medial side is longer than the lateral. The proximal aspect is completely occupied by the articular facet for the trapezium. The facet is rhomboid in outline, gently slopes toward the mediopalmar corner, and is slightly saddle-shaped, convex dorsolaterally to mediopalmarly and gently concave perpendicular to this axis, perfectly matching its counterpart on the trapezium. Dorsally, a sizable fossa surrounded by an elevated rim is present that matches a small tuberosity on the distodorsal aspect of the trapezium (Fig. 30A, E). Laterally, Mc I bears a large and flat facet for Mc II (Fig. 30D). Just dorsal to the facet is a small quadrangular tuberosity that is continuous with a small ridge on the trapezium. A prominent palmar tuberosity is present along the proximal margin of the shaft (Fig. 30B, C). The distal end is asymmetrical. In dorsal view, the medial and lateral sides of the distal end are tilted medially, the lateral more so than the medial (Fig. 30A). The facet for the first proximal manual phalanx is convex, extending well onto the dorsal and palmar aspects of the bone. A single sesamoid bone is present palmar to the distal end of the bone.

The second metacarpal is twice the length of Mc I and is much more slender (Fig. 30). The proximal morphology of Mc II is unique and clearly distinguishes it from the remaining metacarpals. The lateral part of the proximal surfaces is proximolaterally expanded into a block-like structure that overhangs the shaft laterally (Fig. 30A). It forms a deep notch laterally for Mc III and one medially for the trapezoid. The facet for the trapezoid can be divided into a medial part, which articulates with the distal surface of the trapezoid, and a lateral part, which articulates with the lateral aspect of the trapezoid. The two parts of the trapezoid facet join at an angle of almost 90° dorsally. The medial part is gently convex dorsopalmarly; the lateral part is flat (Fig. 30A, B). The most proximal part of the proximal surface, lateral to the trapezoid facet, articulates with the centrale (Fig. 30A). The flat centrale facet is roughly triangular and faces proximally. The capitate also articulates with the expanded proximal surface of Mc II (Figs. 19A, 30A). A small facet is visible lateral to the facet for the centrale. The capitate facet is gently convex and faces proximolaterally. Distal to the capitate facet, Mc III articulates with the distolateral aspect of the overhanging proximal surface of Mc II (Fig. 19A). In medial view, Mc II bears a gently convex facet for Mc I that is positioned slightly distal to the proximal margin of Mc II. The facet for the trapezium is not discernible but, based on our reconstruction (Fig. 19), the trapezium might have contacted Mc II along the proximomedial margin. A small but distinct palmar tuberosity is present on the proximopalmar aspect of Mc II. The dorsal aspect of the shaft is gently convex transversely; the palmar aspect is concave proximodistally. The cross-section of the bone at mid-length is squarish. The distal epiphysis is not completely fused to the shaft; a fine suture separating the two is still present. The facet for the second proximal manual phalanx is convex and extends palmarly and dorsally. The palmar aspect bears a fine ridge in the center of the facet separating the articulation for the two sesamoid bones (Fig. 30B, F).

The third metacarpal is slender (Fig. 30). Whereas the other metacarpals have transversely expanded proximal and distal ends, Mc III is narrow proximally and only gently expanded distally. The proximal facet is gently convex, roughly quadrangular in outline, dorsopalmarly deeper than mediolaterally wide (Fig. 30E). The facet gently tapers palmarly into a flat palmar tuberosity (Fig. 30B, C). The medial and lateral sides are slightly bowed inward. Most of the proximal aspect articulates with the capitate. Just a narrow medial portion of the proximal surface is in contact with Mc II (Fig. 30A–C, E). However, the facet is not preserved well enough on the left manus to definitively determine whether there was a morphological boundary between the two facets or

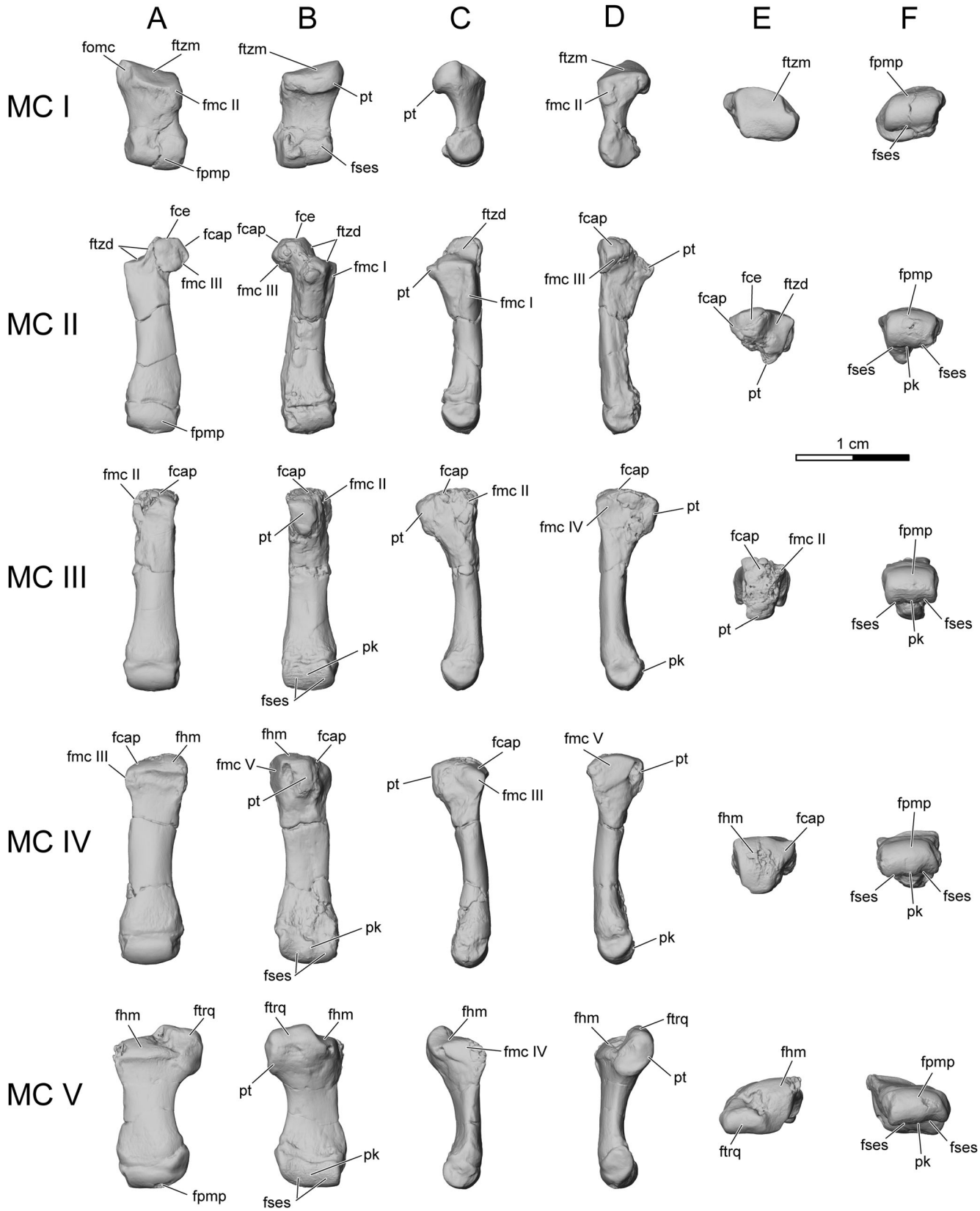

FIGURE 30. Left metacarpals (Mc) I–V of *Adalatherium hui*, holotype (UA 9030), in **A**, dorsal, **B**, palmar (= ventral), **C**, medial, **D**, lateral, **E**, proximal, and **F**, distal views. Rows from top to bottom: Mc I, Mc II, Mc III, Mc IV, and Mc V. **Abbreviations**: **fcap**, facet for capitate; **fce**, facet for centrale; **fhm**, facet for hamate; **fmc**, facet for metacarpal; **fomc**, fossa on metacarpal; **fpmp**, facet for proximal manual phalanx; **fses**, facet for sesamoid; **ftrq**, facet for triquetrum; **ftzd**, facet for trapezoid; **ftzm**, facet for trapezium; **pk**, palmar keel; **pt**, palmar tuberosity.

TABLE 4. Basic metrics of the manus of *Adalatherium hui*, holotype (UA 9030).

Element	PDL	MLWP	DPDP	MLWM	DPDM	MLWD	DPDD	ROB
Mc I	8.8	5.6	4.6	4.6	2.6	4.9	3.1	0.52
Mc II	17.6	5.8	5.2	3.3	2.6	5.0	3.3	0.19
Mc III	18.0	4.1	5.8	3.4	2.6	4.9	3.3	0.19
Mc IV	18.2	5.4	5.1	3.8	2.2	5.4	3.5	0.21
Mc V	14.7	8.0	4.5	4.7	2.1	6.5	3.1	0.32
PMP I	9.8	5.2	4.1	3.6	2.5	3.8	3.1	0.37
PMP II	10.2	5.2	3.7	3.3	2.6	4.0	2.8	0.32
PMP III	9.9	4.9	3.6	3.2	2.2	4.1	2.7	0.32
PMP IV	8.9	5.3	3.5	3.4	2.2	4.2	2.7	0.38
PMP V	7.0	5.4	3.2	3.9	1.8	4.3	2.3	0.56
IMP II	~6.8	4.4	3.0	2.9	1.8	3.2	2.3	0.43
IMP V	5.9	4.2	3.0	2.9	1.8	3.3	2.4	0.49
IMP II*	6.7	4.4	2.7	2.9	1.7	3.0	2.1	0.43
IMP III*	6.7	4.4	2.8	2.6	1.7	2.8	2.3	0.38
IMP IV*	6.5	4.0	3.0	2.6	1.4	2.7	2.2	0.40
IMP V*	5.7	4.3	2.6	2.9	1.4	3.1	2.3	0.51
DMP I	9.9	3.1	3.6	—	—	—	—	—
DMP II	8.0	2.7	3.2	—	—	—	—	—
DMP III	8.0	2.6	2.9	—	—	—	—	—
DMP IV*	7.3	2.5	2.8	—	—	—	—	—
DMP V	6.5	2.2	3.0	—	—	—	—	—

Length measured in proximodistal direction, width in mediolateral direction, and depth in dorsopalmar direction. Most elements from left side; asterisks indicate elements from right side. '—' indicates an accurate measurement could not be taken due to poor preservation. All linear measurements in mm. **Abbreviations**: **DMP**, distal manual phalanx; **DPDD**, dorsopalmar depth distal; **DPDM**, dorsopalmar depth midshaft; **DPDP**, dorsopalmar depth proximal; **IMP**, intermediate manual phalanx; **Mc**, metacarpal; **MLWD**, mediolateral width distal; **MLWM**, mediolateral width midshaft; **MLWP**, mediolateral width proximal; **PMP**, proximal manual phalanx; **PDL**, proximodistal length; **ROB**, robustness (calculated as the ratio of midshaft mediolateral width/proximodistal length).

whether they are completely confluent. The proximomedial aspect of Mc III is gently convex and expands palmarly in medial view (Fig. 30C). The facet for Mc II on the medial aspect of the left Mc III is not well preserved. The proximolateral surface of the bone is concave and articulates with Mc IV (Fig. 30D). The distal articular facet is well preserved and can clearly be separated into a facet for the sesamoid bones and the proximal phalanx. A fine, proximally convex line marks the dorsal extension of the articular facet for the proximal phalanx. The phalangeal facet is evenly convex. Palmarly, a fine ridge separates the phalangeal facet from the sesamoid facet. The palmar facet bears a shallow palmar keel that separates the two gently concave facets for the paired sesamoid bones (Fig. 30B, F).

The fourth metacarpal is expanded both proximally and distally (Fig. 30). The shaft is slightly compressed dorsopalmarly and elliptical in cross-section. The proximal articular facet is roughly triangular in outline (Fig. 30E). The lateral aspect is convex and articulates with the hamate, whereas the medial aspect is concave and articulates with the capitate. A small raised tuberosity along the dorsomedial border indicates the articular facet for Mc III (Fig. 30A, C). The facet is slightly convex and extends along the proximal border of the medial aspect. A blunt and bulbous proximal palmar tubercle is present. The distal aspect resembles that on Mc III but is slightly shallower (i.e., dorsopalmarly lower relative to mediolateral width).

The fifth metacarpal is robust and dorsopalmarly flat (Fig. 30). It possesses a large palmar tuberosity, which protrudes proximally and bears a convex facet for the distal process of the triquetrum (Fig. 30B, D). The lateral aspect of the tuberosity is rugose. The remaining proximal surface is triangular in outline, bearing a convex facet for the hamate (Fig. 30A–E). In medial view, a dorsopalmarly long facet for Mc IV is visible (Fig. 30C). The facet is triangular in outline and flat. The distal end of Mc V is rotated medially relative to the proximal end. The morphology of the distal end is similar to those of Mc II–Mc IV (Fig. 30E). Mc V has a pair of sesamoids associated with its palmar aspect.

Proximal Manual Phalanges—The proximal manual phalanges (PMP) I–V are about half as long as the corresponding metacarpals except PMP I, which is subequal in length to Mc I. Among the proximal manual phalanges, the length decreases in the order PMP II ≈ PMP III ≈ PMP I > PMP IV > PMP V (Table 4). PMP II, PMP III, and PMP IV are very similar in morphology (Fig. 31). The proximal articular facet in all three is convex, with sharp medial and lateral edges that protrude proximally. The facet is elliptical in proximal view, with a slightly rounder dorsal than palmar edge (Fig. 31E). Two distinct tubercles are located just distal to the proximal facet on the palmar aspect (Fig. 31B). In articulation, these tubercles align with the sesamoids of the respective metacarpals. The shaft is semicircular in cross-section at mid-length, convex dorsally and flat plantarly. In side view, the shaft of the bone narrows distally but then expands again transversely and dorsopalmarly at the distal end (Fig. 31A, C, D). The distal articular facet is divided into an evenly convex facet for the intermediate phalanx and a palmar part that articulates with the sesamoid (Fig. 31F). The palmar part is gently convex to accommodate the single, large sesamoid. The facet for the intermediate phalanx extends onto the dorsal and palmar aspects of the distal end, respectively. The medial and lateral aspects of the distal end are disc-like and slightly converge dorsally.

PMP I diverges from this pattern, because it articulates with the distal (rather than intermediate) phalanx. As such, the distal facet forms a distinct trochlea and the shaft is more nearly circular in outline than in PMP II–PMP IV. In addition, PMP I has a shallow fossa on the palmar aspect just distal to the proximal articular facet (Fig. 31B).

PMP V also differs substantially from the other phalanges. It is shorter and more robust, and the proximal articular facet is transversely expanded compared with the distal facet, much more so than those in PMP I–PMP III; PMP IV is somewhat intermediate between PMP III and PMP V in this regard. PMP V has two very prominent tubercles on the palmar lip of the proximal facet, of which the lateral one is larger (Fig. 31B). The shaft of PMP V is

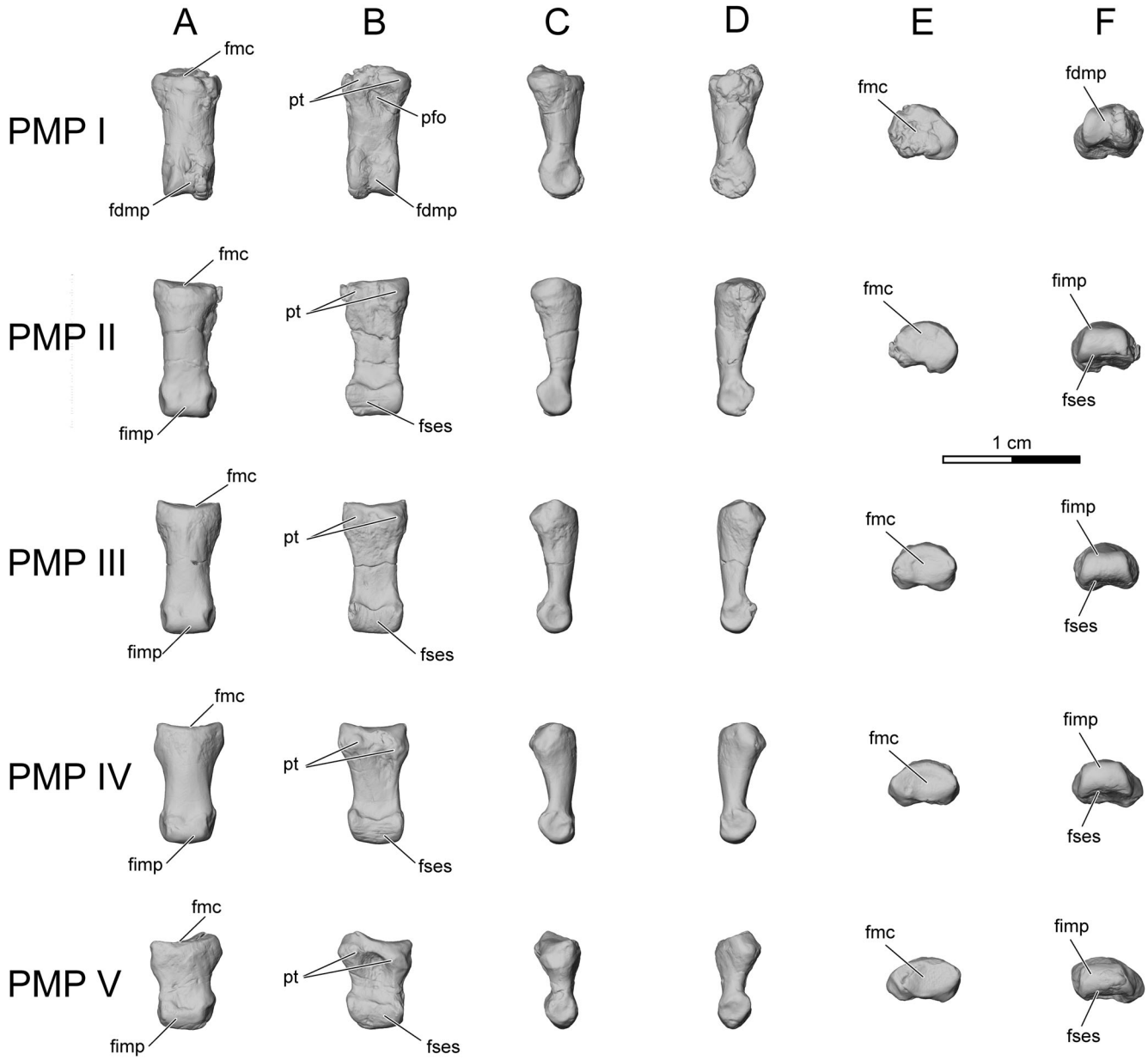

FIGURE 31. Left proximal manual phalanges (PMP) I–V of *Adalatherium hui*, holotype (UA 9030), in **A**, dorsal, **B**, palmar (= ventral), **C**, medial, **D**, lateral, **E**, proximal, and **F**, distal views. Rows from top to bottom: PMP I, PMP II, PMP III, PMP IV, and PMP V. **Abbreviations**: **fdmp**, facet for distal manual phalanx; **fimp**, facet for intermediate manual phalanx; **fmc**, facet for metacarpal; **fses**, facet for sesamoid; **pfo**, palmar fossa; **pt**, palmar tuberosity.

dorsopalmarly compressed. In dorsal view, the lateral side of the distal articular facet is oblique, in contrast to the more vertically oriented medial side (Fig. 31A).

Intermediate Manual Phalanges—The intermediate manual phalanges (IMP) II–V are shorter than the proximal ones (Fig. 32). IMP II–IMP IV are subequal in length, with IMP V being slightly shorter (Table 4). A similar pattern can be seen in the robustness of the intermediate phalanges, with IMP II–IMP IV being roughly equivalent and IMP V being more robust. Generally, the morphology of the intermediate phalanges is uniform. They differ from the proximal phalanges in that their proximal ends are dorsopalmarly more compressed, leading to straighter dorsal and palmar margins in medial or lateral view (Fig. 32C, D). In contrast, the proximal ends are dorsopalmarly expanded in the proximal phalanges, leading to a more triangular outline in medial or lateral view (Fig. 31C, D). Furthermore, the distal articular facet of each IMP forms a trochlea that is better developed than on the proximal phalanges.

Distal Manual Phalanges—The distal manual phalanges (DMP) I–V are similar to, but much smaller than, the corresponding distal phalanges of the pes. The first digit possesses the largest distal phalanx. DMP II and DMP III are subequal in length, with DMP IV being slightly shorter and DMP V shorter still (Table 4). All distal manual phalanges are slightly curved distally, DMP I more so than the other phalanges. None of the phalanges are particularly compressed or expanded mediolaterally nor deep dorsopalmarly. The extensor process is very prominent and is directed proximally (Fig. 33C, D). The articular facet is strongly concave in side view, forming a trochlear notch, with a shallow median ridge (Fig. 33E). The palmar lip is prominent and protrudes palmarly and proximally. A small fossa is present on the palmar aspect of

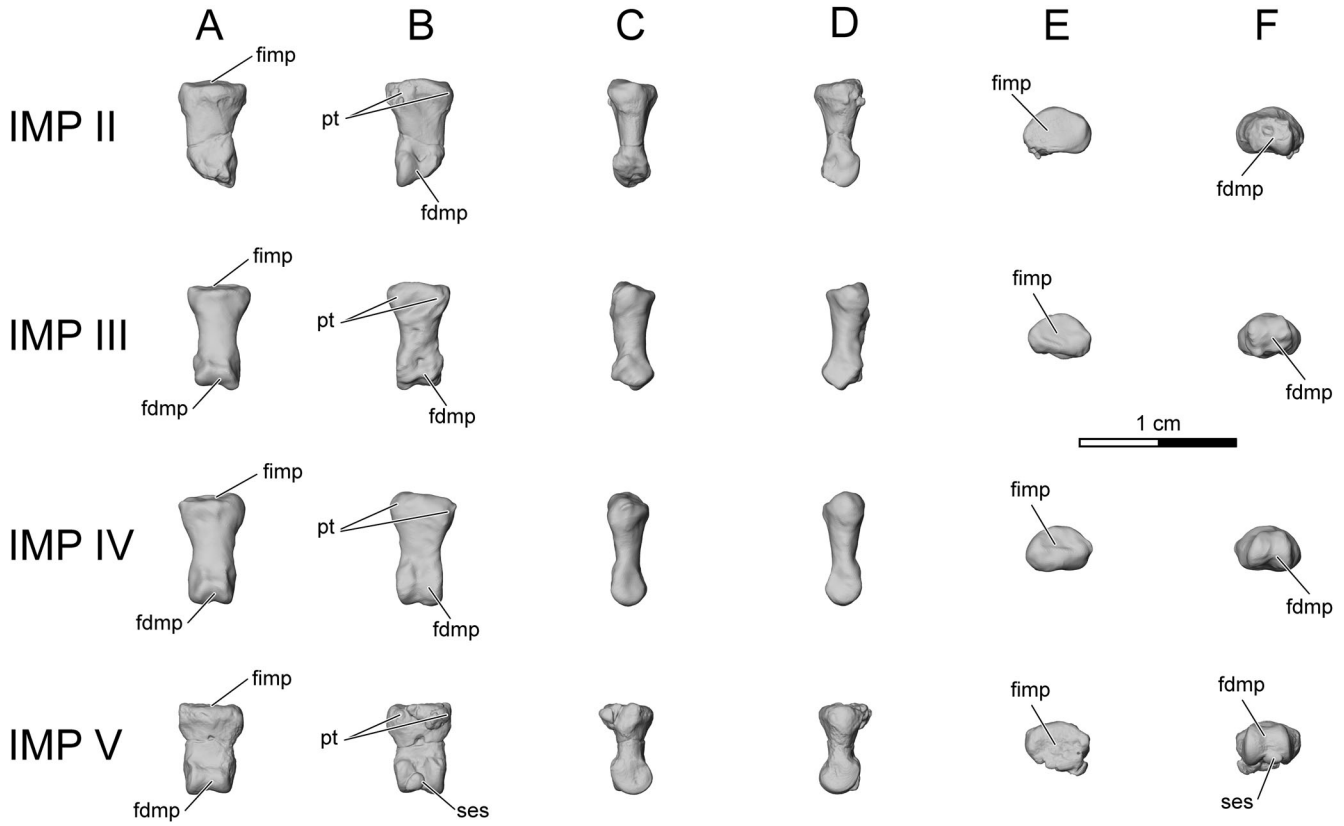

FIGURE 32. Left intermediate manual phalanges (IMP) II–V of *Adalatherium hui*, holotype (UA 9030), in **A**, dorsal, **B**, palmar (= ventral), **C**, medial, **D**, lateral, **E**, proximal, and **F**, distal views. IMP III and IMP IV reversed from right side. Rows from top to bottom: IMP II, IMP III, IMP IV, and IMP V. **Abbreviations**: **fdmp**, facet for distal manual phalanx; **fimp**, facet for intermediate manual phalanx; **pt**, palmar tuberosity; **ses**, sesamoid.

the phalanges just distal to the articular facet. A minute nutrient foramen opens into this fossa. The flexor process is not well developed, and the insertion of the flexor tendon, other than the palmar lip of the trochlear notch, is indistinct. This is one of the major morphological differences between the manual and pedal distal phalanges (see 'Pes' below).

Manual Sesamoid Bones—In addition to the os Daubentonii and the sesamoid associated with the trapezium, paired sesamoid bones are associated with the distal ends of Mc II–Mc V and single sesamoid bones with the distal ends of Mc I, all PMPs, and IMP V. The morphology of the sesamoid bones is generally similar to that of the pedal sesamoids. The sesamoids at the distal ends of Mc II–Mc V are elliptical, proximodistally longer than either mediolaterally wide or dorsopalmarly deep. These sesamoids are convex palmarly and gently concave to flat dorsally. The sesamoids of Mc V are proximodistally shorter and thus rounder in outline than those of Mc II–Mc IV. The single sesamoid of Mc I is larger than those of Mc II–Mc V, covering the whole mediolateral width of its metacarpal. It is convex palmarly and irregular in shape. The single sesamoids of PMP I–PMP V are compressed and squarish, but notched at the distal edge. The sesamoid of PMP I is smaller than those of PMP II–PMP V and more bean-shaped than squarish. The single sesamoid bones of IMP II–IMP V are irregular in shape, although somewhat elliptical in outline, and relatively smaller than those of the proximal phalanges.

Pelvic Girdle

The pelvic girdle consists of the left and right halves of the pelvis, here referred to as os coxae, as well as the epipubic bones. The two os coxae are separated and displaced in UA 9030. The right os coxa is largely missing; only the posterior portions of the ischium and pubis are preserved. The description will thus be based on the more complete left os coxa, which includes the ischium, pubis, and posterior portion of the ilium (Fig. 34). The left os coxa, as well as the caudal vertebrae, were rotated and curled under the lumbar vertebral column prior to or during burial, so that the posterior part of the left ox coxa points anteriorly in UA 9030 (Figs. 1, 2). This twisting severely damaged the sacroiliac joint. As such, the orientation of the pelvic girdle relative to the vertebral column cannot be described precisely. However, if the dorsal edge of the ischium is held horizontally, the ilium extends in a posteroventral to anterodorsal direction, whereas the blade of the pubis is directed ventromedially. In posterior view, the ischia would have probably formed a wide and shallow 'U'-shaped arc in life. The ischium, ilium, and pubis appear to have been fused in UA 9030. The acetabulum is incompletely preserved, and numerous cracks pass through the acetabulum that might obscure possible sutures. However, no suture is clearly discernible on the specimen or in the μCT images.

The acetabulum is large and round; it is almost equal in anteroposterior length and dorsoventral height. The central aspect of the acetabulum does not preserve any detailed morphology in the available left os coxa. It is fractured into numerous fragments. None of these fragments show sutures between the ischium, ilium, and pubis. The rim of the acetabulum is well developed, more salient along the iliac and ischial portions than the pubic portion (Fig. 34A, A′). The dorsal margin would have likely enclosed the femoral head and does not appear to be emarginated. A low eminence, which might represent an

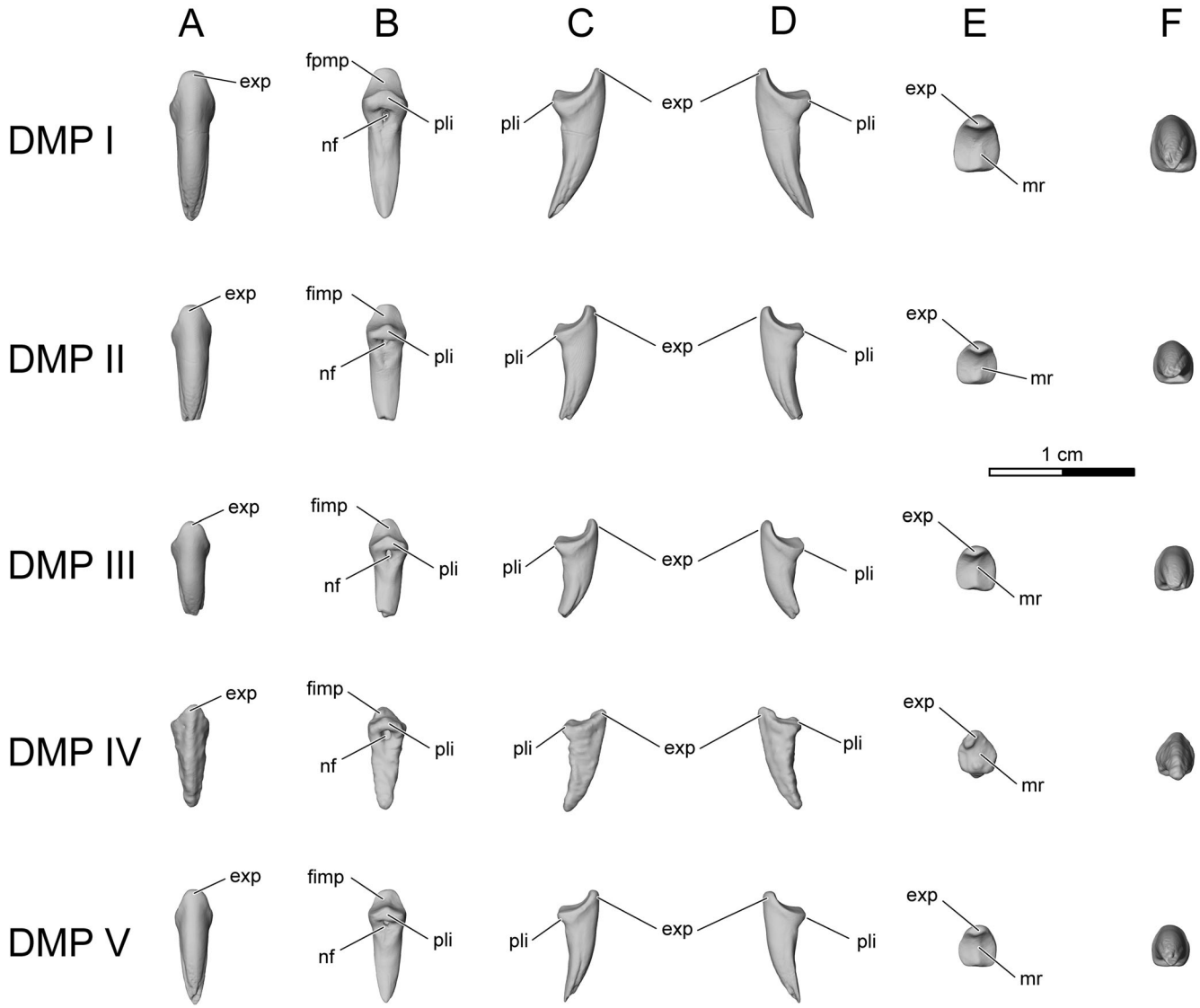

FIGURE 33. Left distal manual phalanges (DMP) I–V of *Adalatherium hui*, holotype (UA 9030), in **A**, dorsal, **B**, palmar (= ventral), **C**, medial, **D**, lateral, **E**, proximal, and **F**, distal views. DMP IV reversed from right side. Rows from top to bottom: DMP I, DMP II, DMP III, DMP IV, and DMP V. **Abbreviations**: **exp**, extensor process; **fimp**, facet for intermediate manual phalanx; **fpmp**, facet for proximal manual phalanx; **mr**, median ridge; **nf**, nutrient foramen; **pli**, plantar lip.

underdeveloped ischial spine, is present along the acetabular rim, roughly where the ilium and ischium meet. A small acetabular notch appears to be present near the ischiopubic junction. But the area is poorly preserved in UA 9030, and it is possible that the notch might just be an artifact.

The obturator foramen opens ventrolaterally and is massive, much larger than the acetabulum. It has the shape of a somewhat rounded trapezoid, with the anterior margin being shorter than the posterior, dorsal, and ventral boundaries. Because of fractures, the shape of the anterior boundary is not clear, but the ventral boundary is almost straight, whereas the dorsal and posterior boundaries are curved.

Ilium—The ilium is a stout element. In life, it would have been divided into the acetabular facet, the body, and the wing, which bears the articular facet for the sacrum; however, the wing and the anterior portion of the body are missing on both ilia. The preserved portion of the iliac body is more robust than the ischium and pubis. The dorsal edge of the body is straight, suggesting that the greater sciatic notch may have been very shallow. The ventral edge of the ilium is also straight. The medial aspect of the iliac body is gently concave, but otherwise featureless. On the lateral aspect of the iliac body, about 10 mm anterior to the rim of the acetabular facet, is a distinct tuberosity for the rectus femoris muscle (Fig. 34A, A′). A rounded ridge extends anteriorly (but oblique to the long axis of the ilium) from the tuberosity and divides the lateral aspect of the iliac body into a gluteal fossa dorsally and an iliac fossa ventrally (Fig. 34A, A′).

Ischium—The ischium consists of a body supporting the acetabular facet, a blade (or table), and an indistinctly restricted neck between them. The body is much thicker than the rest of the bone. The neck is only restricted along the ventral edge, which forms the dorsal border of the obturator foramen. The dorsal edge of the ischium is largely straight except for a possible ischial spine dorsal to the acetabulum and the prominent, laterally flaring, dorsoventrally tall ischial tuberosity at the posterodorsal end of the bone (Fig. 34). The dorsal portion of the ischial

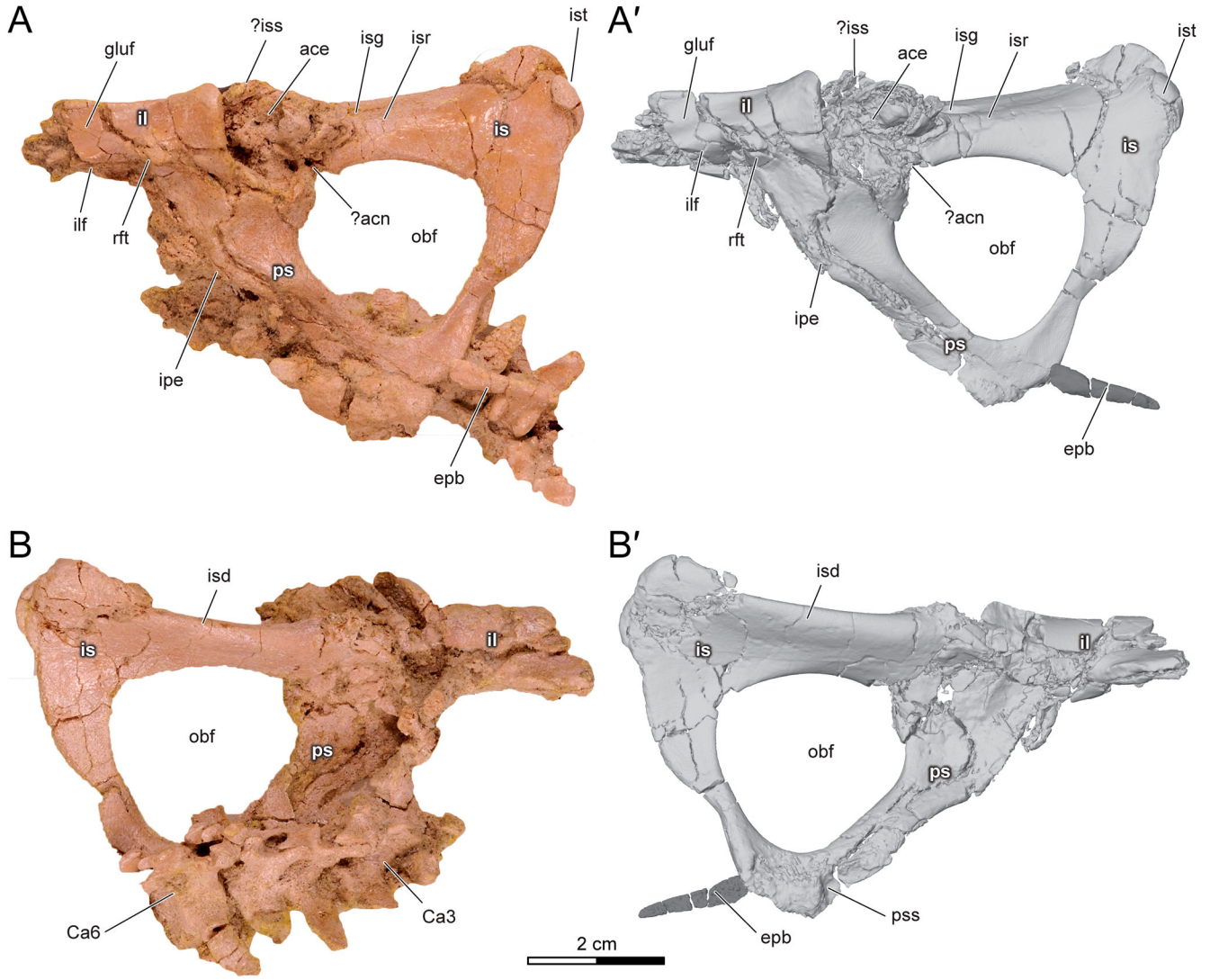

FIGURE 34. Left os coxa of *Adalatherium hui*, holotype (UA 9030), in **A**, **A′**, lateral and **B**, **B′**, medial views. **A**, **B**, original specimen including several caudal vertebrae and slightly displaced epipubis; **A′**, **B′**, reconstruction based on μCT images, with caudal vertebrae removed; os coxa in light gray, epipubis in dark gray. **Abbreviations**: **ace**, acetabulum; **acn**, acetabular notch; **Ca**, caudal vertebra; **epb**, epipubic bone; **gluf**, gluteal fossa; **il**, ilium; **ilf**, iliac fossa; **ipe**, iliopubic eminence; **is**, ischium; **isd**, ischial dorsal margin; **isg**, ischial groove; **isr**, ischial ridge; **iss**, ischial spine; **ist**, ischial tuberosity; **obf**, obturator foramen; **ps**, pubis; **pss**, pubic symphysis; **rft**, rectus femoris tuberosity.

blade, next to the neck and dorsal to the obturator foramen, is dorsoventrally deep and slightly bends laterally in a posterior direction. The medial aspect of the blade is gently convex anteriorly but becomes concave posteriorly. The lateral aspect of the blade bears a shallow, rounded ridge in the midline, termed the ischial ridge here (Fig. 34A, A′). It extends from the posterior margin of the acetabulum to roughly mid-length of the obturator foramen. The ridge is accompanied by a distinct groove dorsal to it. The groove is more prominent and wider anteriorly and gradually becomes indistinct posteriorly. The posterior portion of the ischial blade, which forms the posterior boundary of the obturator foramen, turns medially while extending ventrally. The two portions (dorsal and posterior) of the ischial blade form an acute angle in lateral view. It is uncertain how far the ischium extends ventrally; a suture between the pubis and ischium is not visible. As such, the bone or bones that form the posterior border of the obturator foramen are here described together. The ischial blade gradually decreases in width ventrally and then more drastically to form a narrow constriction at about mid-height of the obturator foramen. At its narrowest, the ischial blade is only 3 mm thick anteroposteriorly, compared with 12.3 mm at the dorsal edge of the obturator foramen. The posterior edge of the ischial blade is convex. Ventral to its narrowest point, the ischial blade (or pubis) expands gradually.

Pubis—The pubis can be divided into a body supporting the acetabular facet and a ramus extending posteroventrally and turning medially. The pubic body is dorsoventrally tall but appears thinner mediolaterally than those of the ilium and ischium. A low iliopubic eminence is present near the junction of the ilium and pubis and ventral to the acetabulum. The pubic ramus is very broad at its base, next to the body, but it narrows slightly as it extends posteriorly toward the pubic symphysis. The posterodorsal edge of the pubic ramus is essentially straight and forms the anteroventral boundary of the obturator foramen. The anteroventral border of the pubic ramus is gently concave. Only the posteroventral portion of the pubic ramus contributed

to the pubic symphysis. The symphysis itself is poorly preserved and can only be seen in the reconstructed surface (Fig. 34B'). A roughened area on the medial aspect of the pubic ramus indicates the extent of the pubic symphysis. It is narrow anteriorly and slightly expands posteriorly, occupying the dorsoventral height of the ramus. A ventrally protruding keel is not preserved in UA 9030 and was likely not present in *Adalatherium*.

Epipubis—A small, rod-like bone is preserved next to the posteromedial corner of the left ischium (Fig. 34). The fragment probably represents an epipubic bone with the base, which would have contacted the pubis in life, missing. This fragment has been displaced relative to the os coxae and would have been directed anteriorly, rather than posteriorly as it is now in UA 9030. It is about 15 mm long, less than 1 mm in thick, and its width decreases distally, from 3 mm anteriorly to 1 mm. Its contralateral counterpart was not preserved.

Femur

Both femora are preserved in UA 9030, but both have suffered some degree of deformation and damage (Figs. 1, 2, 35). The femur will be described as having proximal and distal ends and as being oriented vertically, with anterior, posterior, medial, and lateral aspects.

The femur is the longest element in the skeleton (Figs. 1, 2). It is about 35% longer than the humerus (Tables 2, 5). The femoral head is large, bulbous, and proximomedially oriented. Despite some deformation of its anterolateral region (Fig. 35E), the head is nearly hemispherical. A fovea capitis is present on the proximomedial aspect of the articular surface of the femoral head (Fig. 35C). The femoral neck is short and almost indistinct. Only in medial view is the neck distinctly smaller than the head (Fig. 35C). The bone lateral to the head is crushed and compressed anteroposteriorly; as such, it is uncertain how slender or robust the most proximal aspect of the shaft was in life.

The greater trochanter is subequal to the head in height and anteroposterior depth (Fig. 35A). In proximal view, the greater trochanter extends in an anterolateral to posteromedial direction (Fig. 35E). The greater trochanter is inclined toward the head, with a shallow notch between them. The extent of the notch is uncertain due to crushing of the anterior surfaces of the shaft.

TABLE 5. Basic metrics of the left hind limb elements of *Adalatherium hui*, holotype (UA 9030).

Femur	
Length	90.8
Midshaft depth	9.9
Midshaft width	9.6
Greater trochanter height	22.7
Head diameter	15.8
Epicondylar width	20.1
Tibia	
Length	79.1
Midshaft depth	12.2
Midshaft width	5.5
Fibula	
Length	70.8
Midshaft depth	5.7
Midshaft width	4.4
Parafibula	
Length	14.8
Midshaft depth	4.3
Midshaft width	3.3

Length measured in proximodistal direction, width in mediolateral direction, and depth in anteroposterior direction. All linear measurements in mm.

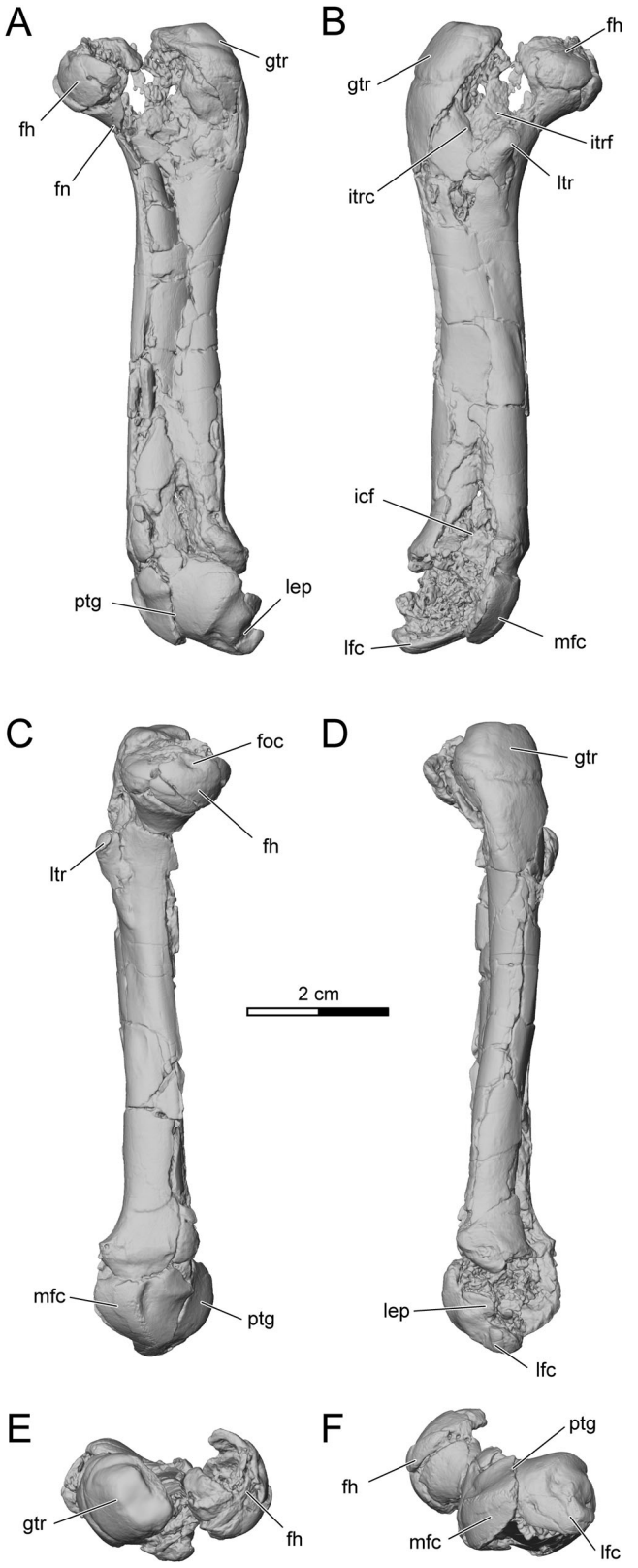

FIGURE 35. Left femur of *Adalatherium hui*, holotype (UA 9030), in **A**, anterior, **B**, posterior, **C**, medial, **D**, lateral, **E**, proximal, and **F**, distal views. **Abbreviations**: **fh**, femoral head; **fn**, femoral neck; **foc**, fovea capitis; **gtr**, greater trochanter; **icf**, intercondylar fossa; **itrc**, intertrochanteric crest; **itrf**, intertrochanteric fossa; **lep**, lateral epicondyle; **lfc**, lateral femoral condyle; **ltr**, lesser trochanter; **mfc**, medial femoral condyle; **ptg**, patellar groove.

The lateral aspect of the greater trochanter is convex and rough in texture (Fig. 35D). It is oriented posterolaterally rather than laterally. The lesser trochanter is located on the posterior aspect of the femur, medial to the (longitudinal) midline of the shaft and distolateral to the head (Fig. 35B, C). The lesser trochanter is small and bulbous, and its apex is curved medially. The base of the lesser trochanter extends distally on the shaft for a very short distance. In posterior view, the two trochanters and the femoral head define a deep concavity, the intertrochanteric fossa (Fig. 35B). The intertrochanteric crest (connecting the greater and lesser trochanters) is low and broad. The surface distal to the lateral aspect of the greater trochanter is rounded and featureless. A third trochanter is absent.

The femoral shaft distal to the lesser trochanter is straight. It is only slightly constricted at mid-length and gently expands mediolaterally near the distal end. The shaft is almost circular in cross-section at mid-length. The left shaft is damaged and the bone collapsed into the marrow cavity anteriorly, thereby obscuring the true outline of the shaft. The right shaft is, however, well preserved and clearly demonstrates a cylindrical shape. Near the distal end, the shaft expands slightly mediolaterally and anteroposteriorly.

The distal end of the bone comprises the distal epiphysis, which articulates with the tibia and fibula. The two condyles for the tibia probably differ in shape and orientation, but the poor preservation of the knee joint on both sides of the skeleton precludes accurate description of the morphology. The lateral condyle appears to protrude posteriorly and slightly laterally (Fig. 35B, D, F). A fine ridge delimits the tibial facet laterally from the lateral aspect of the distal epiphysis. In the center of the lateral aspect is a slightly elevated lateral epicondyle. The epicondyle is formed by a low ridge with a shallow depression in the center (Fig. 35D). A facet for the fibula is not preserved in UA 9030. The medial condyle extends posteromedially and does not protrude as far distally as the lateral condyle. It bears a broad facet for the medial condyle of the tibia, which extends along the posteromedial aspect of the distal epiphysis (Fig. 35C). The facet is convex and smooth. The medial epicondyle is not preserved on either femur. Likewise, the intercondylar region on the posterior aspect of the femur is damaged and poorly preserved. A deep depression on the posterior aspect of the shaft of the left femur represents the proximal extension of an intercondylar fossa, although the deformation probably exaggerates the size of the depression (Fig. 35B). The anterior aspect of the distal epiphysis is only partially preserved on either femur. Nevertheless, it is sufficient to show that it is flat in a mediolateral direction and slightly convex in a proximodistal direction. The anterior surface is triangular in outline, well defined by two fine ridges that separate it from the medial and lateral condyles, respectively. This surface likely would have articulated with a patella in life and is thus termed a shallow but distinct patellar groove (Fig. 35). A patellar bone is, however, not preserved in UA 9030.

Tibia

The tibiae of UA 9030 are generally well preserved; only the proximal ends are significantly damaged on both tibiae. In the following description, the tibia is oriented vertically, with the tibial crest directed anteriorly.

The tibia of *Adalatherium* is highly unusual (Figs. 1, 2, 36). It is mediolaterally compressed and bends anteriorly to a considerable degree. The proximal end articulates with the femur proximally and the fibula laterally. The tibial plateau, the most proximal part of the tibia and including the proximal articular facets, appears asymmetrical, with three sides that face roughly anteromedially, anterolaterally, and posterolaterally (Fig. 36E). Much of the proximal articular facet is damaged on both the left and

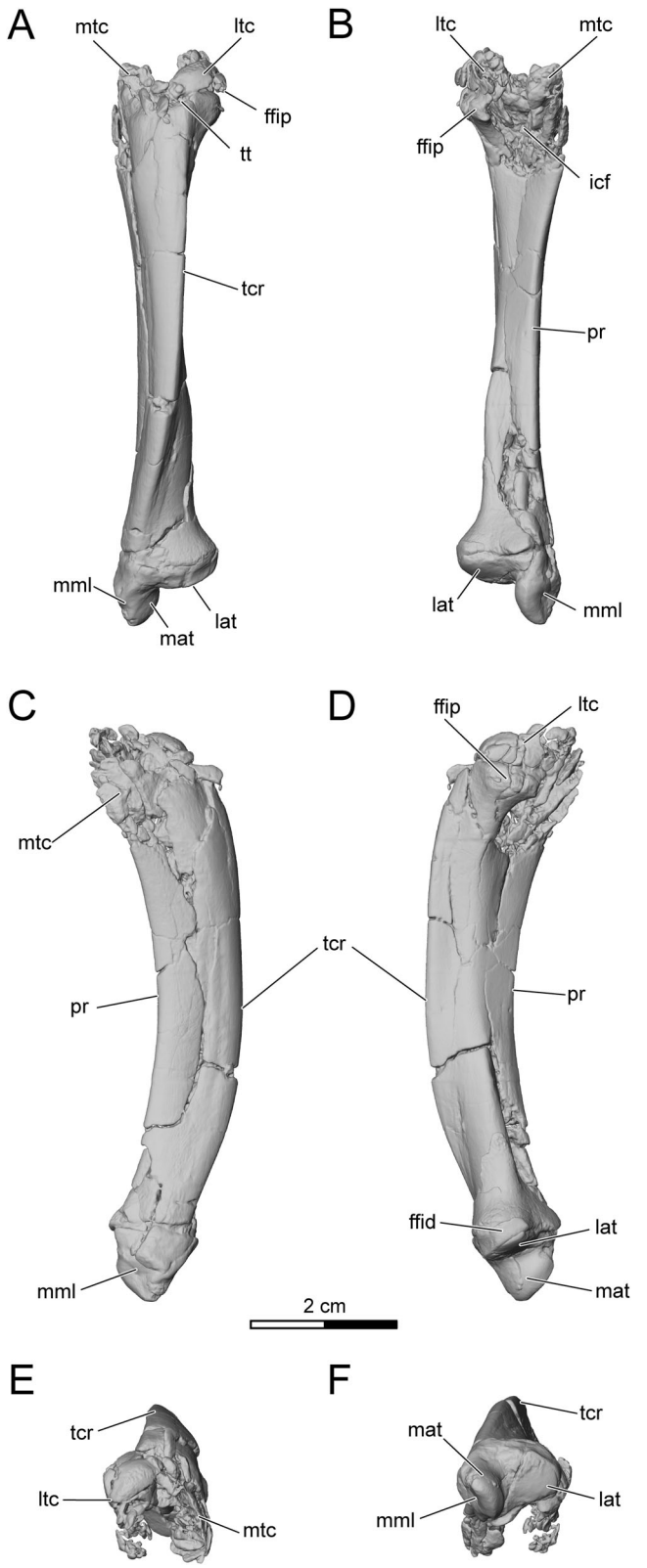

FIGURE 36. Left tibia of *Adalatherium hui*, holotype (UA 9030), in **A**, anterior, **B**, posterior, **C**, medial, **D**, lateral, **E**, proximal, and **F**, distal views. **Abbreviations**: **ffid**, distal facet for fibula; **ffip**, proximal facet for fibula; **icf**, intercondylar fossa; **lat**, lateral astragalotibial facet; **ltc**, lateral tibial condyle; **mat**, medial astragalotibial facet; **mml**, medial malleolus; **mtc**, medial tibial condyle; **pr**, posterior ridge; **tcr**, tibial crest; **tt**, tibial tuberosity.

right tibiae; only the most medial aspect of the medial condyle is preserved on the right tibia. The preserved fragment indicates that the medial condyle was concave and faced proximoposteriorly and that its facet slightly extends medially. Based on the shape of the medial condyle on the distal end of the femur, the facet must have been mediolaterally broad. The lateral aspect of the tibial plateau contains the lateral condyle, but neither the left nor the right tibia preserves the articular facet. Based on the lateral femoral condyle, the lateral tibial condyle was likely anteroposteriorly shorter than the medial condyle. A flat and elliptical facet on the lateral aspect of the tibial plateau represents the proximal facet for the fibula. The posterior aspect of the proximal tibia presents a deeply excavated intercondylar fossa. The depth of the fossa is likely exaggerated on the left tibia by postmortem deformation (Fig. 36B).

In anterior view, the slightly sigmoidal tibial shaft expands proximally and distally and is narrowest at mid-length (Fig. 36A). In medial (or lateral) view, the tibial shaft dramatically bends anteriorly and gradually tapers distally (Fig. 36C, D). The proximal portion of the shaft largely follows the triangular shape of the proximal end, with a long and convex medial side and concave and shorter anterolateral and posterolateral sides. The tibial crest is well defined and prominent, extending distally along the complete length of the shaft (Fig. 36A). The crest arises at the medial edge of the tibial tuberosity and wraps around the anterior surface of the shaft to end just proximal to the medial malleolus. Along its proximal half, the tibial crest extends laterally, slightly overhanging the anterolateral aspect. The posterior edge of the shaft forms a distinct posterior ridge (Fig. 36B) extending from the posterior corner of the medial condyle to the posterior part of the medial malleolus. The posterior ridge also bends anteriorly, with a curvature roughly paralleling that of the tibial crest (Fig. 36C). The medial surface changes from convex and anteromedially oriented proximally to flat and medially oriented distally. The lateral edge is a low but distinct ridge separating the anterolateral and posterolateral aspects of the shaft. It extends from the posterior aspect of the lateral condyle to the posterolateral aspect of the distal articular facet (Fig. 36D). The ridge fades toward mid-length of the bone but does not completely disappear. It emerges again as a distinct crest distally. The posterolateral surface of the tibia distal to the intercondylar fossa quickly flattens toward the midshaft. The distal half of the posterior aspect presents a shallow depression, which is exaggerated on the left tibia by postmortem deformation (Fig. 36B).

The distal end of the tibia is rotated medially about 55° compared with the proximal end. It is characterized by a large medial malleolus, which bears the medial astragalotibial facet on its anterolateral aspect (Fig. 36A, D, F). The medial aspect of the malleolus is rugose, possibly for attachment of the medial collateral ligament (Kielan-Jaworowska and Gambaryan, 1994). The lateral astragalotibial facet is elliptical and flat, facing distally and slightly posteriorly (Fig. 36A, B, D, F). The posterior portion of the facet is in contact with the os calcaris. A small and convex facet on the lateral side of the epiphysis is for the distal part of the fibula (Fig. 36D).

Fibula

In the following description, the fibula is oriented vertically. The fibula is essentially a straight, rod-shaped element that is slightly compressed mediolaterally (Fig. 37). It is shorter than the tibia (Table 5). The proximal end is anteroposteriorly expanded, mediolaterally compressed, and convex proximally in medial or lateral view (Fig. 37C, D). Posteriorly, the proximal epiphysis bears an elliptical, convex, smooth facet for the parafibula that faces posterolaterally (Fig. 37B, D, F). Proximally, the fibula articulated with the tibia and in life probably would have contacted the distal end of the femur to a minor degree. The articulation with the femur likely occurred along the anterior half of the proximal edge, whereas that with the tibia was along

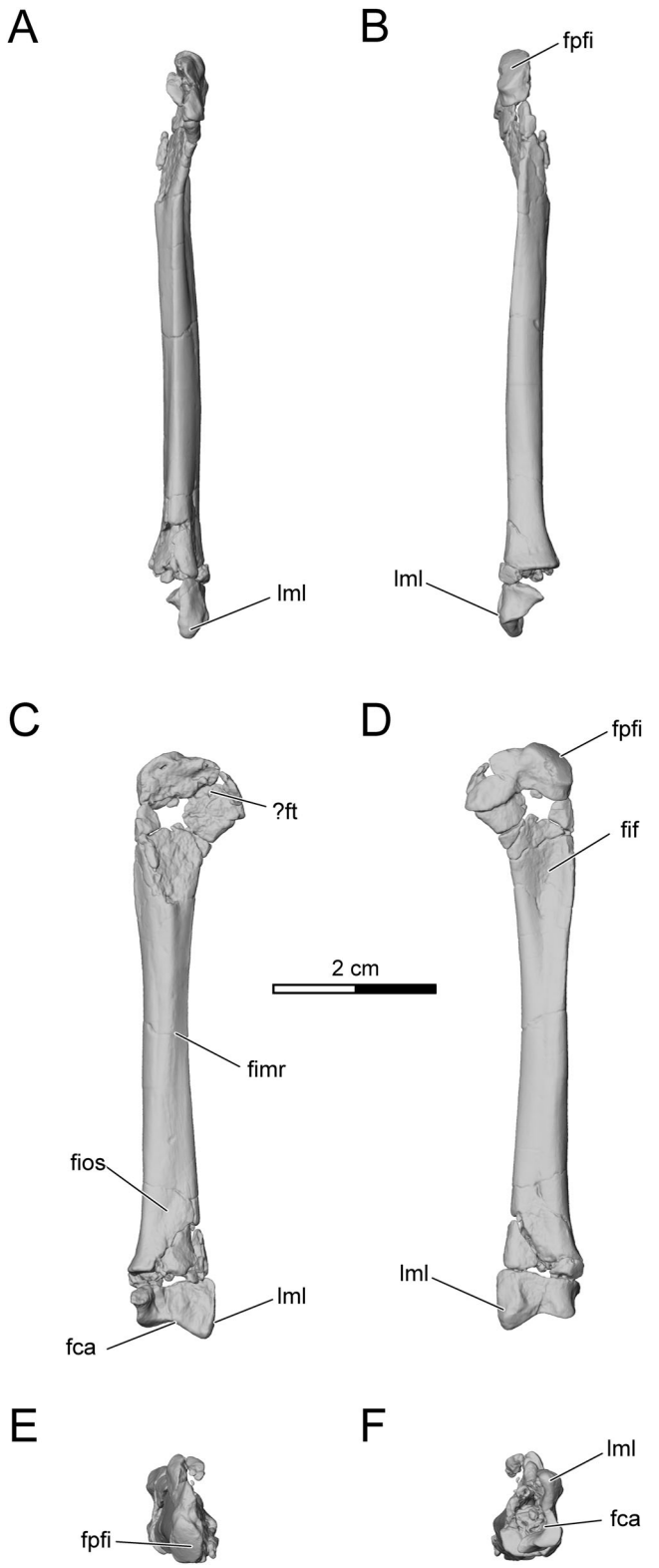

FIGURE 37. Left fibula of *Adalatherium hui*, holotype (UA 9030), in **A**, anterior, **B**, posterior, **C**, medial, **D**, lateral, **E**, proximal, and **F**, distal views. **Abbreviations**: **fca**, facet for calcaneus; **fif**, fossa on proximal aspect of fibula; **fimr**, fibular medial ridge; **fios**, fibular oblique sulcus; **fpfi**, facet for parafibula; **ft**, facet for tibia; **lml**, lateral malleolus.

the proximomedial part of the fibula. The medial aspect is, however, damaged and crushed on both fibulae, obscuring the femoral and tibial facets.

The cross-section of the fibula changes from concavo-convex proximally, to teardrop-shaped at mid-length, to quadrangular distally. In lateral view, the proximal fibular shaft bears a triangular fibular fossa that is bordered posteriorly by a fine and laterally reflected crest (Fig. 37D). The fossa and crest gradually fade distally. A blunt ridge is present along the medial aspect of the fibular shaft (Fig. 37C). The ridge diminishes distally to a point where the medial surface of the shaft, which is rough in texture, is essentially flat. An oblique sulcus is visible proximal to the distal epiphysis, extending in an anterodistal to posteroproximal direction (Fig. 37C).

Distally, the fibula gently expands in an anteroposterior direction. The distal epiphysis is partially damaged on both fibulae. Only the lateral aspect of the distal articular facet is preserved. This part of the facet is concave, faces mediodistally, and articulates with the calcaneus (Fig. 37F). The lateral malleolus is robust and positioned at the anterolateral corner of the distal epiphysis. A small but distinct groove and ridge is visible posterior to the lateral malleolus. The distal articulation with the tibia or astragalus is not preserved in UA 9030.

Parafibula

The parafibula of *Adalatherium* is a small, rod-like, and mediolaterally compressed element bridging the femur and fibula at the knee joint (Figs. 1, 2, 38). In the following description, the parafibula is oriented vertically, with the parafibular tuberosity directed posteriorly. The bone is composed of base, neck, and muscular process. The base articulates with the proximoposterior part of the fibula. The muscular process extends lateral to the distal end of the femur. The base of the parafibula bears the articular facet for the fibula, which is elliptical in outline, convex, and faces distomedially. The slightly constricted neck separates the muscular process and base. Viewed laterally, the muscular process is divided into two raised areas, one proximally and one distally (Fig. 38D). The proximal portion extends posteriorly (and slightly laterally) and the distal one posterodistally. The medial aspect of the muscular process is convex.

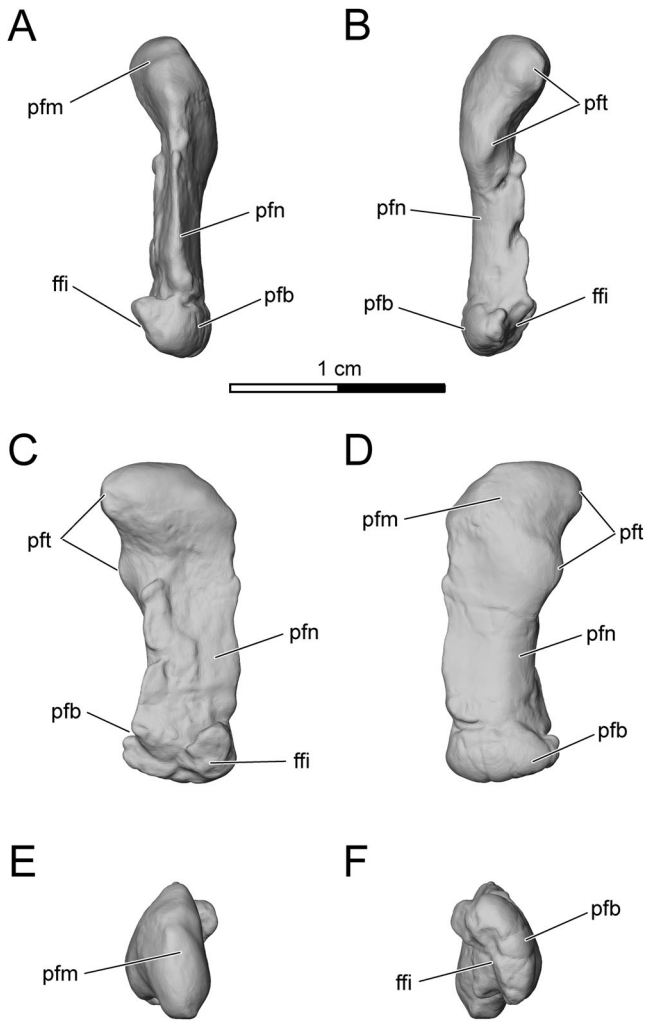

FIGURE 38. Left parafibula of *Adalatherium hui*, holotype (UA 9030), in **A**, anterior, **B**, posterior, **C**, medial, **D**, lateral, **E**, proximal, and **F**, distal views. **Abbreviations**: **ffi**, facet for fibula; **pfb**, parafibular base; **pfm**, parafibular muscular process; **pfn**, parafibular neck; **pft**, parafibular tuberosity.

Pes

Both pedes of UA 9030 are preserved in articulation (Figs. 1, 2, 39–41; Tables 6, 7). Elements of the left pes were physically separated for reconstruction and descriptive purposes (Figs. 42–53). The individual tarsals are described in the order of astragalus, calcaneus, navicular, cuboid, entocuneiform, mesocuneiform, ectocuneiform, and os calcaris and illustrated in dorsal, medial, plantar (= ventral), lateral, proximal, and distal views.

Astragalus—Both astragali are only partially preserved in UA 9030 (Figs. 39–42). The left astragalus was disarticulated from the rest of the tarsus but is still in association with the os calcaris. It preserves the proximal and distal articular facets, the dorsal surface, as well as part of the proximal aspects of the lateral and plantar surfaces. The right astragalus is still articulated with the remainder of the hind foot and can be examined in dorsal and medial views (Figs. 39, 41). It preserves the medial surface (including the medial part of the distal articular facet) and the proximal articular facet. Neither of the astragali preserves the distal articular facets with the calcaneus. Based on µCT imaging, both astragali were digitally segmented. The surface of the better-preserved right astragalus was mirrored and is depicted in Figure 43. The description is based on the original specimen as well as the segmented right astragalus.

The astragalus is highly unusual in several respects; most prominently, it preserves a trochleated navicular facet, consisting of medial and lateral astragalar condyles and an intercondylar groove (Fig. 43A, F). The astragalus is irregular in shape (but resembles the Greek capital letter gamma, Γ), being longer proximodistally than mediolaterally wide. Its margins in dorsal view are proximomedially, distolaterally, proximolaterally, and distomedially positioned (Fig. 43A). Proximally, the astragalus articulates with the tibia medially and proximomedially and the fibula proximolaterally. The lateral astragalotibial facet is triangular in shape, flat, and faces proximally and somewhat medially. A sharp crest defines the distal border of the facet (Fig. 43A), whereas it gently slopes into the astragalofibular facet proximolaterally. The astragalus also articulates with the prominent medial malleolus of the tibia along its medial border. The medial astragalotibial facet is bean-shaped, concave dorsally and convex plantarly. It is proximodistally long and dorsoplantarly narrow. The center of the facet is deeply excavated (Fig. 43B). The astragalofibular facet is smaller than either of the astragalotibial facets. It is gently convex and irregular in shape. The facet expands plantarly and narrows dorsally (Fig. 43E). Dorsally, the facet terminates in a distinctly rounded margin that slightly overhangs the dorsal aspect of the astragalus (Fig. 43A, E). The facet is slightly elevated, and a fine but distinct crest borders it

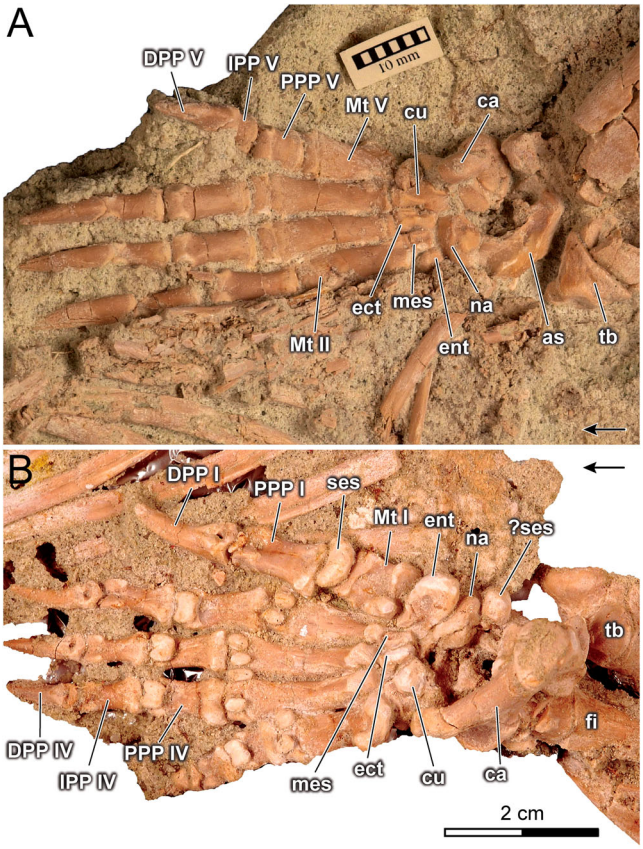

FIGURE 39. Right pes of *Adalatherium hui*, holotype (UA 9030), in **A**, dorsal and **B**, plantar (= ventral) views. Arrows point anteriorly. **Abbreviations**: **as**, astragalus; **ca**, calcaneus; **cu**, cuboid; **DPP**, distal pedal phalanx; **ect**, ectocuneiform; **ent**, entocuneiform; **fi**, fibula; **IPP**, intermediate pedal phalanx; **mes**, mesocuneiform; **Mt**, metatarsal; **na**, navicular; **PPP**, proximal pedal phalanx; **ses**, sesamoid; **tb**, tibia.

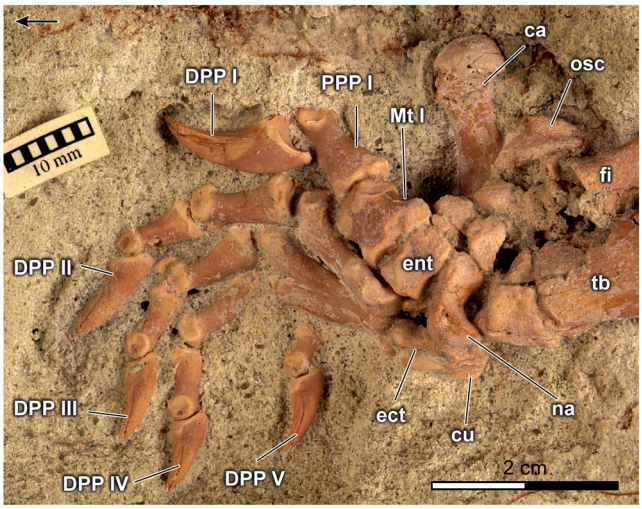

FIGURE 40. Left pes of *Adalatherium hui*, holotype (UA 9030), in dorsal view. Arrow points anteriorly. **Abbreviations**: **ca**, calcaneus; **cu**, cuboid; **DPP**, distal pedal phalanx; **ect**, ectocuneiform; **ent**, entocuneiform; **fi**, fibula; **Mt**, metatarsal; **na**, navicular; **osc**, os calcaris; **PPP**, proximal pedal phalanx; **tb**, tibia.

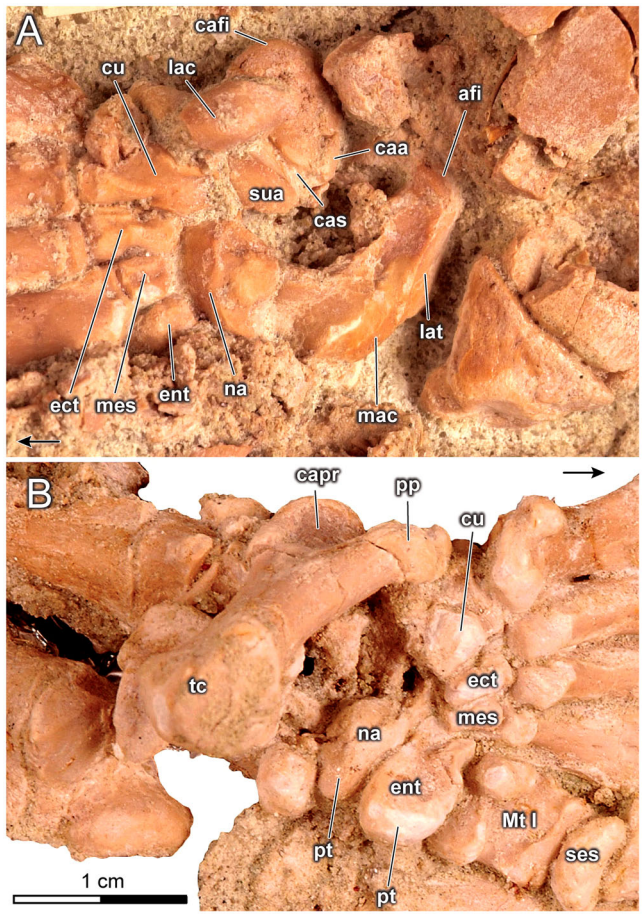

FIGURE 41. Tarsals of right pes of *Adalatherium hui*, holotype (UA 9030), in **A**, dorsal and **B**, plantar (= ventral) views. Arrows point anteriorly. **Abbreviations**: **afi**, astragalofibular facet; **caa**, calcaneoastragalar facet; **cafi**, calcaneofibular facet; **capr**, calcaneal protuberance; **cas**, calcaneal sulcus; **cu**, cuboid; **ect**, ectocuneiform; **ent**, entocuneiform; **lac**, lateral astragalar condyle (displaced); **lat**, lateral astragalotibial facet; **mac**, medial astragalar condyle; **mes**, mesocuneiform; **Mt**, metatarsal; **na**, navicular; **pp**, peroneal process; **pt**, plantar tuberosity; **ses**, sesamoid; **sua**, sustentacular facet; **tc**, tuber calcanei.

TABLE 6. Basic metrics of the tarsals of *Adalatherium hui*, holotype (UA 9030).

Element	Length	Width	Depth
Astragalus	16.6	11.6	8.9
Calcaneus	29.1	10.9	11.3
Navicular	5.4	7.6	15.7
Cuboid	9.1	7.0	7.1
Entocuneiform*	5.0	4.9	12.5
Mesocuneiform*	3.5	2.7	4.1
Ectocuneiform	6.4	3.3	6.5

Length measured in proximodistal direction, width in mediolateral direction, and depth in dorsoplantar direction. Most elements from left side; asterisks indicate elements from right side. All linear measurements in mm.

laterally (Fig. 43D). The area lateral to the astragalofibular facet is mediolaterally narrow and does not extend as far dorsally (Fig. 43E). This part of the astragalus does not appear to contact the

TABLE 7. Basic metrics of the left pes of *Adalatherium hui*, holotype (UA 9030).

Element	PDL	MLWP	DPDP	MLWM	DPDM	MLWD	DPDD	ROB
Mt I	9.4	8.8	4.4	7.5	3.4	7.4	4.5	0.79
Mt II	17.9	4.7	4.7	4.5	2.9	6.6	4.3	0.25
Mt III	20.8	3.9	—	4.4	3.0	5.6	4.1	0.21
Mt IV	22.0	5.3	5.9	4.2	3.0	6.2	4.5	0.19
Mt V	16.4	9.4	5.0	5.3	2.3	6.5	3.8	0.32
PPP I	13.1	7.9	5.8	5.1	4.0	5.5	4.7	0.39
PPP II	12.6	6.3	5.1	4.2	3.6	5.4	3.9	0.33
PPP III	11.7	5.9	4.4	3.9	2.9	—	3.7	0.33
PPP IV	11.9	5.5	3.6	4.1	2.9	5.5	3.9	0.35
PPP V	8.0	6.5	4.1	4.6	2.4	5.4	3.3	0.58
IPP II	10.3	5.7	4.1	3.8	2.6	4.3	3.8	0.37
IPP III	9.2	—	—	3.2	2.1	3.8	2.9	0.34
IPP IV	9.3	5.2	3.6	3.2	2.2	3.9	2.9	0.34
IPP V	7.0	5.2	3.5	3.8	2.4	3.9	3.0	0.54
DPP I	16.8	4.6	6.9	—	—	—	—	—
DPP II	12.9	4.0	4.3	—	—	—	—	—
DPP III	11.1	3.4	3.7	—	—	—	—	—
DPP IV	11.0	3.4	3.7	—	—	—	—	—
DPP V	10.3	3.6	3.6	—	—	—	—	—

Length measured in proximodistal direction, width in mediolateral direction, and depth in dorsoplantar direction. '—' indicates an accurate measurement could not be taken due to poor preservation. All linear measurements in mm. **Abbreviations**: **DPDD**, dorsoplantar depth distal; **DPDM**, dorsoplantar depth midshaft; **DPDP**, dorsoplantar depth proximal; **DPP**, distal pedal phalanx; **IPP**, intermediate pedal phalanx; **MLWD**, mediolateral width distal; **MLWM**, mediolateral width midshaft; **MLWP**, mediolateral width proximal; **Mt**, metatarsal; **PDL**, proximodistal length; **PPP**, proximal pedal phalanx; **ROB**, robustness (calculated as the ratio of midshaft mediolateral width/proximodistal length).

fibula, but the fibula is damaged along its distomedial margin and thus it is uncertain whether the proximolateral margin of the astragalus would have articulated with the fibula in life. The most prominent feature on the proximodorsal part of the astragalus is the rounded edge of the proximal aspect of the astragalar foramen (Fig. 43A, F). In both astragali, the distal part of the canal is broken and not preserved. The astragalar foramen is positioned distolateral to the astragalofibular facet.

The plantar surface of the astragalus, in particular the distal part, is poorly preserved in UA 9030. Only the proximal aspect of the plantar surface, which is bulbous and rough in texture, is preserved on the right astragalus. A relatively smooth and slightly raised area in the center of the plantar aspect likely articulated with the os calcaris in life (Fig. 43). On the right pes, a rounded and bulbous fragment is preserved mediodistal to the astragalus (Fig. 39B). This fragment is here tentatively identified as a large sesamoid that would have been positioned plantar to the astragalus in life.

The distal articular facet is distinctly more slender than the proximal part of the astragalus in mediolateral width, but there is no constricted part (neck) between the proximal and distal ends of the astragalus. In other words, the astragalar head typical of extant therian mammals (Szalay, 1994, and references therein) does not exist in *Adalatherium*. The trochlear-shaped astragalonavicular facet occupies the distal aspects of the astragalus (Fig. 43A, F). The facet consists of two prominent and distinct ridges, here termed the medial and lateral astragalar condyles, which are separated by a deeply excavated intercondylar groove to form a half-pulley-like structure. The intercondylar groove tightly articulates with the medial ridge of the navicular (Fig. 42A). The lateral astragalar condyle is mediolaterally narrower and dorsoplantarly deeper than the medial astragalar condyle and tightly fits into the groove on the navicular (Fig. 42A). The medial astragalar condyle is broader and shallower than the lateral condyle. Only the lateral and distal aspects of the medial astragalar condyle articulate with the medial aspect of the navicular. In the articulated hind foot, the astragalar condyles would have been oriented in a proximolateral to distomedial direction (Fig. 42A).

The proximolateral aspect of the astragalus bears a flat facet for the calcaneus (Fig. 43D). Only the proximal part of the calcaneoastragalar facet is preserved and appears to articulate with two facets on the calcaneus. The calcaneoastragalar facet is gently convex and meets with the proximal aspect of the astragalus at a right angle. Much of the morphology of the sustentacular facet and the distal aspect of the calcaneoastragalar facet can only be deduced from their counterparts on the calcaneus. The astragalus shows no clear facet for the cuboid, and based on the reconstructed hind foot, it seems unlikely that the two bones articulated in life (Fig. 42).

Calcaneus—Both calcanei of UA 9030 are well preserved and almost complete (Figs. 39–42). Most of the description is based on the disarticulated left calcaneus. However, the proximomedial part, including the sustentaculum tali, is damaged on the left calcaneus. Thus, this part of the right calcaneus was used to complement the description and was incorporated to make a composite calcaneus in Figure 44.

The calcaneus is the longest element (29.1 mm) of the tarsus in *Adalatherium*, being almost twice as long as the astragalus (Table 6). The calcaneal tuber is large and elongate, comprising more than half of the total calcaneal length (Fig. 44A–D). The tuber gradually expands distally and is reflected dorsally. A suture between the distal-most part of the tuber and the remainder of the calcaneus is still visible. The distal end of the tuber is rugose and bulbous, with a maximal convexity dorsomedial to the center. In distal view, the tuber is triangular in outline, with dorsal, lateroplantar, and medioplantar corners (Fig. 44F). From these corners, three rounded edges extend proximally along the shaft of the tuber. The dorsomedial side of the tuber is flat and featureless, whereas the dorsolateral side contains a very shallow longitudinal sulcus in the midline (Fig. 44D). This sulcus is dorsolaterally oriented distally and twists to face laterally farther proximally. The plantar aspect of the tuber is gently concave proximodistally and convex mediolaterally (Fig. 44C). Its boundaries with the medial and lateral sides of the tuber are indistinct. The dorsoplantar height of the tuber does not change much along its length, but the mediolateral width of the tuber is reduced proximally. At midshaft, the tuber is little more than half as wide as at its distal end (Fig. 44A).

The calcaneus articulates with the fibula dorsally, the astragalus medially, and the cuboid plantarly. The calcaneofibular facet is

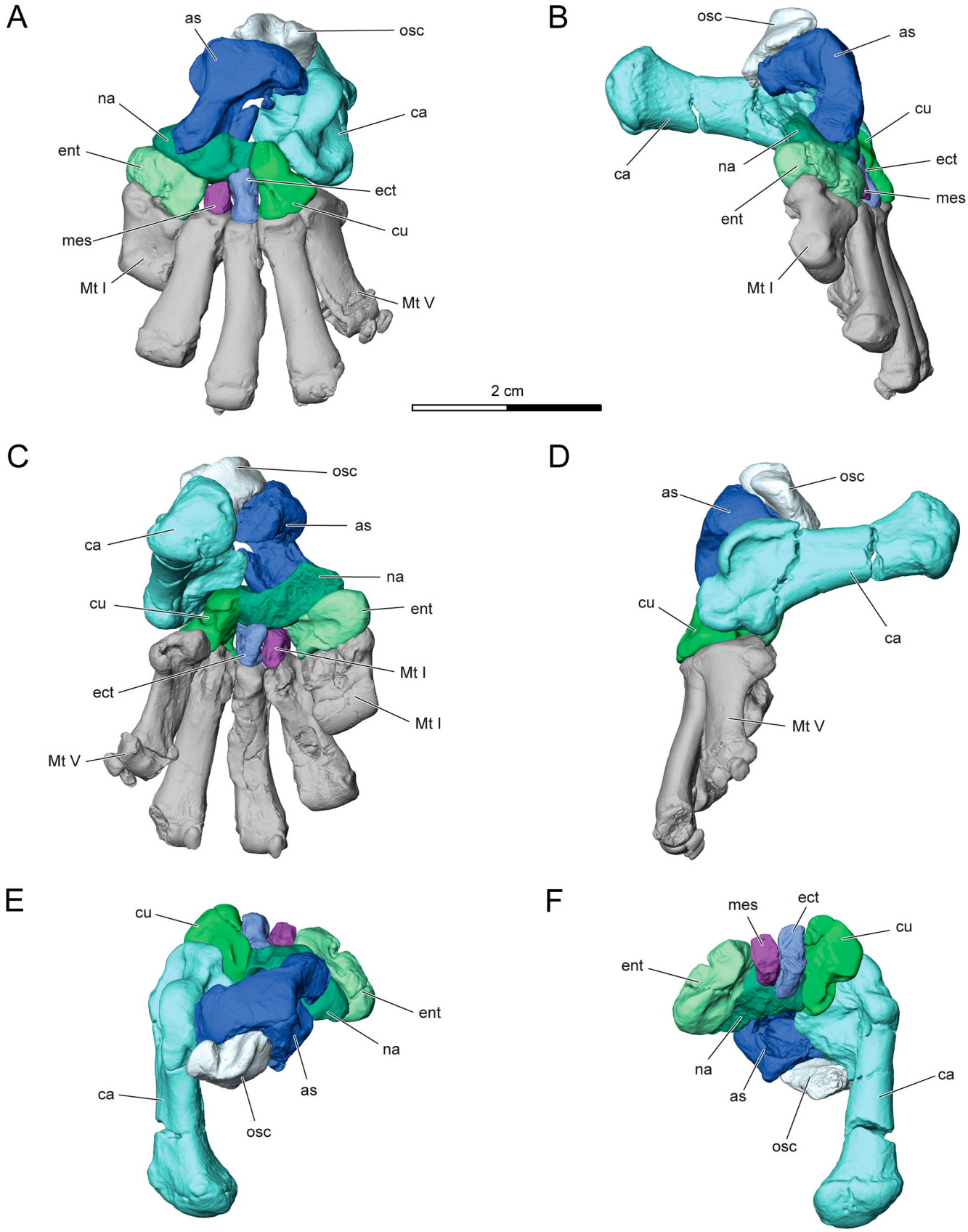

FIGURE 42. Reconstruction of left tarsals and metatarsals of *Adalatherium hui*, holotype (UA 9030), based on digital surfaces derived from µCT scans, in **A**, dorsal, **B**, medial, **C**, plantar (= ventral), **D**, lateral **E**, proximal, and **F**, distal views. Astragalus, mesocuneiform, and ectocuneiform reversed from right side; calcaneus and entocuneiform composite reconstructions of left and right elements. **Abbreviations**: **as**, astragalus; **ca**, calcaneus; **cu**, cuboid; **ect**, ectocuneiform; **ent**, entocuneiform; **mes**, mesocuneiform; **Mt**, metatarsal; **na**, navicular, **osc**, os calcaris.

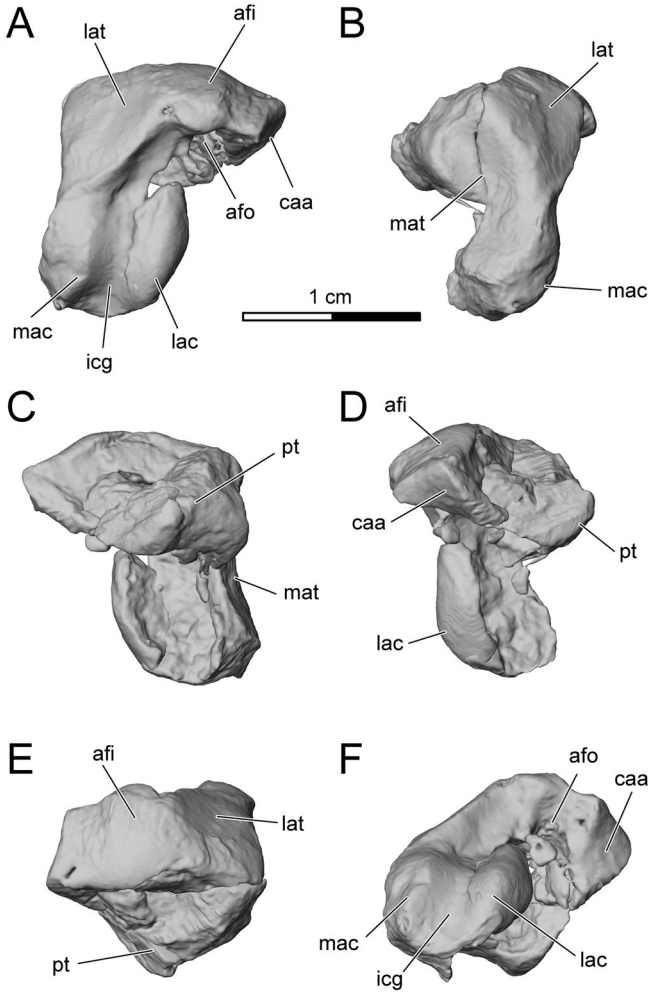

FIGURE 43. Left astragalus (reversed from right side) of *Adalatherium hui*, holotype (UA 9030), in **A**, dorsal, **B**, medial, **C**, plantar (= ventral), **D**, lateral, **E**, proximal, and **F**, distal views. **Abbreviations**: **afi**, astragalofibular facet; **afo**, astragalar foramen; **caa**, calcaneoastragalar facet; **icg**, intercondylar groove; **lac**, lateral astragalar condyle; **lat**, lateral astragalotibial facet; **mac**, medial astragalar condyle; **mat**, medial astragalotibial facet; **pt**, plantar tubercle.

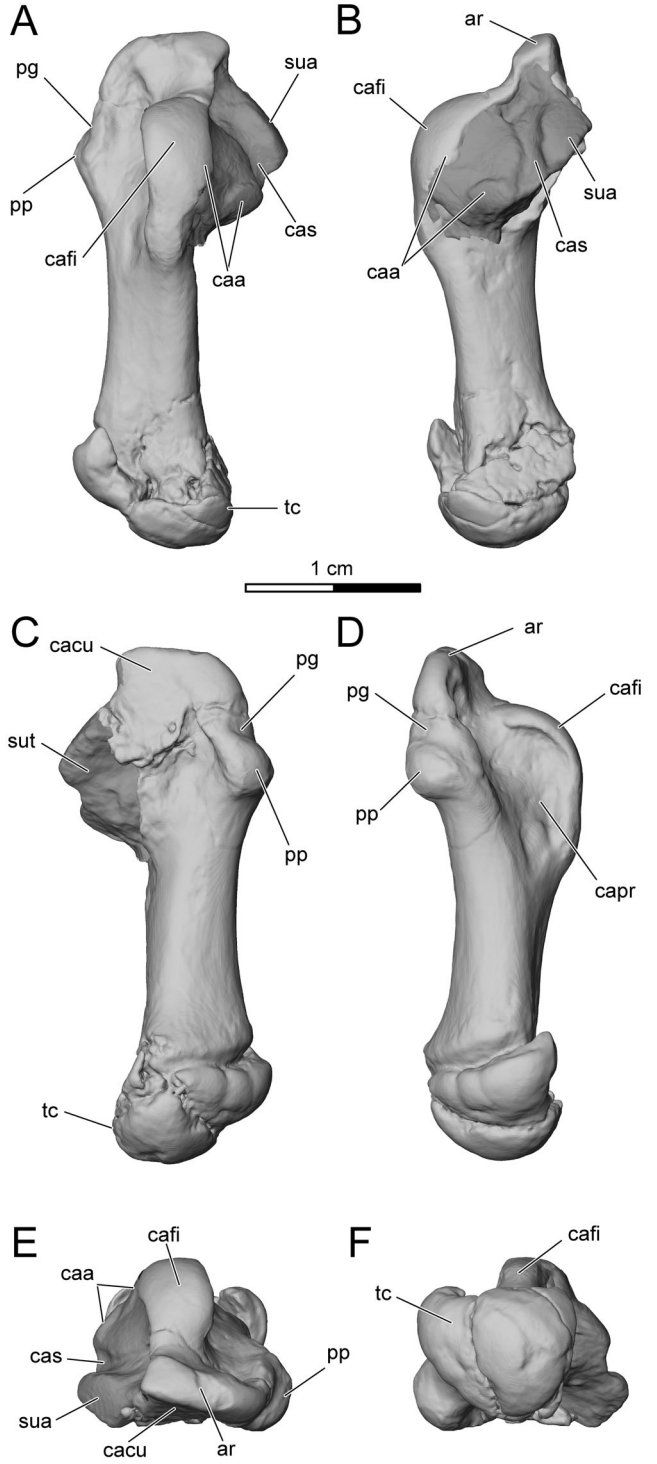

FIGURE 44. Left calcaneus of *Adalatherium hui*, holotype (UA 9030), in **A**, dorsal, **B**, medial, **C**, plantar (= ventral), **D**, lateral, **E**, proximal, and **F**, distal views. Composite reconstruction based on right (dark gray) and left (light gray) elements. **Abbreviations**: **ar**, anterior ridge; **caa**, calcaneoastragalar facet; **cacu**, calcaneocuboid facet; **cafi**, calcaneofibular facet; **capr**, calcaneal protuberance; **cas**, calcaneal sulcus; **pg**, peroneal groove; **pp**, peroneal process; **sua**, sustentacular facet; **sut**, sustentaculum tali; **tc**, tuber calcanei.

situated on the calcaneal protuberance on the dorsal aspect of the calcaneus, proximal to and in line with the dorsal ridge of the tuber (Fig. 44A). In dorsal view, the calcaneofibular facet is roughly rectangular in shape, being considerably longer proximodistally than mediolaterally wide. The facet is strongly curved in lateral (or medial) view, being strongly convex proximodorsally and gently so mediolaterally (Fig. 44B, D). The lateral border of the calcaneofibular facet forms a fine crest overhanging the calcaneal protuberance. Medially, the calcaneofibular facet is continuous with one of the calcaneoastragalar facets. This facet is the more slender of the two calcaneoastragalar facets and extends along the posteromedial margin of the calcaneal protuberance. Medially, the calcaneal protuberance slopes into a broad, medially projecting sustentacular process. A second, more robust, calcaneoastragalar facet is positioned on the sustentaculum tali. The second calcaneoastragalar facet is convex, facing distomedially and slightly dorsally. The facet is mediolaterally wider than dorsoplantarly deep. The two calcaneoastragalar facets are not continuous, although they appear to articulate with a single facet on the astragalus.

The sustentacular facet is preserved on the right calcaneus (Figs. 41A, 44) but is fragmentary on the left. The facet is slightly convex and faces proximomedially (Fig. 41A, B, F). A distinct

sulcus, here identified as the calcaneal sulcus, separates the calcaneoastragalar facet from the more anteriorly positioned sustentacular facet (Fig. 41A, B, F). It should be noted that two separate calcaneoastragalar facets have not been described for Mesozoic mammaliaforms. Most Mesozoic mammaliaforms have one calcaneoastragalar facet, which is usually more posteriorly positioned (close to the calcaneofibular facet), and an anteriorly positioned sustentacular facet. It is possible that the three facets in *Adalatherium* are more appropriately homologized with the posterior calcaneoastragalar facet, sustentacular facet, and anterior calcaneoastragalar facet (from posterior to anterior), as seen in some extant therians. The partial preservation of the astragalus hinders a definite assessment. The calcaneocuboid facet forms a large, triangular, and slightly concave surface, situated plantar to the sustentaculum tali (Fig. 44C, E). The distal border of the calcaneocuboid facet forms a lip that borders a deep concavity on the medioplantar aspect of the bone and plantar to the sustentaculum tali.

The peroneal process protrudes proximolaterally from the lateroplantar edge of the calcaneus (Fig. 44A, C–E). It is small and bulbous. A peroneal groove separates the peroneal process from the proximal end of the calcaneus. In proximal view, a ridge extends along the proximal surface of the calcaneus, bounding the calcaneocuboid facet dorsolaterally (Fig. 44E). The texture of this anterior ridge is smooth, but none of the tarsals articulate with it. The anterior ridge is convex and ends at the proximomedial extension of the calcaneofibular facet.

Navicular—The navicular articulates with the astragalus proximally, the cuboid and ectocuneiform distolaterally, the mesocuneiform distally, and the entocuneiform distomedially (Figs. 39–42, 45). The long axis of the navicular is oriented dorsolateral to medioplantar and is 15.7 mm in length along this axis (Table 6). In proximal (or distal) view, the navicular tapers plantarly (Fig. 45E, F). This tapering is exaggerated in the left navicular, where the lateral aspect of the plantar tuberosity is missing. In the right navicular, the dorsal aspect is still mediolaterally wider than the plantar aspect but the difference is less extreme. Proximally, the navicular articulates with the astragalus (Fig. 42). The astragalar articulation consists of two deeply excavated and asymmetrical facets that receive the trochleated navicular facet of the astragalus (Fig. 45E). The lateral astragalar facet is dorsoplantarly deeper and mediolaterally wider than the medial astragalar facet. The medial and lateral facets are separated by a well-defined midline ridge here termed the navicular ridge (Fig. 45E). The navicular ridge is more prominent on the dorsoproximal aspect of the navicular and becomes shallower medioplantarly. The medial astragalar facet gently slopes into the medial aspect of the bone.

The dorsal aspect of the navicular is mediolaterally wider than proximodistally tall. There is a shallow but large tuberosity in the middle that is laterally bounded by a proximodistally oriented sulcus, here termed the navicular sulcus (Fig. 45A). Lateral to the navicular sulcus is the facet for the cuboid. The cuboid facet is rectangular and slightly convex laterally (Fig. 45A), thus matching its slightly concave counterpart on the cuboid. The distal aspect of the navicular forms a small arc to articulate with the entocuneiform and the mesocuneiform and distolaterally with the ectocuneiform (Fig. 45A, F). The boundaries between the facets are hardly discernible. The facet for the entocuneiform is by far the largest cuneiform facet. It is triangular in shape and extends medioplantarly along most of the length of the navicular. Dorsally, the entocuneiform facet terminates at the medial end of the dorsal tuberosity. The facet for the mesocuneiform is distally oriented, slightly convex, and dorsoplantarly longer than mediolaterally wide. The facet for the ectocuneiform is slightly convex and distolaterally oriented. The plantar aspect of the navicular bears a plantar tuberosity. The tuberosity is not as well preserved in the left navicular, but the right navicular shows a sizable plantar tuberosity (Figs. 39B, 41B, 45C).

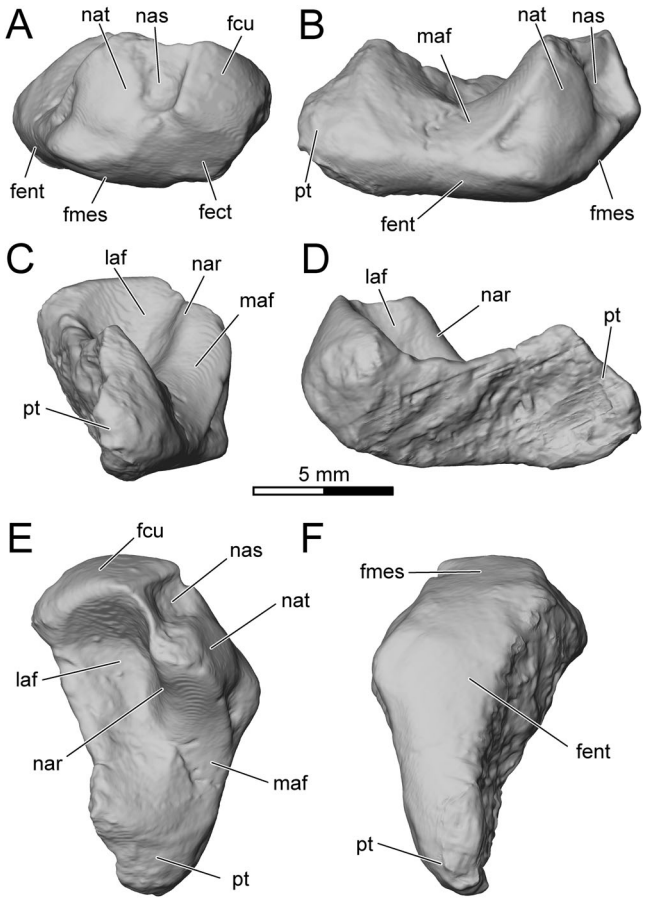

FIGURE 45. Left navicular of *Adalatherium hui*, holotype (UA 9030), in **A**, dorsal, **B**, medial, **C**, plantar (= ventral), **D**, lateral **E**, proximal, and **F**, distal views. **Abbreviations**: **fcu**, facet for cuboid; **fect**, facet for ectocuneiform; **fent**, facet for entocuneiform; **fmes**, facet for mesocuneiform; **laf**, lateral astragalar facet; **maf**, medial astragalar facet; **nar**, navicular ridge; **nas**, navicular sulcus; **nat**, navicular tuberosity; **pt**, plantar tuberosity.

Cuboid—The cuboid (Figs. 39–42, 46) articulates with the calcaneus proximolaterally, the navicular proximomedially, the ectocuneiform medially, and the fourth and fifth metatarsals distally. In dorsal view, the cuboid is roughly triangular in outline and forms a wedge fitting between the calcaneus and the navicular plus ectocuneiform (Fig. 42A). The dorsal surface is gently concave and bears several small ridges that are associated with articular facets for neighboring bones (Fig. 46A). The ridge along the proximolateral edge represents the dorsal extent of the calcaneocuboid facet. This ridge terminates at the dorsal end of a sulcus that extends along the lateral aspect of the bone (Fig. 46A, D). Medially, the ectocuneiform facet and the navicular facet form two fine ridges on the dorsal surface of the cuboid (Fig. 46B). The proximal ridge is associated with the navicular facet and ends roughly at mid-length of the cuboid. The distal ridge curves laterally and is associated with the facet for the ectocuneiform.

Laterally, the cuboid bears two facets, separated by the cuboid sulcus in the middle, which is deeply excavated on the plantar side and extends along the lateral aspect (Fig. 46D). Only a shallow extension of the sulcus reaches the dorsal side of the bone. The proximal facet, the facet for the calcaneus, is proximolaterally

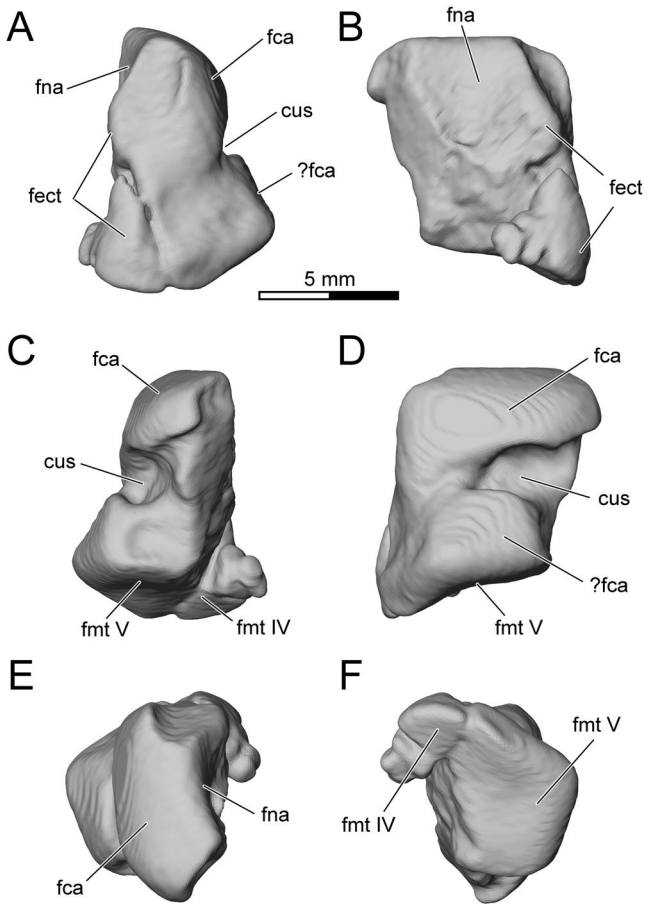

FIGURE 46. Left cuboid of *Adalatherium hui*, holotype (UA 9030), in **A**, dorsal, **B**, medial, **C**, plantar (= ventral), **D**, lateral **E**, proximal, and **F**, distal views. **Abbreviations**: **cus**, cuboid sulcus; **fca**, facet for calcaneus; **fect**, facet for ectocuneiform; **fmt**, facet for metatarsal; **fna**, facet for navicular.

oriented and extends along the dorsoplantar depth of the bone. The facet is convex transversely and moderately convex dorsally. Proximally, there is a fine ridge that separates the facet for the calcaneus from the facet for the navicular medially (Fig. 46E). Distal to the calcaneal facet appears to be another facet (labeled '?fca' in Fig. 46A, D) that is approximately half as deep (dorsoplantarly) as the facet for the calcaneus. It too probably articulated with the calcaneus but is oriented dorsolaterally rather than strictly laterally.

In medial view, the cuboid bears the navicular facet and the ectocuneiform facet (Fig. 46B). The facet for the navicular is concave laterally and faces proximomedially. It extends along the dorsoplantar depth of the bone. The facet for the ectocuneiform is damaged on the left bone and only partially exposed on the right cuboid. It is divided into two parts: the proximal part is flat and positioned distal to the navicular facet, whereas the distal part is slightly concave and wraps around the medial border of the cuboid onto its dorsal surface. The distal aspect of the cuboid is roughly trapezoidal in outline and is almost as mediolaterally wide as it is dorsoplantarly deep (Fig. 46F). Its concave surface presents facets for metatarsals IV and V. The two facets are largely indistinguishable, except for a very shallow ridge extending plantarly from the middle of the dorsal edge of the cuboid (Fig. 46F). In plantar view, the cuboid sulcus, on the lateral side of the bone, extends onto the plantar aspect, forming a deep notch (Fig. 46C).

Entocuneiform—The entocuneiform is damaged on the left side but is well preserved on the right (Figs. 39–42); as such, Figure 47 illustrates the mirrored right entocuneiform. The bone is large and roughly rectangular in shape in medial or lateral view (Fig. 47B, D). The long axis of the entocuneiform is oriented dorsolateral to medioplantar; it is 12.5 mm dorsoplantarly deep (Table 6).

The entocuneiform articulates with the navicular proximally, the mesocuneiform laterally, metatarsal II distolaterally, and metatarsal I distally (Fig. 42). The proximal aspect of the entocuneiform bears the concave articular facet for the navicular (Fig. 47E). The facet extends onto the base of the large plantar tuberosity. The medial aspect of the entocuneiform is convex and bears a distinct concavity, here termed the entocuneiform sulcus, which opens distally (Fig. 47B). The lateral aspect is concave dorsally and convex plantarly, leading into the plantar tuberosity. On the right pes, a shallow sulcus is visible on the lateral aspect of the plantar tuberosity (Fig. 47D). The facet for the mesocuneiform occupies the dorsolateral aspect of the entocuneiform; only a small distal portion articulates with the proximomedial corner of metatarsal II (Fig. 47A). The distal surface of the entocuneiform articulates with metatarsal I. The lateral half of the facet is convex, but the medial half is flat and would have accommodated the tuberosity at the proximomedial corner of metatarsal I in life.

Mesocuneiform—The mesocuneiform is damaged on the left pes but is well preserved on the right pes (Figs. 39–42); as such, Figure 48 shows the mirrored right mesocuneiform. The mesocuneiform is the smallest element of the tarsus; it is only 3.5 mm in proximodistal length and 2.7 mm in mediolateral width (Table 6).

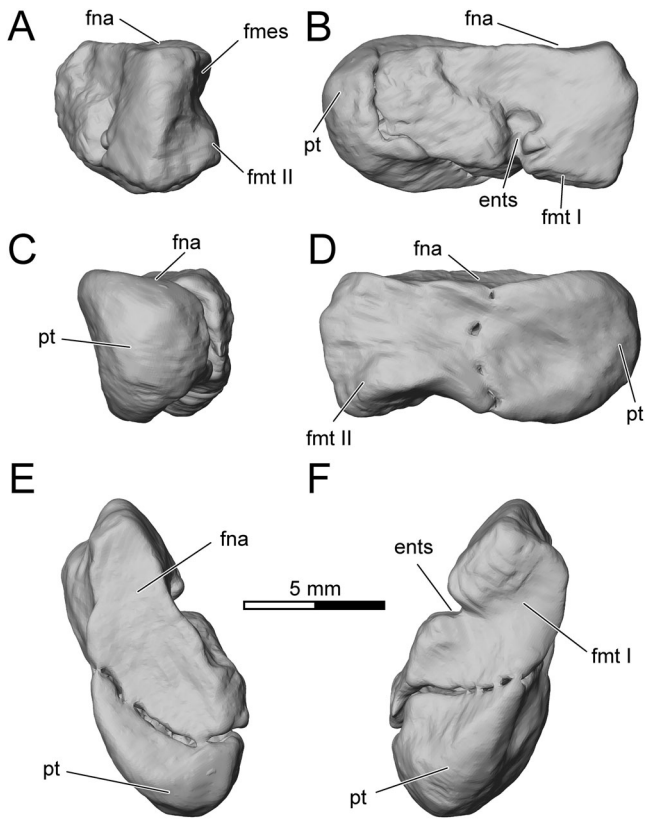

FIGURE 47. Left entocuneiform (reversed from right side) of *Adalatherium hui*, holotype (UA 9030), in **A**, dorsal, **B**, medial, **C**, plantar (= ventral), **D**, lateral **E**, proximal, and **F**, distal views. **Abbreviations**: **ents**, entocuneiform sulcus; **fmes**, facet for mesocuneiform; **fmt**, facet for metatarsal; **fna**, facet for navicular; **pt**, plantar tuberosity.

The mesocuneiform articulates with the navicular proximally, the ectocuneiform laterally, the entocuneiform medially, and metatarsal II distally. The dorsal aspect of the bone is gently concave and surrounded by fine lips (Fig. 48A). In the right pes, the mesocuneiform is not aligned distally with the ectocuneiform but is more proximally positioned (Fig. 41A). The gently concave facet for the navicular occupies the proximal aspect (Fig. 48E). The facets for the neighboring cuneiforms on the lateral (for the ectocuneiform) and medial (for the entocuneiform) aspects are flat to gently convex. The facet for metatarsal II on the distal aspect is deeply excavated and almost semicircular in medial view (Fig. 48B). The plantar aspect of the bone is dominated by a small plantar tuberosity (Fig. 48B–D).

Ectocuneiform—The ectocuneiform articulates with the navicular proximally, the cuboid laterally, metatarsal III distally, and the mesocuneiform medially. It is mediolaterally compressed and proximodistally tall in dorsal (or plantar) view (Figs. 39–42, 49A, C). The dorsal surface is mediolaterally constricted at mid-length, roughly resembling the shape of an hourglass (Fig. 49A). In proximal view, the navicular facet is gently concave and faces slightly medially (Fig. 49E). On the lateral aspect, the facet for the cuboid can be divided into a small and gently convex proximal portion and a large and slightly concave distal portion, which match its counterparts on the cuboid (Fig. 49D). The medial aspect of the ectocuneiform is concave and bears the facet for the mesocuneiform along its proximal margin (Fig. 49B). The distal aspect of the ectocuneiform presents the concave facet for metatarsal III, which slightly narrows plantarly (Fig. 49F). A large plantar tuberosity is visible in plantar view of the right pes (Figs. 39B, 49C, D). It extends along the proximodistal length of the plantar surface of the ectocuneiform.

Os Calcaris—The os calcaris is an element not commonly present in the mammalian tarsus. The os calcaris is well preserved in both tarsi of UA 9030 (Figs. 40, 42, 50). As preserved, it is located distal to the posterior edge of the tibia and contacts the astragalus anteriorly. In plantar view, the bone tapers distally, with a blunt apex that is located laterally (Fig. 50C). Proximally, the os calcaris expands into a comma-shaped process. The rugose plantar aspect is convex. In dorsal view, the os calcaris is gently concave, bearing articular facets for the astragalus (medially) and possibly for the fibula (laterally) (Fig. 50A). An ossified cornu calcaris, the ossified core of the extratarsal spur, is not preserved in UA 9030; as such, it remains uncertain whether an extratarsal spur was present in *Adalatherium*.

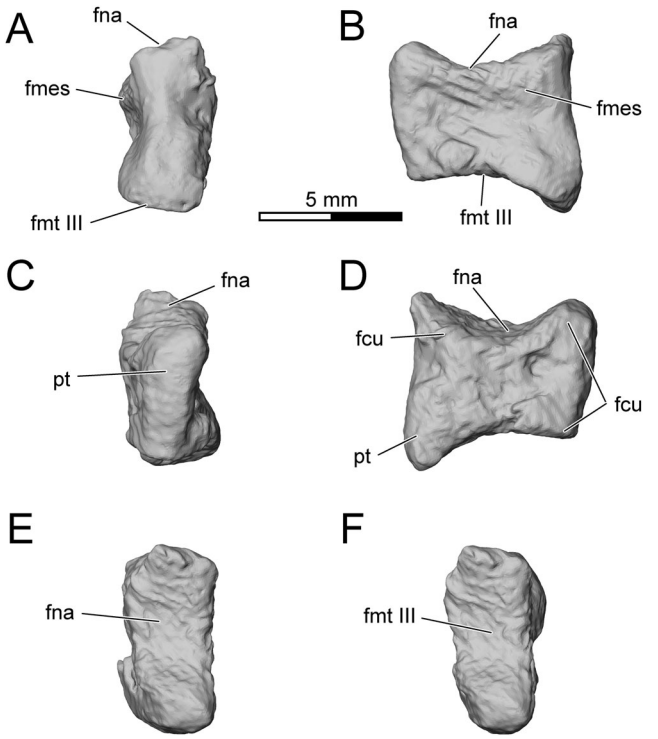

FIGURE 49. Left ectocuneiform (reversed from right side) of *Adalatherium hui*, holotype (UA 9030), in **A**, dorsal, **B**, medial, **C**, plantar (= ventral), **D**, lateral **E**, proximal, and **F**, distal views. **Abbreviations**: **fcu**, facet for cuboid; **fmes**, facet for mesocuneiform; **fmt**, facet for metatarsal; **fna**, facet for navicular; **pt**, plantar tuberosity.

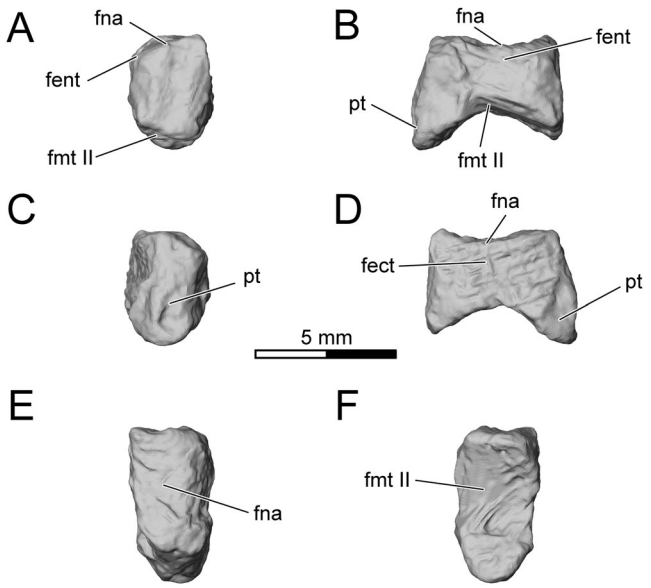

FIGURE 48. Left mesocuneiform (reversed from right side) of *Adalatherium hui*, holotype (UA 9030), in **A**, dorsal, **B**, medial, **C**, plantar (= ventral), **D**, lateral **E**, proximal, and **F**, distal views. **Abbreviations**: **fect**, facet for ectocuneiform; **fent**, facet for entocuneiform; **fmt**, facet for metatarsal; **fna**, facet for navicular; **pt**, plantar tuberosity.

Metatarsals—Metatarsals (Mt) I–V of UA 9030 are well preserved on both sides, except for the proximal aspect of the left Mt III (Figs. 39, 40, 42). Those of the left side were disarticulated and are illustrated in Figure 51. The lengths of the metatarsals are in the order Mt I < Mt V < Mt II < Mt III < Mt IV; conversely, their robustness is in the opposite order (Table 7). Metatarsals II, III, and IV are more similar to one another than each is to Mt I or Mt V. The metatarsals form a moderate arch that is convex dorsally when all the elements are articulated with their facets tightly approximated, as shown for the left pes in Figure 42. They also form an arch proximally and distally, in dorsal or ventral view (Figs. 39A, 42A).

The first metatarsal is a broad and somewhat dorsoventrally compressed element (Fig. 51, top row). Its length is only about half that of Mt II. The proximal facet for the entocuneiform is asymmetrical, with the lateral half being gently concave and the medial half being flat (Fig. 51E). Two tuberosities extend plantarly from the articular facet for the entocuneiform (Fig. 51B). The lateral tuberosity is dorsoplantarly long and mediolaterally narrow, whereas the medial tuberosity is mediolaterally wide and flat. The lateral tuberosity protrudes farther plantarly than the medial tuberosity. Due to the presence of these prominent tuberosities, the proximal end of Mt I expands plantarly and is mediolaterally wider than the remainder of the bone. The

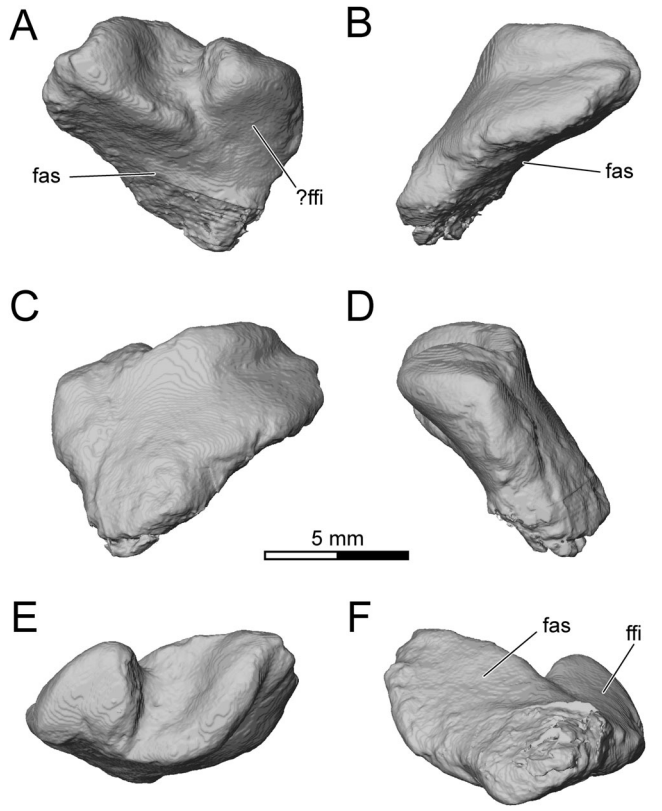

FIGURE 50. Left os calcaris of *Adalatherium hui*, holotype (UA 9030), in **A**, dorsal, **B**, medial, **C**, plantar (= ventral), **D**, lateral **E**, proximal, and **F**, distal views. **Abbreviations**: **fas**, facet for astragalus; **ffi**, facet for fibula.

lateral aspect of the proximal end bears a small and flat facet for Mt II. Both the medial and lateral edges of the bone are straight, but they are not strictly parallel to one another. A small concavity is present on the dorsomedial aspect of the proximal end (Fig. 51A, B). In the articulated pes, this small concavity is aligned with the fossa on the dorsodistal aspect of the entocuneiform (Fig. 42A). The dorsal aspect of Mt I is concave near the distal end before leading into the distal articular facet. The ventral aspect of the bone is even more concave, delimited proximally by the plantar tuberosities and distally by the distal articular facet. The distal end is slightly narrower mediolaterally than the shaft. Both the medial and lateral sides of the distal end are elliptical in outline, with a shallow rugosity and depression in the center. The distal articular facet is convex, extending onto the dorsal and plantar aspects of the distal end, respectively. A large sesamoid bone is preserved on the plantar aspect of the distal end (Fig. 39B).

Metatarsals II to IV are slightly bowed dorsally, and markedly more slender than Mt I (Fig. 51). The second and third metatarsals are slightly bent medially, whereas the shaft of Mt IV is straight (Fig. 51B). The proximal facet on Mt II is almost square in proximal view, and shallowly convex (Fig. 51E). A slight groove extends dorsoplantarly in the center of the facet. The proximal facets on Mt III and Mt IV are gently convex and taper plantarly, particularly that on Mt IV (Fig. 51E). The medial and lateral aspects of the proximal ends of all three central metatarsals bear facets for intermetatarsal articulation (Fig. 51C, D). The articular facet on Mt II for Mt I is gently convex and faces medioplantarly. The proximomedial end of Mt II is notched to accommodate the distolateral corner of the entocuneiform (Fig. 51A). Laterally, the articular facet on Mt II for Mt III is flat and semilunar in outline. Mt III is mediolaterally narrower proximally than either Mt II or Mt IV (Fig. 51A). The medial and lateral intermetatarsal facets are only partly preserved on the left Mt III. Its narrow width is, however, confirmed in its counterpart on the right side. Both intermetatarsal facets appear to be flat and are either semilunar or triangular in shape. On Mt IV, the medial facet for Mt III is small, triangular, and flat, whereas the articular facet for Mt V is large, slightly concave, and faces lateroplantarly. The distal ends of Mt II–Mt IV are generally similar to that of Mt I. They differ, however, in that they are wider mediolaterally than the shaft. A plantar tuberosity is present on the plantar aspects of the proximal ends of Mt II–Mt IV.

Mt V has a dorsoplantarly compressed shaft and, compared with those of Mt II–Mt IV, its proximal end is much more expanded mediolaterally. Unlike the shafts of Mt I and Mt IV, which are straight, and Mt II and Mt III, which are bowed medially, the shaft of Mt V is bowed laterally. The proximal aspect is triangular in outline, having a large nonarticular surface lateral to the facet for the cuboid (Fig. 51E). It is similar to Mt I in having two proximal plantar tuberosities. However, it differs from Mt I in that the lateral tuberosity, rather than the medial, is expanded and protrudes laterally, forming a distinct process, probably for attachment of the peroneus tendon. The medial tuberosity is separated from the lateral tuberosity by a deep notch on the plantar aspect (Fig. 51B). The distal end of Mt V is similar to those of Mt II–Mt IV. Unique among the metatarsals, the distal end of Mt V is rotated medially relative to the proximal end. A pair of sesamoid bones is present on the plantar aspect of the distal ends of Mt II–Mt V (Fig. 39B). Accordingly, a plantar keel is present along the midline of the distal articular facet of these metatarsals but is absent in Mt I (Fig. 51F).

Proximal Pedal Phalanges—The proximal pedal phalanges (PPP) I–V of *Adalatherium* are well preserved on both pedes (Figs. 39, 40), and their detailed morphology is depicted in the disarticulated left side (Fig. 42). They are short and robust elements. This is particularly true for PPP V, which is much shorter and, because of that, relatively more robust than those of digits I to IV. Overall, the proximal phalanges decrease in length and increase in robustness from PPP I to PPP V, with PPP III and PPP IV being approximately equal (Table 7; Fig. 52A). The proximal articular facets of all proximal phalanges are concave, slightly slanted dorsally, and dorsoplantarly compressed (Fig. 52). Small tuberosities are present along the lateroplantar and medioplantar aspects of the proximal articular facets (Fig. 52B). The shafts of the proximal phalanges are semicircular to bell-shaped in cross-section, being flat plantarly and convex dorsally. The dorsal doming of the shaft decreases from PPP II to PPP V; the shaft of PPP II is more circular, whereas the shaft of PPP V is dorsoplantarly compressed and mediolaterally broad. In lateral (or medial) view, the shafts decrease in dorsoplantar depth distally, leading to a triangular appearance (Fig. 52C, D). In dorsal (or plantar) view, the shafts expand toward the proximal and distal ends and are gently constricted at mid-length (Fig. 52A, B). A depression is visible on the dorsomedial (PPP II, PPP III) and dorsolateral (PPP III–PPP V) aspects of the shafts just distal to the proximal articular facets. The dorsomedial aspect of PPP III is damaged, and it is uncertain whether a depression was present or not. The distal articular facets are similar to each other in PPP II–PPP V, whereas the distal facet of PPP I is naturally more similar to the distal articular facets of the intermediate phalanges. PPP I has a trochlea-like distal facet, with more distinct medial and lateral ridges and a central groove. A small nutrient foramen is present on the plantar aspect of the shaft proximal to the distal facet. The distal facets in PPP II–PPP V are dorsoplantarly convex and extend onto the dorsal and plantar aspects of the phalanges (Fig. 52F). In lateral view, the distal ends are elliptical in

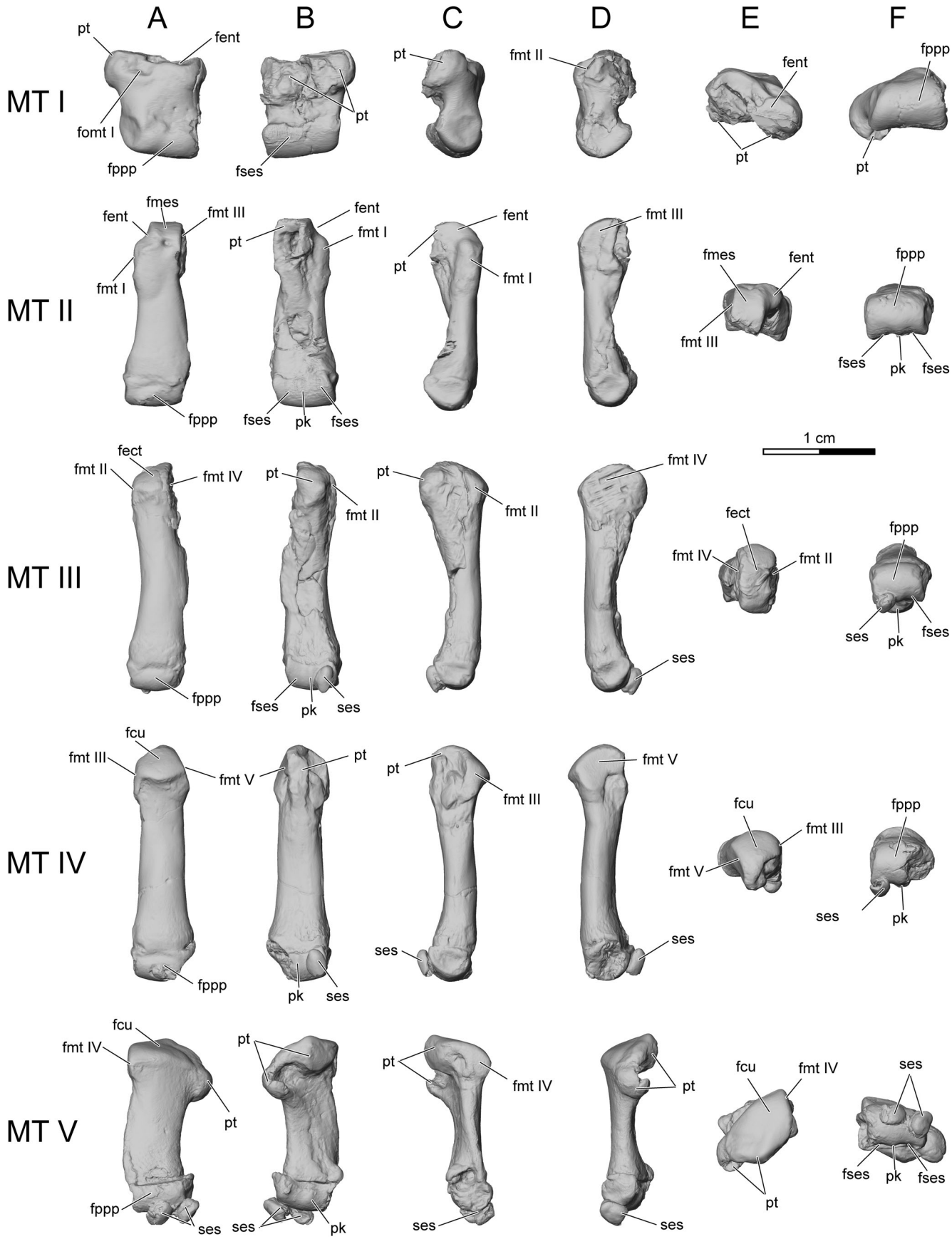

FIGURE 51. Left metatarsals (Mt) I–V of *Adalatherium hui*, holotype (UA 9030), in **A**, dorsal, **B**, plantar (= ventral), **C**, medial, **D**, lateral **E**, proximal, and **F**, distal views. Mt III is a composite reconstruction of left and right elements. Rows from top to bottom: Mt I, Mt II, Mt III, Mt IV, and Mt V. **Abbreviations**: **fcu**, facet for cuboid; **fect**, facet for ectocuneiform; **fent**, facet for entocuneiform; **fmes**, facet for mesocuneiform; **fmt**, facet for metatarsal; **fomt**, fossa on metatarsal; **fppp**, facet for proximal pedal phalanx; **fses**, facet for sesamoid; **pk**, plantar keel; **pt**, plantar tuberosity; **ses**, sesamoid.

outline, with the long axis oriented dorsodistally to proximoplantarly. The medial and lateral aspects of the distal ends slant slightly toward the midline dorsally (Fig. 52A). Thus, the articular facets are narrower dorsally and wider plantarly in distal view (Fig. 52F). A single large sesamoid bone is present on the plantar aspects of the distal ends of PPP II–PPP V (Fig. 39B). Two small sesamoid bones are present on the plantar aspect of PPP I (Fig. 52A–D, F).

Intermediate Pedal Phalanges—The four intermediate pedal phalanges (IPP) II–V are well preserved on both pedes (Figs. 39, 40). The disarticulated elements from the left side are depicted in Figure 53. They are more than two-thirds of the length of the corresponding proximal phalanges (Table 7). IPP II–IPP IV are similar in appearance, whereas IPP V is proximodistally shorter. The intermediate phalanges are generally similar to the proximal phalanges in their overall gestalt. They differ from the proximal

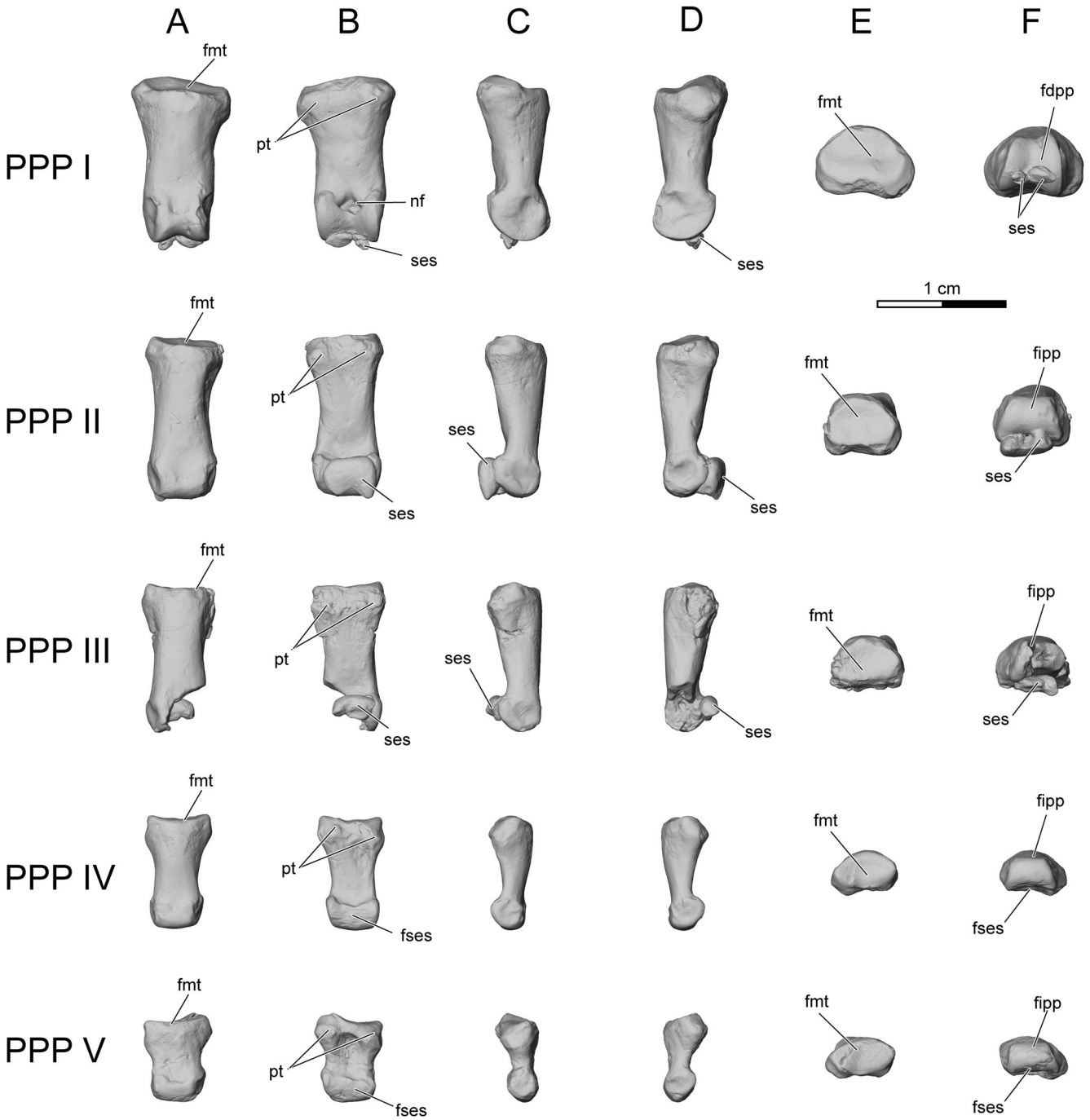

FIGURE 52. Left proximal pedal phalanges (PPP) I–V of *Adalatherium hui*, holotype (UA 9030), in **A**, dorsal, **B**, plantar (= ventral), **C**, medial, **D**, lateral, **E**, proximal, and **F**, distal views. Rows from top to bottom: PPP I, PPP II, PPP III, PPP IV, and PPP V. **Abbreviations**: **fdpp**, facet for distal pedal phalanx; **fipp**, facet for intermediate pedal phalanx; **fmt**, facet for metatarsal; **fses**, facet for sesamoid; **nf**, nutrient foramen; **pt**, plantar tuberosity; **ses**, sesamoid.

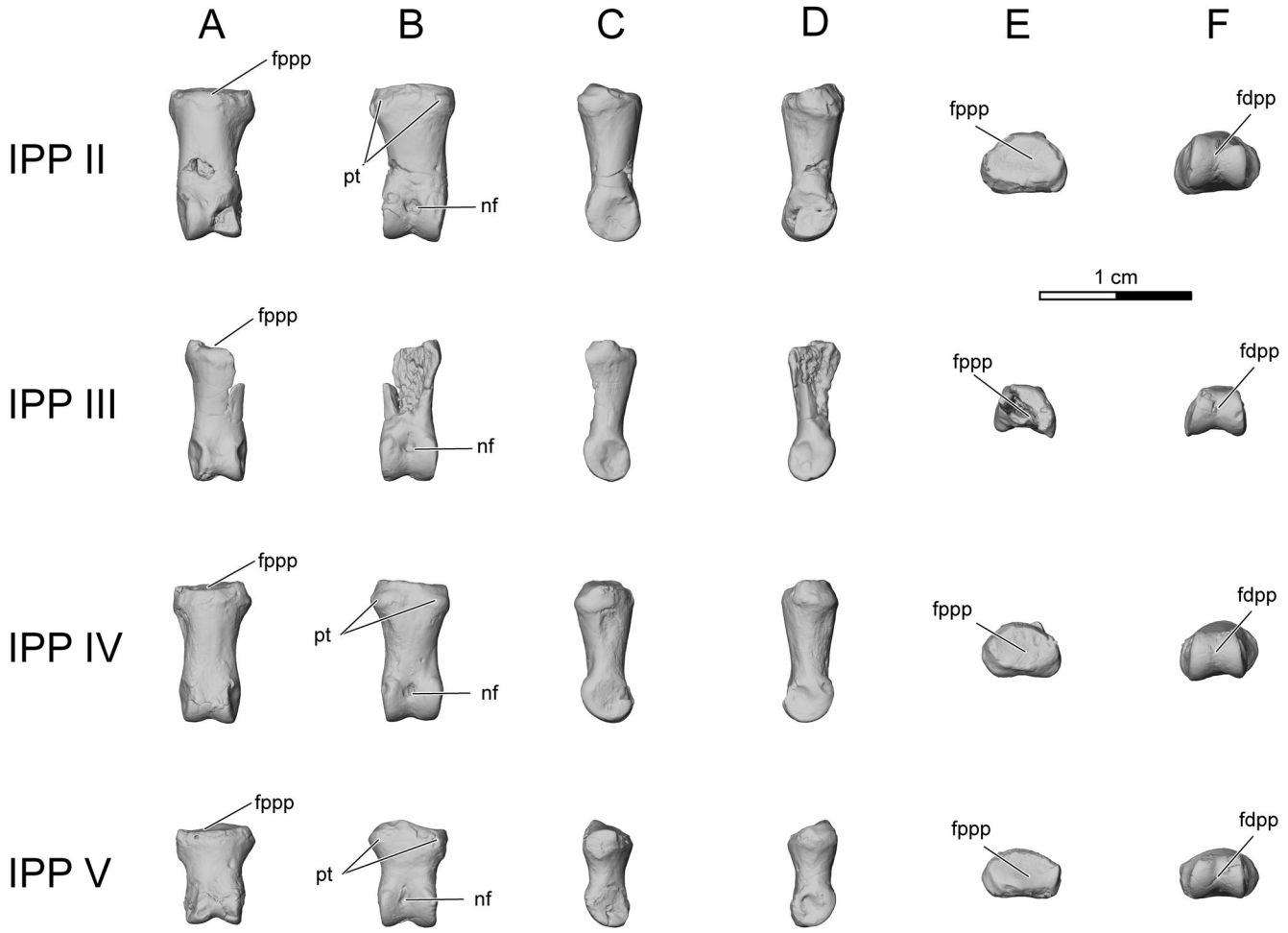

FIGURE 53. Left intermediate pedal phalanges (IPP) II–V of *Adalatherium hui*, holotype (UA 9030), in **A**, dorsal, **B**, plantar (= ventral), **C**, medial, **D**, lateral, **E**, proximal, and **F**, distal views. Rows from top to bottom: IPP II, IPP III, IPP IV, and IPP V. **Abbreviations**: **fdpp**, facet for distal pedal phalanx; **fppp**, facet for proximal pedal phalanx; **nf**, nutrient foramen; **pt**, plantar tuberosity.

phalanges, however, in that the distal articular facet on each forms a trochlea, plantar sesamoid bones are absent, and there is a nutrient foramen present on the plantar aspect just proximal to the groove of the trochlea.

Distal Pedal Phalanges—The distal pedal phalanges (DPP) I–V are well preserved on both pedes (Figs. 39, 40). Those from the left side are disarticulated and shown in Figure 54. They are more robust and longer (approximately 140–170%) than the distal manual phalanges (Tables 7, 8; Figs. 33, 54). The extreme length of the distal pedal phalanges is particularly evident in the first digit. The distal phalanges are generally longer than their respective proximal and intermediate phalanges, except for DPP III and DPP IV, which are exceeded slightly in length by PPP III and PPP IV (Table 7). The length of the distal phalanges decreases from medial to lateral, with DPP III and DPP IV being subequal in length.

Generally, the distal pedal phalanges are similar in morphology (Fig. 54). They are moderately curved, DPP I more so than the others, and dorsoplantarly taller than mediolaterally wide. The proximal facets are bell-shaped, with a nearly flat plantar base (Fig. 54E). The medial and lateral facets form a trochlear notch with a strong median ridge and surrounding raised lips. In close-packed position (maximum articulation), the distal phalanges assume a position that is strongly flexed. The intermediate and distal phalanges form an angle of almost 90° in flexion. The extensor process on the dorsal aspect of the articular facet is moderately developed and is directed proximally, preventing strong hyperextension at the distal interphalangeal joint. The flexor tubercle has a triangular outline and forms a rugose and slightly raised surface distal to the plantar lip of the proximal facet (Fig. 54B). A fossa is developed in the middle of the tubercle and just distal to the proximal lip. It contains a nutrient foramen that is directed plantarly. The plantar aspect of the bone distal to the flexor tubercle is gently convex. Fine ridges separate the plantar aspect from the dorsolateral and dorsomedial sides, respectively. There is a fine groove accompanying each ridge on the dorsolateral and dorsomedial aspects of the phalanges (Fig. 54). The distal tip is sharp and slightly curved. The cross-section of the DPPs at mid-length is bell-shaped, with height subequal to width. The distal parts of the dorsal aspects of the phalanges are rugose, indicating the attachment of keratinous claws.

Pedal Sesamoid Bones—The locations of the pedal sesamoid bones in UA 9030 are as follows: two sesamoid bones on the distoplantar aspects of Mt II–Mt V and one sesamoid bone on the distoplantar articulations of PPP II–PPP V (Fig. 39B). The first digit diverges from this pattern, having one sesamoid for the metatarsal and probably two smaller sesamoid bones for the proximal phalanx (Figs. 39B, 41B). The paired sesamoids at the distal ends of Mt II–Mt V are similar in morphology. Each

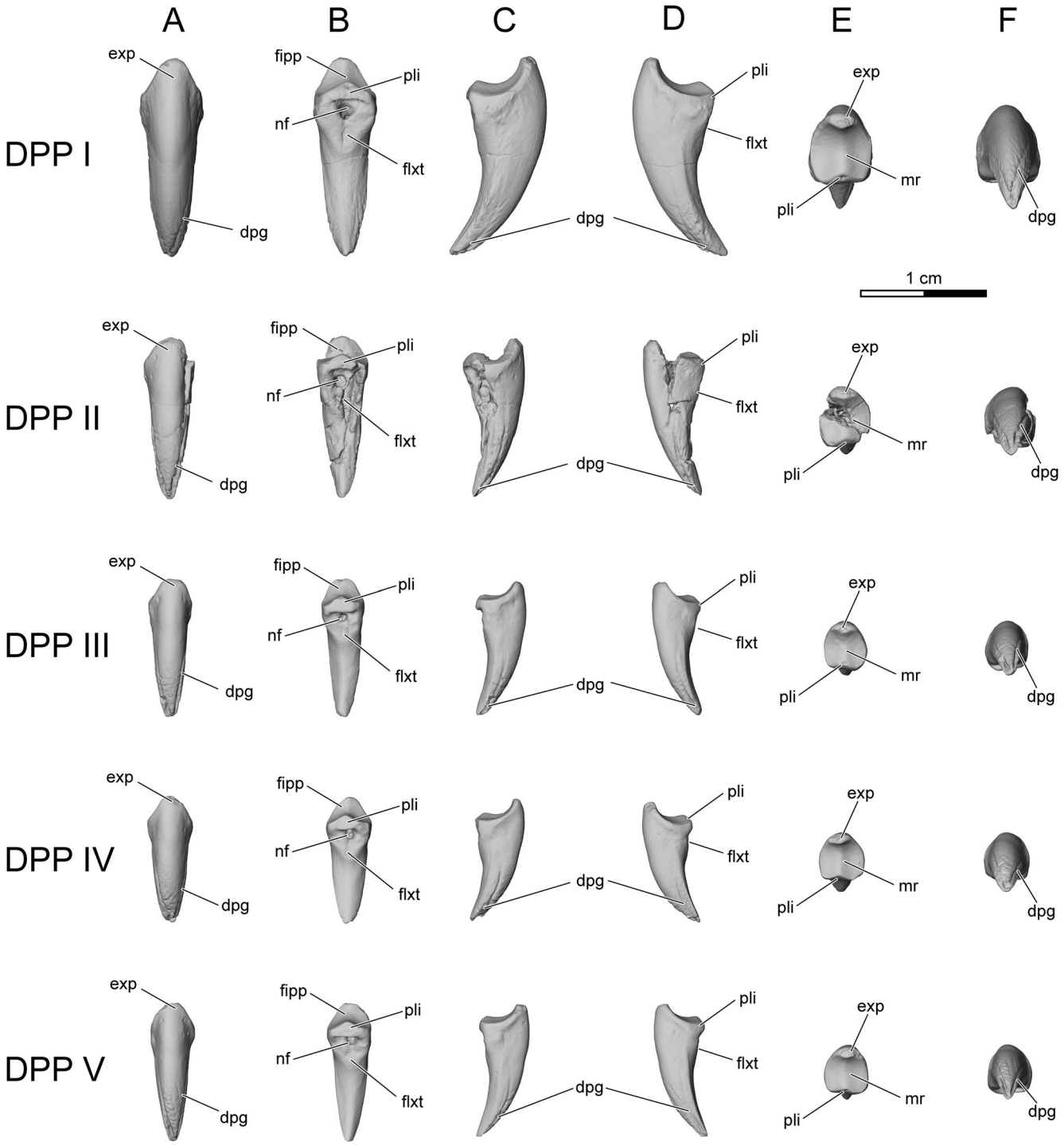

FIGURE 54. Left distal pedal phalanges (DPP) I–V of *Adalatherium hui*, holotype (UA 9030), in **A**, dorsal, **B**, plantar (= ventral), **C**, medial, **D**, lateral, **E**, proximal; and **F**, distal views. Rows from top to bottom: DPP I, DPP II, DPP III, DPP IV, and DPP V. **Abbreviations**: **dpg**, distal phalangeal groove; **exp**, extensor process; **fipp**, facet for intermediate pedal phalanx; **flxt**, flexor tubercle; **mr**, median ridge; **nf**, nutrient foramen; **pli**, plantar lip.

individual bone is elliptical, proximodistally longer than either mediolaterally wide or dorsoplantarly deep (Fig. 39B). The sesamoid of Mt I is the largest of all pedal sesamoids, covering the whole width of its metatarsal (Figs. 39B, 41B). The sesamoid is crescent-shaped in plantar view and convex plantarly. The single sesamoids of PPP II–PPP V are compressed and squarish, but notched at the distal edge (Fig. 39B). The sesamoid of PPP I is somewhat ambiguous; two small sesamoid bones are visible on the disarticulated left pes. They are elliptical and contact each other in the midline of the articular facet. It is, however, possible that the sesamoids were initially connected and formed one sesamoid similar to the ones in the other digits. In either case, the sesamoids of PPP I are smaller than the other single sesamoids (Fig. 39B). Neither the left nor the right pes preserves

TABLE 8. Limb indices of *Adalatherium hui*, holotype (UA 9030).

Brachial index	RL/HL	0.65
Humeral robustness	HMLW/HL	0.18
Humeral epicondylar breadth	HEW/HL	0.29
Ulnar robustness	UMLW/FUL	0.09
Olecranon length	UOL/FUL	0.31
Manus proportions	PMP3L/MC3L	0.55
Claw length index	DMP3L/DPP3L	0.72
Crural index	TL/FL	0.87
Femoral robustness	FAPD/FL	0.11
Gluteal index	FGT/FL	0.25
Femoral epicondylar breadth	FEW/FL	0.22
Tibial robustness	TMLW/TL	0.07
Tibial spine	TSL/TL	0.18
Pes length index	MT3L/FL	0.23
Intermembral index	HL + RL/FL + TL	0.69

Abbreviations: **DMP3L**, distal manual phalanx III length; **DPP3L**, distal pedal phalanx III length; **FAPD**, femur anteroposterior depth; **FEW**, femur epicondylar width; **FGT**, femur greater trochanter height; **FL**, femur length; **FUL**, functional ulnar length (ulnar length excluding olecranon); **HEW**, humerus epicondyle width; **HL**, humerus length; **HMLW**, humerus mediolateral width; **MC3L**, metacarpal III length; **MT3L**, metatarsal III length; **PMP3L**, proximal manual phalanx III length; **RL**, radius length; **TL**, tibia length; **TMLW**, tibia mediolateral width; **TSL**, tibial tuberosity length; **UMLW**, ulna mediolateral width; **UOL**, ulna olecranon length.

any sesamoids on the distoplantar aspect of the intermediate phalanges (Fig. 39B).

COMPARISONS

Postcranial Axial Skeleton

Atlas—Three-dimensionally preserved atlantes are only known from a handful of early mammaliaforms, including the morganucodontans *Morganucodon* and *Megazostrodon* (Jenkins and Parrington, 1976; Gow, 1986); the eutriconodontan *Repenomamus* (Hu, 2006); the multituberculates *Nemegtbaatar*, *Chulsanbaatar*, and *Kryptobaatar* (Kielan-Jaworowska and Gambaryan, 1994; Wible and Rougier, 2000); the stem therian *Vincelestes* (Rougier, 1993); the eutherians *Asioryctes*, *Kennalestes*, and *Maelestes* (Kielan-Jaworowska, 1977); and the metatherian *Pucadelphys* (Marshall and Sigogneau-Russell, 1995). Several other mammaliaforms preserve compressed and distorted atlantes and are scored in the recent phylogenetic analyses of Huttenlocker et al. (2018). These include *Agilodocodon*, *Megaconus*, *Maiopatagium*, *Vilevolodon*, *Rugosodon*, *Sinobaatar,* *Yanoconodon*, *Jeholodens*, *Zhangheotherium*, *Maotherium*, *Eomaia*, and *Juramaia*. Furthermore, Jenkins et al. (1997) indicated that the structure of the atlas arch in *Haramiyavia* is similar to that of morganucodontids, but no illustrations or further descriptions were presented, neither is the other postcranial material scored in the most recent assessment of *Haramiyavia* (Luo et al., 2015a). The well-preserved neural arches of the atlas of *Adalatherium* therefore add significantly to the limited sample of early mammaliaform atlantes.

Generally, the mammaliaform atlas is composed of four elements: the left and right halves of the neural arch (including the lamina and the pedicle), the intercentrum, and the centrum. Within cynodonts, the four different parts of the atlas fuse to varying degrees (Jenkins, 1969, 1971; Kemp, 1969). In the basal cynodont *Thrinaxodon*, the four components are still completely separate, whereas the atlantal centrum sutures with the axis to form the odontoid process in *Cynognathus*, *Diademodon*, *Gomphognathus*, *Massetognathus*, and *Tritylodon* (Broom, 1903; Jenkins, 1971; Gaetano et al., 2017, 2018). The suture between the atlantal centrum and the axis is, however, still visible in some of these forms. This incomplete fusion is also present in *Sinoconodon*, *Morganucodon*, and *Megazostrodon*, as well as in the eutriconodontan *Jeholodens* (Huttenlocker et al., 2018:char. 225). Huttenlocker et al. (2018) scored the odontoid process (atlantal centrum) as completely fused with the axis in *Xianshou*, *Rugosodon*, cimolodontans, *Gobiconodon*, *Repenomamus*, *Yanoconodon*, and *Zhangheotherium*, among others. In addition, Han et al. (2017:char. 217) provided evidence that the odontoid process is fused with the axis in *Shenshou* (scored '?' in Huttenlocker et al., 2018) and *Arboroharamiya allinhopsoni* (not included in Huttenlocker et al., 2018). In *Adalatherium*, the odontoid process is not well preserved but appears to be at least partially fused with the axis.

In extant mammals, the intercentrum fuses with the neural arch to form a ring-like structure (Lessertisseur and Saban, 1967; Kemp, 1969; Jenkins, 1971). This fusion is present in a few early mammaliaforms, including *Rugosodon* (Huttenlocker et al., 2018:char. 222), *Zhangheotherium* (Bi et al., 2018:char. 338), *Eomaia* (Bi et al., 2018:char. 338), and *Juramaia* (Bi et al., 2018:char. 338), but is absent in *Morganucodon*, *Megazostrodon*, eutriconodontans, *Adalatherium*, *Maiopatagium*, *Vilevolodon*, *Vincelestes*, *Kennalestes*, *Asioryctes*, and *Pucadelphys* (O'Leary et al., 2013:char. 2743; Bi et al., 2018:char. 338; Huttenlocker et al., 2018:char. 222; note that *Pucadelphys* is scored as fused in Huttenlocker et al. [2018] but as unfused in O'Leary et al. [2013] and Bi et al. [2018]). As is the case in UA 9030, in most of these taxa the intercentrum itself is not preserved, but rather assumed to have been present based on the attachment scars on the neural arches of the atlas.

In addition, the two halves of the neural arch fuse in extant mammals (O'Leary et al., 2013:char. 2745). Jenkins and Parrington (1976) argued that the neural hemiarches were likely unfused in *Morganucodon* and *Megazostrodon*, which was later supported by the description of unfused hemiarches in *Megazostrodon* by Gow (1986). The two halves of the neural arch appear to be unfused in *Chulsanbaatar* (ZPAL MgM-I/111; Kielan-Jaworowska and Gambaryan, 1994:fig. 20c), and only one half of the neural arch is preserved in *Nemegtbaatar* (ZPAL MgM-I/81, ZPAL MgM-I/82; Kielan-Jaworowska and Gambaryan, 1994:fig. 8b–d) and *Kryptobaatar* (PSS-MAE 101; Wible and Rougier, 2000:fig.16), suggesting that the hemiarches remained unfused in multituberculates. In the eutriconodontan *Yanoconodon*, the neural hemiarches are unfused (Chen et al., 2017), whereas they are fused in adult *Repenomamus* (Hu, 2006). Note that Hu (2006) described the neural arches as separated in a juvenile specimen of *Repenomamus*. The halves of the neural arches are fused in *Zhangheotherium* and in stem and early therians with the exception of *Vincelestes* (Rougier, 1993), *Maelestes*, and *Pucadelphys* (O'Leary et al., 2013:char. 2745). In the subadult holotype (UA 9030) of *Adalatherium hui*, it is uncertain whether the neural arches were fused. The dorsal margins of both halves are not preserved, and the remaining parts were separated and dislocated. It is possible that the neural halves were unfused and would have synostosed completely only later in life, similar to the pattern seen in *Repenomamus* (Hu, 2006).

The lamina of the neural arch of *Adalatherium* is broad, similar to that of *Morganucodon* (Jenkins and Parrington, 1976), whereas the lamina is more slender in *Repenomamus* (Hu, 2006). In both *Morganucodon* (Jenkins and Parrington, 1976) and *Repenomamus* (Hu, 2006), a distinct groove separates the lamina from the cranial articular facet, whereas the groove is much more shallow in *Adalatherium*.

Axis—The axis is poorly preserved in UA 9030 and only allows for limited comparison. Parts of the spinous process and lamina, as well as a questionable odontoid process, are present in UA 9030. In general, three-dimensionally preserved axes are rare in non-therian mammaliaforms, only being present in *Morganucodon* (centra of C1 and C2; Jenkins and Parrington,

1976), *Megazostrodon* (Gow, 1986), *Repenomamus* (Hu, 2006), *Gobiconodon* (centrum of C1; Jenkins and Schaff, 1988), *Nemegtbaatar* (Kielan-Jaworowska and Gambaryan, 1994), *Chulsanbaatar* (Kielan-Jaworowska and Gambaryan, 1994), *Kryptobaatar* (Kielan-Jaworowska and Gambaryan, 1994; Sereno and McKenna, 1995; Wible and Rougier, 2000), ?*Lambdopsalis* (centra of C1 and C2; Kielan-Jaworowska and Qi, 1990), an unidentified taeniolabidoid (Kielan-Jaworowska, 1989), *Litovoi* (centrum of C2; Csiki-Sava et al., 2018), and *Vincelestes* (Rougier, 1993). Compressed and partially preserved axes are known for *Megaconus* (Zhou et al., 2013); the euharamiyidans *Arboroharamiya allinhopsoni*, *Maiopatagium*, *Qishou*, *Shenshou*, *Vilevolodon*, and *Xianshou* (Bi et al., 2014; Han et al., 2017; Luo et al., 2017; Meng et al., 2017, Mao and Meng, 2019); the multituberculates *Sinobaatar*, *Rugosodon*, and *Jeholbaatar* (Hu and Wang, 2002; Yuan et al., 2013, Wang et al., 2019); the eutriconodontans *Yanoconodon*, *Liaoconodon*, *Jeholodens*, and *Spinolestes* (Ji et al., 1999; Meng et al., 2011; Martin et al., 2015; Chen et al., 2017); and the spalacotherioids *Zhangheotherium* and *Maotherium* (Hu et al., 1997; Rougier et al., 2003).

The axis of *Adalatherium* generally appears more robust than the axes of *Nemegtbaatar* and *Chulsanbaatar* (Kielan-Jaworowska and Gambaryan, 1994) and is more similar in shape to that of *Kryptobaatar* (Sereno, 2006), but less robust than that of *Repenomamus* (Hu, 2006). The spinous process is short and stout in *Nemegtbaatar* and *Chulsanbaatar*, but greatly expanded in *Repenomamus* and *Vincelestes*. It is uncertain whether a large, expanded spinous process was present in *Adalatherium*. The odontoid process appears long and slender in *Adalatherium*, whereas it is short and more bulbous in *Morganucodon* (Jenkins and Parrington, 1976:fig. 1g) and the multituberculates *Kryptobaatar* (Sereno, 2006:fig. 10.3), *Nemegtbaatar* (Kielan-Jaworowska and Gambaryan, 1994:fig. 9), *Chulsanbaatar* (Kielan-Jaworowska and Gambaryan, 1994:fig. 20), and an unidentified taeniolabidoid (Kielan-Jaworowska, 1989:fig. 1). The odontoid process appears slightly longer in *Repenomamus* (Hu, 2006:figs. 3.1–3.5).

It is uncertain whether axial ribs are present in *Adalatherium*. Axial ribs are scored as present in *Morganucodon*, *Megazostrodon*, monotremes, *Repenomamus*, *Yanoconodon*, *Jeholodens*, *Zhangheotherium*, and *Maotherium* and absent in *Arboroharamiya allinhopsoni*, *Maiopatagium*, *Shenshou* (scored '?' in Huttenlocker et al., 2018), *Vilevolodon*, *Xianshou*, *Rugosodon*, *Sinobaatar*, cimolodontan multituberculates, and therians (Han et al., 2017:char. 218; Huttenlocker et al., 2018:char. 226). However, Kielan-Jaworowska and Gambaryan (1994) noted the presence of axial ribs in *Chulsanbaatar* and *Nemegtbaatar*, whereas they appear to be absent or fused to the transverse processes in an unidentified taeniolabidoid.

Postaxial Cervical Vertebrae—The postaxial cervical vertebrae are only partially preserved in UA 9030 and are of limited use for comparison. Most interestingly, *Adalatherium* possesses ribs on at least the posterior cervical vertebrae. Facets on the transverse processes of C4–C7 indicate that the ribs remained unfused in *Adalatherium*. Postaxial cervical ribs are scored by Huttenlocker et al. (2018:char. 228) as present and separate in *Morganucodon*, *Megazostrodon*, *Megaconus*, *Maiopatagium*, *Vilevolodon*, *Gobiconodon*, *Repenomamus*, *Yanoconodon*, *Jeholodens*, *Zhangheotherium* (scored as fused in O'Leary et al. [2013:char. 2785] but unfused in Bi et al. [2018:char. 342]), and *Maotherium*. In contrast, cervical ribs are scored as fused in *Xianshou* (Han et al. [2017] and Luo et al. [2017]; but '?' in Huttenlocker et al. [2018]), *Shenshou* (Han et al. [2017]; but '?' in Luo et al. [2017] and Huttenlocker et al. [2018]), *Arboroharamiya allinhopsoni* (Han et al., 2017), *Jeholbaatar* (Wang et al., 2019), *Rugosodon*, *Sinobaatar*, cimolodontans, *Vincelestes* (note that the rib of C7 seems incompletely fused in Rougier, 1993:fig. 67), and therians. However, Kielan-Jaworowska and Gambaryan (1994) reported the presence of cervical ribs in the multituberculates *Nemegtbaatar* and *Chulsanbaatar* but concluded that they were likely absent or fused to the transverse process in an unidentified taeniolabidoid. Bolortsetseg (2008) described fused cervical ribs for *Mangasbaatar* (= Udan multituberculate). Similar to *Nemegtbaatar* and *Repenomamus*, *Adalatherium* exhibits a robust and cylindrical dorsal root of the transverse process that extends ventrolaterally and posteriorly. In all three taxa, the dorsal root of C7 is larger and shorter than those of more anterior cervicals. A robust ventral root arising from the vertebral body, as seen in *Nemegtbaatar* and *Repenomamus*, was possibly also present in *Adalatherium* but is not preserved in UA 9030.

The laminae of the cervical vertebrae in *Adalatherium* are dorsoventrally tall and decrease in width posteriorly, similar to those of *Nemegtbaatar*, whereas the laminae appear more robust in *Repenomamus* (Hu, 2006:fig. 3.5). Similar to multituberculates and *Repenomamus*, the prezygapophyses are large and extend much farther anteriorly in *Adalatherium* than those of *Vincelestes* (Rougier, 1993:figs. 65–67).

Thoracolumbar Vertebrae—The thoracic and lumbar vertebrae are compared here as one unit because the regions are not clearly differentiated in all Mammaliaformes. Different studies have used different characteristics to identify thoracic versus lumbar vertebrae (e.g., orientation of zygapophyses, mobile ribs, shape and size of ribs, or shape and size of vertebral bodies), thus making it difficult to compare counts in these regions. Furthermore, several Mesozoic mammaliaforms are characterized as retaining mobile lumbar ribs, as is the case in *Megaconus*; the docodontans *Microdocodon*, *Agilodocodon*, and *Docofossor*; the eutriconodontans *Gobiconodon*, *Repenomamus*, *Yanoconodon*, *Liaoconodon*, and *Spinolestes* (but not in *Jeholodens* and *Chaoyangodens*); and the spalacotherioid *Akidolestes* (Jenkins and Schaff, 1988; Hu et al., 1997; Ji et al., 1999; Rougier et al., 2003; Hu, 2006; Meng et al., 2011; Chen and Luo, 2013; Zhou et al., 2013, 2019; Hou and Meng, 2014; Luo et al., 2015b; Martin et al., 2015; Meng et al., 2015; Chen et al., 2017). The lumbar ribs are fused to the vertebrae to form transverse processes in *Arboroharamiya*, *Qishou*, *Shenshou*, *Vilevolodon*, *Xianshou*, multituberculates, *Zhangheotherium*, *Maotherium*, and cladotherians (Huttenlocker et al., 2018:char. 234; Mao and Meng, 2019; Wang et al., 2019). Huttenlocker et al. (2018) also scored the lumbar ribs as fused in *Morganucodon*, *Megazostrodon*, and *Maiopatagium*. Jenkins and Parrington (1976) mention short transverse processes on the vertebrae of *Morganucodon* and *Megazostrodon* that they identify as possibly lumbar but also state that the area is poorly preserved. As such, the condition in morganucodontans is here regarded as unknown. Furthermore, Meng et al. (2017:S9) identify 15 dorsal vertebrae with mobile ribs in *Maiopatagium* but placed the thoracolumbar transition at dorsal vertebra 13 based on "vertebral body and neural arch features" and at dorsal vertebrae 12–13 based on zygapophyseal orientation (the diaphragmatic vertebra). Hence, at least the anterior two lumbar vertebrae would have had mobile ribs in *Maiopatagium*. Clearly, scoring the presence or absence of lumbar ribs is influenced by the criteria used to define the thoracolumbar transition. If thoracic vertebrae are identified based on the presence of mobile ribs, as is the case for many Mesozoic mammaliaforms (see below), then, by default, all dorsal vertebrae that have ribs are thoracic and all dorsal vertebrae without ribs are lumbar.

The number of thoracolumbar vertebrae varies greatly among Mesozoic mammaliaforms. However, no Mesozoic mammaliaform known to date reaches a count as high as in *Adalatherium*, which has at least 28 dorsal vertebrae, divided into 16 thoracics and 12 lumbars based on rib morphology. A high number of thoracolumbar vertebrae is otherwise known for eutriconodontans, with 26 vertebrae in *Repenomamus* (20 + 6, based on rib

morphology; Hu, 2006), 26 in *Liaoconodon* (18 + 8, criterion not specified; Meng et al., 2011), 25 in *Yanoconodon* (14 + 11, based on zygapophyses; Chen et al., 2017), 23 in *Spinolestes* (16 + 7, based on zygapophyses; Martin et al., 2015), and 22 in *Jeholodens* (15 + 7, criterion not specified; Ji et al., 1999:fig. 1). *Megaconus* likewise exhibits a high thoracolumbar count of 24 vertebrae (15 + 9, criterion not specified; Zhou et al., 2013), whereas the count is lower in the docodontan *Microdocodon* with 20 vertebrae (13 + 7, based on fossae around intervertebral foramina; Zhou et al., 2019); the shuotheriid *Pseudotribos* with 22 vertebrae (16 + 6, based on zygapophyses; Luo et al., 2007); the euharamiyidans *Vilevolodon* with 22 (15 + 7, based on rib morphology; Luo et al., 2017), *Maiopatagium* with 21 (13 + 8, based on neural arch/lamina; Meng et al., 2017), *Arboroharamiya* with 19 (13 + 6, based on rib morphology; Han et al., 2017), and *Qishou*, *Shenshou*, and *Xianshou* with 19 (13 + 6, based on zygapophyses and rib morphology; Bi et al., 2014; note that JZT-CK005 [*Qishou* sp.] possibly has as many as 14 ribs); the spalacotherioids *Maotherium* with 22 (15 + 7, criterion not specified but likely rib morphology; Rougier et al., 2003), *Akidolestes* with 19 (13 + 6, based on zygapophyseal orientation, vertebral body and rib shape; Chen and Luo, 2013), and *Zhangheotherium* with 18 (13 + 5, criterion not specified but likely rib morphology; Hu et al., 1997:fig. 1); and the eutherian *Eomaia* with 19 vertebrae (13 + 6, criterion not specified but likely rib morphology; Ji et al., 2002:fig. 1). The docodontan *Castorocauda* was originally estimated to have only 20 or 21 (14 + 6 [Ji et al., 2006:1126] or 7 [1126]), based on rib and vertebral body morphology) thoracolumbar vertebrae, but this was revised by Chen and Luo (2013) to 23 (17 + 6, criterion not specified). To date, *Rugosodon* provides the only exact count for multituberculates with 19 dorsal vertebrae (13 + 6, criterion not specified but likely rib morphology; Yuan et al., 2013:fig. 1). The number of dorsal vertebrae is uncertain in other well-preserved multituberculates such as *Kryptobaatar*, *Chulsanbaatar*, *Nemegtbaatar*, and *Ptilodus*. Kielan-Jaworowska and Gambaryan (1994) suggested a count of 19 dorsal vertebrae (12 + 7, criterion not specified but likely rib morphology) for *Chulsanbaatar*. At least six lumbar vertebrae are known for *Nemegtbaatar* (Kielan-Jaworowska and Gambaryan, 1994; note that the authors assigned these to L2–L7), seven for *Ptilodus* (Krause and Jenkins, 1983), and eight for *Kryptobaatar* (Bolortsetseg, 2008).

Sánchez-Villagra et al. (2007) reconstructed the ancestral thoracolumbar count for the Mammalia and Theria nodes as 19. Many extant mammals indeed have 19 thoracolumbar vertebrae, although Afrotheria (20–31), Xenarthra (14–29), and Perissodactyla (22–24) provide some of the most notable exceptions (e.g., Narita and Kuratani, 2005; Sánchez-Villagra et al., 2007). The thoracolumbar vertebral counts tend, on average, to be higher in extinct non-therian mammaliaforms (ranging from 18 to 28) than the reconstructed ancestral state of 19 based on extant mammals. In any case, *Adalatherium* is exceptional in not only having more thoracolumbar vertebrae than in any known Mesozoic mammaliaform but also in being equaled or exceeded among Recent mammals by only the hyracoids *Dendrohyrax* (three species; 29–31 in Sánchez-Villagra et al., 2007:appendix; 27–30 in Asher et al., 2011:appendix) and *Procavia* (one species; 27–32 in Asher et al., 2011:appendix) and the sloth *Choloepus* (two species; 26–28 in Hautier et al., 2010:data set S04; 24–27 in Asher et al., 2011:appendix). Furthermore, *Adalatherium* is unique in having a lumbar vertebral count of 12, which exceeds that of any other mammaliaform, extinct or extant (Schultz, 1961; Narita and Kuratani, 2005; Sánchez-Villagra et al., 2007; Hautier et al., 2010; Asher et al., 2011; Galis et al., 2014; Kawashima et al., 2018).

Adalatherium further differs from many Mesozoic mammaliaforms in that the thoracic and lumbar vertebrae are very distinct in morphology and size. Even though the changes occur gradually along the thoracolumbar vertebral column, the morphological disparity is impressive. The bodies of the posterior lumbar vertebrae are ~1.5 times wider transversely than posterior thoracic or anterior lumbar vertebrae (e.g., L1 = ~10.5 mm vs. L8 = 15.8 mm). The vertebral bodies barely change in size and are only slightly enlarged in the lumbar regions of the docodontan *Microdocodon* (Zhou et al., 2019); the eutriconodontans *Jeholodens*, *Yanoconodon* (posterior dorsal vertebrae are slightly larger), *Liaoconodon*, and *Repenomamus* (Ji et al., 1999; Hu, 2006; Meng et al., 2011; Chen et al., 2017); the euharamiyidans *Qishou*, *Shenshou*, and *Xianshou* (Bi et al., 2014; Mao and Meng, 2019); the spalacotherioid *Akidolestes* (Chen and Luo, 2013); the multituberculate *Rugosodon* (Yuan et al., 2013); and the basal therians *Eomaia*, *Ukhaatherium*, and *Asiatherium* (Szalay and Trofimov, 1996; Ji et al., 2002; Horovitz, 2003). Slightly more differentiated dorsal vertebrae can be seen in *Megaconus* (Zhou et al., 2013), and even more so in the multituberculates *Kryptobaatar* and *Ptilodus* (Krause and Jenkins, 1983; Bolortsetseg, 2008) and the spalacotherioids *Zhangheotherium* and *Maotherium* (Hu et al., 1997; Rougier et al., 2003).

The spinous processes are dorsoventrally tall for all dorsal vertebrae in *Adalatherium*, but they are more slender and pointed in anterior thoracic vertebrae and robust and dorsally expanded in lumbar vertebrae. Few Mesozoic mammaliaforms preserve the spinous processes as pristinely as in UA 9030. In particular, for the flattened specimens, the dorsal aspect of the vertebral column is often exposed only in certain sections, and even if the spinous processes are visible they might only be partially interpretable (e.g., exposed in direct dorsal view, which preserves the outline of the spinous process but not the height or orientation). Even when preserved in lateral view, favorable for documenting the height and orientation of the spinous process, they are oftentimes too damaged to evaluate details of morphology. This disparity in preservation limits meaningful comparison.

The spinous processes are well preserved in *Repenomamus*; they are similar to those of *Adalatherium* in being dorsoventrally tall and anteroposteriorly more slender in anterior thoracic vertebrae and robust in more posterior thoracolumbar vertebrae (Hu, 2006). A similar pattern can be seen in *Gobiconodon*; Jenkins and Schaff (1988) reconstructed the anterior spinous processes as slender and tall, whereas the posterior processes are anteroposteriorly long and robust. The thoracic spinous processes appear low and broad in the eutriconodontans *Yanoconodon* (Chen et al., 2017) and *Liaoconodon* (Meng et al., 2011); the multituberculates *Rugosodon* (Yuan et al., 2013) and *Ptilodus* (Krause and Jenkins, 1983); the spalacotherioids *Zhangheotherium* (in the last thoracic vertebra; Luo and Ji, 2005) and *Akidolestes* (Chen and Luo, 2013); and the therians *Eomaia* (Ji et al., 2002) and *Asiatherium* (Szalay and Trofimov, 1996). The spinous processes are dorsoventrally tall and slender in the anterior thoracic region of *Ukhaatherium* but are described as short and low in the posterior thoracic vertebrae (Horovitz, 2003).

The spinous processes of lumbar vertebrae are uniformly low and anteroposteriorly long in *Megaconus*; the docodontan *Microdocodon* (Zhou et al., 2019); the euharamiyidans *Qishou*, *Shenshou*, and *Maiopatagium*; the eutriconodontans *Jeholodens* (Ji et al., 1999:fig. 1) and *Yanoconodon* (Chen et al., 2017); and the therians *Eomaia* (Ji et al., 2002:fig. 1) and *Asiatherium* (Szalay and Trofimov, 1996), whereas a steady increase in size posteriorly can be observed in *Zhangheotherium* (Hu et al., 1997). The spinous processes are also dorsoventrally tall and slender in posterior lumbar vertebrae of *Ukhaatherium* (Horovitz, 2003) and *Zalambdalestes* (Novacek et al., 1997). In multituberculates, the spinous processes remain low and uniform in *Rugosodon* (Yuan et al., 2013) but become slender and more erect in more posterior vertebrae in *Ptilodus* (Krause and Jenkins, 1983). In *Kryptobaatar*, at least the last lumbar vertebra

bears a long spinous process; unfortunately, the anterior ones are broken (Bolortsetseg, 2008).

The orientation of the spinous processes remains approximately the same along the thoracolumbar column in the eutriconodontans *Gobiconodon* and *Repenomamus* (Jenkins and Schaff, 1988; Hu, 2006). In *Adalatherium*, as well as in most other Mesozoic mammaliaforms that preserve substantial parts of the thoracolumbar column, the orientation of the spinous processes changes from posteriorly inclined to anteriorly inclined at the anticlinal vertebra. In *Adalatherium*, the anticlinal vertebra is positioned at L4 (or dorsal vertebra 20 of 28), posterior to the thoracolumbar transition. The anticlinal vertebra is also more posteriorly positioned in *Megaconus* (dorsal vertebra 21 of 24; Zhou et al., 2013), *Microdocodon* (dorsal vertebra 18 of 20; Zhou et al., 2019), *Shenshou* (dorsal vertebra 17 of 19; Bi et al., 2014), *Maiopatagium* (dorsal vertebra 19 or 20 of 21; Meng et al., 2017), and *Pucadelphys* (dorsal vertebra 15 of 19; Marshall and Sigogneau-Russell, 1995). A lumbar anticlinal vertebra might also occur in *Zalambdalestes*; even though the number of lumbar vertebrae, and thus the exact position of the anticlinal vertebra, is uncertain, a clear change in orientation of the spinous processes can be seen in the lumbar region (Novacek et al., 1997:fig. 3). In contrast, Huttenlocker et al. (2018:char. 233) scored the anticlinal vertebra as more anteriorly positioned relative to the thoracolumbar transition in *Rugosodon* (dorsal vertebra 10 of 19; Yuan et al., 2013), *Sinobaatar*, cimolodontans, *Zhangheotherium*, *Eomaia* (scored as not presently available in O'Leary et al., 2013:char. 2838), *Sinodelphys*, and *Asiatherium*. Furthermore, Krause and Jenkins (1983) concluded that the anticlinal vertebra must have been anterior to the penultimate thoracic in the Paleocene multituberculate *Ptilodus*, which is consistent with the condition reconstructed for *Nemegtbaatar* (Kielan-Jaworowska and Gambaryan, 1994:fig. 45)

The transverse processes in the lumbar series are extremely long and anterolaterally directed in *Adalatherium*, and distinct from the short processes of anterior thoracics. Long and anterolaterally directed lumbar transverse processes are also known for several multituberculates, namely, *Kryptobaatar*, *Nemegtbaatar*, and *Ptilodus* (Krause and Jenkins, 1983; Kielan-Jaworowska and Gambaryan, 1994; Bolortsetseg, 2008). However, these differ from *Adalatherium* in that they are much broader at the base and gradually increase in length posteriorly. The transverse processes of *Adalatherium* are slender and already very long at L3; only the first two lumbar vertebrae bear shorter transverse processes. In contrast, in taxa that retain mobile lumbar ribs, the ribs generally decrease in size posteriorly and are often absent in the most posterior vertebrae. This is the case for the docodontans *Microdocodon* and *Docofossor*; the eutriconodontans *Yanoconodon*, *Liaoconodon*, and *Repenomamus*; and the spalacotherioid *Akidolestes* (Hu, 2006; Meng et al., 2011; Chen and Luo, 2013; Luo et al., 2015b; Chen et al., 2017; Zhou et al., 2019). The transverse processes are short and posteriorly directed in the eutriconodontan *Jeholodens* (Ji et al., 1999) and the euharamiyidans *Qishou*, *Shenshou*, and *Maiopatagium*, slightly longer and laterally directed in *Maotherium*, *Zhangheotherium*, and *Eomaia* (Ji et al., 2002; Rougier et al., 2003; Luo and Ji, 2005), and long and slender in *Zalambdalestes* (Novacek et al., 1997).

Caudal Vertebrae—Among Mesozoic mammaliaforms, complete tails are only preserved in the docodontan *Castorocauda* (Ji et al., 2006); the eutriconodontans *Jeholodens*, *Spinolestes*, and *Liaoconodon* (Ji et al., 1999; Meng et al., 2011; Martin et al., 2015); the euharamiyidans *Qishou* and *Arboroharamiya allinhopsoni* (Han et al., 2017; Mao and Meng, 2019); the spalacotherioid *Maotherium* (Rougier et al., 2003); and the eutherian *Eomaia* (Ji et al., 2002). Nearly complete tail skeletons are known for the docodontan *Microdocodon* (Zhou et al., 2019); the euharamiyidans *Arboroharamiya jenkinsi*, *Shenshou*, and *Xianshou songae* (Zheng et al., 2013; Bi et al., 2014); the eutriconodontan *Repenomamus* (Hu, 2006); the multituberculate *Ptilodus* (Krause and Jenkins, 1983; Jenkins and Krause, 1983); and the spalacotherioid *Akidolestes* (Li and Luo, 2006; Chen and Luo, 2013).

Adalatherium has at least 24 caudal vertebrae; the sacral region is poorly preserved, and it is uncertain whether any caudal vertebrae were present anterior to the preserved vertebrae in the caudal series. With at least 24 caudal vertebrae, *Adalatherium* is similar to other Mesozoic mammaliaforms that preserve complete tail skeletons, such as *Qishou* with 22 caudal vertebrae (Mao and Meng, 2019), *Arboroharamiya allinhopsoni* with at least 22 (Han et al., 2017), *Maotherium* with 22 (Rougier et al., 2003), *Spinolestes* with 22 (Martin et al., 2015), *Liaoconodon* with 23 (Meng et al., 2011), *Eomaia* with 25 (Ji et al., 2002), and *Castorocauda* with 25 (Ji et al., 2006). *Jeholodens*, with 30, has a considerably higher count of caudal vertebrae (Ji et al., 1999). Based on an almost complete tail skeleton in the multituberculate *Ptilodus*, Krause and Jenkins (1983) estimated the number of caudal vertebrae at 24–28. The tail is much shorter in extant monotremes, with 13–20 vertebrae.

Despite the similar caudal vertebral count, the tail in *Adalatherium* is unusual relative to those of other early mammaliaforms in being extremely short, only about half of the length of the thoracolumbar series and thus much shorter than its body length (from tip of snout to sacrum). In contrast, the tail is longer than the body in *Jeholodens*, *Qishou*, *Shenshou*, *Xianshou*, *Eomaia*, and likely *Ptilodus* (Krause and Jenkins, 1983; Jenkins and Krause, 1983; Ji et al., 1999, 2002; Bi et al., 2014). Even the partially preserved tails of *Microdocodon* and *Arboroharamiya* are longer than their bodies (Zheng et al., 2013; Zhou et al., 2019). The tail is similar in length to the body in *Castorocauda*, *Liaoconodon*, *Maotherium*, and probably *Repenomamus* and *Akidolestes*, despite the fact that the tails in the latter two taxa might be missing several distal caudal vertebrae (Rougier et al., 2003; Hu, 2006; Ji et al., 2006; Meng et al., 2011; Chen and Luo, 2013).

Adalatherium is unique among these early mammaliaforms in that almost all of the caudal vertebrae are transversely wider than anteroposteriorly long; only the three distal-most caudals differ. In many early mammaliaforms, the first few vertebrae are wider than long but the more posterior vertebrae are cylindrical, narrow, and elongate. Longer than wide bodies of the caudal vertebrae can be seen from Ca3 onward in *Qishou* (Bi et al., 2014: ED fig. 4; Mao and Meng, 2019:fig. 1); from Ca4 onward in *Arboroharamiya allinhopsoni* (Han et al., 2017:fig. 1); from Ca6 onward in *Arboroharamiya jenkinsi*, *Maotherium*, *Eomaia*, *Jeholodens*, and *Liaoconodon* (Ji et al., 1999:fig. 1, 2002:fig. 1; Rougier et al., 2003:pl. I; Meng et al., 2011:fig. 1; Zheng et al., 2013:fig. 1); and from Ca8 onward in *Repenomamus* and *Castorocauda* (Hu, 2006:fig. 3.16; Ji et al., 2006:fig. 1). In *Ptilodus* and *Akidolestes*, all preserved caudal vertebrae appear anteroposteriorly longer than they are transversely wide (Krause and Jenkins, 1983:figs. 1, 2; Chen and Luo, 2013:fig. 2).

In *Adalatherium*, the transverse processes are transversely wide and relatively slender in the anterior caudals (up to Ca9) and gradually decrease in transverse width but become anteroposteriorly longer until Ca12. A faint double transverse process is developed on Ca14 and more posterior vertebrae in *Adalatherium*. Prominent double transverse processes are also present in *Castorocauda* (Ji et al., 2006), but these are well defined and differ greatly from the condition in *Adalatherium*. Definitive transverse processes are present in the first nine caudal vertebrae of *Repenomamus* (Hu, 2006), the first six caudal vertebrae of *Arboroharamiya jenkinsi* (Zheng et al., 2013:fig. 1), the first five caudal vertebrae of *Ptilodus* (Krause and Jenkins, 1983), the first five caudal vertebrae of *Akidolestes* (Chen and Luo, 2013:fig. 2), likely present in the first three caudal vertebrae of *Maotherium* (Rougier et al., 2003:pl. I), and at least in some anterior caudal vertebrae in *Arboroharamiya*

allinhopsoni, *Maiopatagium*, and *Qishou*. Caudal transverse processes appear less developed in *Xianshou songae* (Bi et al., 2014: ED fig. 1) and are certainly absent posterior to Ca6 in *Eomaia* (Ji et al., 2002:fig. 1).

Sternal Apparatus and Interclavicle—The anterior-most sternal element (manubrium) and the interclavicle will be discussed together because identification of these elements is not always obvious in fossil taxa. Among extant mammals, only monotremes retain the interclavicle as a separate bone, whereas parts of the interclavicle fuse with the manubrium in therians (Klima 1973, 1987; Vickaryous and Hall, 2006). Klima (1973, 1987) detailed homologies of the interclavicle and manubrium, and his nomenclature and identification are followed here. We do, however, note that homologies might need to be revised in the future based on recent, still unpublished studies by Buchholtz et al. (2018). Understanding the developmental history of the interclavicle can aid in identification of homologous structures in the fossil record. In short, in monotremes, the interclavicle develops from an unpaired endochondral condensation (pars chondralis interclaviculae) and a paired intramembranous condensation (pars dermalis interclaviculae). The paired intramembranous condensations fuse early in embryogenesis to form a 'V'-shaped element dorsal to the clavicles. This element later fuses with the unpaired endochondral condensation to form the interclavicle. The manubrium of monotremes is formed solely by the fusion of the two sternal bands (Sternalleiste). Furthermore, monotremes retain ossification centers for the procoracoid and metacoracoid that contact the interclavicle and manubrium, respectively. Therians do not have a separate interclavicle in the adult. Whereas the intramembranous condensation of the interclavicle is completely lost in therians, the unpaired pars chondralis interclaviculae fuses with the sternal bands to form the manubrium. In addition, the medial aspects of the metacoracoid join the manubrium to form the lateral wings of the manubrium. The manubrium of therians is formed by the fusion of the pars chondralis interclaviculae, the two sternal bands, and the metacoracoids.

Regarding homologous elements, the unpaired endochondral condensation forms the posterior process of the interclavicle in monotremes, the anterior median process of the manubrium in marsupials, and the center of the manubrium in placentals (Klima 1973, 1987). The paired intramembranous condensations form the lateral processes of the interclavicle in monotremes but are lost in therians. The lateral wings of the therian manubrium are formed by the medial part of the metacoracoid, which is part of the coracoid in monotremes. Clearly identifying these homologous structures is particularly important for phylogenetic analyses. Several characters in recent Mesozoic mammal matrices treat aspects of the interclavicle and manubrium as the same. For example, Huttenlocker et al. (2018:char. 241; as well as previous and subsequent iterations of this matrix) homologize the cranial margin of the interclavicle and manubrium and score it either as (0) emarginated or flat or (1) with a median process. The cranial margin of the interclavicle and manubrium are, following Klima (1973, 1987), not homologous as they are formed from different condensations. Likewise, Huttenlocker et al. (2018:S63, char. 243) treat the contact between the clavicle and the interclavicle/manubrium as the same with the explicit assumption "that homologous elements of the interclavicle and the manubrium are fused to each other in therians." However, the part of the interclavicle that articulates with the clavicle in monotremes (paired intramembranous condensations) is lost in therians (Klima, 1987).

In addition to their utility in character scorings, topographic relationships of these homologous elements might aid in identification of the interclavicle and manubrium in fossil taxa. The interclavicle should be anterior to the manubrium, in contact with the clavicle and manubrium, and should seldom contact the first rib (if so, only in conjunction with the manubrium). The manubrium always contacts the first rib.

In order to assess the condition in *Adalatherium*, we attempt to provide a detailed account of the occurrence and morphology of interclavicles in Mesozoic cynodonts. An interclavicle has been unambiguously identified in non-mammaliaform cynodonts, *Morganucodon*, *Microdocodon*, several eutriconodontans, *Kryptobaatar*, and *Zhangheotherium* (Jenkins and Parrington, 1976; Hu et al., 1997; Hu, 2006; Sereno, 2006; Chen et al., 2017; Zhou et al., 2019). Interestingly, the interclavicle shows a fair degree of variability in non-mammaliaform cynodonts. It is cruciform, with short lateral processes, in *Thrinaxodon* (Jenkins, 1971), *Diademodon* (Gaetano et al., 2018), and *Pachygenelus* (Gow, 2001). In the derived traversodontid *Exaeretodon*, the interclavicle is short and triangular (Bonaparte, 1963). In the tritylodontid *Bienotheroides*, the interclavicle is identical to the mammaliaform 'T'-shaped pattern (Sun and Li, 1985), whereas the interclavicle is stout, with short lateral processes in *Oligokyphus* (Kühne, 1956). In *Morganucodon*, *Sinoconodon*, and monotremes, the interclavicle is large and 'T'-shaped, with long lateral processes that broadly contact the clavicle (Fig. 55D; Jenkins and Parrington, 1976; Luo et al., 2007; Luo, 2015). In *Microdocodon*, the interclavicle is preserved in situ and has a distinct posterior process overlapping the manubrium and slender lateral processes that contact the clavicles (Fig. 55B; Zhou et al., 2019:fig. S10).

Presence of the interclavicle is ambiguous in several Mesozoic mammaliaforms, where contact with the first rib, manubrium, and clavicle is only partially preserved or not at all. In *Megaconus*, a small rectangular element posterior to the glenohumeral joint has been identified as the interclavicle by Zhou et al. (2013:fig. 1), but it is not in contact with either the sternebrae or the clavicle. A possible first rib was found along the posterior edge of the element, but it does not clearly articulate with the fragment in question. An interclavicle has been identified in several euharamiyidans. Neither *Arboroharamiya* nor *Xianshou linglong* preserves the sternal region, and presence of the interclavicle is, as such, uncertain (Zheng et al., 2013:fig. 1; Bi et al., 2014:fig. 1b). In contrast, the pectoral region and rib cage are well preserved in *Xianshou songae* (Bi et al., 2014:figs. 1c, ED1); the manubrium, sternebrae, and most costal cartilages remain in articulation and in association with the clavicles. The manubrium of *Xianshou songae* is larger than the other sternebrae and has two rounded anterolateral wings. It is not clear whether an interclavicle is present anterior to the manubrium; some broken fragments can be seen just anterior and dorsal to the manubrium, but whether these belong to an interclavicle is questionable. Although an interclavicle is scored as present in *Xianshou songae* by Bi et al. (2014), Han et al. (2017), and Huttenlocker et al. (2018), we find the evidence based on BMNHC 3253 ambiguous.

The interclavicle is reconstructed deep to the clavicle and hidden from view by the clavicle in *Vilevolodon* (Meng et al., 2017:ED fig. 5c). Although it is possible that *Vilevolodon* had a separate 'V'-shaped interclavicle, it is not visible on the actual specimen (Meng et al., 2017:ED fig. 5d). In the holotype (BMNHC 2940) of *Maiopatagium furculiferum*, the interclavicle is reconstructed as a small, 'V'-shaped element (Meng et al., 2017:ED fig. 5a, b). Based on published images and observing the specimen itself, we believe that an interclavicle is not visible in BMNHC 2940 and, if present, must have been completely hidden from view by the clavicle. The CT images of a juvenile euharamiyidan (BMNHC 3258; Meng et al., 2017:ED fig. 6a), possibly closely related to *Vilevolodon* and *Maiopatagium*, do not show an interclavicle (Fig. 55C). Meng et al. (2017) argued that the interclavicle is not fully ossified in this young individual. The specimen clearly represents a young individual because the manubrium and at least one other sternebra are not fully fused (Meng et al., 2017:ED fig. 4). At least in monotremes, however, the interclavicle contains intramembranous condensations (pars

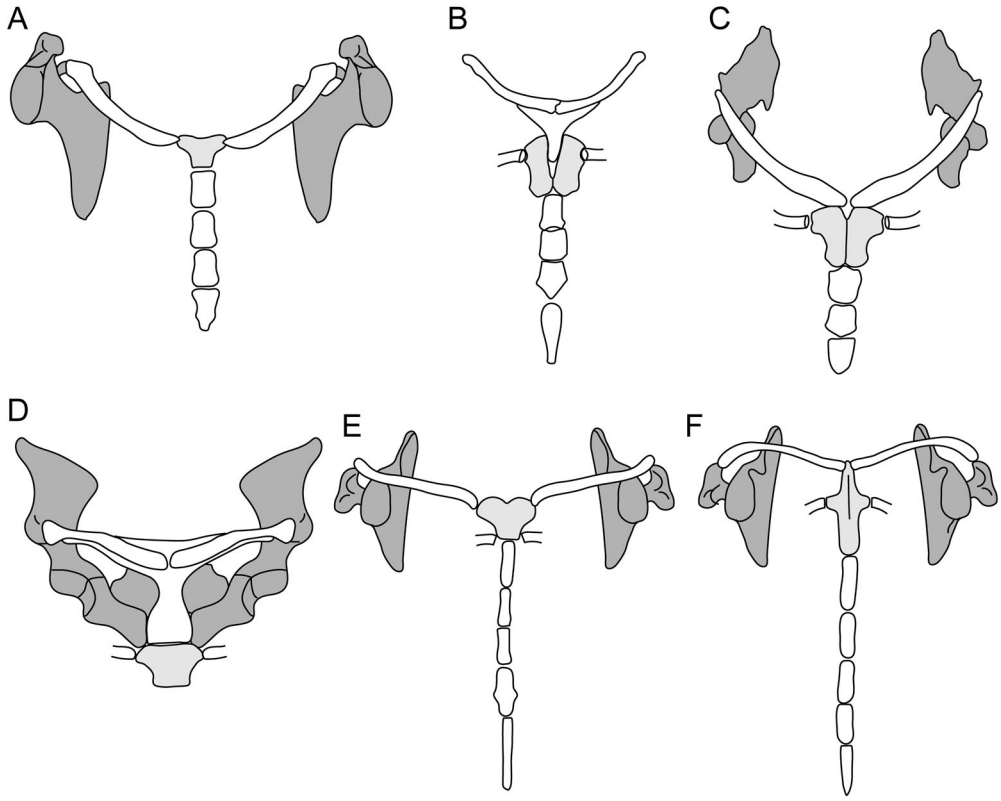

FIGURE 55. Comparison of pectoral girdle in mammaliaforms in ventral view. **A**, *Adalatherium*; **B**, the docodontan *Microdocodon* (after Zhou et al., 2019:fig. S10a); **C**, unnamed euharamiyidan (after Meng et al., 2015:ED fig. 6a); **D**, the monotreme *Tachyglossus* (after Luo, 2015:fig. 10.4); **E**, the placental *Mus* (after Luo, 2015:fig. 10.4); and **F**, the marsupial *Didelphis* (after Luo, 2015:fig. 10.4). Scapulocoracoid indicated in dark gray; manubrium in light gray; clavicle, interclavicle (**B** and **D** only), sternebrae, and ribs in white.

dermalis interclaviculae in Klima, 1973), which directly ossify during embryogenesis. Klima (1973) recorded ossification of the pars dermalis interclaviculae during the same stage as ossification of the clavicle in monotremes. In BMNHC 3258, the clavicles are fully ossified and the manubrium and all sternebrae are preserved. As such, one would expect to see at least the ossified lateral processes of the interclavicle if an interclavicle was present in this unnamed euharamiyidan.

The most compelling evidence for the presence of an interclavicle among euharamiyidans is in *Shenshou* and *Qishou*. Whereas the anterior aspect of the pectoral girdle is not exposed in paratype 1 of *Shenshou lui* (WGMV-001), the sternal region is preserved in association in the holotype (LDNHMF 2001), in which a small triangular fragment has been identified as the interclavicle (Bi et al., 2014:ED figs. 1, 7f). The element is positioned close to the manubrium but does not articulate with it or with the clavicles. Alternatively, this element could be part of the left coracoid. The left scapula is pushed underneath the sternum and clavicles, and the element in question is close to the expected position of a coracoid. Neither the contact relationship between the interclavicle and the manubrium nor that of the first rib and the manubrium is preserved in the holotype. In *Qishou* (JZTCK005), the manubrium, sternebrae, clavicles, most ribs, and the possible interclavicle are preserved in articulation. The manubrium is large and has two laterally projecting anterior wings. Anterior to the manubrium, the clavicles contact each other in the midline. Bi et al. (2014) identified 13 ribs in *Qishou*, with the anterior-most rib articulating between the manubrium and the next sternebra. There appears to be a more anterior and smaller rib close to the clavicle. This rib likely articulated with the anterolateral wing of the manubrium, but the articulation is not preserved. A somewhat triangular bony element is present anterior to the midline contact of the clavicles. The impression of the element is visible on side B, whereas the actual bone is preserved on side A (Bi et al., 2014:ED fig. 3b). The element is incomplete and broken along the lateral and posterior margins. The bony fragment differs in shape and size from the interclavicle identified in the holotype of *Shensou lui*; it is transversely wider and overall larger. The contact between the possible interclavicle and the clavicle appears much more extensive in *Qishou* than in *Shenshou*, covering about one-fourth to one-fifth of the clavicle. If correctly identified as interclavicles, then the two elements substantially differ in size and morphology in the two euharamiyidans.

In multituberculates, interclavicles are reported for *Kryptobaatar* (Sereno and McKenna, 1995; Sereno, 2006; Bolortsetseg, 2008), *Rugosodon* (Yuan et al., 2013), and *Sinobaatar* (Huttenlocker et al., 2018:char. 238). Sereno and McKenna (1995) were the first to note the presence of an interclavicle in multituberculates. Sereno (2006:figs. 10.3–10.5, 10.7) described the interclavicle as a small triangular element with two shallow fossae for articulation with the clavicles in *Kryptobaatar* (PSS-MAE 103) and reconstructed the clavicles as not touching in the midline and the interclavicle-clavicle joint as mobile. In contrast, Bolortsetseg (2008) suggested that the interclavicle is cruciform in *Kryptobaatar* (PSS-MAE 00-22) and that the lateral processes

form wing-like expansions. The ventral surface of the interclavicle is obscured from view in PSS-MAE 00-22, leaving the extent of the interclavicle-clavicle joint uncertain in this specimen (Bolortsetseg, 2008:figs. 23, 24). In *Rugosodon*, a triangular element has been identified as an interclavicle that is possibly fused with the manubrium (Yuan et al., 2013:fig. 1). The contact relationships with the clavicle, first rib, or other sternebrae are not preserved (indeed, sternebrae and costal cartilages are not preserved at all in *Rugosodon*). The interclavicle has been scored as present in *Sinobaatar* (Huttenlocker et al., 2018:char. 238), but the specimen described by Hu and Wang (2002) does not preserve the sternal region; we must therefore assume that undescribed specimens of *Sinobaatar* preserve the interclavicle.

Questionable records of interclavicles, scored as present by Huttenlocker et al. (2018:char. 238), have been reported for the stem therians *Akidolestes* and *Maotherium*. Chen and Luo (2013:fig. 5) described and imaged a large element next to the humeral head as the interclavicle of *Akidolestes*. The sternebrae are disarticulated in *Akidolestes*, and the relationships with the ribs or clavicles are not preserved. The sternal region of *Maotherium asiaticus* does not seem to be preserved, and an interclavicle is not labeled in Ji et al. (2009:fig. 1). The interclavicle is not mentioned in the description of *Maotherium sinensis*, and it is not apparent in the illustrations (Rougier et al., 2003:pl. 1, 2). Based on the published specimen (NGMC-97-4-15), we interpret the condition in *Maotherium* as unknown, although it is plausible that the scoring in Huttenlocker et al. (2018) is based on additional unpublished specimens that preserve an interclavicle. Given the fragmentary record, it is uncertain how common loss of the interclavicle (and fusion of the endochondral part of the interclavicle with the manubrium) was among early mammaliaforms. Whether the interclavicle was present in *Adalatherium* and just not preserved in UA 9030 or indeed absent in life cannot be fully resolved. Limited in our knowledge to only UA 9030, we tentatively conclude that the interclavicle is absent in *Adalatherium* (Fig. 55A).

The shape of the manubrium varies among Mesozoic mammaliaforms. It is large, with broad anterolateral wings and a distinct anterior notch in *Maiopatagium*, *Qishou*, *Shenshou*, *Vilevolodon*, and *Xianshou* (Bi et al., 2014:ED figs. 1, 3, 7; Meng et al., 2017: ED figs. 4, 5); quadrangular in outline with gently expanded anterolateral wings in *Adalatherium* and *Vincelestes* (Rougier, 1993); long and transversely constricted at mid-length in the eutriconodontan *Repenomamus* (Hu, 2006:fig. 3.17); cruciform to pentagonal in *Kryptobaatar*, *Zhangheotherium*, and some marsupials (Klima, 1987; Hu et al., 1997:fig. 1; Sereno, 2006: figs. 10.3–10.5); and small and roughly heart-shaped in *Eomaia* (Ji et al., 2002:fig. 1).

The remaining sternebrae in *Adalatherium* are unfused, as is the case in most Mesozoic mammaliaforms, including the docodontans *Agilodocodon* (Meng et al., 2015) and *Microdocodon* (Zhou et al., 2019); the eutriconodontans *Jeholodens* (Ji et al., 1999), *Repenomamus* (Hu, 2006), *Spinolestes* (Martin et al., 2015), and *Yanoconodon* (Chen et al., 2017); the shuotheriid *Pseudotribos* (Luo et al., 2007); an unidentified taeniolabidoid multituberculate (Kielan-Jaworowska, 1989; Kielan-Jaworowska and Gambaryan, 1994); the euharamiyidans *Maiopatagium*, *Qishou*, *Shenshou*, *Vilevolodon*, and *Xianshou* (Bi et al., 2014; Luo et al., 2017; Meng et al., 2017; Mao and Meng, 2019); the spalacotherioids *Maotherium* (Rougier et al., 2003) and *Akidolestes* (Chen and Luo, 2013); and the therians *Eomaia* (Ji et al., 2002), *Ambolestes* (Bi et al., 2018), and *Sinodelphys* (Luo et al., 2003; Bi et al., 2018). Fusion of the postmanubrial elements is a derived feature in mammals and, among extinct non-therian mammals, only occurs in *Zhangheotherium* (Hu et al., 1997).

Pectoral Girdle

The evolutionary history of the mammalian pectoral girdle is reasonably well documented (e.g., Jenkins and Weijs, 1979; Luo, 2015). The pectoral girdle of *Adalatherium* reflects a mosaic of plesiomorphic and derived features. The scapular blade is surprisingly therian-like, but the large coracoid is reminiscent of a more plesiomorphic condition in mammaliaforms.

The scapulocoracoid of *Adalatherium* is derived in several respects: (1) presence of a large supraspinous fossa, (2) gently convex infraspinous fossa, (3) absence of separate procoracoid, and (4) ventrally facing glenoid fossa. In *Adalatherium*, the scapular spine divides the lateral aspect of the scapular blade into almost equally sized supraspinous and infraspinous fossae. In this regard, *Adalatherium* is similar to cladotherians (Krebs, 1991; Luo, 2015) and spalacotherioids (Hu et al., 1997; Ji et al., 2009; Chen and Luo, 2013), but this condition is also present in eutriconodontans (Jenkins and Schaff, 1988; Ji et al., 1999; Hu, 2006; Meng et al., 2011; Hou and Meng, 2014; Chen et al., 2017). In contrast, the scapular spine is positioned along the anterior border of the scapular blade, the supraspinous fossa is either absent or incipient, and the infraspinous fossa takes up most of the lateral aspect of the scapular blade in non-mammaliaform cynodonts (e.g., Bonaparte, 1963; Jenkins, 1971; Jenkins and Weijs, 1979; Kammerer, 2008; Pavanatto et al., 2016; Gaetano et al., 2017, 2018; Butler et al., 2019; Guignard et al., 2019); the basal mammaliaforms *Morganucodon* and *Megazostrodon* (Jenkins and Parrington, 1976), *Haldanodon* (Martin, 2005), *Microdocodon* (Zhou et al., 2019), *Agilodocodon* (Meng et al., 2015), and *Megaconus* (Zhou et al., 2013); the multituberculates *Ectypodus*, *Kryptobaatar*, *Mangasbaatar*, ?*Mesodma*, *Nemegtbaatar*, *Rugosodon*, and an unidentified taeniolabidoid (Krause and Jenkins, 1983; Kielan-Jaworowska and Gambaryan, 1994; Sereno and McKenna, 1995; Bolortsetseg, 2008; Yuan et al., 2013); the euharamiyidans *Arboroharamiya*, *Maiopatagium*, and *Shenshou* (Bi et al., 2014; Han et al., 2017; Meng et al., 2017); and extant monotremes (Gambaryan et al., 2015; Luo, 2015).

Despite the fact that the posterior margin of the scapular blade is only partly preserved in UA 9030, the infraspinous fossa is gently concave and is neither trough-shaped nor bounded by a posterior spine. In contrast, a trough-shaped infraspinous fossa is common in morganucodontans (Jenkins and Parrington, 1976), *Haldanodon* (Martin, 2005), *Microdocodon* (Zhou et al., 2019), *Agilodocodon* (Meng et al., 2015), *Repenomamus* (Hu, 2006), *Chaoyangodens* (Hou and Meng, 2014), *Zhangheotherium* (Hu et al., 1997), *Akidolestes* (Chen and Luo, 2013), *Shenshou* (Bi et al., 2014), *Maiopatagium* (Meng et al., 2017), and multituberculates (Krause and Jenkins, 1983; Kielan-Jaworowska and Gambaryan, 1994; Sereno, 2006; Bolortsetseg, 2008; Wang et al., 2019). The posterodorsal aspect of the scapular blade is relatively featureless in *Adalatherium*; only a slightly raised tuberosity is present along the posterodorsal margin that probably served as the attachment site for the teres major muscle. In several Mesozoic mammaliaforms, the attachment site for the teres major muscle is greatly enlarged, either as an expansion of the caudal angle of the scapular blade, as in *Repenomamus* (Hu, 2006) and *Akidolestes* (Chen and Luo, 2013), or as a sizable fossa posterior to the infraspinous fossa, as in *Haldanodon* (Martin, 2005), *Fruitafossor* (Luo and Wible, 2005), and monotremes (Gambaryan et al., 2015). In *Jeholodens* (Ji et al., 1999), a small crest within the infraspinous fossa possibly separates the former from the teres major fossa. It is uncertain whether a prominent attachment site is present in early-branching mammaliaforms. The posterodorsal margin is

not preserved in either *Morganucodon* or *Megazostrodon* (Jenkins and Parrington, 1976), and a distinct teres major fossa is lacking in *Shenshou* (Bi et al., 2014) and multituberculates (Sereno, 2006; Yuan et al., 2013). The greatly enlarged fossa in *Haldanodon*, *Fruitafossor*, and monotremes is likely a derived adaptation to powerful forelimb motion during swimming and digging. The expansion of the caudal angle of the scapular blade is not consistently present in eutriconodontans or spalacotherioids, being only slightly expanded in *Yanoconodon*, *Liaoconodon*, and *Zhangheotherium* (contrary to scoring in Huttenlocker et al., 2018:char. 251).

The acromion itself is not preserved in UA 9030, but the large articular facet on the clavicle suggests that a sizable acromion was present. A prominent and ventrally projecting acromion is preserved in the multituberculates *Chulsanbaatar* (Kielan-Jaworowska and Gambaryan, 1994), *Jeholbaatar* (Wang et al., 2019), *Kryptobaatar* (Sereno, 2006), *Mangasbaatar* (Bolorsetseg, 2008), and *Nemegtbaatar* (Kielan-Jaworowska and Gambaryan, 1994); the eutriconodontans *Jeholodens* (Ji et al., 1999), *Repenomamus* (Hu, 2006), *Yanoconodon* (Chen et al., 2017), and *Liaoconodon* (Meng et al., 2011); the spalacotherioids *Akidolestes* (Chen and Luo, 2013) and *Maotherium* (Ji et al., 2009); as well as in several therians (O'Leary et al., 2013:char. 2964). In contrast, the acromion is scored as short and level with or dorsal to the glenoid in the morganucodontans *Morganucodon* and *Megazostrodon*; the docodontans *Haldanodon* and *Agilodocodon*; and the euharamiyidans *Shenshou*, *Maiopatagium*, and *Vilevolodon* by Huttenlocker et al. (2018:char. 250).

Adalatherium is also derived in possessing a ventrally facing glenoid fossa. In *Morganucodon*, *Megazostrodon* (Jenkins and Parrington, 1976), *Haldanodon* (Martin, 2005), *Microdocodon* (Zhou et al., 2019), and *Fruitafossor* (Luo and Wible, 2005), the glenoid faces laterally and is aligned with the long axis of the blade, indicating a relatively sprawling posture. In many Mesozoic mammals, the glenoid is positioned oblique to the long axis of the scapular blade and faces more posteriorly. This intermediate condition can be seen in the eutriconodontans *Gobiconodon* (Jenkins and Schaff, 1988), *Jeholodens* (Ji et al., 1999), *Repenomamus* (Hu, 2006), and *Liaoconodon* (Meng et al., 2011); the euharamiyidans *Arboroharamiya* (Han et al., 2017) and *Shenshou* (Bi et al., 2014); and the spalacotherioids *Akidolestes* (Chen and Luo, 2013) and *Maotherium* (Ji et al., 2009). Cimolodontan multituberculates have long been known to possess a ventrally facing glenoid perpendicular to the long axis of the scapular blade (Krause and Jenkins, 1983; Kielan-Jaworowska and Gambaryan, 1994; Sereno and McKenna, 1995) but are scored in Huttenlocker et al. (2018) as obliquely oriented, which appears to be an error. The relatively complete scapulocoracoids of *Ectypodus* (Bolortsetseg, 2008:fig. 8) and *Kryptobaatar* (Sereno, 2006:figs. 10.3, 10.7) confirm the perpendicular orientation. The euharamiyidans *Maiopatagium*, *Shenshou*, *Vilevolodon*, and *Xianshou* are scored as aligned with the long axis of the scapular blade by Huttenlocker et al. (2018:char. 258), but as obliquely oriented by Han et al. (2017: char. 247; note that *Maiopatagium* and *Vilevolodon* are not included in their analysis). Due to the flattened preservation of the specimens, the orientation of the glenoid fossa is difficult to characterize in *Maiopatagium*, *Vilevolodon*, and *Xianshou*, but it appears to be oblique in *Shenshou* (Han et al., 2017:S87).

In contrast to these derived scapulocoracoid traits, *Adalatherium* possesses a coracoid that is very large and forms half of the glenohumeral joint. The suture between the coracoid and the scapula is still unfused in UA 9030. In extant therians and monotremes, the suture between the coracoid and the scapula fuses during development (Klima, 1973, 1987). In various extinct mammaliaforms, a suture is still visible in specimens of *Morganucodon*, *Megazostrodon*, *Haldanodon*, *Microdocodon*, *Fruitafossor*, *Repenomamus*, *Maiopatagium*, *Shenshou*, *Vilevolodon*, *Xianshou*, and *Nemegtbaatar* (Jenkins and Parrington, 1976; Kielan-Jaworowska and Gambaryan, 1994; Luo and Wible, 2005; Martin, 2005; Hu, 2006; Bi et al., 2014; Luo et al., 2017; Meng et al., 2017; Zhou et al., 2019), whereas it is indiscernible in most multituberculates (Krause and Jenkins, 1983; Kielan-Jaworowska and Gambaryan, 1994; Bolortsetseg, 2008; Wang et al., 2019). Specimen UA 9030 represents a subadult individual; it is therefore entirely possible that the suture would have fused later in life in *Adalatherium*. The shape of the coracoid-scapula suture is quite unusual in *Adalatherium* (Fig. 14). The coracoid forms the anterior half of the glenoid fossa, but it tapers posterodorsally. At mid-length of the glenoid fossa, the coracoid only forms the medial margin and the suture extends roughly in parallel to the long axis of the glenoid fossa. This is in stark contrast to the morphology in other early mammaliaforms. In *Morganucodon*, *Megazostrodon* (Jenkins and Parrington, 1976), *Haldanodon* (Martin, 2005), *Microdocodon* (Zhou et al., 2019), *Fruitafossor* (Luo and Wible, 2005), and *Repenomamus* (Hu, 2006), the suture between the coracoid and the scapula crosses the glenoid fossa at mid-length, roughly perpendicular to the long axis of the fossa. The coracoid and scapula contribute equally to the glenoid fossa in length and width. In these taxa, the coracoid also extends beyond the glenoid fossa, forming a pointed muscular process (Jenkins and Parrington, 1976; Luo and Wible, 2005; Martin, 2005; Hu, 2006), whereas the glenoid fossa extends most of the length of the coracoid in *Adalatherium*. This is also the condition in various multituberculates (e.g., ?*Mesodma*: Krause and Jenkins, 1983:fig. 10; *Kryptobaatar*: Kielan-Jaworowska and Gambaryan, 1994:fig. 5b, c; *Nemegtbaatar*: Kielan-Jaworowska and Gambaryan, 1994:fig. 13g–j; *Ectypodus*: Bolortsetseg, 2008:fig. 8), all of which show an articular surface to the tip of the coracoid process. *Mangasbaatar* is unusual in possessing a greater mediolateral flare of the distal end of the coracoid process, but it still retains an articular surface that extends to the tip (Bolortsetseg, 2008:fig. 41). Luo (2015:fig. 10.3) depicted the glenoid fossa as more restricted to the proximal aspect of the coracoid process in multituberculates, similar to the condition seen in *Morganucodon*, *Haldanodon*, *Fruitafossor*, and *Repenomamus*, but this is incorrect.

The coracoid completely fuses with the scapula and does not contribute to the glenohumeral articulation in therians (Luo, 2015). A separate procoracoid is absent in *Adalatherium*, as is the case in most mammaliaforms. A separate procoracoid is only present in monotremes, *Megazostrodon*, *Morganucodon*, and possibly some euharamiyidans (Jenkins and Parrington, 1976; Luo et al., 2017; Meng et al., 2017). Among mammaliaforms, a separate procoracoid has been documented in an unnamed juvenile euharamiyidan (BMNHC 3258; Meng et al., 2017:ED fig. 4), but whether the procoracoid would have been fused to the scapula in the adult is uncertain. Meng et al. (2017: ED fig. 5) also identified a procoracoid in *Maiopatagium* and *Vilevolodon*, but the elements in question appear fragmentary and it is uncertain whether they are broken or unfused. A separate procoracoid is also scored as present in *Shenshou* by Huttenlocker et al. (2018:char. 252) but as fused to the scapula in Han et al. (2017:char. 241).

Humerus

Proximal End—The head of the humerus is spherical and strongly inflected in *Adalatherium* (Fig. 56), as is the case in multituberculates (Krause and Jenkins, 1983; Kielan-Jaworowska and Qi, 1990; Kielan-Jaworowska and Gambaryan, 1994; Sereno and McKenna, 1995; Sereno, 2006; Bolortsetseg, 2008; Yuan et al., 2013; Wang et al., 2019), *Zhangheotherium* (Hu et al.,

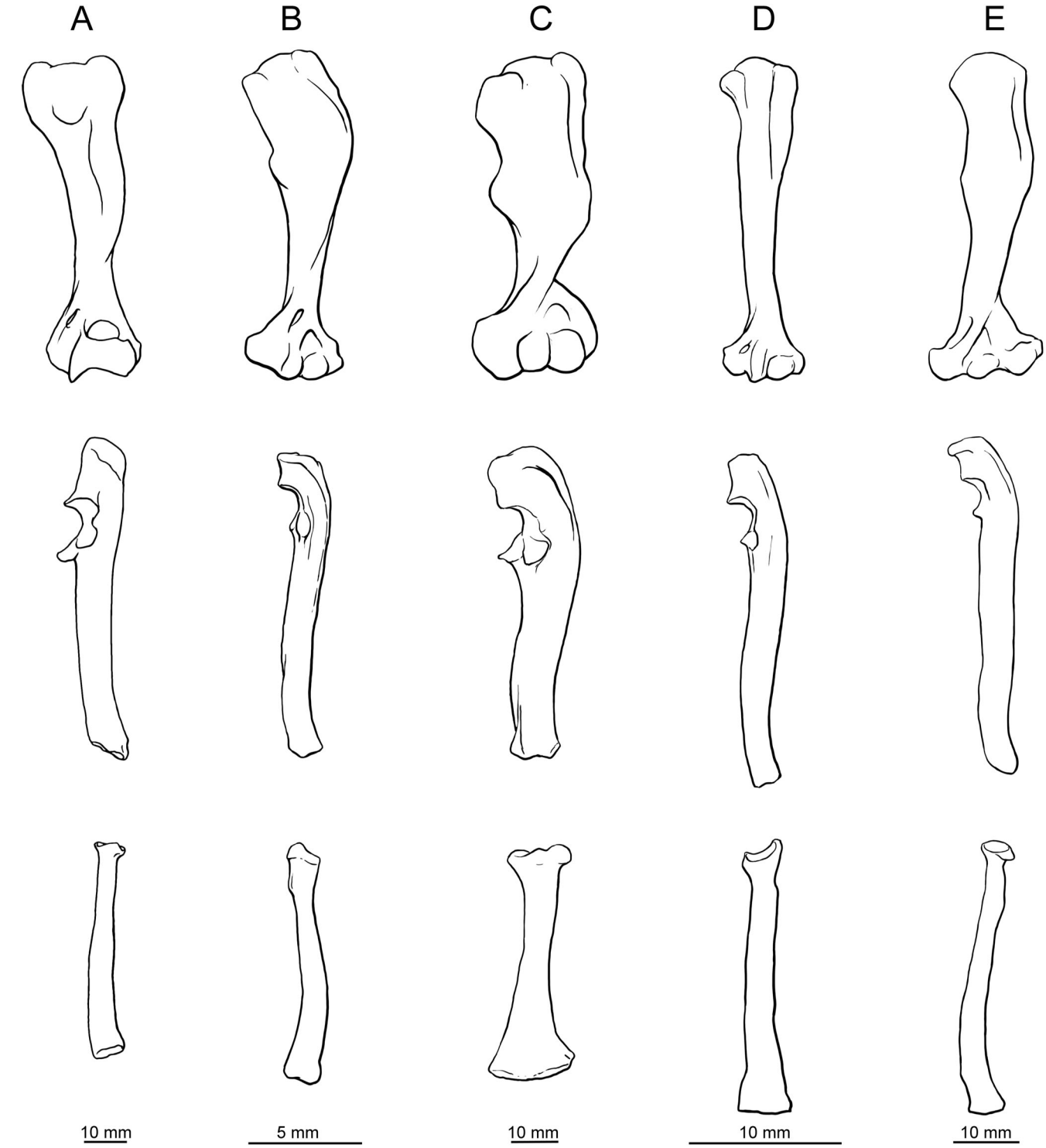

FIGURE 56. Comparison of left humerus (top row), ulna (middle row), and radius (bottom row) in five Mesozoic mammaliaforms. Humeri in anterior view; ulnae and radii in lateral view. All humeri at same length; ulnae and radii at lengths relative to humeri. **A**, *Adalatherium*; **B**, the morganucodontan *Morganucodon* (after Jenkins and Parrington, 1976:figs. 5, 10); **C**, the eutriconodontan *Repenomamus* (after Hu, 2006:figs. 3-22, 3-23); **D**, the multituberculates *Nemegtbaatar* (humerus) and *Kryptobaatar* (radius and ulna) (after Bolortsertseg, 2008:fig. 32); and **E**, the stem therian *Vincelestes* (after Rougier, 1993:figs. 84, 87, 88).

1997), *Maotherium* (Ji et al., 2009), and cladotherians (Huttenlocker et al., 2018:char. 262). A spherical head is likely also present in *Akidolestes*, *Eomaia*, and *Juramaia* (Ji et al., 2002; Luo et al., 2011; Chen and Luo, 2013). The humeral head is partly, but not fully, exposed in specimens of these taxa. In contrast, morganucodontans (Jenkins and Parrington, 1976), docodontans (Martin, 2005; Zhou et al., 2019), eutriconodontans (Jenkins and Schaff, 1988; Ji et al., 1999; Hu, 2006; Chen et al.,

2017), and monotremes possess a spindle-shaped humeral head. The humeral head appears to be relatively wide mediolaterally in the euharamiyidans *Maiopatagium*, *Qishou*, *Shenshou*, *Vilevolodon*, and *Xianshou* (Bi et al., 2014; Meng et al., 2017; Mao and Meng, 2019) and is scored as hemispherical in Huttenlocker et al. (2018:char. 262); unfortunately, however, the heads are only partially exposed or incompletely preserved and do not allow a confident determination of shape. This has also been noted by Han et al. (2017), who scored the humeral heads of *Arboroharamiya allinhopsoni*, *Shenshou*, and both species of *Xianshou* as both hemispherical and spherical.

The greater tubercle is distinct from the humeral head and separated by a small notch in *Adalatherium*. This contrasts with the condition in morganucodontans (Jenkins and Parrington, 1976) and docodontans (Martin, 2005; Zhou et al., 2019), in which the greater tubercle is confluent with the head. In multituberculates, the greater tubercle is distinct (Krause and Jenkins, 1983; Kielan-Jaworowska and Qi, 1990:fig. 2; Kielan-Jaworowska and Gambaryan, 1994:figs. 13, 22, 23; Wang et al., 2019), but not as separated from the head as in *Adalatherium*. The greater and lesser tubercles are equal in height in *Adalatherium* and do not protrude much farther proximally than the head of the humerus. This is the case for most Mesozoic mammaliaforms. The proximal aspect of the intertubercular groove, between the greater and lesser tubercles, bears a prominent and 'U'-shaped intertubercular fossa in *Adalatherium*. The intertubercular fossa is also present, albeit with a more circular distal edge, in *Morganucodon*. A distinct intertubercular fossa is absent in humeri of *Haldanodon* (Martin, 2005:fig. 8), *Microdocodon* (Zhou et al., 2019:fig. S10c), and *Repenomamus* (Hu, 2006:fig. 3.22) and appears also to be lacking in *Gobiconodon* (Jenkins and Schaff, 1988:fig. 14). The tubercles are not preserved in *Gobiconodon*, but the proximal part of the shaft does not seem to exhibit a deep fossa. The proximal aspect of the humerus is not well enough preserved in *Yanoconodon*, *Arboroharamiya*, *Maiopatagium*, *Qishou*, *Shenshou*, *Vilevolodon*, *Xianshou*, *Akidolestes*, or *Dryolestes* to unambiguously determine whether such a fossa was present. The evidence from multituberculates is also ambiguous. The fossa is clearly absent in *Nemegtbaatar* (Kielan-Jaworowska and Gambaryan, 1994:fig. 13) and *Kryptobaatar* (Sereno, 2006:fig. 10.7) but seems to be present in *Chulsanbaatar* (Kielan-Jaworowska and Gambaryan, 1994:fig. 23) and *Lambdopsalis* (Kielan-Jaworowska and Qi, 1990:fig. 2; Gambaryan and Kielan-Jaworowska, 1997:fig. 9). It is unclear whether an intertubercular fossa was present in *Ptilodus* (Krause and Jenkins, 1983:fig. 11). The intertubercular groove is shallow in *Adalatherium*, as is the case in most Mesozoic mammaliaforms. In contrast, the intertubercular groove is scored as narrow and deep in *Zhangheotherium*, *Maotherium*, *Akidolestes*, and several therians by Huttenlocker et al. (2018:char. 263).

Humeral Shaft—The greater tubercle gives rise to a well-developed deltopectoral crest that extends about half the length of the humeral shaft in *Adalatherium*. A prominent deltopectoral crest is also present in morganucodontans (Jenkins and Parrington, 1976), eutriconodontans (Jenkins and Schaff, 1988; Hu, 2006; Chen et al., 2017), some docodontans (Martin, 2005; Meng et al., 2015), *Zhangheotherium* (Hu et al., 1997), and monotremes. The deltopectoral crest does not extend as far distally in the multituberculates *Rugosodon*, *Sinobaatar*, *Nemegtbaatar*, *Ptilodus*, *Kryptobaatar*, *Jeholbaatar*, and *Mangasbaatar* (Krause and Jenkins, 1983; Kielan-Jaworowska and Gambaryan, 1994; Sereno and McKenna, 1995; Sereno, 2006; Bolortsetseg, 2008; Huttenlocker et al., 2018; Wang et al., 2019) as in other early mammals. *Lambdopsalis* is exceptional in having a more prominent deltopectoral crest (Kielan-Jaworowska and Qi, 1990). The deltopectoral crest in *Arboroharamiya*, *Maiopatagium*, *Shenshou*, *Vilevolodon*, and *Xianshou* extends distally about one-third of the humeral shaft (Huttenlocker et al., 2018:char. 266) and is therefore much shorter than in *Adalatherium*.

The tuberosity for the teres major muscle is indistinct and cannot be identified in *Adalatherium*. Mesozoic mammaliaforms show a variety of shapes for the teres major tuberosity; it is a small but distinct crest in morganucodontans (Jenkins and Parrington, 1976) but a large and prominent tuberosity in the docodontan *Haldanodon* (Martin, 2005), the eutriconodontans *Repenomamus* and *Gobiconodon* (Jenkins and Schaff, 1988; Hu, 2006), and the spalacotherioid *Akidolestes* (Chen and Luo, 2013). It is present as a gentle elevation in the eutriconodontan *Yanoconodon* (Chen et al., 2017), the stem therian *Vincelestes* (Rougier, 1993), and multituberculates (in particular in *Lambdopsalis*; Kielan-Jaworowska and Gambaryan, 1994). The teres major tuberosity is scored as absent in the euharamiyidans *Maiopatagium*, *Shenshou*, *Vilevolodon*, and *Xianshou*; the spalacotherioid *Zhangheotherium*; and many cladotherians (Huttenlocker et al., 2018:char. 267).

The lateral supracondylar crest (= supinator crest) is sharp but not expanded in *Adalatherium*. A well-developed and expanded lateral supracondylar crest can be seen in morganucodontans, *Haldanodon*, and *Repenomamus* (Jenkins and Parrington, 1976; Martin, 2005; Hu, 2006). It is slightly less expanded but still prominent in *Gobiconodon* (Jenkins and Schaff, 1988), *Agilodocodon* (Meng et al., 2015), and *Liaoconodon* (Meng et al., 2011). The size of the lateral supracondylar crest is more similar to that of *Adalatherium* in *Yanoconodon* (Chen et al., 2017), *Jeholodens* (Ji et al., 1999), *Maiopatagium* (Meng et al., 2017), *Qishou* (Mao and Meng, 2019), *Shenshou* (Bi et al., 2014), *Akidolestes* (Chen and Luo, 2013), *Zhangheotherium* (Hu et al., 1997), *Dryolestes* (Martin, 2013), and *Henkelotherium* (Krebs, 1991; Jäger et al., 2019). In most multituberculates, the lateral supracondylar crest forms a gently raised crest, with the exception of *Lambdopsalis*, where the crest is more rounded and prominent (Kielan-Jaworowska and Gambaryan, 1994).

The degree of humeral torsion has been reported and scored for many Mesozoic mammals (Luo et al., 2015a:char. 254). Although approximate values can be obtained from compressed specimens, measuring the degree of torsion following Kielan-Jaworowska and Gambaryan (1994) can only be done on three-dimensionally preserved specimens in which the proximal articulation is exposed and well preserved. Relatively complete humeri are known for *Morganucodon*, *Megazostrodon*, *Haldanodon*, several multituberculates, *Repenomamus*, *Gobiconodon*, *Priacodon*, *Dryolestes*, *Henkelotherium*, *Vincelestes*, and several extinct therians (Jenkins and Parrington, 1976; Krause and Jenkins, 1983; Jenkins and Schaff, 1988; Kielan-Jaworowska and Qi, 1990; Krebs, 1991; Rougier, 1993; Kielan-Jaworowska and Gambaryan, 1994; Sereno and McKenna, 1995; Engelmann and Callison, 1998; Kielan-Jaworowska, 1998; Vázquez-Molinero et al., 2001; Martin, 2005, 2013; Hu, 2006; Sereno, 2006; Bolortsetseg, 2008; Chester et al., 2010).

Jenkins and Parrington (1976) list the humeral torsion in morganucodontans as 50°. This represents the angle between an imaginary plane through the tubercles and the epicondyles, which is similar to but not exactly the same as the measurement used by Kielan-Jaworowska and Gambaryan (1994). Martin (2005) reported an extreme degree of humeral torsion in the fossorial *Haldanodon* (60°). The degree of torsion varies between 15° and 38° in multituberculates (Kielan-Jaworowska and Qi, 1990; Kielan-Jaworowska and Gambaryan, 1994; Sereno and McKenna, 1995; Kielan-Jaworowska, 1998; Bolortsetseg, 2008). Some of the variation might be attributable to slightly different methods in measuring the angle but, overall, multituberculates seem to vary considerably. The humerus is moderately twisted in the eutriconodontan *Repenomamus* (25°; Hu, 2006), and slightly more strongly in *Gobiconodon* (33°; Jenkins and Schaff, 1988). In cladotherians, the degree of torsion is considerably lower (e.g., *Dryolestes*: 15–20°; Martin, 2013). The degree of torsion in *Adalatherium* (25°) is comparable to that in *Repenomamus* and slightly higher than in cladotherians.

Distal End—The distal end of the humerus is comparatively slender in *Adalatherium*. The entepicondyle is pointed, anteroposteriorly flat, projects medially, and is larger than the ectepicondyle. Both the ectepicondyle and entepicondyle are well developed in morganucodontans (Jenkins and Parrington, 1976), *Haldanodon* (Martin, 2005), *Microdocodon* (Zhou et al., 2019), *Repenomamus* (Hu, 2006), *Gobiconodon* (Jenkins and Schaff, 1988), *Qishou* (Mao and Meng, 2019), *Shenshou* (Bi et al., 2014), and *Xianshou* (Bi et al., 2014). In these taxa, the entepicondyle expands distally to the level of the distal end of the ulnar condyle, whereas in *Adalatherium* it ends proximal to the distal margin of the trochlea. The entepicondyle is well developed and bulbous in multituberculates (Krause and Jenkins, 1983; Kielan-Jaworowska and Qi, 1990; Kielan-Jaworowska and Gambaryan, 1994; Sereno and McKenna, 1995; Hu and Wang, 2002; Sereno, 2006; Bolortsetseg, 2008; Hurum and Kielan-Jaworowska, 2008; Wang et al., 2019). The ectepicondyle is generally less well developed than the entepicondyle in multituberculates (Kielan-Jaworowska and Gambaryan, 1994). Slightly less pronounced epicondyles are present in the arboreal docodontan *Agilodocodon* (Meng et al., 2015), the eutriconodontans *Yanoconodon* (Chen et al., 2017) and *Jeholodens* (Ji et al., 1999), and the spalacotherioid *Zhangheotherium* (Hu et al., 1997).

Most Mesozoic mammaliaforms bear an entepicondylar foramen; it varies in size and shape, however. The entepicondylar foramen is long and narrow in *Adalatherium* as well as in morganucodontans (Jenkins and Parrington, 1976), *Gobiconodon* (Jenkins and Schaff, 1988), *Liaoconodon* (Meng et al., 2011), *Yanoconodon* (Chen et al., 2017), *Qishou* (Mao and Meng, 2019), *Shenshou* (Bi et al., 2014), *Xianshou* (Bi et al., 2014), *Maiopatagium* (Meng et al., 2017), *Zhangheotherium* (Hu et al., 1997), and *Dryolestes* (Martin, 2013). It is smaller and rounder in *Repenomamus* (Hu, 2006), and round and large in *Haldanodon* (Martin, 2005). In contrast, it is a fairly small and circular foramen in multituberculates (Krause and Jenkins, 1983; Kielan-Jaworowska and Qi, 1990; Kielan-Jaworowska and Gambaryan, 1994; Sereno, 2006; Bolortsetseg, 2008; Hurum and Kielan-Jaworowska, 2008).

Adalatherium is unique among non-therian mammaliaforms in possessing a large supratrochlear foramen (Fig. 56). Generally, supratrochlear foramina are extremely rare in early mammaliaforms; the only other non-therian mammaliaforms possibly possessing a supratrochlear foramen are multituberculates. In most multituberculates, the radial and olecranon fossae are deep, but still separated by a bony sheath. This bony lamina is pierced in a few specimens of the following taxa: *Lambdopsalis* (IVPP 8408), *Kryptobaatar* (GI PST 8-2), *Catopsbaatar* (PM 120/07), and an unidentified multituberculate from Bissekty (URBAC 03-076; Chester et al., 2010). It is uncertain, however, whether these foramina were present in life or represent postmortem breakage. The first definitive supratrochlear foramina are known in *Zalambdalestes*, *Barunlestes*, zhelestids, and early metatherians (Gambaryan and Kielan-Jaworowska, 1997; Chester et al., 2010). Even in these taxa, the size and presence of the supratrochlear foramen is variable and, with the exception of *Barunlestes*, does not reach the extent of the foramen in *Adalatherium*.

The most intriguing feature of the humerus in *Adalatherium* is the fully developed trochlea, which stands in strong contrast to the distal humeral articulation of most non-therian mammaliaforms (Fig. 56). The presence of this unusually derived feature in *Adalatherium* warrants a detailed review of the distal articular facet in Mesozoic mammaliaforms. Typically, basal mammaliaforms possess radial and ulnar condyles that both are well rounded (Jenkins, 1973). This condition can be seen in *Morganucodon* and was likely present in *Megazostrodon* as well (Jenkins and Parrington, 1976). The distal part of the humerus of *Megazostrodon* is poorly preserved, indicating the positions of the condyles but not their full shape. In *Morganucodon*, the radial condyle is almost perfectly spherical anteriorly and slightly flatter, but still convex, posteriorly. The ulnar condyle is narrower mediolaterally and wraps around the distal end of the humerus, starting in a more medial position on the anterior aspect of the humerus and ending slightly more laterally on the posterior aspect. The intercondylar groove between the radial and ulnar condyles is narrow. This configuration of the ulnar condyle is here referred to as 'spiral,' following the terminology of Jenkins (1973). In most Mesozoic mammaliaform phylogenies, this condition is referred to as 'bulbous ulnar condyle' (see, for example, Han et al., 2017:char. 257; Luo et al., 2017:char. 257; Huttenlocker et al., 2018:char. 268). We find the descriptor 'bulbous,' meaning fat and round, not as fitting to describe the generally mediolaterally narrow condyle of most basal mammaliaforms and therefore prefer Jenkins' earlier 'spiral' descriptor.

A prominent spiral ulnar condyle is also described for monotremes (Jenkins, 1973), the haramiyidan *Haramiyavia* (Jenkins et al., 1997), the docodontans *Haldanodon* (Martin, 2005) and *Microdocodon* (Zhou et al., 2019), and the euharamiyidans *Shenshou* and *Xianshou songae* (see Bi et al., 2014:fig. 1c), and at least the anterior aspect of the ulnar condyle is spiral in the docodontan *Agilodocodon* (Meng et al., 2015:fig. 3a, b) and the multituberculate *Rugosodon* (Yuan et al., 2013:fig. S1). The ulnar condyle has further been scored as 'bulbous' (here considered 'spiral') in the enigmatic *Megaconus*, the shuotheriid *Pseudotribos*, and the euharamiyidans *Maiopatagium* and *Vilevolodon* by Huttenlocker et al. (2018:char. 268). Even though it may be reasonable to assume that a spiral ulnar condyle is retained in these taxa, the specimens do not preserve the detailed morphology necessary to unambiguously determine the size of the intercondylar groove, the shape and extent of the ulnar condyle, or the presence or absence of an incipient trochlea on the posterior aspect. A spiral ulnar condyle is unambiguously present in the multituberculates *Nemegtbaatar* (Kielan-Jaworowska and Gambaryan, 1994), *Catopsbaatar* (Hurum and Kielan-Jaworowska, 2008), *Sinobaatar* (Hu and Wang, 2002), *Lambdopsalis* (Kielan-Jaworowska and Qi, 1990; Kielan-Jaworowska and Gambaryan, 1994), ?*Stygimys* (Krause and Jenkins, 1983), *Ptilodus* (Krause and Jenkins, 1983), ?*Mesodma* (Krause and Jenkins, 1983), *Mangasbaatar* (Bolortsetseg, 2008), and *Jeholbaatar* (Wang et al., 2019) and an unidentified multituberculate from the Bissekty Formation (Chester et al., 2010). The presence of an incipient trochlea has been discussed for *Kryptobaatar*. Sereno and McKenna (1995:146) described the ulnar condyle as hinge-like and narrow and the intercondylar groove as broad and "approaching the form of the therian trochlear joint." Sereno reanalyzed the specimen in 2006, and the depicted ventral view of the humerus (fig. 10.6) clearly shows a spiral ulnar condyle that extends onto the distal surface of the articulation, similar to the spiral ulnar condyle in other multituberculates. The presence of a spiral ulnar condyle in *Kryptobaatar* is further corroborated by the distal epiphysis of PSS-MAE 00-22 described by Bolortsetseg (2008) and the humerus of GI PST 8-2 (initially described as *Tugrigbaatar* by Kielan-Jaworowska and Dashzeveg [1978] but later assigned to *Kryptobaatar* by Gambaryan and Kielan-Jaworowska [1997]). We follow Gambaryan and Kielan-Jaworowska (1997) and Kielan-Jaworowska and Hurum (2006) in their assessments that there is no incipient trochlea in multituberculates.

Presence of an incipient trochlea with a vestigial ulnar condyle anteriorly has been suggested for eutriconodontans. Huttenlocker et al. (2018:char. 268) defined the incipient state as a "cylindrical trochlea in posterior view with a vestigial ulnar condyle in anterior view." The only complete and three-dimensionally preserved and described eutriconodontan humeri belong to *Repenomamus* (Hu, 2006) and *Priacodon* (Engelmann and Callison, 1998). Both preserve a spherical radial condyle and

a narrower ulnar condyle in anterior view. The ulnar condyle seems less pronounced than in multituberculates and *Morganucodon*, but nevertheless wraps around the distal surface of the humerus. The intercondylar groove of *Repenomamus* still appears to be narrow, particularly in distal view (Hu, 2006:fig. 3.22). However, Hu (2006) described the presence of a shallow and wide trochlea between the condyles that wraps around the distal aspect of the humerus and extends onto the dorsal surface. In anterior and distal views (Hu, 2006:fig. 3.22a, f), the groove appears as narrow as in multituberculates, but the width of the groove cannot be clearly determined based on the images of the posterior view (Hu, 2006:fig. 3.22d). It is possible that the posterior aspect of the distal articulation is indeed more trochlea-like than in multituberculates. Jenkins and Schaff (1988) further mentioned, but did not depict, two partial trochleae and a radial condyle that were found in association with, but could not be precisely fitted to, the humerus of *Gobiconodon*. Jenkins and Schaff (1988:15) described the trochleae as "grooved, as in advanced mammals, rather than bulbous as in monotremes, morganucodontids, and multituberculates" and the isolated radial condyle as "circular in outline and hemispherical." If the fragments indeed belong to *Gobiconodon*, then an incipient trochlea might already be present in some eutriconodontans. Further support for an early incipient trochlea in eutriconodontans is provided by Ji et al. (1999:328), who identified "radial and ulnar condyles on its anterior aspect" and "an incipient ulnar trochlea on its posteroventral aspect" in *Jeholodens*. For this study, only a cast of the holotype specimen of *Jeholodens jenkinsi* was available, in which the posterior aspect of the humerus is not well shown. The anterior and posterior surfaces of the humerus seem to be preserved in *Liaoconodon* (Meng et al., 2011:fig. 1), but the images presented do not allow unambiguous identification of the presence of a trochlea. Lastly, *Yanoconodon* appears to only preserve the anterior aspect of the distal articulation, which presents two low condyles (Chen et al., 2017:fig. 8c). It is thus inconclusive whether an incipient trochlea was present in eutriconodontans. The general morphology of a spherical radial condyle and a narrower ulnar condyle is similar to the condition in morganucodontans and multituberculates, but the ulnar condyle was likely less exaggerated in eutriconodontans.

An incipient trochlea is also scored as present in *Akidolestes*, *Zhangheotherium*, *Maotherium*, *Henkelotherium*, and *Vincelestes* (Huttenlocker et al., 2018:char. 268). Chen and Luo (2013:fig. 4) illustrated the posterior surface of the distal humerus of *Akidolestes*. The distal articular facet seems to be largely damaged, and the images do not convey the presence of an incipient trochlea, but it is entirely possible that a trochlea can be identified more clearly in the original specimen. *Zhangheotherium quinquecuspidens* more clearly shows an incipient trochlea (Hu et al., 1997, 1998:fig. 3b). The radial condyle is prominent, and a shallow intercondylar groove is present medial to it. The ulnar condyle is vestigial. The posterior aspect of the humerus is not preserved in the holotype, but Luo and Ji (2005:344) described the posterior aspect as "trochlea-like" in CAGS97-07352. An incipient trochlea cannot be confirmed in *Maotherium* because the distal articular facet is blocked from view in Ji et al. (2009:fig. 1).

The distal humeral articulation in dryolestoids has been a point of contention. In *Henkelotherium guimarotae*, the right distal humerus is obscured from view and has undergone considerable postmortem compression, to the point that Krebs (1991), in the description of the holotype, considered it impossible to decide whether a trochlea was present. Vázquez-Molinero et al. (2001:210) stated that the radial and ulnar condyles "are clearly separated by a wide intercondylar groove." As such, a bulbous ulnar condyle is scored for *Henkelotherium* in O'Leary et al. (2013:char. 3056). However, new specimens of *Dryolestes* (Martin, 2013:fig. 4) reveal that the ulnar condyle is spiral and the intercondylar groove is narrow along the anterior aspect. This is more similar to the condition in multituberculates. However, the posterior aspect of the humerus is gently concave; thus, neither the radial nor the ulnar condyle extends onto the posterior side. In this respect, the articular facet is reminiscent of an incipient, therian-like trochlea. Jäger et al. (2019) confirmed the presence of a radial and ulnar condyle on the anterior surface and an incipient trochlea on the posterior aspect in *Henkelotherium* similar to that of *Dryolestes*, based on CT data. A fully developed trochlea and absence of an ulnar condyle is scored for *Eomaia*, *Juramaia*, *Ukhaatherium*, *Zalambdalestes*, *Asiatherium*, and *Pucadelphys*, as well as for extant therians, by Huttenlocker et al. (2018:char. 268; note that *Zalambdalestes* is scored as unknown in Bi et al., 2018); these scorings were corroborated by Chester et al. (2010). Despite the uncertainty surrounding the presence of an incipient trochlea in several early mammalian lineages, it is obvious from this discussion that *Adalatherium* is unique among non-therian mammaliaforms in possessing a fully developed trochlea, a feature that is associated with a parasagittal forelimb stance (e.g., Gambaryan and Kielan-Jaworowska, 1997).

Ulna

Adalatherium shares several ulnar characteristics with derived therians that are not present in any other Mesozoic mammaliaform. One of the more prominent features, aside from the proximal articular facet for the humeral trochlea, is the shape of the shaft. In lateral view, the ulnar shaft is concave posteriorly and the large olecranon is directed posteriorly (Fig. 56). In this respect, the ulna is markedly different from those of early mammaliaforms in which the olecranon bends anteriorly and the shaft is sigmoid in lateral view, as in *Morganucodon* (Jenkins and Parrington, 1976); the docodontans *Haldanodon* (Martin, 2005), *Agilodocodon* (Meng et al., 2015), and *Microdocodon* (Zhou et al., 2019); the eutriconodontans *Repenomamus* (Hu, 2006), *Gobiconodon* (Jenkins and Schaff, 1988), *Yanoconodon* (slightly less so; Chen et al., 2017), and *Liaoconodon* (Meng et al., 2011); the euharamiyidans *Arboroharamiya* (Han et al., 2017), *Maiopatagium* (Meng et al., 2017), *Vilevolodon* (Luo et al., 2017), *Qishou* (Mao and Meng, 2019), *Shenshou* (Bi et al., 2014), and *Xianshou* (Bi et al., 2014); the spalacotherioids *Akidolestes* (Chen and Luo, 2013) and *Maotherium* (Ji et al., 2009); the multituberculates ?*Mesodma* (Krause and Jenkins, 1983), *Sinobaatar* (Hu and Wang, 2002), *Kryptobaatar* (Sereno, 2006; Bolortsetseg, 2008), *Catopsbaatar* (Hurum and Kielan-Jaworowska, 2008), *Litovoi* (Csiki-Sava et al., 2018), *Jeholbaatar* (Wang et al., 2019), and possibly also *Nemegtbaatar* (Kielan-Jaworowska and Gambaryan, 1994; the preserved fragment indicates that the shaft was convex; however, the distal aspect is missing); and the cladotherians *Vincelestes* (Rougier, 1993), *Dryolestes* (Martin, 2013), *Henkelotherium* (Krebs, 1991; Jäger et al., 2019), *Eomaia* (Ji et al., 2002), *Ambolestes* (Bi et al., 2018), *Deltatheridium* (O'Leary et al., 2013), and *Ukhaatherium* (Horovitz, 2003). The olecranon is still bent anteriorly, but the shaft is straight distal to the ulnar notch in the multituberculates *Yubaatar* (Xu et al., 2015) and an unidentified paulchoffatiid from Guimarota (Martin, 2013), the eutriconodontan *Jeholodens* (Ji et al., 1999), and the spalacotherioid *Zhangheotherium* (Hu et al., 1997, 1998; Luo and Ji, 2005). Among extant therians, a posteriorly bent ulnar shaft and a posteriorly inflected olecranon are present in several artiodactyls and perissodactyls (O'Leary et al., 2013:chars. 3091, 3081). A posteriorly bent ulna, but straight olecranon, can also be seen in the hyrax *Procavia*, as well as in the lagomorph *Oryctolagus* (O'Leary et al., 2013:chars. 3091, 3081).

The olecranon process in *Adalatherium* is long (31% of the ulnar portion distal to the pivot of the semilunar notch) and straight in posterior view, neither medially nor laterally inflected. In many Mesozoic mammaliaforms, the olecranon process is

short, rounded, and gently bent medially, as is the case in *Morganucodon* (Jenkins and Parrington, 1976), several multituberculates (Krause and Jenkins, 1983; Kielan-Jaworowska and Gambaryan, 1994), *Dryolestes* (Martin, 2013), and *Henkelotherium* (Krebs, 1991; Jäger et al., 2019). In particular, the medial inflection is difficult to recognize in compressed specimens because it can only be seen clearly in posterior or anterior view. A similarly short and rounded olecranon (that might or might not be medially inflected) is additionally present in docodontans (Meng et al., 2015; Zhou et al., 2019), several eutriconodontans (Ji et al., 1999; Meng et al., 2011; Chen et al., 2017), spalacotherioids (Hu et al., 1997; Ji et al., 2009; Chen and Luo, 2013), euharamiyidans (Zheng et al., 2013; Bi et al., 2014; Han et al., 2017; Luo et al., 2017; Meng et al., 2017), multituberculates (Sereno and McKenna, 1995; Sereno, 2006; Bolortsetseg, 2008; Yuan et al., 2013; Csiki-Sava et al., 2018; Wang et al., 2019), *Ambolestes* (Bi et al., 2018), and *Ukhaatherium* (Horovitz, 2003). The olecranon is greatly enlarged and medially inflected in the fossorial *Fruitafossor* (66%; Luo and Wible, 2005) and the docodontans *Haldanodon* (47%; Martin, 2005) and *Docofossor* (47%; Luo et al., 2015b). The olecranon in *Adalatherium* is more similar in size to those of the eutriconodontans *Repenomamus* (30%; Hu, 2006:fig. 3.23) and *Gobiconodon* (26%; Jenkins and Schaff, 1988:fig. 15), and this also appears to be the case, but could not be precisely measured, in the multituberculate *Yubaatar* (Xu et al., 2015). It may be of relevance to note that *Repenomamus*, *Gobiconodon*, *Yubaatar*, and *Adalatherium* are among the largest Mesozoic mammaliaforms known from postcranial material.

Several changes to the proximal articular facet can be noted in *Adalatherium* that relate to the development of a trochlea. The coronoid process is prominent, projecting anteriorly and medially to articulate with the medial aspect of the trochlea. The coronoid process is absent in *Morganucodon* (Jenkins and Parrington, 1976), *Erythrotherium* (Jenkins and Parrington, 1976), and *Haldanodon* (Martin, 2005) and is only developed as a slightly raised crest in several euharamiyidans and multituberculates (Krause and Jenkins, 1983; Kielan-Jaworowska and Gambaryan, 1994; Martin, 2013; Bi et al., 2014; Han et al., 2017; Csiki-Sava et al., 2018; Wang et al., 2019). It appears that *Yubaatar* has a more prominent coronoid process, but the extent is difficult to evaluate based on Xu et al. (2015:fig. 1). The coronoid process is well developed and anteriorly projecting in the eutriconodontans *Repenomamus* (Hu, 2006) and *Gobiconodon* (Jenkins and Schaff, 1988), whereas only a small crest indicates its presence in *Yanoconodon* (Chen et al., 2017). The coronoid process is shallow in *Akidolestes* (Chen and Luo, 2013), *Zhangheotherium* (Hu et al., 1997), *Vincelestes* (Rougier, 1993), *Dryolestes* (Martin, 2013), and *Henkelotherium* (Krebs, 1991; Jäger et al., 2019).

Adalatherium retains a distinct ulnar crest along the distal aspect of the shaft. The ulnar crest or 'ulnar flange' is prominently developed in the non-mammaliaform cynodonts *Thrinaxodon* (Jenkins, 1971), *Massetognathus* (Jenkins, 1971), *Galeosaurus* (Butler et al., 2019), *Trucidocynodon* (Oliveira et al., 2010; Oliveira and Schultz, 2015), and *Diademodon* (Gaetano et al., 2018). Haines (1946) proposed that the crest served as the attachment of the interosseous membrane. The ulnar crest in *Adalatherium* is less prominent than that in basal cynodonts; it is mediolaterally narrower and does not extend as far anteriorly and proximally. A narrower and lower ulnar crest has also been described for the basal mammaliaform *Morganucodon* (Jenkins and Parrington, 1976) and is depicted for the eutriconodontan *Repenomamus* (Hu, 2006:fig. 3.23)

A prominent ulnar styloid process is present in *Adalatherium* but absent in *Morganucodon*, *Haldanodon*, *Microdocodon*, *Agilodocodon*, *Arboroharamiya*, *Maiopatagium*, *Qishou*, *Shenshou*, *Xianshou*, *Repenomamus*, *Gobiconodon*, *Yanoconodon*, *Liaoconodon*, and *Vincelestes* (Jenkins and Parrington, 1976; Jenkins and Schaff, 1988; Rougier, 1993; Martin, 2005; Hu, 2006; Meng et al., 2011; Zheng et al., 2013; Bi et al., 2014; Meng et al., 2015, 2017; Chen et al., 2017; Han et al., 2017; Mao and Meng, 2019; Zhou et al., 2019). A styloid process is present in *Fruitafossor* (Luo and Wible, 2005) and *Akidolestes* (Chen and Luo, 2013), well developed in *Ectypodus* (Bolortsetseg, 2008), and short and blunt in *Kryptobaatar* (Bolortsetseg, 2008).

Radius

The radius varies considerably in length and diameter among Mesozoic mammaliaforms, ranging from slender and gracile to robust and stout (Fig. 56). More substantial variation is evident in the proximal articular facet, which reflects shape changes previously discussed for the radial condyle of the humerus. Taxa with a spherical and large radial condyle tend to have circular proximal facets (e.g., *Morganucodon,* multituberculates), whereas the outline is elliptical in *Adalatherium*, *Repenomamus* (Hu, 2006), *Gobiconodon* (Jenkins and Schaff, 1988), *Haldanodon* (Martin, 2005), *Agilodocodon* (Meng et al., 2015), and possibly *Docofossor* (Luo et al., 2015b). Due to the compressed preservation of most of the Chinese specimens, it is difficult to evaluate the exact outline of the proximal facet; it appears to be circular in *Sinobaatar* (Hu and Wang, 2002), *Arboroharamiya* (Zheng et al., 2013, Han et al., 2017), *Maiopatagium* (Meng et al., 2017), *Vilevolodon* (Luo et al., 2017), *Qishou* (Mao and Meng, 2019), *Shenshou* (Bi et al., 2014), and *Xianshou* (Bi et al., 2014).

The bicipital tuberosity is rarely preserved in Mesozoic mammaliaforms; therefore, comparison is limited to only a few taxa. The tuberosity is indistinct in *Adalatherium*. It is slightly raised in *Morganucodon* (Jenkins and Parrington, 1976), prominent in *Repenomamus* (Hu, 2006) but not in *Gobiconodon* (Jenkins and Schaff, 1988), and enlarged in *Vincelestes* (Rougier, 1993) and the multituberculates *Ptilodus* (Krause and Jenkins, 1983) and *Yubaatar* (Xu et al., 2015), whereas it is only a low tuberosity in *Kryptobaatar* (Bolortsetseg, 2008).

The distal articular facets for the carpals on the ulna and radius are subequal in size in *Morganucodon* (Jenkins and Parrington, 1976), *Gobiconodon* (Jenkins and Schaff, 1988), and *Arboroharamiya* (Zheng et al., 2013), whereas the distal articular facet on the radius is substantially larger than the distal articular facet on the ulna in *Adalatherium*, *Haldanodon* (Martin, 2005), *Repenomamus* (Hu, 2006), *Liaoconodon* (Meng et al., 2011), *Maiopatagium* (Meng et al., 2017), *Qishou* (Mao and Meng, 2019), *Shenshou* (Bi et al., 2014), *Xianshou* (Bi et al., 2014), *Catopsbaatar* (Hurum and Kielan-Jaworowska, 2008), *Kryptobaatar* (Sereno, 2006), *Jeholbaatar* (Wang et al., 2019), and *Sinobaatar* (Hu and Wang, 2002).

Adalatherium has a small but distinct radial styloid process that is relatively larger than the process in *Haldanodon* (Martin, 2005), *Kryptobaatar* (Bolortsetseg, 2008), *Nemegtbaatar* (Kielan-Jaworowska and Gambaryan, 1994), *Vincelestes* (Rougier, 1993), and *Akidolestes* (Chen and Luo, 2013). The styloid process is very weak or absent in *Morganucodon* (Jenkins and Parrington, 1976), *Repenomamus* (Hu, 2006), *Gobiconodon* (Jenkins and Schaff, 1988), *Yanoconodon* (Chen et al., 2017), *Liaoconodon* (Meng et al., 2011), *Arboroharamiya* (Zheng et al., 2013; Han et al., 2017); *Maiopatagium* (Meng et al., 2017), *Qishou* (Mao and Meng, 2019), *Shenshou* (Bi et al., 2014), *Vilevolodon* (Luo et al., 2017), *Xianshou* (Bi et al., 2014), and *Zhangheotherium* (Hu et al., 1997).

Carpus

The manus of *Adalatherium* is among the best-preserved manual remains for any Mesozoic mammaliaform. Very limited information is available on the carpals of Mesozoic

mammaliaforms. Carpals are unknown for otherwise well-known taxa such as *Morganucodon*, *Megazostrodon*, *Haldanodon*, *Gobiconodon*, *Vilevolodon*, paulchoffatiids, *Catopsbaatar*, and *Dryolestes* and are only illustrated or reconstructed, but not specifically described, in *Agilodocodon* (Meng et al., 2015:fig. 3c, e), *Yubaatar* (Xu et al., 2015:fig. 2), *Rugosodon* (Yuan et al., 2013:fig. 1d), *Jeholbaatar* (Wang et al., 2019:fig. 7c), *Arboroharamiya* (Han et al., 2017:ED fig. 7), *Shenshou* (Bi et al., 2014:fig. 3f), *Xianshou* (Bi et al., 2014:ED fig. 1), *Qishou* (Bi et al., 2014: ED figs. 3b, 4a), *Fruitafossor* (Luo and Wible, 2005:fig. 2i), *Chaoyangodens* (Hou and Meng, 2014:fig. 1), *Liaoconodon* (Meng et al., 2011:fig. 1), *Jeholodens* (Ji et al., 1999:fig. 1), and *Juramaia* (Luo et al., 2011:fig. 1d). Brief descriptions mainly focusing on the relative size of the different carpals as well as contact relationships are provided for *Docofossor* (Luo et al., 2015b), *Maiopatagium* (Meng et al., 2017), *Ptilodus* (Krause and Jenkins, 1983; Bolortsetseg, 2008), *Sinobaatar* (Hu and Wang, 2002), *Zhangheotherium* (Hu et al., 1998), *Sinodelphys* (Luo et al., 2003), *Eomaia* (Ji et al., 2002), *Ambolestes* (Bi et al., 2018), *Asioryctes* (Kielan-Jaworowska, 1977), *Barunlestes* (Kielan-Jaworowska, 1978), and *Asiatherium* (Trofimov and Szalay, 1994; Szalay and Trofimov, 1996). Isolated carpals have been described in greater detail for *Repenomamus* (trapezium, ?trapezoid; Hu, 2006), *Nemegtbaatar* (scaphoid, lunate, ?triquetrum, ?pisiform; Kielan-Jaworowska and Gambaryan, 1994), *Ectypodus* (scaphoid, hamate; Bolortsetseg, 2008), *Mangasbaatar* (trapezoid; Bolortsetseg, 2008), *Henkelotherium* (lunate, scaphoid, triquetrum; Krebs, 1991; Jäger et al., 2019), and *Ukhaatherium* (hamate; Horovitz, 2003). But the identification of isolated elements often remains tentative and ambiguous, because carpal morphology is unknown for many early mammaliaforms.

Detailed descriptions of associated carpals are limited to *Yanoconodon* (Chen et al., 2017), *Kryptobaatar* (Bolortsetseg, 2008), *Vincelestes* (Rougier, 1993), and *Akidolestes* (Chen and Luo, 2013). But even in these cases carpal identification remains ambiguous and problematic. Chen and Luo (2013:fig. 9), for instance, interpreted the carpal that articulates with Mc IV as the capitate and the carpal that articulates with Mc III as the trapezoid. Following, among others, Holmgren (1952), Romer (1966), Yalden (1966), and Lewis (1989), the carpal in articulation with Mc III should be the capitate (= magnum). As such, we suggest revising Chen and Luo's (2013) interpretation as follows (former/new): hamate/pisiform, unlabeled fragment proximal to Mc II/trapezoid, trapezoid/capitate, and capitate/hamate.

Given the dearth of comparative material, this section mainly focuses on size and position of the carpals, and less on detailed morphology. General trends within carpal evolution previously focused on distinguishing metatherians and eutherians (Trofimov and Szalay, 1994; Szalay and Trofimov, 1996; Ji et al., 2002; Luo et al., 2003). Metatherians are characterized by a hypertrophied hamate (relative to the triquetrum), large scaphoid (relative to the lunate), large triquetrum (relative to the lunate and distal ulna), and a small, bean-shaped trapezium (e.g., Trofimov and Szalay, 1994; Szalay and Trofimov, 1996). The hamate is also large, but not hypertrophied, in *Zhangheotherium* (Hu et al., 1998), *Eomaia* (Ji et al., 2002), *Barunlestes* (Kielan-Jaworowska, 1978), and *Asioryctes* (Kielan-Jaworowska, 1977). As such, an enlarged hamate might have evolved earlier within mammals and only later hypertrophied in metatherians. In addition, Bi et al. (2018) recently placed *Sinodelphys*, which also bears a large scaphoid, triquetrum, and hamate, within eutherians, indicating that carpal size and shape might have been more plastic at the base of Theria.

The scaphoid is clearly larger than the lunate in *Adalatherium*; the euharamiyidans *Shenshou* and possibly *Arboroharamiya* (Bi et al., 2014; Han et al., 2017; but scored as not hypertrophied in Huttenlocker et al., 2018:char. 274); the multituberculate *Ptilodus* (Bolortsetseg, 2008); and the therians *Sinodelphys* (Luo et al., 2003), *Ambolestes* (Bi et al., 2018), *Asiatherium* (Trofimov and Szalay, 1994; Szalay and Trofimov, 1996), and *Asioryctes* (Kielan-Jaworowska, 1977:fig. 3a; note that this is scored as unknown in Bi et al., 2018:char. 361). It is similar in size or only slightly larger than the lunate in most other Mesozoic mammaliaforms.

The hamate is similar in size to the triquetrum in *Adalatherium*, but it is large relative to the capitate and trapezoid. The hamate is smaller or similar in size to the triquetrum in the docodontan *Agilodocodon* (Meng et al., 2015); the eutriconodontans *Jeholodens* (Ji et al., 1999) and *Yanoconodon* (Chen et al., 2017); and the multituberculates *Sinobaatar* (Hu and Wang, 2002), *Ptilodus* (Bolortsetseg, 2008), and *Kryptobaatar* (Bolortsetseg, 2008). The hamate is larger than the triquetrum in the docodontan *Docofossor* (Luo et al., 2015b); in the euharamiyidans *Arboroharamiya* (Han et al., 2017), *Xianshou linglong* (Bi et al., 2014), and *Shenshou* (Bi et al., 2014); as well as in several therians (Bi et al., 2018:char. 362). The triquetrum is similar in size to the lunate or the distal ulna in *Adalatherium*; the docodontan *Agilodocodon* (Meng et al., 2015); the eutriconodontans *Yanoconodon* (Chen et al., 2017) and *Jeholodens* (Ji et al., 1999); the euharamiyidan *Arboroharamiya* (Han et al., 2017); the multituberculates *Kryptobaatar* (Bolortsetseg, 2008) and *Jeholbaatar* (Wang et al., 2019); the stem therian *Vincelestes* (Rougier, 1993); and the eutherians *Eomaia* (Ji et al., 2002), *Barunlestes* (Kielan-Jaworowska, 1978), and *Asioryctes* (Kielan-Jaworowska, 1977). In contrast, the triquetrum is enlarged relative to the lunate in *Shenshou* and *Xianshou* (Bi et al., 2014), as well as in *Zhangheotherium*, *Sinodelphys*, *Ambolestes*, and several metatherians (Bi et al., 2018:char. 364). The trapezium is well developed and larger than the trapezoid in *Adalatherium*, as is the case in most Mesozoic mammaliaforms with the exception of *Vincelestes*, *Sinodelphys*, and *Asiatherium* (Bi et al., 2018:char. 363; Huttenlocker et al., 2018:char. 276).

The number of carpals varies in extant therians. Fusion of several carpals (centrale, scaphoid, or lunate) or loss of elements (trapezium) is common (Holmgren, 1952; Lewis, 1989; Stafford and Thorington, 1998; O'Leary et al., 2013). It appears that the number of carpals is more consistent in Mesozoic mammaliaforms, being either eight or nine. Eight carpals consisting of four proximal carpals (scaphoid, lunate, triquetrum, pisiform) and four distal carpals (trapezium, trapezoid, capitate, hamate) are known for *Agilodocodon* (Meng et al., 2015), *Jeholodens* (Ji et al., 1999), *Sinodelphys* (Luo et al., 2003), *Ambolestes* (Bi et al., 2018), and *Eomaia* (Ji et al., 2002). In several early mammals, a centrale is retained between the proximal and distal rows, as is the case in *Arboroharamiya* (not labeled in Han et al., 2017:ED fig. 7), *Shenshou* (Bi et al., 2014), *Sinobaatar* (Hu and Wang, 2002), *Kryptobaatar* (Bolortsetseg, 2008), *Zhangheotherium* (Hu et al., 1998), *Akidolestes* (Chen and Luo, 2013), *Vincelestes* (Rougier, 1993), *Asioryctes* (Kielan-Jaworowska, 1977), and *Barunlestes* (Kielan-Jaworowska, 1978). *Adalatherium* further possesses an additional sesamoid, the os Daubentonii, which is positioned between the ulna, radius, lunate, and triquetrum. The os Daubentonii is known in several primates (Lewis et al., 1970), and has been described in the eutherian *Barunlestes* (Kielan-Jaworowska, 1978). A small element also appears to be present between the radius and ulna in *Arboroharamiya* (Han et al., 2017:ED fig. 7). The element is not labeled but, at least in palmar view, appears to be a separate element that could represent an os Daubentonii.

Metacarpals and Manual Phalanges

Detailed descriptions of the metacarpals and phalanges are rare for Mesozoic mammaliaforms. Most studies focus on the proportion of the elements, which is most commonly assessed by

calculating the phalangeal index (lengths of the proximal and intermediate phalanges × 100 divided by the length of the metapodial of the third digit). The phalangeal index has been widely used to estimate the degree of prehensility for the forefoot and hind foot in extant mammals (Lemelin and Grafton, 1998; Lemelin, 1999; Weisbecker and Warton, 2006; Weisbecker and Schmid, 2007; Kirk et al., 2008) and has been more recently applied in Mesozoic mammaliaforms (e.g., Chen and Luo, 2013; Zheng et al., 2013; Bi et al., 2014; Meng et al., 2015, 2017; Han et al., 2017). Here, the phalangeal index is used to quantitatively compare manual proportions in Mesozoic mammaliaforms.

The metacarpals (Mc), except Mc I, are long compared with the phalanges in *Adalatherium*. As such, the phalangeal index for the third digit is low (93%). This is comparable to or higher than the phalangeal index of *Kryptobaatar* (92% in Bolortsetseg, 2008:fig. 42; 81% in Wang et al., 2019), and higher than in the spalacotherioids *Zhangheotherium* (83% in Chen and Luo, 2013) and possibly *Maotherium* (83% in Chen and Luo, 2013; 95% in Zheng et al., 2013, and Wang et al., 2019). The phalangeal index is much higher in the multituberculates *Sinobaatar* (108% in Chen and Luo, 2013:ED7a, and Wang et al., 2019; 102% in Zheng et al., 2013), *Rugosodon* (117% in Yuan et al., 2013, and Wang et al., 2019), *Ptilodus* (118% in Wang et al., 2019), ?*Eucosmodon* (119% in Wang et al., 2019), and *Jeholbaatar* (126% in Wang et al., 2019); the eutriconodontans *Yanoconodon* (103% in Chen and Luo, 2013, and 113% in Chen et al., 2017:table 1), *Jeholodens* (113% in Chen and Luo, 2013; 111% in Zheng et al., 2013), and *Spinolestes* (121% in Martin et al., 2015); the spalacotherioid *Akidolestes* (105–111% in Chen and Luo, 2013); and the therians *Sinodelphys* (137% in Chen and Luo, 2013), *Ambolestes* (111% in Bi et al., 2018:table S2), *Eomaia* (130% in Chen and Luo, 2013, and Wang et al., 2019), and *Juramaia* (121% in Luo et al., 2011). By far the greatest elongation of the phalanges compared with the metacarpals is present in the euharamiyidans *Arboroharamiya*, *Maiopatagium*, *Shenshou*, *Vilevolodon*, and *Xianshou*. All of these forms have phalangeal indices above 200% (Meng et al., 2017:ED fig. 7a; Wang et al., 2019:ED table 1). Several taxa, including *Repenomamus*, *Liaoconodon*, *Chaoyangodens*, *Fruitafossor*, and *Docofossor*, which appear to have manual proportions shorter or more similar to *Adalatherium*, could not be included because measurements were not given in the descriptions of the specimens or the third digit was not completely preserved.

Comparing digit length in *Adalatherium* overall, digits I and V are similar in length and both are shorter than digits II–IV. These relative proportions are also seen in the docodontans *Docofossor* and *Agilodocodon* (Luo et al., 2015b; Meng et al., 2015), the eutriconodontans *Spinolestes* and *Yanoconodon* (Martin et al., 2015; Chen et al., 2017), the multituberculate *Sinobaatar* (Hu and Wang, 2002), and the spalacotherioid *Akidolestes* (Chen and Luo, 2013). In contrast, digit I is much shorter than digits II–V in the euharamiyidans *Arboroharamiya*, *Maiopatagium*, and *Shenshou* (Bi et al., 2014; Han et al., 2017; Meng et al., 2017); the eutriconodontan *Jeholodens* (Ji et al., 2002); the spalacotherioid *Zhangheotherium* (Hu et al., 1998); and the therians *Sinodelphys* (Luo et al., 2003), *Eomaia* (Ji et al., 2002), *Ambolestes* (Bi et al., 2018), and *Juramaia* (Luo et al., 2011).

Interestingly, the comparable lengths of digits I and V are the result of different patterns in the taxa listed above. In *Adalatherium*, Mc I is short and robust, but the proximal phalanx of digit I is relatively long, whereas Mc V is relatively long (only slightly shorter than Mc II–IV), and the proximal and intermediate phalanges of digit V are short. In *Agilodocodon*, *Spinolestes*, *Yanoconodon*, *Sinobaatar*, and *Akidolestes*, Mc V is shorter and more robust than Mc I, but the phalanges are comparable in length to the other digits (Chen and Luo, 2013; Martin et al., 2015; Meng et al., 2015; Chen et al., 2017). *Docofossor* is excluded here because the proximal and intermediate phalanges are fused in all digits (Luo et al., 2015b).

The metacarpals and phalanges are neither very stout nor very slender in *Adalatherium*, but comparable to those in mammals of a generalized terrestrial habitus. Similarly, the metacarpals are intermediate in robustness in the eutriconodontans *Chaoyangodens* (Hou and Meng, 2014), *Yanoconodon* (Chen et al., 2017), and *Jeholodens* (Ji et al., 2002:fig. 3); the multituberculates *Rugosodon* (Yuan et al., 2013) and *Sinobaatar* (Hu and Wang, 2002); and the spalacotherioid *Zhangheotherium* (Hu et al., 1998). The metacarpals are more robust than in *Adalatherium* in the eutriconodontans *Spinolestes*, *Liaoconodon*, and *Repenomamus* (Hu, 2006; Meng et al., 2011; Martin et al., 2015), whereas the euharamiyidans *Arboroharamiya*, *Maiopatagium*, and *Shenshou* (Bi et al., 2014; Han et al., 2017; Meng et al., 2017) exhibit short metacarpals but extremely long and slender proximal and intermediate phalanges. The metacarpals and phalanges are relatively long and slender in *Agilodocodon*, *Akidolestes*, *Sinodelphys*, *Ambolestes*, *Eomaia*, and *Juramaia* (Ji et al., 2002; Luo et al., 2003, 2011; Chen and Luo, 2013; Meng et al., 2015; Bi et al., 2018) and appear to be slender in the preserved digits of *Megaconus* (Zhou et al., 2013) and *Kryptobaatar* (Bolortsetseg, 2008).

The proximal alignment of the metacarpals differs within early mammals. The positions of Mc I and Mc V are of particular interest. In *Adalatherium*, the proximal end of Mc I is not aligned with that of Mc II but is more distally positioned to accommodate the trapezium. A similar arrangement has also been reconstructed for *Agilodocodon* (Meng et al., 2015), *Docofossor* (Luo et al., 2015b), *Arboroharamiya* (Han et al., 2017), *Maiopatagium* (Meng et al., 2017), *Shenshou* (Bi et al., 2014:fig. 1), *Qishou* (Bi et al., 2014: ED fig. 4a), *Sinobaatar* (Hu and Wang, 2002), *Zhangheotherium* (Hu et al., 1998), *Akidolestes* (Chen and Luo, 2013), *Ambolestes* (Bi et al., 2018), and *Eomaia* (Ji et al., 2002). By contrast, Mc I is proximally aligned with Mc II in *Chaoyangodens* (Hou and Meng, 2014), *Spinolestes* (Martin et al., 2015), *Rugosodon* (Yuan et al., 2013), *Barunlestes* (Kielan-Jaworowska, 1978), *Sinodelphys* (Luo et al., 2003), and *Asiatherium* (Trofimov and Szalay, 1994; Szalay and Trofimov, 1996). Furthermore, Mc V is in line with Mc IV and is positioned distal to the hamate in *Adalatherium*, as is the case in *Docofossor* (Luo et al., 2015b), *Chaoyangodens* (Hou and Meng, 2014), *Yanoconodon* (Chen et al., 2017), *Spinolestes* (Martin et al., 2015), *Arboroharamiya* (Han et al., 2017), *Maiopatagium* (Meng et al., 2017), *Sinobaatar* (Hu and Wang, 2002), *Sinodelphys* (Luo et al., 2003), *Ambolestes* (Bi et al., 2018), *Eomaia* (Ji et al., 2002), and *Barunlestes* (Kielan-Jaworowska, 1978). Metacarpal V is more proximally positioned than Mc IV in *Agilodocodon* (Meng et al., 2015), *Jeholodens* (Ji et al., 2002:fig. 3), *Liaoconodon* (Meng et al., 2011), *Zhangheotherium* (Hu et al., 1998), and monotremes (Ji et al., 2002:fig. 3).

The distal phalanges are uniform in *Adalatherium*, similar in length to the intermediate phalanges, and only gently curved. This is similar to the condition reconstructed for *Spinolestes* (Martin et al., 2015:fig. 1d) and *Kryptobaatar* (Bolortsetseg, 2008: fig. 34). In the eutriconodontans *Chaoyangodens*, *Yanoconodon*, and *Jeholodens* (Ji et al., 1999; Hou and Meng, 2014; Chen et al., 2017), the euharamiyidans *Arboroharamiya*, *Maiopatagium*, *Xianshou*, and *Shenshou* (Bi et al., 2014; Han et al., 2017; Meng et al., 2017), and the spalacotherioids *Zhangheotherium* and *Akidolestes* (Hu et al., 1998; Chen and Luo, 2013), the distal phalanges are gently curved but shorter than the intermediate phalanges, whereas the distal phalanges are curved, much shorter than the intermediate phalanges, and dorsopalmarly tall in *Eomaia* and *Sinodelphys* (Ji et al., 2002; Luo et al., 2003).

Pelvic Girdle

The most prominent feature of the pelvis of *Adalatherium* is the large size of the obturator foramen. It is more than twice as large

as the acetabulum. Such an enlarged obturator foramen is only known for cladotherians such as *Vincelestes*, *Henkelotherium*, *Eomaia*, *Ukhaatherium*, *Zalambdalestes*, *Barunlestes*, and *Pucadelphys* (Kielan-Jaworowska, 1978; Krebs, 1991; Rougier, 1993; Novacek et al., 1997; Ji et al., 2002; Horovitz, 2003; Jäger et al., 2019). The obturator foramen is intermediate in size (larger than, but not more than twice the size of, the acetabulum) in *Morganucodon*, *Repenomamus*, *Gobiconodon*, *Maiopatagium*, *Zhangheotherium*, and *Akidolestes* (Jenkins and Parrington, 1976; Jenkins and Schaff, 1988; Luo and Ji, 2005; Hu, 2006; Chen and Luo, 2013; Meng et al., 2017). The obturator foramen appears slightly larger than the acetabulum in *Xianshou* (Bi et al., 2014: ED fig. 1), but it is reconstructed as equivalent in size to the acetabulum by Bi et al. (2014:fig. 3a). The obturator foramen is much smaller and similar in size to the acetabulum in multituberculates and monotremes (Krause and Jenkins, 1983; Kielan-Jaworowska and Gambaryan, 1994; Bolortsetseg, 2008; Xu et al., 2015). It is also described as small in the eutriconodontan *Yanoconodon* (Chen et al., 2017).

Adalatherium also seems derived in having a straight dorsal edge of the ischium, a feature that is known in some euharamiyidans (Bi et al., 2014; Meng et al., 2017) and the cladotherians *Henkelotherium*, *Vincelestes*, *Eomaia*, *Ukhaatherium*, *Zalambdalestes*, *Barunlestes*, and *Pucadelphys* (Kielan-Jaworowska, 1978; Krebs, 1991; Rougier, 1993; Novacek et al., 1997; Ji et al., 2002; Horovitz, 2003; Jäger et al., 2019). The dorsal edge of the ischium is gently concave in eutriconodontans and *Arboroharamiya* (Jenkins and Schaff, 1988; Hu, 2006; Meng et al., 2011; Hou and Meng, 2014; Chen et al., 2017; Han et al., 2017) and greatly curved into a prominent, posterodorsally directed ischial tuberosity in *Morganucodon*, *Erythrotherium*, *Akidolestes*, multituberculates, and monotremes (Jenkins and Parrington, 1976; Krause and Jenkins, 1983; Kielan-Jaworowska and Gambaryan, 1994; Bolortsetseg, 2008; Chen and Luo, 2013; Yuan et al., 2013; Xu et al., 2015). The ischial tuberosity is also well developed in *Adalatherium*; it is laterally reflected but not posteriorly expanded as in multituberculates.

The ilium, ischium, and pubis appear to be fused in *Adalatherium*, a feature that is shared with most multituberculates, monotremes, *Akidolestes*, *Zhangheotherium*, *Maotherium*, *Vincelestes*, and therians (Huttenlocker et al., 2018:char. 282). The pelvic bones remain unfused in morganucodontans, docodontans, euharamiyidans, *Rugosodon*, *Sinobaatar, Jeholbaatar*, and eutriconodontans (Huttenlocker et al., 2018:char. 281; Wang et al., 2019; Zhou et al., 2019). Huttenlocker et al. (2018) also scored the pelvis as unfused in *Megaconus*, but the region does not seem to be well enough preserved to make such a determination unambiguously.

The dorsal margin of the acetabulum does not appear to be emarginated in *Adalatherium*. The femoral head is enclosed by the acetabulum, whereas in many early mammaliaforms the dorsal margin of the acetabulum is concave and the femoral head is exposed in dorsal view. An open and emarginated dorsal aspect of the acetabulum has been scored as present in morganucodontans, euharamiyidans, multituberculates, eutriconodontans, *Vincelestes*, *Ukhaatherium*, and *Asiatherium* by Huttenlocker et al. (2018:char. 281), whereas it is closed in spalacotherioids and most therians.

A small acetabular notch appears to be present in *Adalatherium*, but the posterior aspect of the acetabulum is poorly preserved and it is possible that the notch might just be an artifact. An acetabular notch is present in most mammaliaforms and is absent in monotremes (Jenkins and Parrington, 1976). A tuberosity for the lesser psoas muscle is absent in *Adalatherium*, as is the case in most mammaliaforms (Huttenlocker et al., 2018:char. 291). A prominent and well-developed, ventrally directed tuberosity is only present in monotremes and *Akidolestes* (Chen and Luo, 2013).

A postobturator notch (or possibly foramen), which has been identified in all multituberculates that preserve this region (Krause and Jenkins, 1983; Kielan-Jaworowska and Gambaryan, 1994; Bolortsetseg, 2008), is absent in *Adalatherium*. It is, however, interesting to note that the postobturator notch in multituberculates lies posterior to the obturator foramen in roughly the same position as the narrow constriction along the ischial blade extending from the ischium to the pubis in UA 9030.

The epipubis is present in *Adalatherium*, as is the case in morganucodontans, multituberculates, eutriconodontans, spalacotherioids, and early therians (Huttenlocker et al., 2018:char. 285). The only Mesozoic mammals reported to lack an epipubic bone are euharamiyidans (Bi et al., 2014; Han et al., 2017; Luo et al., 2017; Meng et al., 2017; Huttenlocker et al., 2018:char. 285; Mao and Meng, 2019).

Femur

The femur of *Adalatherium* is generally more similar to that of trechnotherians than to that of basal mammaliaforms (Fig. 57). For a detailed comparison of multituberculate, euharamiyidan, and gondwanatherian femoral morphology, see Krause et al. (2017). In *Adalatherium*, the femoral head is separated from the shaft by a short but distinct neck, a feature that is scored as present in *Zhangheotherium*, *Maotherium*, *Henkelotherium*, *Vincelestes*, *Eomaia*, *Ukhaatherium*, *Zalambdalestes*, *Sinodelphys*, *Asiatherium*, *Pucadelphys*, and multituberculates by Huttenlocker et al. (2018:char. 292). The femoral neck in multituberculates differs greatly from the short and broad morphology of the femoral neck in *Adalatherium* (Krause and Jenkins, 1983; Kielan-Jaworowska and Gambaryan, 1994; Hu and Wang, 2002; Bolortsetseg, 2008; Yuan et al., 2013; DeBey and Wilson, 2014; Xu et al., 2015; Mao et al., 2016; Krause et al., 2017; Csiki-Sava et al., 2018). In particular, in *Sinobaatar* (IVPP 12517), ?*Mesodma*, ?*Eucosmodon*, *Ptilodus*, *Kryptobaatar*, *Nemegtbaatar*, *Chulsanbaatar*, and *Litovoi* (Krause and Jenkins, 1983; Kielan-Jaworowska and Gambaryan, 1994; Bolortsetseg, 2008; Csiki-Sava et al., 2018), the femoral neck is long and slender and clearly separated from the greater trochanter proximolaterally by a deep incision. In *Adalatherium*, only a shallow indentation separates the greater trochanter from the femoral neck proximally. A similarly broad and short neck has also been described and imaged for the euharamiyidans *Arboroharamiya*, *Qishou*, *Shenshou*, and *Xianshou* (Bi et al., 2014; Han et al., 2017:S95) and has been scored as present in these forms by Han et al. (2017:char. 281). A broad and short neck is also present in *Maiopatagium* (Meng et al., 2017:ED fig. 1, contra scoring in Huttenlocker et al., 2018:char. 292), the eutriconodontans *Repenomamus* (Hu, 2006:fig. 3.31), *Gobiconodon* (Jenkins and Schaff, 1988), and possibly *Jeholodens* (Ji et al., 1999:fig. 1), and *Vincelestes* (Rougier, 1993:fig. 98). The femoral neck is also described as "short and indistinctive" in the spalacotherioid *Akidolestes* (Chen and Luo, 2013:173), but it is scored as present in Huttenlocker et al. (2018: char. 292). The femoral neck is absent in morganucodontans, docodontans, and monotremes (Huttenlocker et al., 2018:char. 292). It also appears to be absent in *Volaticotherium* (Meng et al., 2006), *Yanoconodon* (Chen et al., 2017:fig. 14), and *Liaoconodon* (Meng et al., 2011:fig. 1).

A small fovea capitis is preserved close to the center of the femoral head in *Adalatherium*, which is also present in morganucodontans, multituberculates, *Henkelotherium*, *Vincelestes*, and therians (Huttenlocker et al., 2018:char. 293). Monotremes, the docodontan *Haldanodon* (Martin, 2005), and the eutriconodontans *Gobiconodon* (Jenkins and Schaff, 1988) and *Repenomamus* (Hu, 2006) clearly lack a fovea on the femoral head.

The shape of the greater trochanter of *Adalatherium*, which is anteroposteriorly broad, obliquely oriented, and expands proximally, is markedly different from the condition seen in other

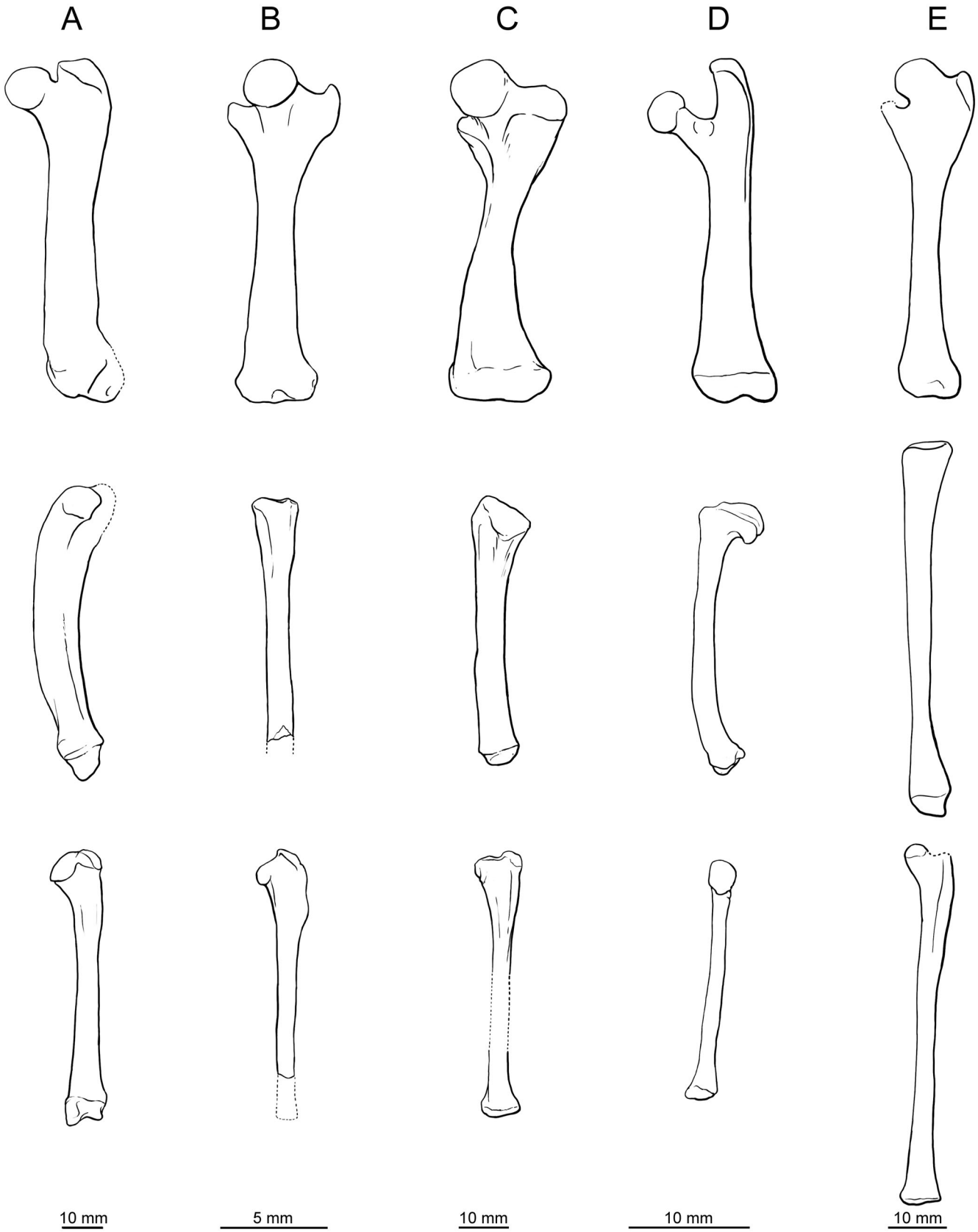

FIGURE 57. Comparison of left femur (top row), tibia (middle row), and fibula (bottom row) in five Mesozoic mammaliaforms. Femora in anterior view; tibiae and fibulae in lateral view. All femora at same length; tibiae and fibulae at lengths relative to femora. **A**, *Adalatherium*; **B**, the morganucododontan *Morganucodon* (after Jenkins and Parrington, 1976:figs. 12, 15, 16); **C**, the eutriconodontan *Repenomamus* (after Hu, 2006:figs. 3-31, 3-32); **D**, the multituberculate *Nemegtbaatar* (after Kielan-Jaworowska and Hurum, 2004:figs. 16, 17); and **E**, the stem therian *Vincelestes* (after Rougier, 1993: figs. 98–101).

Mesozoic mammaliaforms. In many non-therian mammaliaforms, the greater trochanter is flange-like, mediolaterally expanded, and tapers proximally, as is the case in morganucodontans (Jenkins and Parrington, 1976); docodontans (Martin, 2005; Meng et al., 2015; Zhou et al., 2019); euharamiyidans (Zheng et al., 2013; Bi et al., 2014; Han et al., 2017; Meng et al., 2017); monotremes; the shuotheriid *Pseudotribos* (Luo et al., 2007); the eutriconodontans *Repenomamus*, *Yanoconodon*, *Volaticotherium*, and *Liaconodon* (Hu, 2006; Meng et al., 2006, 2011; Chen et al., 2017); and the stem therian *Akidolestes* (Li and Luo, 2006:fig. 4d). The greater trochanter is rod-like and is directed proximally in multituberculates (e.g., Krause and Jenkins, 1983; Kielan-Jaworowska and Gambaryan, 1994; Bolortsetseg, 2008; DeBey and Wilson, 2014; Krause et al., 2017; Csiki-Sava et al., 2018) and the spalacotherioids *Zhangheotherium* (Hu et al., 1997) and *Maotherium* (Rougier et al., 2003; Ji et al., 2009). The greater trochanter of *Adalatherium* is most similar to that of *Pucadelphys* in being anteroposteriorly broad (Marshall and Sigogneau-Russell, 1995). *Adalatherium* is also similar to *Pucadelphys* in that the greater trochanter is level with the proximal extent of the femoral head. This is also the case in the eutriconodontans *Jeholodens*, *Yanoconodon*, *Volaticotherium*, and *Liaoconodon* (Ji et al., 1999; Meng et al., 2006, 2011; Chen et al., 2017). In most Mesozoic mammaliaforms, the greater trochanter is much shorter than the femoral head, as seen in morganucodontans, *Haldanodon*, *Microdocodon*, *Repenomamus*, *Arboroharamiya*, *Maiopatagium*, *Qishou*, *Shenshou*, *Xianshou*, *Vincelestes*, and *Akidolestes* (Jenkins and Parrington, 1976; Rougier, 1993; Martin, 2005; Hu, 2006; Li and Luo, 2006; Chen and Luo, 2013; Zheng et al., 2013; Bi et al., 2014; Han et al., 2017; Meng et al., 2017; Mao and Meng, 2019; Zhou et al., 2019). Multituberculates and the spalacotherioids *Zhangheotherium* and *Maotherium* are exceptional; the greater trochanter projects even farther proximally beyond the proximal extent of the femoral head (Krause and Jenkins, 1983; Kielan-Jaworowska and Gambaryan, 1994; Hu et al., 1997; Rougier et al., 2003; Bolortsetseg, 2008; Ji et al., 2009; Csiki-Sava et al., 2018).

Adalatherium further differs from basal mammaliaforms in possessing a small lesser trochanter that is positioned along the posterior margin of the femur. A posteriorly positioned lesser trochanter is also present in multituberculates (e.g., Krause and Jenkins, 1983; Kielan-Jaworowska and Gambaryan, 1994; Bolortsetseg, 2008; Krause et al., 2017; Csiki-Sava et al., 2018), but the posteromedially pointing flange is much larger than the small, knob-like process in *Adalatherium*. The lesser trochanter is also positioned on the posterior or posteromedial aspect of the femur in the spalacotherioids *Zhangheotherium* and *Maotherium*, as well as in therians, and is scored as such by Huttenlocker et al. (2018:char. 296). In contrast, the lesser trochanter is large, flange-like, and medially directed in morganucodontans, *Haldanodon*, *Microdocodon*, monotremes, *Pseudotribos*, *Gobiconodon*, *Repenomamus*, *Akidolestes*, *Vincelestes*, and *Henkelotherium* (Huttenlocker et al., 2018:char. 296; Zhou et al., 2019). The position of the lesser trochanter in euharamiyidans is contentious. Huttenlocker et al. (2018) scored the lesser trochanter as large and medially positioned in *Xianshou linglong*, *Xianshou songae*, *Shenshou*, *Maiopatagium*, and *Vilevolodon*, whereas Han et al. (2017) scored the trochanter as posteriorly positioned in *Shenshou* and *Xianshou linglong* and unknown in *Xianshou songae*. The compressed preservation of *Xianshou linglong*, *Xianshou songae*, and *Vilevolodon* seems to prevent an accurate assessment of the position, and it is here regarded as unknown. The lesser trochanter seems to be medially positioned in *Qishou* (Bi et al., 2014:ED fig. 4) and *Maiopatagium* (Meng et al., 2017:ED fig. 1).

A third trochanter is absent in *Adalatherium*, as is the case in most Mesozoic mammaliaforms. A third trochanter has only been described for the eutriconodontans *Repenomamus* and *Gobiconodon* (Jenkins and Schaff, 1988; Hu, 2006) and the docodontan *Haldanodon* (Martin, 2005). The compressed preservation of many early mammaliaforms might prevent the accurate identification of a third trochanter, in particular if it is only developed as a gentle ridge or a small and posteriorly directed process.

The presence and depth of the patellar groove have been variously identified in early mammaliaforms (see, for example, scorings by Huttenlocker et al. [2018] or O'Leary et al. [2013]). Here, a patellar groove is assumed to be present only if a distinct and smooth articular surface is preserved. Under this definition, a patellar groove is absent in *Morganucodon*, *Megazostrodon*, *Erythrotherium*, *Haldanodon*, *Repenomamus*, and *Gobiconodon*. Hu (2006:140) described the patellar groove as "broad and shallow" in *Repenomamus* but scored the patella as absent in that taxon. Hu (2006:fig. 3.31) illustrated a shallow concavity along the anterodistal margin of the femur, but the area is similar in texture to the shaft; as such, the patellar groove is treated as absent. A similar situation occurs in *Gobiconodon*; Jenkins and Schaff (1988:17) described a "broad, shallow patellar groove," but it cannot be clearly identified in their figures. A patellar groove was also likely absent in *Yanoconodon* (Chen et al., 2017:fig. 14) and *Jeholodens*; Ji et al. (1999:329) described it as "far less developed than in monotremes, multituberculates, and therians" in *Jeholodens*. A distinct and smooth patellar groove is present in *Adalatherium*, monotremes, multituberculates, *Zhangheotherium*, *Maotherium*, and therians (Krause and Jenkins, 1983; Kielan-Jaworowska and Gambaryan, 1994; Bolortsetseg, 2008; O'Leary et al., 2013; Mao et al., 2016; Wang et al., 2019). The patellar groove is shallow in *Adalatherium* and monotremes, but distinctly concave in *Maotherium* (Ji et al., 2009), *Pucadelphys* (Marshall and Sigogneau-Russell, 1995), *Ukhaatherium* (Horovitz, 2003), and the multituberculates *Ectypodus*, ?*Eucosomodon*, ?*Mesodma*, *Ptilodus*, *Sphenopsalis*, *Mangasbaatar*, *Kryptobaatar*, *Nemegtbaatar*, and *Chulsanbaatar* (Krause and Jenkins, 1983; Kielan-Jaworowska and Gambaryan, 1994; Bolortsetseg, 2008; Mao et al., 2016).

Tibia

The most prominent feature of the tibia in *Adalatherium* is its strong curvature (convex anteriorly, concave posteriorly) in side view. Among early mammaliaforms, curved tibiae, albeit less prominently curved, are only described for the metatherians *Mayulestes* and *Pucadelphys* (Argot, 2002). In both taxa, however, the tibia is not as compressed mediolaterally and expanded anteroposteriorly as in *Adalatherium*. In most Mesozoic mammaliaforms, the tibia is sigmoid in anterior view but relatively straight in side view, as seen in morganucodontans (Jenkins and Parrington, 1976), the docodontans *Agilodocodon*, *Haldanodon*, and *Microdocodon* (Martin, 2005; Meng et al., 2015; Zhou et al., 2019), monotremes, the eutriconodontans *Gobiconodon* and *Repenomamus* (Jenkins and Schaff, 1988; Hu, 2006), multituberculates (Krause and Jenkins, 1983; Kielan-Jaworowska and Gambaryan, 1994), the euharamiyidan *Arboroharamiya* (Han et al., 2017), the spalacotherioid *Akidolestes* (Chen and Luo, 2013), and many basal therians (Novacek et al., 1997; Szalay and Sargis, 2001; Horovitz, 2003; Bi et al., 2018). Presence of a sigmoid shaft might be obscured by the compressed preservation of some specimens. However, the tibia appears to be only gently curved to relatively straight in anterior view in the euharamiyidans *Qishou*, *Shenshou*, *Xianshou*, *Maiopatagium*, and *Vilevolodon* (Bi et al., 2014; Luo et al., 2017; Meng et al., 2017); the eutriconodontans *Jeholodens*, *Liaoconodon*, and *Yanoconodon* (Ji et al., 1999; Meng et al., 2011; Chen et al., 2017); and the spalacotherioids *Zhangheotherium* and *Maotherium* (Luo and Ji, 2005; Ji et al., 2009).

In *Adalatherium*, the tibia is gently sigmoid in anterior view, which is accentuated by the presence of a sharp, sinuous tibial crest (= anterior crest; cranial crest in Kielan-Jaworowska and Gambaryan, 1994; cnemial crest in Jenkins and Parrington, 1976) that extends along the entire length of the tibia. A short and rounded crest is present in morganucodontans (Jenkins and Parrington, 1976), the docodontans *Haldanodon* (Martin, 2005) and *Microdocodon* (Zhou et al., 2019), eutriconodontans (Jenkins and Schaff, 1988; Hu, 2006), and some multituberculates (Kielan-Jaworowska and Gambaryan, 1994), whereas it is indistinct in others (Krause and Jenkins, 1983). In none of these mammaliaforms does the tibial crest extend farther distally than mid-length of the tibia and nor is it as sharp or well defined as in *Adalatherium*.

The tibia is shorter than the femur (crural index [tibial length/femoral length] = 87%) in *Adalatherium*. Similarly, a relatively short tibia is known in *Haldanodon* (80% in Martin, 2005), *Repenomamus* (71–78% in Hu, 2006), *Yanoconodon* (87% in Chen et al., 2017), *Shenshou* (84% in Meng et al., 2017), and several multituberculates (71–79% in Krause and Jenkins, 1983; Kielan-Jaworowska and Gambaryan, 1994; Bolortsetseg, 2008; Meng et al., 2017). In contrast, the tibia is longer than the femur in the euharamiyidans *Arboroharamiya jenkinsi* (110% in Meng et al., 2017) and *Xianshou songae* (108% in Meng et al., 2017); the docodontans *Agilodocodon* (106% in Meng et al., 2017) and *Microdocodon* (116% in Zhou et al., 2019); the spalacotherioids *Akidolestes* and *Zhangheotherium* (107% in Meng et al., 2017); the monotreme *Ornithorhynchus* (150%); and the therians *Eomaia* (125% in Meng et al., 2017), *Sinodelphys* (122% in Meng et al., 2017), *Ambolestes* (120% in Bi et al., 2018), *Ukhaatherium* (~116% in Horovitz, 2003), and *Pucadelphys* (107% in Argot, 2002). The tibia is roughly comparable in length to the femur in *Jeholodens* (100% in Meng et al., 2017), *Maiopatagium* (104% in Meng et al., 2017), *Vilevolodon* (104% in Meng et al., 2017), *Maotherium* (95% in Meng et al., 2017), and *Henkelotherium* (90% in Molinero, 2003).

The tibia is slender and gracile in morganucodontans, euharamiyidans, the multituberculates *Ptilodus* and ?*Eucosmodon*, the spalacotherioid *Akidolestes*, and several Mesozoic therians (Jenkins and Parrington, 1976; Krause and Jenkins, 1983; Novacek et al., 1997; Ji et al., 2002; Horovitz, 2003; Chen and Luo, 2013; Bi et al., 2014; Han et al., 2017; Meng et al., 2017). By contrast, the tibia is remarkably robust in *Adalatherium* (Fig. 57). It is also robust in the docodontans *Haldanodon* and *Docofossor*; the eutriconodontans *Repenomamus*, *Jeholodens*, *Yanoconodon*, *Liaoconodon*, and *Spinolestes*; and the multituberculates *Yubaatar* and *Sphenopsalis* (Ji et al., 1999; Martin, 2005; Hu, 2006; Meng et al., 2011, 2015; Martin et al., 2015; Xu et al., 2015; Mao et al., 2016; Chen et al., 2017). The tibia is more intermediate in morphology, neither particularly robust nor slender, in the multituberculates *Rugosodon*, *Sinobaatar*, *Jeholbaatar, Nemegtbaatar*, *Kryptobaatar*, and *Catopsbaatar*, as well as the spalacotherioids *Zhangheotherium* and *Maotherium* (Kielan-Jaworowska and Gambaryan, 1994; Hu et al., 1997; Hu and Wang, 2002; Hurum and Kielan-Jaworowska, 2008; Ji et al., 2009; Yuan et al., 2013; Wang et al., 2019).

The proximal end of the tibia is poorly preserved in *Adalatherium*, but a laterally projecting tubercle for articulation with the fibula does not seem to be present. Such a hook-like proximolateral tubercle is a plesiomorphic feature within mammaliaforms and has been scored as present in morganucodontans, docodontans, euharamiyidans, multituberculates, *Pseudotribos*, and monotremes by Huttenlocker et al. (2018:char. 300). The hook-like process is particularly well developed in multituberculates (Krause and Jenkins, 1983; Kielan-Jaworowska and Gambaryan, 1994; Bolortsetseg, 2008, Csiki-Sava et al., 2018; Wang et al., 2019) but is less prominent in morganucodontans (Jenkins and Parrington, 1976). The process is indistinct in spalacotherioids, *Henkelotherium*, *Vincelestes*, and many basal therians (Huttenlocker et al., 2018:char. 300).

The distal articular facet on the tibia of *Adalatherium* bears a large medial malleolus that articulates with the medial aspect of the astragalus, as is the case in many cladotherians (Huttenlocker et al., 2018:char. 301). A small and bulbous medial malleolus is present in monotremes; the docodontans *Agilodocodon*, *Microdocodon*, and *Docofossor*; and the multituberculates *Rugosodon*, *Sinobaatar*, *Kryptobaatar*, *Ptilodus*, and ?*Eucosmodon* (Krause and Jenkins, 1983; Kielan-Jaworowska and Gambaryan, 1994; Hu and Wang, 2002; Yuan et al., 2013; Luo et al., 2015b; Meng et al., 2015; Zhou et al., 2019), but it is entirely absent or weakly developed in morganucodontans, euharamiyidans, eutriconodontans, spalacotherioids, and the multituberculate *Nemegtbaatar* (Kielan-Jaworowska and Gambaryan, 1994; Huttenlocker et al., 2018:char. 301), thus differing greatly from the condition in *Adalatherium*.

Fibula

The fibula is robust and large in *Adalatherium*, which is in stark contrast to the slender and gracile fibulae of most multituberculates, euharamiyidans, spalacotherioids, and basal therians (Krause and Jenkins, 1983; Kielan-Jaworowska and Gambaryan, 1994; Ji et al., 2002; Horovitz, 2003; Luo and Ji, 2005; Ji et al., 2009; Bi et al., 2014; Chen and Wilson, 2015; Han et al., 2017; Meng et al., 2017). The fibula of *Adalatherium* is similar in general appearance and robustness to those of morganucodontans; the eutriconodontans *Repenomamus*, *Gobiconodon*, and *Yanoconodon*; and the multituberculate *Yubaatar* (Jenkins and Parrington, 1976; Jenkins and Schaff, 1988; Hu, 2006; Xu et al., 2015; Chen et al., 2017). The proximal end of the fibula in *Adalatherium* is anteroposteriorly long and gently narrows distally, as it does in morganucodontans (Jenkins and Parrington, 1976), eutriconodontans (Jenkins and Schaff, 1988; Hu, 2006; Chen et al., 2017), docodontans (Meng et al., 2015; Zhou et al., 2019), and the eutherians *Eomaia* and *Ukhaatherium* (Ji et al., 2002; Horovitz, 2003). The proximal end is bulbous and not as anteroposteriorly expanded in the multituberculates *Nemegtbaatar*, *Kryptobaatar*, *Chulsanbaatar*, *Ptilodus*, *Rugosodon*, and *Sinobaatar* (Krause and Jenkins, 1983; Kielan-Jaworowska and Gambaryan, 1994; Hu and Wang, 2002; Yuan et al., 2013); the euharamiyidans *Arboroharamiya*, *Maiopatagium*, *Qishou*, *Shenshou, Vilevolodon*, and *Xianshou* (Bi et al., 2014; Han et al., 2017; Luo et al., 2017; Meng et al., 2017; Mao and Meng, 2019); and the spalacotherioid *Zhangheotherium* (based on the reconstruction of Luo and Ji, 2005:fig. 5). Multituberculates further differ from *Adalatherium* in possessing a hook-like process that extends posteriorly and bears the articular facet for the parafibula (Krause and Jenkins, 1983; Kielan-Jaworowska and Gambaryan, 1994; Hu and Wang, 2002; Yuan et al., 2013). The parafibular facet is also well developed in *Adalatherium* but, in contrast to multituberculates, it is positioned along the proximoposterior margin of the fibula and does not project any farther posteriorly or overhang the posterior margin. Horovitz (2000) described a similar facet for the eutherian *Ukhaatherium*.

Adalatherium is derived in possessing a large lateral malleolus (= styloid process), which is scored as weak or absent in all non-cladotherian mammaliaforms by Huttenlocker et al. (2018:char. 307). It is scored as present and distinct in *Henkelotherium*, *Vincelestes*, and several extant placentals. *Adalatherium* retains an extensive contact between the fibula and the calcaneus, which is reduced in many therians (Huttenlocker et al., 2018: char. 308). An extensive contact between the fibula and the calcaneus (relative to the extreme reduction seen in extant therians) is present in morganucodontans, monotremes, eutriconodontans, euharamiyidans, multituberculates, spalacotherioids, and several stem therians (Huttenlocker et al., 2018:char. 308). But even in

taxa that are scored as having an extensive contact between the fibula and the calcaneus, the facets vary in size and shape. In multituberculates and morganucodontans, the calcaneofibular facet is small and circular in outline, whereas it is large and elongate in *Adalatherium*.

Parafibula

Presence of a separate parafibula is shared by *Adalatherium*, multituberculates, *Ukhaatherium*, *Ambolestes*, and several extant therians (Krause and Jenkins, 1983; Kielan-Jaworowska and Gambaryan, 1994; Horovitz, 2000, 2003; Hu and Wang, 2002; Hurum and Kielan-Jaworowska, 2008; O'Leary et al., 2013; Yuan et al., 2013; Bi et al., 2018; Wang et al., 2019). To date, *Adalatherium* and multituberculates represent the only records of a separate parafibula in non-therian mammaliaforms. In multituberculates, the parafibula is large and ellipsoid in *Sinobaatar* (Hu and Wang, 2002; Hu, 2006), *Jeholbaatar* (Wang et al., 2019), and *Rugosodon* (Yuan et al., 2013; Luo et al., 2016) and elongate and slender in *Ptilodus* (Krause and Jenkins, 1983), *Ectypodus* (Bolortsetseg, 2008), *Kryptobaatar*, and *Chulsanbaatar* (Kielan-Jaworowska and Gambaryan, 1994). The preserved fragments in *Nemegtbaatar* (Kielan-Jaworowska and Gambaryan, 1994) and *Catopsbaatar* (Hurum and Kielan-Jaworowska, 2008) do not allow reconstruction of the size and shape of the parafibula. In placentals and most marsupials, the parafibula is generally a small and elliptical sesamoid bone that articulates with the proximal end of the fibula and ligamentously connects to the lateral femoral condyle. A sizable parafibula is known for the wombat *Vombatus* (= *Phascolomys*), the Tasmanian devil *Sarcophilus*, the brushtail possum *Trichosurus* (= *Phalangista*), the wallaby *Macropus*, and the bandicoot *Macrotis* (= *Perameles*) (Pearson and Davin, 1921). In these taxa, it is elongate and more similar in shape to that of *Adalatherium*, but still not quite as robust.

In extant therians, the parafibula provides the origin for the plantarflexors of the hind foot, gastrocnemius and plantaris (Vickaryous and Olson, 2007). The parafibula was first described in marsupials and was later homologized with the sesamoids of placentals, either as a complex of the placental cyamella (the sesamoid in the popliteus tendon) and lateral fabella (the sesamoid in the lateral head of gastrocnemius or plantaris) (Pearson and Davin, 1921) or as the lateral fabella alone (Haines, 1942). Detailed morphological descriptions by Pearson and Davin (1921), Haines (1942), and Lewis (1962) documented the presence of the parafibula in numerous placental and marsupial genera; as such, a parafibula is scored as present in *Didelphis*, *Tamandua*, *Solenodon*, *Echinops*, *Galeopterus*, *Ptilocerus*, *Tupaia*, and *Tarsius* (O'Leary et al., 2013). In monotremes and some marsupials, the parafibula is fused with the fibula, forming a distinct process (Pearson and Davin, 1921; Barnett and Lewis, 1958). Gambaryan et al. (2002) indicated that the parafibular process in monotremes serves as the attachment for an array of lower limb muscles, including extensors (extensor digitorum profundus, extensor hallucis longus, peroneus digiti quinti, peroneus longus, tibialis cranialis) and flexors (flexor digitorum fibularis, flexor digitorum tibialis, tibialis caudalis) of the hind foot and toes, thus exceeding the function of the parafibula in extant therians. Luo et al. (2016:160) speculated that the presence of a parafibula would provide for "a greater volume of muscles for plantarflexion, eversion and dorsiflexion of the ankle" during locomotion.

It is impossible to know whether the parafibula in *Adalatherium* and multituberculates served solely as the attachment for the lateral head of the gastrocnemius as in therians or whether it was functionally more diverse, as is the case in monotremes. Among Mesozoic mammaliaforms, a more prominent parafibular process similar to that in monotremes is known for the spalacotherioid *Akidolestes* (Li and Luo, 2006; Chen and Luo, 2013) and the docodontans *Docofossor* and *Microdocodon* (Luo et al., 2015b; Zhou et al., 2019). Despite the fact that the parafibula is fused to the fibula in monotremes and even in non-mammalian mammaliaforms, Lewis (1989) argued that a mobile parafibula is the plesiomorphic condition for mammals and that the prominent parafibular process is apomorphic.

Tarsus

The ankle joint has undergone remarkable changes in mammaliaform evolution, including superposition of the astragalus over the calcaneus (e.g., Jenkins, 1971; Szalay, 1993, 1994; Horovitz, 2000). In basal mammaliaforms, the two tarsals remain side by side and equally transmitted weight to the ground. A side-by-side configuration with little overlap is scored as present in morganucodontans, docodonts, monotremes, and eutriconodontans by Huttenlocker et al. (2018:char. 309). The astragalus partially overlaps the calcaneus in *Adalatherium*, the multituberculates *Rugosodon*, *Sinobaatar*, *Jeholbaatar*, *Kryptobaatar*, *Chulsanbaatar*, *Ptilodus*, and ?*Eucosmodon*, and the spalacotherioids *Akidolestes*, *Zhangheotherium*, and *Maotherium* (Krause and Jenkins, 1983; Kielan-Jaworowska and Gambaryan, 1994; Hu and Wang, 2002; Kielan-Jaworowska et al., 2004; Luo and Ji, 2005; Ji et al., 2009; Chen and Luo, 2013; Yuan et al., 2013; Luo et al., 2016; Wang et al., 2019), whereas complete superposition is only seen in *Vincelestes* and therians (Huttenlocker et al., 2018:char. 309). The degree of overlap is more contentious in euharamiyidans. The ankle joint of *Arboroharamiya jenkinsi* was originally scored as unknown for this feature by Zheng et al. (2013:char. 243) and Bi et al. (2014:char. 298). The scoring for astragalar superposition was changed to absent by Luo et al. (2015a:char. 298) and to unknown by Luo et al. (2017:char. 298). Han et al. (2017) confirmed that the hind foot of *Arboroharamiya jenkinsi* is too poorly preserved to assign a state. However, the ventral side of the hind foot is exposed in *Arboroharamiya allinhopsoni*, and the calcaneus appears large. Han et al. (2017) suggested that the astragalus would have partially or even completely overlapped the calcaneus. The scorings also differ between different matrices for *Shenshou* and *Xianshou*. Whereas Huttenlocker et al. (2018: char. 309) scored superposition as slight or absent in *Shenshou* and *Xianshou songae*, Han et al. (2017:char. 298) scored it as partially overlapping. Several morphological changes are associated with this transformation, including the size of the sustentacular process on the calcaneus, as well as the orientation, size, and position of the facets between the two bones (e.g., Jenkins, 1971; Szalay, 1993, 1994; Horovitz, 2000), which are discussed in detail below with the calcaneus.

Astragalus—The astragalus of *Adalatherium* is positioned obliquely within the hind foot and bears a well-developed trochlear facet distally to articulate with the navicular. An obliquely positioned astragalus and grooved navicular joint is also known for multituberculates (Krause and Jenkins, 1983; Kielan-Jaworowska and Gambaryan, 1994; Kielan-Jaworowska et al., 2004; Bolortsetseg, 2008; Yuan et al., 2013). In most Mesozoic mammaliaforms, the astragalus bears either a flat (*Morganucodon*, *Megazostrodon*, *Microdocodon*, *Agilodocodon*, *Yanoconodon*, *Jeholodens*, *Maiopatagium*, *Vincelestes*) or a convex navicular facet (*Repenomamus*, *Zhangheotherium*, *Akidolestes*), which, evolutionarily, expands into the convex head of the astragalus in therians (Jenkins and Parrington, 1976; Ji et al., 1999; Horovitz, 2000; Hu, 2006; Li and Luo, 2006; Chen and Luo, 2013; Zhou et al., 2013; Chen et al., 2017; Meng et al., 2017). In *Adalatherium* and multituberculates, the navicular possesses a well-defined ridge that glides in between two condyles on the astragalus. However, the astragalonavicular joint in *Adalatherium* differs from that of multituberculates in several respects. Most prominently, in *Adalatherium* the navicular not only articulates with

the groove but also completely encloses the lateral condyle (forming a trochlea), whereas in multituberculates the articulation appears to be limited to the groove itself, leading to a more saddle-shaped facet (Krause and Jenkins, 1983; Kielan-Jaworowska and Gambaryan, 1994; Bolortsetseg, 2008; Yuan et al., 2013; Luo et al., 2016). In other words, in multituberculates and *Adalatherium*, the distal articular facet bears medial and lateral condyles and a groove between the two. In multituberculates, the navicular facet extends from the center of the lateral condyle to the center of the medial condyle, whereas in *Adalatherium* it ranges from the center of the medial condyle to and including the lateral surfaces of the lateral condyle. As such, the medial and lateral condyles in *Adalatherium* enclose a narrow groove, whereas in *Rugosodon* (Yuan et al., 2013; Luo et al., 2016), *Sinobaatar* (Luo et al., 2016), *Kryptobaatar* (Kielan-Jaworowska and Gambaryan, 1994), ?*Eucosmodon* (Szalay, 1994), and *Ectypodus* (Bolortsetseg, 2008) the groove appears wider. In *Adalatherium*, the lateral condyle (which would have fully articulated with the navicular) is narrower and rounder and the medial condyle is more bulbous. The ridges appear similar in size in *Kryptobaatar*, *Rugosodon*, *Sinobaatar*, and ?*Eucosmodon*, whereas the medial ridge is narrower and the lateral ridge wider in *Ectypodus* (Kielan-Jaworowska and Gambaryan, 1994; Szalay 1994; Bolortsetseg, 2008; Yuan et al., 2013; Luo et al., 2016).

Compared with those of multituberculates, the astragalus of *Adalatherium* is more elongate and nearly square, whereas it tapers proximally in multituberculates, more so in *Rugosodon* and ?*Eucosmodon* and less so in *Kryptobaatar*, *Sinobaatar*, and *Ectypodus* (Krause and Jenkins, 1983; Kielan-Jaworowska and Gambaryan, 1994; Hu and Wang, 2002; Bolortsetseg, 2008; Yuan et al., 2013; Luo et al., 2016). In general, the astragalus is elongate in both multituberculates and *Adalatherium*, whereas it is round and kidney-shaped in *Morganucodon*, *Megazostrodon*, *Megaconus* and the eutriconodontans *Repenomamus* and *Yanoconodon* (Jenkins and Parrington, 1976; Hu, 2006; Zhou et al., 2013; Chen et al., 2017).

Proximally, the astragalofibular and lateral astragalotibial facets are distinct and separated in *Adalatherium* and multituberculates. The two facets meet at an angle of ~110° in *Adalatherium*, which appears to be similar in multituberculates but could not be precisely measured based on published images (Krause and Jenkins, 1983; Kielan-Jaworowska and Gambaryan, 1994; Bolortsetseg, 2008; Yuan et al., 2013; Luo et al., 2016). The lateral astragalotibial facet is flat and almost triangular in shape in *Adalatherium*. It most closely resembles the condition in the multituberculates *Kryptobaatar* (Kielan-Jaworowska and Gambaryan, 1994) and likely *Sinobaatar* (Luo et al., 2016:fig. 10) but differs from the concave and irregularly shaped articular facets in ?*Eucosmodon* (Szalay, 1994:fig. 5.9) and *Ectypodus* (Bolortsetseg, 2008:fig. 17). In morganucodontans, *Repenomamus*, and *Vincelestes*, the astragalotibial and astragalofibular facets are convex, almost confluent, and separated only by a fine crest (Jenkins and Parrington, 1976; Hu, 2006). The astragalotibial and astragalofibular facets also appear to be continuous in the reconstruction of the astragalus in *Yanoconodon* and *Jeholodens* (Chen et al., 2017:fig. 16c, e), but the poor preservation of their astragali precludes definite assessment of the proximal articular facet. In monotremes and the docodontans *Docofossor*, *Microdocodon*, and *Agilodocodon* (Luo et al., 2015b; Meng et al., 2015; Zhou et al., 2019), the astragalotibial and astragalofibular facets develop into two distinct condyles, resembling a trochlea (note that the trochlea of monotremes differs substantially and is not homologous with the therian trochlea). In therians, only the lateral astragalotibial facet develops into a pulley-shaped trochlea, and the astragalofibular facet faces laterally and the medial astragalotibial facet medially, almost in parallel to the former (Horovitz, 2000).

The medial astragalotibial facet is large and concave in *Adalatherium*, reflective of the large, convex medial malleolus of the tibia (Fig. 43B, C). A medial malleolus is absent or weak in morganucodontans, euharamiyidans, eutriconodontans, and spalacotherioids (Huttenlocker et al., 2018:char. 301); as such, a medial astragalotibial facet is small and indistinct in these taxa. A small medial malleolus is present in multituberculates, and a distinct, corresponding medial facet has been described for *Ectypodus* (Bolortsetseg, 2008:figs. 16, 17), ?*Eucosmodon* (Szalay, 1994:fig. 5.9), and *Rugosodon* (Yuan et al., 2013; Luo et al., 2016). In these multituberculates, the medial and lateral astragalotibial facets seem to be more aligned, whereas the medial astragalotibial facet is more medioplantarly positioned in *Adalatherium* and cannot be seen in dorsal view.

An astragalar neck, separating the body from the head, is absent in *Adalatherium*, as is the case in most non-therian mammaliaforms, including *Morganucodon*, *Megazostrodon*, *Megaconus*, monotremes, *Docofossor*, *Microdocodon*, *Repenomamus*, *Yanoconodon*, multituberculates, and *Zhangheotherium* (Jenkins and Parrington, 1976; Krause and Jenkins, 1983; Kielan-Jaworowska and Gambaryan, 1994; Luo and Ji, 2005; Hu, 2006; Bolortsetseg, 2008; Zhou et al., 2013, 2019; Luo et al., 2015b, 2016; Chen et al., 2017; Wang et al., 2019). It is uncertain whether an astragalar neck was present in the eutriconodontan *Jeholodens*. *Jeholodens* is reconstructed as having a constricted neck distal to the body of the astragalus (Ji et al., 1999); however, the distal articular facet is not expanded into a head and therefore differs from the condition seen in therians. Furthermore, Chen and Luo (2013:178) described the neck in *Akidolestes* as "more distinctive and longer than that of *Zhangheotherium*." Despite the fact that the neck is absent in *Zhangheotherium* and thus not a good qualifier to describe the length in *Akidolestes*, the figures provided by Chen and Luo (2013:fig. 17) support the presence of a short neck that separates the head from the body of the astragalus. A distinct astragalar neck is present in the therians *Ukhaatherium*, *Asioryctes*, *Zalambdalestes*, *Eomaia*, *Sinodelphys*, and *Pucadelphys* (Kielan-Jaworowska, 1977, 1978; Horovitz, 2000; Ji et al., 2002; Luo et al., 2003).

Calcaneus—The calcaneus of *Adalatherium* has a mediolaterally compressed and long tuber calcanei (56% of calcaneal length, measured in dorsal or side view from the posterior aspect of the calcaneofibular or calcaneoastragalar facets to the terminus of the tubercle). A long calcaneal tuber is a derived feature in mammals and is present in the multituberculates *Kryptobaatar* (48%; Bolortsetseg, 2008:figs. 39, 40), *Mangasbaatar* (56%; Bolortsetseg, 2008:figs. 47, 49), *Rugosodon* (42%; Luo et al., 2016:fig. 6c), ?*Eucosmodon* (46%; Szalay, 1994:fig. 5.9a), *Ptilodus* (51%; Krause and Jenkins, 1983:fig. 26a), ?*Stygimys* (48%; Krause and Jenkins, 1983:fig. 26c), and ?*Mesodma* (41%; Krause and Jenkins, 1983:fig. 26b) and the therians *Zalambdalestes* (46%; Kielan-Jaworowska, 1978:fig. 15b), *Pucadelphys* (51%; Muizon, 1998:table 11), and *Asioryctes* (46%; Kielan-Jaworowska, 1977: fig. a2). Based on ventral views, the tuber calcanei also appears long in *Sinodelphys* and *Eomaia* and is scored as elongate by Bi et al. (2018:char. 386). In contrast, the tuber is short in morganucodontans (33%; Szalay, 1994:fig. 5.5b); the eutriconodontans *Repenomamus* (34%; Hu, 2006:fig. 3.35a), *Jeholodens* (18%; Chen et al., 2017:fig. 16e), and *Yanoconodon* (18%; Chen et al., 2017:fig. 16b); the spalacotherioid *Zhangheotherium* (35%; Luo and Ji, 2005:fig. 7e); and monotremes (30%; Szalay, 1994:fig. 5.2a). The tuber calcanei is also scored as short in *Maiopatagium*, *Vilevolodon*, *Arboroharamiya allinhopsoni*, *Shenshou*, and *Xianshou* by Han et al. (2017:char. 307) and Huttenlocker et al. (2018:char. 318). Only the ventral view of the calcaneus is exposed in these taxa; indeed, the tuber does appear short but cannot be precisely measured in relationship to the proximal articular facets.

The tuber calcanei has a distinct swelling at its terminus in *Adalatherium*, docodontans, multituberculates, spalacotherioids, and cladotherians (Huttenlocker et al., 2018:char. 318). The terminal swelling is absent in morganucodontans and the euharamiyidans *Maiopatagium*, *Vilevolodon*, *Arboroharamiya allinhopsoni*, *Qishou*, *Shenshou*, and *Xianshou songae*. The ventral surface of the calcaneal tuber is straight in *Adalatherium*, as is the case in multituberculates, *Zhangheotherium*, *Vincelestes*, *Pucadelphys*, *Eomaia*, *Zalambdalestes*, and several extant therians (Krause and Jenkins, 1983; Rougier, 1993; Kielan-Jaworowska and Gambaryan, 1994; Szalay, 1994; O'Leary et al., 2013:char. 3527; Wang et al., 2019). In contrast, the tuber calcanei is ventrally curved in morganucodontans, docodontans, eutriconodontans, *Ukhaatherium*, and *Asioryctes* (Kielan-Jaworowska, 1977; Szalay, 1994; Jenkins and Schaff, 1988; Horovitz, 2000; Hu, 2006; Meng et al., 2015; Chen et al., 2017; Zhou et al., 2019). It should be noted that these character assignments more closely follow O'Leary et al. (2013:char. 3527), whereas Bi et al. (2018: char. 396) and Huttenlocker et al. (2018:char. 337) scored the ventral curvature as present in *Zhangheotherium*, *Vincelestes*, *Eomaia*, *Asioryctes*, *Ukhaatherium*, *Zalambdalestes*, and *Sinodelphys*, and absent in only a few therians.

Adalatherium and some multituberculates are derived in possessing a small and distinct peroneal process. In basal mammaliaforms, the peroneal process forms a large shelf that extends from the tuber calcanei to the calcaneocuboid facet. Such a process is present in morganucodontans, docodontans, *Arboroharamiya*, *Maiopatagium*, *Shenshou*, *Rugosodon*, *Gobiconodon*, *Repenomamus*, *Yanoconodon*, *Jeholodens*, and *Akidolestes*. Note that a large peroneal process is also scored as present in *Sinobaatar*, *Xianshou*, and *Vilevolodon*, but the process appears to be more restricted in *Sinobaatar* (Luo et al., 2016:fig. 8) and the preservation and views of the calcaneus in *Xianshou* and *Vilevolodon* do not allow for an accurate assessment of their morphology. The peroneal shelf is much smaller and does not extend anteriorly to the calcaneocuboid facet in *Zhangheotherium*, *Maotherium*, *Vincelestes*, *Eomaia*, *Asioryctes*, *Ukhaatherium*, and several therians (Huttenlocker et al., 2018: char. 320).

A small but distinct peroneal groove separates the peroneal process from the rest of the calcaneus anteriorly in *Adalatherium*. A shallow peroneal groove is also scored for *Zhangheotherium*, *Akidolestes*, *Maotherium*, *Vincelestes*, *Eomaia*, *Ukhaatherium*, *Asioryctes*, *Zalambdalestes*, *Sinodelphys*, and *Pucadelphys* (Huttenlocker et al., 2018:char. 322). In contrast, the peroneal groove is deep in the derived multituberculates ?*Eucosmodon*, *Kryptobaatar*, *Mangasbaatar*, *Ptilodus*, ?*Mesodma*, and ?*Stygimys* (Krause and Jenkins, 1983; Kielan-Jaworowska and Gambaryan, 1994; Bolortsetseg, 2008). In addition, Huttenlocker et al. (2018: char. 322) scored the peroneal groove as indistinct in *Arboroharamiya*, *Maiopatagium*, *Vilevolodon*, and *Xianshou*, but the poor preservation of the calcaneus prohibits assessment for *Arboroharamiya* and *Xianshou* (which was also noted by Han et al., 2017).

Compared with these derived features, *Adalatherium* is plesiomorphic in retaining a large articular facet for the fibula. Most of the proximal aspect of the calcaneal protuberance articulated with the fibula in *Adalatherium*. The astragalus would have articulated only along the medial margin of the protuberance. Similarly, the calcaneofibular facet occupies most of the calcanel protuberance in morganucodontans, docodontans, monotremes, and eutriconodontans (Jenkins and Parrington, 1976; Szalay, 1994; Hu, 2006; Zhou et al., 2013, 2019; Meng et al., 2015), whereas the calcaneoastragalar facet is similar in size to, or larger than, the calcaneofibular facet in multituberculates, spalacotherioids, and basal therians (Krause and Jenkins, 1983; Szalay, 1994; Horovitz, 2000; Bolortsetseg, 2008; Chen and Luo, 2013).

The sustentaculum tali is a medially directed shelf in *Adalatherium* that is positioned along the anterior one-third of the calcaneus. This is similar to the condition in cimolodontans, *Asioryctes*, *Ukhaatherium*, *Zalambdalestes*, *Sinodelphys*, *Deltatheridium*, and *Pucadelphys*. The sustentaculum tali is positioned farther posteriorly, near the midpoint of the calcaneus, in morganucodontans, docodontans, the multituberculates *Rugosodon* and *Sinobaatar*, monotremes, eutriconodontans, and spalacotherioids (Huttenlocker et al., 2018:char. 330). The sustentacular facet is vertically oriented and placed anterior to the calcaneoastragalar facet along the anteromedial edge of the calcaneus in *Adalatherium*. This is presumably the plesiomorphic condition among mammaliaforms, being present in *Morganucodon*, *Megazostrodon*, monotremes, *Gobiconodon*, *Repenomamus*, *Yanoconodon*, and *Jeholodens*. Note that Huttenlocker et al. (2018:char. 326, 327) also scored the sustentacular facet as vertical and placed along the medial edge in *Maiopatagium*, *Shenshou*, *Vilevolodon*, and *Xianshou*. Unfortunately, however, the calcanei are only preserved in ventral or partial side view in these taxa and do not allow for accurate assessment of the sustentacular facet. The position of the sustentacular facet is often used as an indicator for the degree of superposition in early mammaliaforms. The sustentacular facet is scored as anteromedially positioned with respect to the calcaneoastragalar facet in multituberculates, spalacotherioids, *Vincelestes*, *Sinodelphys*, *Deltatheridium*, and *Pucadelphys*, whereas it is strictly anteriorly positioned in *Eomaia*, *Asioryctes*, *Ukhaatherium*, and *Zalambdalestes* (Huttenlocker et al., 2018:char. 327).

Similar to the condition in multituberculates, the calcaneocuboid facet is ventromedially oriented in *Adalatherium*, whereas it is scored as ventrally oriented in *Morganucodon*, *Megazostrodon*, monotremes, *Agilodocodon*, *Docofossor*, *Gobiconodon* (note that Jenkins and Schaff [1988] described the facet as distally oriented), *Repenomamus*, *Yanoconodon*, and *Jeholodens* (Huttenlocker et al., 2018:char. 324). Huttenlocker et al. (2018) scored the calcaneocuboid facet of *Shenshou*, *Vilevolodon*, and *Xianshou* as ventrally oriented, but Han et al. (2017) described and scored the facet as ventromedially oriented in *Shenshou*, *Xianshou* and *Arboroharamiya allinhopsoni*, similar to the condition in multituberculates and *Adalatherium*. Although the cuboid appears to be more medially positioned relative to the calcaneus in *Shenshou lui* (paratype 1) and *Xianshou songae*, the joints are too poorly preserved to assess the orientation of the facet. Neither the position of the cuboid relative to the calcaneus nor the joint surface of the calcaneus is well enough preserved to describe the orientation of the facet in *Xianshou linglong*, *Vilevolodon*, or *Arboroharamiya*. In spalacotherioids, *Vincelestes*, and extant therians, the calcaneocuboid facet is distally oriented (Huttenlocker et al., 2018:char. 324).

Navicular, Cuboid, Cuneiforms—Detailed descriptions of the remaining tarsals (those other than the astragalus and calcaneus) that go beyond noting relative proportions and contact relationships are rare for non-therian mammaliaforms. For instance, although these remaining tarsals are preserved in several taxa, including the docodontans *Agilodocodon*, *Microdocodon*, and *Docofossor*; the eutriconodontans *Chaoyangodens*, *Jeholodens*, *Yanoconodon*, and *Liaoconodon*; the euharamiyidans *Arboroharamiya*, *Maiopatagium*, *Qishou*, *Shenshou*, and *Xianshou*; the multituberculates *Chulsanbaatar*, *Catopsbaatar*, *Jeholbaatar*, and *Yubaatar*; and the spalacotherioid *Maotherium* (Ji et al., 1999; Rougier et al., 2003; Hurum and Kielan-Jaworowska, 2008; Ji et al., 2009; Meng et al., 2011; Bi et al., 2014; Hou and Meng, 2014; Luo et al., 2015b; Meng et al., 2015, 2017; Xu et al., 2015; Chen et al., 2017; Han et al., 2017; Mao and Meng, 2019; Wang et al., 2019; Zhou et al., 2019), they have not been described in any significant detail and knowledge is frequently limited to the coarseness of scorings in phylogenetic matrices. Detailed understanding of tarsal

morphology other than the astragalus and calcaneus among early mammaliaforms is essentially limited to the morganucodontans *Morganucodon* and *Megazostrodon*; the eutriconodontan *Repenomamus* and *Yanoconodon*; the multituberculates *Rugosodon*, *Sinobaatar*, *Kryptobaatar*, *Ectypodus* (navicular), *Ptilodus*, and ?*Eucosmodon*; the spalacotherioids *Akidolestes* and *Zhangheotherium*; and the stem therian *Vincelestes* (Jenkins and Parrington, 1976; Krause and Jenkins, 1983; Rougier, 1993; Kielan-Jaworowska and Gambaryan, 1994; Luo and Ji, 2005; Hu, 2006; Bolortsetseg, 2008; Chen and Luo, 2013; Luo et al., 2016; Chen et al., 2017).

In dorsal view, the navicular is approximately equal in width to the cuboid in *Adalatherium*, a feature that it shares with multituberculates; the eutriconodontans *Repenomamus*, *Yanoconodon*, and *Jeholodens*; and several therians (Huttenlocker et al., 2018:char. 338). Huttenlocker et al. (2018) also scored the navicular as more slender in the euharamiyidans *Maiopatagium*, *Vilevolodon*, *Shenshou*, and *Xianshou*, but it is scored as unknown in *Xianshou* and *Shenshou* in the original descriptions by Bi et al. (2014) and as mediolaterally wider than the cuboid in at least *Xianshou linglong* and *Shenshou* by Han et al. (2017). The navicular is mediolaterally wider than the cuboid in *Megazostrodon*, docodontans, monotremes, *Akidolestes*, *Zhangheotherium*, *Maotherium*, and *Sinodelphys* (Huttenlocker et al., 2018:char. 338).

The articular facet for the astragalus on the navicular varies in how far it encloses medial or lateral aspects of the astragalus (Szalay, 1994; Horovitz, 2000; Luo et al., 2003). In most Mesozoic mammaliaforms, the proximal articular facet for the astragalus is gently concave or convex, matching its counterpart on the astragalus. The articular facet of *Adalatherium* and multituberculates differs from this pattern. The two dorsoplantarly elongate facets for the saddle-shaped astragalus are more gently concave in *Kryptobaatar* (Bolortsetseg, 2008:fig. 18), whereas, in particular, the lateral facet is deeply excavated in *Adalatherium* to accommodate the lateral condyle of the astragalus. The general shape of the navicular is similar in *Adalatherium* and multituberculates (Krause and Jenkins, 1983; Kielan-Jaworowska and Gambaryan, 1994:figs. 7, 25; Bolortsetseg, 2008:fig. 18; Yuan et al., 2013) in being roughly rectangular, dorsoplantarly deep, and mediolaterally short. *Adalatherium* and at least the multituberculates *Kryptobaatar* and *Ectypodus* bear a sizable plantar tuberosity (Kielan-Jaworowska and Gambaryan, 1994; Bolortsetseg, 2008). The navicular of *Repenomamus* resembles the shape of a cube, being almost equal in length, width, and height (Hu, 2006:fig. 3.36). It also bears a plantar tuberosity, but the bulbous tubercle is much smaller than that of *Adalatherium*.

The cuboid and navicular contact each other broadly in *Adalatherium*, the convex articular facet on the navicular matching the large and concave facet on the cuboid. In the eutriconodontan *Repenomamus*, the navicular appears to barely contact the cuboid in the articulated hind foot and a navicular facet is not described for the cuboid (Hu, 2006). Similarly, the contact appears limited in *Kryptobaatar* (ZPAL MgM-I/41; Kielan-Jaworowska and Gambaryan, 1994:fig. 7), whereas Bolortsetseg (2008) described the cuboid facet on the navicular of *Kryptobaatar* and *Ectypodus* as long and convex. It is likely that the cuboid and navicular are only displaced in ZPAL MgM-I/41 and would have broadly articulated in life. A large and convex articular facet is also described for ?*Eucosmodon* and *Ptilodus* (Krause and Jenkins, 1983).

The entocuneiform (proximodistally short, mediolaterally compressed, and dorsoplantarly long) of *Adalatherium* differs in shape from that of most Mesozoic mammaliaforms. Among multituberculates, it is most similar to those of *Rugosodon* and *Ectypodus* (Bolortsetseg, 2008; Yuan et al., 2013), whereas it appears proximodistally longer and dorsoplantarly shorter in *Kryptobaatar*, *Chulsanbaatar*, ?*Eucosmodon*, and *Ptilodus* (Krause and Jenkins, 1983; Kielan-Jaworowska and Gambaryan, 1994). In most early mammaliaforms, the entocuneiform is proximodistally longer than mediolaterally wide. In extreme cases such as *Zalambdalestes*, it is slender and comparable to the metatarsals in proportions (Kielan-Jaworowska, 1978). A long and narrow entocuneiform is also present in the basal mammaliaforms *Megazostrodon* and *Megaconus* (Jenkins and Parrington, 1976; Zhou et al., 2013); the euharamiyidans *Xianshou* and possibly *Qishou* (Bi et al., 2014:fig. 3g) and *Maiopatagium* (Meng et al., 2017); the spalacotherioid *Akidolestes* (Chen and Luo, 2013); and the therians *Sinodelphys*, *Eomaia*, *Zalambdalestes*, and *Asioryctes* (Kielan-Jaworowska, 1977, 1978; Ji et al., 2002; Luo et al., 2003). The entocuneiform is slightly more squarish but still longer than mediolaterally wide in the eutriconodontans *Jeholodens*, *Yanoconodon*, and *Repenomamus* (Ji et al., 1999; Hu, 2006; Chen et al., 2017).

Adalatherium differs from all multituberculates in that the distal facet of the entocuneiform is concave, whereas it is distinctly saddle-shaped in multituberculates (Huttenlocker et al., 2018:char. 340). The saddle-shaped distal facet of the entocuneiform is an autapomorphic feature of multituberculates not seen in any other Mesozoic mammaliaform. It should be noted that a saddle-shaped articulation is also scored as present for *Shenshou* and *Xianshou* in the original description of Bi et al. (2014) and in Han et al. (2017), but as absent in Huttenlocker et al. (2018). In this case, the scorings for *Shenshou*, if solely reliant on JTZ-D061, should now pertain to the morphology of *Qishou*. Based on the published figures in Bi et al. (2014:fig. 1, ED fig. 8b), it is difficult to determine whether a prominent saddle-shaped articulation was present in *Qishou*, but it appears to be more concave and similar to *Adalatherium* than to multituberculates.

The ectocuneiform and mesocuneiform are slender and small in most mammaliaforms, as is the case in *Adalatherium*. In contrast, the combined mediolateral width of the mesocuneiform and ectocuneiform is scored as wider than that of the entocuneiform in *Sinobaatar*, *Rugosodon*, cimolodontans, *Sinodelphys*, and *Pucadelphys* by Huttenlocker et al. (2018:char. 339). The mesocuneiform and ectocuneiform also seem to be equal in size to, or larger than, the entocuneiform in *Qishou*, *Jeholodens*, *Yanoconodon*, *Repenomamus*, *Zhangheotherium*, *Zalambdalestes*, and *Asioryctes* (Kielan-Jaworowska, 1977, 1978; Hu et al., 1997; Ji et al., 1999; Hu, 2006; Bi et al., 2014; Chen et al., 2017).

Os Calcaris—The os calcaris, which provides the base of the extratarsal spur in some mammaliaforms, is preserved in *Adalatherium* (Figs. 40, 42, 50). In monotremes, the tarsal spur consists of the os calcaris, which articulates with the distal end of the astragalus and tibia, and the ossified cornu calcaris, the bony core of the keratinous spur (Lewis, 1963, 1964; Hurum et al., 2006). An os calcaris is preserved in the multituberculates *Catopsbaatar*, *Kryptobaatar*, *Chulsanbaatar*, and *Rugosodon* (Hurum et al., 2006; Bolortsetseg, 2008; Hurum and Kielan-Jaworowska, 2008; Luo et al., 2016) but is absent in preserved specimens of *Sinobaatar* and *Ptilodus* (Krause and Jenkins, 1983; Hu and Wang, 2002). An os calcaris is also preserved in the euharamiyidans *Shenshou* and *Xianshou songae* (Bi et al., 2014). A similarly shaped element is also present in *Maiopatagium* and an unnamed juvenile euharamiyidan but is identified as a calcar because of its articular relationship with the calcaneus (Meng et al., 2017:ED fig. 7). Ossified calcaria are known in some bats and are associated with the uropatagium. Jenkins and Schaff (1988) first described the presence of an extratarsal spur in the eutriconodontan *Gobiconodon*, which preserves the co-ossified os calcaris and ossified cornu calcaris. The extratarsal spur is, however, missing in other well-preserved eutriconodontans such as *Jeholodens*, *Repenomamus*, and *Yanoconodon* (Ji et al., 1999; Hu, 2006; Chen et al., 2017). A partial extratarsal spur (co-ossified os calcaris and part of the ossified cornu calcaris) is also preserved in *Megaconus* (Zhou et al., 2013), *Zhangheotherium* (Hu et al., 1997; Hurum et al., 2006), *Akidolestes* (Li and Luo, 2006; Chen and Luo, 2013), and *Maotherium* (Ji et al., 2009).

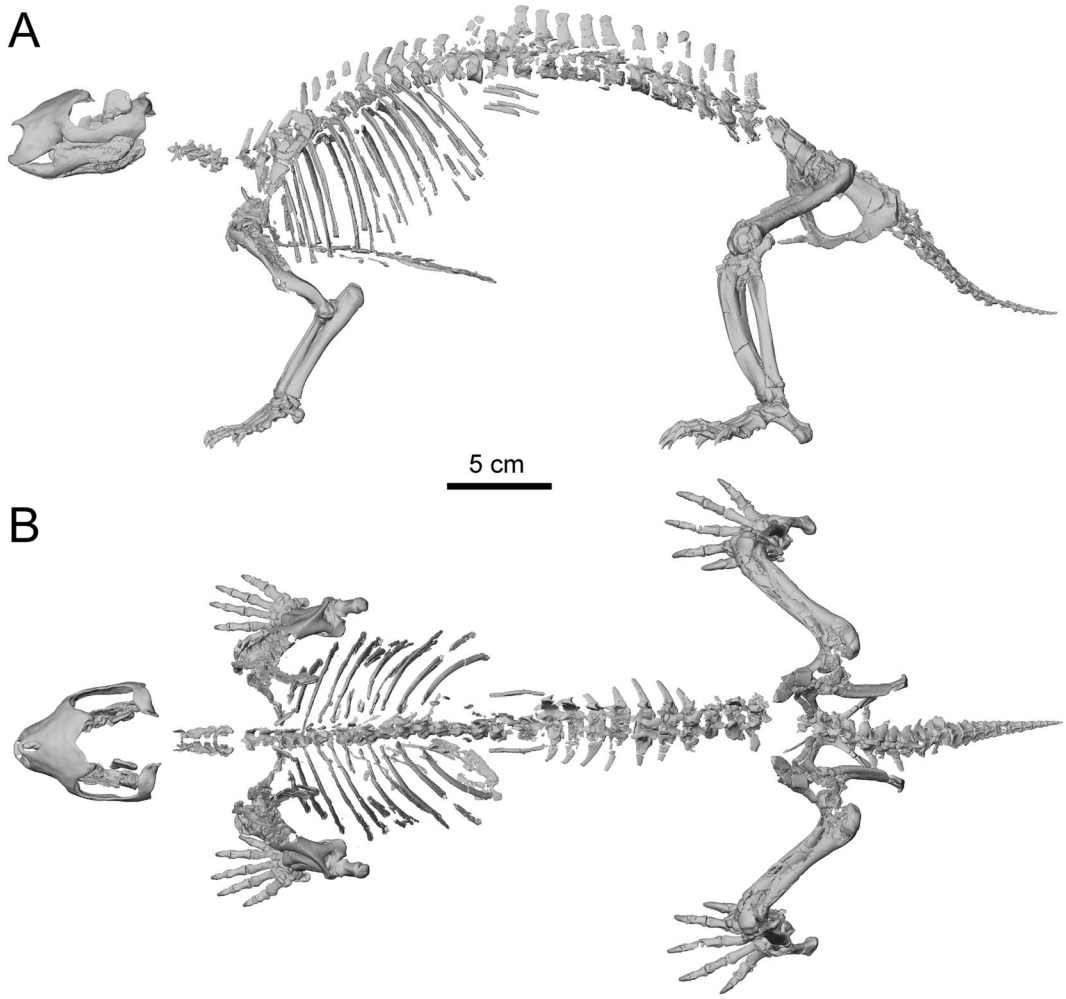

FIGURE 58. Skeletal reconstruction of *Adalatherium hui*, holotype (UA 9030), in **A**, left lateral and **B**, dorsal views based on three-dimensional surface files of elements.

Metatarsals and Pedal Phalanges

The first pedal digit is particularly prominent in *Adalatherium*. The first metatarsal is broad and short, the proximal phalanx is long and robust, and the first distal phalanx is larger than any other distal phalanx in the fore- or hind foot. Such prominence is not known for any other early mammaliaform. The metatarsals are generally slender and more uniform in *Megazostrodon*, the multituberculate *Kryptobaatar*, the spalacotherioids *Zhangheotherium* and *Maotherium*, and the cladotherians *Henkelotherium*, *Sinodelphys*, *Pucadelphys*, *Eomaia*, *Asioryctes*, and *Zalambdalestes* (Jenkins and Parrington, 1976; Kielan-Jaworowska, 1977, 1978; Krebs, 1991; Argot, 2002; Ji et al., 2002; Luo et al., 2003; Rougier et al., 2003; Luo and Ji, 2005; Bolortsetseg, 2008; Ji et al., 2009), whereas they are intermediate, not slender but also not robust (as is the case for metatarsals II–IV in *Adalatherium*), in the multituberculates *Sinobaatar*, *Rugosodon*, *Jeholbaatar*, *Catopsbaatar*, and ?*Eucosmodon*; the docodontan *Agilodocodon*; and the eutriconodontans *Jeholodens*, *Yanoconodon*, and *Chaoyangodens* (Krause and Jenkins, 1983; Ji et al., 1999; Hu and Wang, 2002; Hurum and Kielan-Jaworowska, 2008; Yuan et al., 2013; Hou and Meng, 2014; Meng et al., 2015; Luo et al., 2016; Chen et al., 2017; Wang et al., 2019). The metatarsals are stouter, but still relatively uniform in size and shape, in the eutriconodontan *Repenomamus* (Hu, 2006) and the spalacotherioid *Akidolestes* (Chen and Luo, 2013). In *Arboroharamiya*, *Maiopatagium*, *Qishou, Shenshou*, *Vilevolodon*, and *Xianshou*, the metatarsals are very short and almost stout compared with the long and slender phalanges (Zheng et al., 2013; Bi et al., 2014; Han et al., 2017; Luo et al., 2017; Meng et al., 2017; Mao and Meng, 2019).

Mt V is shorter and slightly broader than Mt II–Mt IV in *Adalatherium*. It bears a prominent ventrolateral tubercle at the proximal end, a feature that is also known for cimolodontans, *Sinobaatar*, *Rugosodon*, *Repenomamus*, *Yanoconodon*, *Akidolestes*, *Vincelestes*, *Eomaia*, *Sinodelphys*, and *Pucadelphys* (Huttenlocker et al., 2018:char. 345). In contrast, the tubercle is scored as indistinct or absent in *Megazostrodon*, *Jeholodens*, *Maiopatagium*, *Shenshou*, *Vilevolodon*, *Xianshou*, monotremes, *Zhangheotherium*, *Henkelotherium*, *Asioryctes*, *Ukhaatherium*, and *Zalambdalestes* (Huttenlocker et al., 2018:char. 345).

The distal phalanges are similar in size across digits in the euharamiyidans *Agilodocodon*, *Arboroharamiya*, *Maiopatagium*, *Qishou, Shenshou*, *Vilevolodon*, and *Xianshou*; the multituberculates *Sinobaatar*, *Jeholbaatar*, ?*Eucosmodon*, and *Kryptobaatar*; the eutriconodontans *Jeholodens* and *Chaoyangodens*; and the spalacotherioids *Zhangheotherium* and *Maotherium* (Krause and Jenkins, 1983; Kielan-Jaworowska and Gambaryan, 1994; Ji et al., 1999; Hu and Wang, 2002; Rougier et al., 2003; Luo and Ji, 2005; Ji et al., 2009; Zheng et al., 2013; Bi et al., 2014; Hou and Meng, 2014; Meng et al., 2015, 2017; Han et al., 2017; Luo

et al., 2017; Wang et al., 2019). The first distal phalanx is even shorter than the distal phalanges of digits II–V in *Akidolestes* (Chen and Luo, 2013).

CONCLUSIONS

Adalatherium hui is the first gondwanatherian and only the fourth Mesozoic mammaliaform from the entire supercontinent Gondwana that is represented by articulated postcranial material. The skeleton of the holotype and only known specimen, UA 9030, is exceptionally complete and well preserved, including manual and pedal sesamoid bones and costal cartilages. As such, it ranks among the most outstanding Mesozoic mammaliaform specimens and substantially expands knowledge of the mammalian fossil record of Gondwana.

The postcranial remains of *Adalatherium* reveal a unique mosaic of plesiomorphic and derived traits. *Adalatherium* possesses numerous features that are highly derived and even unique among Mesozoic mammaliaforms, including an unusually high number of trunk vertebrae (at least 16 thoracic and 12 lumbar vertebrae), a short tail with almost all 24 caudal vertebrae (all except the three distal-most) wider than long, a trochleated navicular facet on the astragalus, and a mediolaterally compressed and anteroposteriorly bowed tibia. Of the unusually derived postcranial features of *Adalatherium*, several resemble those found in cladotherians. Considering the deeply nested position of *Adalatherium* (and other gondwanatherians) within Allotheria (Hoffmann, Beck, et al., 2020; Krause, Hoffmann, et al., 2020), we tentatively conclude that these features evolved convergently or in parallel. For instance, the scapula of *Adalatherium* has a fully developed spine dividing the lateral surface into supraspinous and infraspinous fossae, thus resembling the condition in cladotherians. The os coxa bears an exceptionally large obturator foramen much like that seen in some cladotherians, and the calcaneus has a long, mediolaterally compressed, and dorsoventrally deep tuber, a feature that is otherwise found in various therians. Most prominently, *Adalatherium* possesses a fully developed humeral trochlea, a feature that is not seen in any other non-therian mammaliaform. Accordingly, the morphology of the proximal aspect of the radius and ulna is more similar to that of extant therians than to that of more basal mammaliaforms.

In conjunction with a ventrally facing glenoid fossa of the scapulocoracoid and a mobile sternoclavicular joint, the above-listed features of the brachium and antebrachium indicate a parasagittal forelimb posture in *Adalatherium* (Fig. 58), similar to that of therians and different from the relatively sprawling posture reconstructed for morganucodontans, docodontans, multituberculates, eutriconodontans, and some spalacotherioids (Jenkins, 1973; Kielan-Jaworowska and Gambaryan, 1994; Gambaryan and Kielan-Jaworowska, 1997; Hu et al., 1997; Ji et al., 1999; Kielan-Jaworowska et al., 2004; Kielan-Jaworowska and Hurum, 2006). Surprisingly, the dorsoventral depth of the pelvis, the asymmetrical distal articular facets of the femur, and the torsion of the tibia indicate a relatively abducted, 'sprawling' posture of the femur (Fig. 58). The femur was likely less abducted than in, for example, docodontans, multituberculates, or monotremes. In contrast to these taxa, *Adalatherium* lacks several of the features identified in Kielan-Jaworowska and Hurum (2006) as indicative of a sprawling stance in multituberculates, such as diameter of the tibia larger in a mediolateral than in an anteroposterior direction and metatarsal III abducted relative to the calcaneus. As such, the locomotion of *Adalatherium* appears to have been distinctly different from that of early mammaliaforms with a sprawling gait, but also different from that of most extant therians that place both the forelimb and hind limb more directly underneath the body.

In contrast to these derived features, some aspects of the postcranial morphology of *Adalatherium* are plesiomorphic, such as the large unfused coracoid, the separate parafibula, and the extensive contact between the calcaneus and the fibula. This combination of plesiomorphic and derived traits is likely reflective of the long evolutionary history in geographic isolation on Madagascar. This pattern is not only evident in *Adalatherium* but has also been documented for numerous other Late Cretaceous vertebrates from Madagascar, including another gondwanatherian mammal, *Vintana* (Krause, 2014; Krause et al., 2014b).

ACKNOWLEDGMENTS

We gratefully acknowledge V. Heisey (Stony Brook University) and J. Groenke (Ohio University) for mechanical preparation of the skeleton of UA 9030; B.-A. S. Bhullar (Yale University), J. Groenke (Ohio University), M. Hill (AMNH), P. O'Connor (Ohio University), and K. Hurdle (New York Institute of Technology) for μCT imaging of the skeleton and individual postcranial elements; J. Groenke (Ohio University) for assistance with digital imaging; J. Neville and M. Stewart (both Stony Brook University) for taking photographs; L. Betti-Nash (Stony Brook University) for executing the drawings in Figures 56 and 57 and editing photographs of several other figures; J. Molnar (New York Institute of Technology) for assistance in reconstructing thoracic and lumbar vertebrae for Figures 7 and 10; and K. Pan (New York Institute of Technology) for digitally articulating the postcranial skeleton. We also thank the following curators, collection managers, and colleagues for allowing access to specimens as well as for their accessibility and hospitality during visits: J. Galkin, J. Meng, and E. Westwig (AMNH); Q.-J. Meng (BMNHC); C. Jin, H. Wang, and Y. Wang (IVPP); P. Brewer and J. Hooker (NHM); C. Zhou (PMOL); T. Martin (University of Bonn); P. Gill (University of Bristol); Z.-X. Luo (University of Chicago); R. Asher, J. Clack, M. Lowe, and R. O'Meara (University Museum of Zoology, Cambridge); and Ł. Fostowicz (ZPAL). We also thank countless individuals for fruitful discussions on Mesozoic mammaliaform evolution in the context of postcranial morphology but here single out in particular M. Chen (NJU), J. Meng (AMNH), Z.-X. Luo (University of Chicago), and E. Seiffert (University of Southern California). Finally, we are immensely grateful to M. Chen (NJU) and L. Gaetano (National Scientific and Technical Research Council), whose thorough reviews of the manuscript have improved it considerably. This research was supported by the National Science Foundation (grants DEB-1501497 and MRI-1828305 to S.H. and EAR-9706302, EAR-0106477, EAR-0446488, EAR-1122642, EAR-1528273, and EAR-1664432 to D.W.K.) and a grant from the Office of the Vice President for Research, Stony Brook University (2005–2007), to support the late Y. Hu as a postdoctoral associate.

ORCID

Simone Hoffmann http://orcid.org/0000-0001-8984-0601
David W. Krause http://orcid.org/0000-0001-7860-6828

LITERATURE CITED

Anantharaman, S., G. P. Wilson, D. C. D. Sarma, and W. A. Clemens. 2006. A possible Late Cretaceous "haramiyidan" from India. Journal of Vertebrate Paleontology 26:488–490.

Argot, C. 2002. Functional-adaptive analysis of the hindlimb anatomy of extant marsupials and the paleobiology of the Paleocene marsupials *Mayulestes ferox* and *Pucadelphys andinus*. Journal of Morphology 253:76–108.

Asher, R. J., K. H. Lin, N. Kardjilov, and L. Hautier. 2011. Variability and constraint in the mammalian vertebral column. Journal of Evolutionary Biology 24:1080–1090.

Barnett, C. H., and O. J. Lewis. 1958. The evolution of some traction epiphyses in birds and mammals. Journal of Anatomy 92:593–601.
Bi, S., Y. Wang, J. Guan, X. Sheng, and J. Meng. 2014. Three new Jurassic euharamiyidan species reinforce early divergence of mammals. Nature 514:579–584.
Bi, S., X. Zheng, X. Wang, N. E. Cignetti, S. Yang, and J. R. Wible. 2018. An Early Cretaceous eutherian and the placental–marsupial dichotomy. Nature 228:390–395.
Bolortsetseg, B. 2008. Description of three new specimens of cimolodontans and a phylogenetic study of the postcranial anatomy of Multituberculata (Mammalia, Synapsida). Ph.D. dissertation, The City University of New York, New York, New York, 304 pp.
Bonaparte, J. F. 1963. Descripción del esqueleto postcraneano de *Exaeretodon* (Cynodontia-Traversodontidae). Acta Geológica Lilloana 4:5–53.
Bonaparte, J. F. 1986. Sobre *Mesungulatum houssayi* y nuevos mamıferos Cretacicos de Patagonia, Argentina. Actas IV Congreso Argentino de Paleontologıa y Bioestratigrafıa, Mendoza, Argentina, 23–27 November 1986, 2:48–61.
Bordy, E. M., and P. Eriksson. 2015. Lithostratigraphy of the Elliot Formation (Karoo Supergroup), South Africa. South African Journal of Geology 118:311–316.
Bordy, E. M., A. J. Bumby, O. Catuneanu, and P. G. Eriksson. 2004. Advanced Early Jurassic termite (Insecta: Isoptera) nests: evidence from the Clarens Formation in the Tuli basin, southern Africa. Palaios 19:68–78.
Broom, R. 1903. On the axis, atlas and proatlas in the higher theriodonts. Proceedings of the Zoological Society of London 73:177–218.
Buchholtz, E., A. Feldman, and Z. Yozgyur. 2018. Composite structure and homology in the therian presternum: a hypothesis. Journal of Vertebrate Paleontology 38(Program and Abstracts):98.
Butler, E., F. Abdala, and J. Botha-Brink. 2019. Postcranial morphology of the Early Triassic epicynodont *Galesaurus planiceps* (Owen) from the Karoo Basin, South Africa. Papers in Palaeontology 5:1–32.
Chen, M., and Z.-X. Luo. 2013. Postcranial skeleton of the Cretaceous mammal *Akidolestes cifellii* and its locomotor adaptations. Journal of Mammalian Evolution 20:159–189.
Chen, M., and G. P. Wilson. 2015. A multivariate approach to infer locomotor modes in Mesozoic mammals. Paleobiology 41:280–312.
Chen, M., Z.-X. Luo, and G. P. Wilson. 2017. The postcranial skeleton of *Yanoconodon allini* from the Early Cretaceous of Hebei, China, and its implications for locomotor adaptation in eutriconodontan mammals. Journal of Vertebrate Paleontology 37:e1315425.
Chester, S. G. B., E. J. Sargis, F. S. Szalay, J. D. Archibald, and A. O. Averianov. 2010. Mammalian distal humeri from the Late Cretaceous of Uzbekistan. Acta Palaeontologica Polonica 55:199–211.
Crompton, A. W. 1974. The dentition and relationships of the southern African Triassic mammals, *Erythrotherium parringtoni* and *Megazostrodon rudnerae*. Bulletin of the British Museum (Natural History) Geology 24:397–437.
Crompton, A. W., and F. A. Jenkins Jr. 1968. Molar occlusion in Late Triassic mammals. Biological Reviews 43:427–458.
Crompton, A. W., and F. A. Jenkins Jr. 1973. Mammals from reptiles: a review of mammalian origins. Annual Review of Earth and Planetary Sciences 1:131–155.
Csiki-Sava, Z., M. Vremir, J. Meng, S. L. Brusatte, and M. A. Norell. 2018. Dome-headed, small-brained island mammal from the Late Cretaceous of Romania. Proceedings of the National Academy of Sciences of the United States of America 115:4857–4862.
DeBey, L. B., and G. P. Wilson. 2014. Mammalian femora across the Cretaceous–Paleogene boundary in eastern Montana. Cretaceous Research 51:361–385.
Engelmann, G. F., and G. Callison. 1998. Mammalian faunas of the Morrison Formation. Modern Geology 23:343–379.
Evans, H. E. 1993. Miller's Anatomy of the Dog. W. B. Saunders, Philadelphia, Pennsylvania, 1,113 pp.
Gaetano, L. C., and G. W. Rougier. 2011. New materials of *Argentoconodon fariasorum* (Mammaliaformes, Triconodontidae) from the Jurassic of Argentina and its bearing on triconodont phylogeny. Journal of Vertebrate Paleontology 31:829–843.
Gaetano, L. C., F. Abdala, and R. Govender. 2017. The postcranial skeleton of the Lower Jurassic *Tritylodon longaevus* from southern Africa. Ameghiniana 54:1–35.
Gaetano, L. C., C. A. Marsicano, and G. W. Rougier. 2013. A revision of the putative Late Cretaceous triconodonts from South America. Cretaceous Research 46:90–100.
Gaetano, L. C., H. Mocke, and F. Abdala. 2018. The postcranial anatomy of *Diademodon tetragonus* (Cynodontia, Cynognathia). Journal of Vertebrate Paleontology 38:e1451872.
Galis, F. 1999. Why do almost all mammals have seven cervical vertebrae? Developmental constraints, Hox genes, and cancer. Journal of Experimental Zoology 285:19–26.
Galis, F., D. R. Carrier, J. van Alphen, S. D. van der Mije, T. J. M. Van Dooren, J. A. J. Metz, and C. M. A. ten Broek. 2014. Fast running restricts evolutionary change of the vertebral column in mammals. Proceedings of the National Academy of Sciences of the United States of America 111:11401–11406.
Gambaryan, P. P., and Z. Kielan-Jaworowska. 1997. Sprawling versus parasagittal stance in multituberculate mammals. Acta Palaeontologica Polonica 42:13–44.
Gambaryan, P. P., A. A. Aristov, J. M. Dixon, and G. Y. Zubtsova. 2002. Peculiarities of the hind limb musculature in monotremes: an anatomical description and functional approach. Russian Journal of Theriology 1:1–36.
Gambaryan, P. P., A. N. Kuznetsov, A. A. Panyutina, and S. V. Gerasimov. 2015. Shoulder girdle and forelimb myology of extant Monotremata. Russian Journal of Theriology 14:1–56.
Gow, C. E. 1986. A new skull of *Megazostrodon* (Mammalia, Triconodonta) from the Elliot Formation (Lower Jurassic) of southern Africa. Palaeontologia africana 26:13–23.
Gow, C. E. 2001. A partial skeleton of the tritheledontid *Pachygenelus* (Therapsida: Cynodontia). Palaeontologia africana 37:93–97.
Guignard, M. L., A. G. Martinelli, and M. B. Soares. 2019. Postcranial anatomy of *Riograndia guaibensis* (Cynodontia: Ictidosauria). Geobios 53:9–21.
Gurovich, Y. 2006. Bio-evolutionary aspects of Mesozoic mammals: description, phylogenetic relationships and evolution of the Gondwanatheria (Late Cretaceous and Paleocene of Gondwana). Ph.D. dissertation, Universidad Nacional de Buenos Aires, Buenos Aires, Argentina, 621 pp.
Gurovich, Y. 2008. Additional specimens of sudamericid (Gondwanatheria) mammals from the early Paleocene of Argentina. Palaeontology 51:1069–1089.
Haines, R. W. 1942. The tetrapod knee joint. Journal of Anatomy 76:270–301.
Haines, R. W. 1946. A revision of the movements of the forearm in tetrapods. Journal of Anatomy 80:1–11.
Han, G., and J. Meng. 2016. A new spalacolestine mammal from the Early Cretaceous Jehol Biota and implications for the morphology, phylogeny, and palaeobiology of Laurasian 'symmetrodontans.' Zoological Journal of the Linnean Society 178:343–380.
Han, G., F. Mao, S. Bi, Y. Wang, and J. Meng. 2017. A Jurassic gliding euharamiyidan mammal with an ear of five auditory bones. Nature 551:451–456.
Hautier, L., V. Weisbecker, M. R. Sánchez-Villagras, A. Goswami, and R. J. Asher. 2010. Skeletal development in sloths and the evolution of mammalian vertebral patterning. Proceedings of the National Academy of Sciences of the United States of America 107:18903–18908.
Hoffmann S., R. M. D. Beck, J. R. Wible, G. W. Rougier, and D. W. Krause. 2020. Phylogenetic placement of *Adalatherium hui* (Mammalia, Gondwanatheria) from the Late Cretaceous of Madagascar: implications for allotherian relationships; pp. 213–234 in D. W. Krause and S. Hoffmann (eds.), *Adalatherium hui* (Mammalia, Gondwanatheria) from the Late Cretaceous of Madagascar. Society of Vertebrate Paleontology 21. Journal of Vertebrate Paleontology 40(2, Supplement).
Holmgren, N. 1952. An embryological analysis of the mammalian carpus and its bearing upon the question of the origin of the tetrapod limb. Acta Zoologica 33:1–115.
Horovitz, I. 2000. The tarsus of *Ukhaatherium nessovi* (Eutheria, Mammalia) from the Late Cretaceous of Mongolia: an appraisal of the evolution of the ankle in basal therians. Journal of Vertebrate Paleontology 20:547–560.
Horovitz, I. 2003. Postcranial skeleton of *Ukhaatherium nessov*i (Eutheria, Mammalia) from the Late Cretaceous of Mongolia. Journal of Vertebrate Paleontology 23:857–868.

Hou, S., and J. Meng. 2014. A new eutriconodont mammal from the early Cretaceous Jehol Biota of Liaoning, China. Chinese Science Bulletin 59:546–553.
Hu, Y. 2006. Postcranial morphology of *Repenomamus* (Eutriconodonta, Mammalia): implications for the higher-level phylogeny of mammals. Ph.D. dissertation, City University of New York, New York, New York, 405 pp.
Hu, Y., and Y. Wang. 2002. *Sinobaatar* gen. nov.: first multituberculate from the Jehol Biota of Liaoning, Northeast China. Chinese Science Bulletin 47:933–938.
Hu, Y., Y. Wang, C.-K. Li, and Z.-X. Luo. 1998. Morphology of dentition and forelimb of *Zhangheotherium*. Vertebrata PalAsiatica 36:102–125.
Hu, Y., Y. Wang, Z.-X. Luo, and C.-K. Li. 1997. A new symmetrodont mammal from China and its implications for mammalian evolution. Nature 390:137–142.
Hurum, J. H., and Z. Kielan-Jaworowska. 2008. Postcranial skeleton of a Cretaceous multituberculate mammal *Catopsbaatar*. Acta Palaeontologica Polonica 53:545–566.
Hurum, J. H., Z.-X. Luo, and Z. Kielan-Jaworowska. 2006. Were mammals originally venomous? Acta Palaeontologica Polonica 51:1–11.
Huttenlocker, A. K., D. M. Grossnickle, J. L. Kirkland, J. A. Schultz, and Z.-X. Luo. 2018. Late-surviving stem mammal links the lowermost Cretaceous of North America and Gondwana. Nature 558:108–112.
Jäger, K., Z.-X. Luo, and T. Martin. 2019. Postcranial skeleton of *Henkelotherium guimarotae* (Cladotheria, Mammalia) and locomotor adaptation. Journal of Mammalian Evolution 27:349–372.
Jenkins, F. A., Jr. 1969. The evolution and development of the dens of the mammalian axis. The Anatomical Record 164:173–184.
Jenkins, F. A., Jr. 1970. Cynodont postcranial anatomy and the "prototherian" level of mammalian organization. Evolution 24:230–252.
Jenkins, F. A., Jr. 1971. The postcranial skeleton of African cynodonts: problems in the early evolution of the mammalian postcranial skeleton. Bulletin, Peabody Museum of Natural History 36:1–216.
Jenkins, F. A., Jr. 1973. The functional anatomy and evolution of the mammalian humero-ulnar articulation. The American Journal of Anatomy 137:281–297.
Jenkins, F. A., Jr., and D. W. Krause. 1983. Adaptations for climbing in North American multituberculates (Mammalia). Science 220:712–715.
Jenkins, F. A., Jr., and F. R. Parrington. 1976. The postcranial skeletons of the Triassic mammals *Eozostrodon*, *Megazostrodon* and *Erythrotherium*. Philosophical Transactions of the Royal Society of London B: Biological Sciences 273:387–431.
Jenkins, F. A., Jr., and C. R. Schaff. 1988. The Early Cretaceous mammal *Gobiconodon* (Mammalia, Triconodonta) from the Cloverly Formation in Montana. Journal of Vertebrate Paleontology 8:1–24.
Jenkins, F. A., Jr., and W. A. Weijs. 1979. The functional anatomy of the shoulder in the Virginia opossum (*Didelphis virginiana*). Journal of Zoology 188:379–410.
Jenkins, F. A., Jr., S. M. Gatesy, N. H. Shubin, and W. W. Amaral. 1997. Haramiyids and Triassic mammalian evolution. Nature 385:715–718.
Ji, Q., Z.-X. Luo, and S.-A. Ji. 1999. A Chinese triconodont mammal and mosaic evolution of the mammalian skeleton. Nature 398:326–330.
Ji, Q., Z.-X. Luo, C.-X. Yuan, and A. R. Tabrum. 2006. A swimming mammaliaform from the Middle Jurassic and ecomorphological diversification of early mammals. Science 311:1123–1127.
Ji, Q., Z.-X. Luo, X. Zhang, C.-X. Yuan, and L. Xu. 2009. Evolutionary development of the middle ear in Mesozoic therian mammals. Science 326:278–281.
Ji, Q., Z.-X. Luo, C.-X. Yuan, J. R. Wible, J.-P. Zhang, and J. A. Georgi. 2002. The earliest known eutherian mammal. Nature 416:816–822.
Kammerer, C. F., J. J. Flynn, L. Ranivoharimanana, and A. R. Wyss. 2008. New material of *Menadon besairiei* (Cynodontia: Traversodontidae) from the Triassic of Madagascar. Journal of Vertebrate Paleontology 28:445–462.
Kawashima, T., R. W. Thorington Jr., P. W. Bohaska, and F. Sato. 2018. Variability and constraint of vertebral formulae and proportions in colugos, tree shrews, and rodents, with special reference to vertebral modification by aerodynamic adaptation. Folia Morphologica 77:44–56.
Kemp, T. S. 1969. The atlas-axis complex of the mammal-like reptiles. Journal of Zoology 159:223–248.
Kielan-Jaworowska, Z. 1977. Evolution of the therian mammals in the Late Cretaceous of Asia. Part II. Postcranial skeleton in *Kennalestes* and *Asioryctes*. Palaeontologia Polonica 37:65–82.
Kielan-Jaworowska, Z. 1978. Evolution of the therian mammals in the Late Cretaceous of Asia. Part III. Postcranial skeleton in Zalambdalestidae. Palaeontologia Polonica 38:5–41.
Kielan-Jaworowska, Z. 1989. Postcranial skeleton of a Cretaceous multituberculate mammal. Acta Palaeontologica Polonica 34:75–85.
Kielan-Jaworowska, Z. 1998. Humeral torsion in multituberculate mammals. Acta Palaeontologica Polonica 43:131–134.
Kielan-Jaworowska, Z., and D. Dashzeveg. 1978. New Late Cretaceous mammal locality in Mongolia and a description of a new multituberculate. Acta Palaeontologica Polonica 23:115–130.
Kielan-Jaworowska, Z., and P. P. Gambaryan. 1994. Postcranial anatomy and habits of Asian multituberculate mammals. Fossils and Strata 36:1–92.
Kielan-Jaworowska, Z., and J. H. Hurum. 2006. Limb posture in early mammals: sprawling or parasagittal. Acta Palaeontologica Polonica 51:393–406.
Kielan-Jaworowska, Z., and T. Qi. 1990. Fossorial adaptations of a taeniolabidoid multituberculate mammal from the Eocene of China. Vertebrata PalAsiatica 28:81–94.
Kielan-Jaworowska, Z., R. L. Cifelli, and Z.-X. Luo. 2004. Mammals from the Age of Dinosaurs: Origins, Evolution, and Structure. Columbia University Press, New York, New York, 630 pp.
Kielan-Jaworowska, Z., J. H. Hurum, P. J. Currie, and R. Barsbold. 2002. New data on anatomy of the Late Cretaceous multituberculate mammal *Catopsbaatar*. Acta Palaeontologica Polonica 47:557–560.
Kielan-Jaworowska, Z., E. Ortiz-Jaureguizar, C. Vieytes, R. Pascual, and F. J. Goin. 2007. First ?cimolodontan multituberculate mammal from South America. Acta Palaeontologica Polonica 52:257–262.
Kirk, E. C., S. Hoffmann, A. D. Kemp, D. W. Krause, and P. M. O'Connor. 2014. Sensory anatomy and sensory ecology of *Vintana sertichi* (Mammalia, Gondwanatheria) from the Late Cretaceous of Madagascar; pp. 203–222 in D. W. Krause (ed.), *Vintana sertichi* (Mammalia, Gondwanatheria) from the Late Cretaceous of Madagascar. Society of Vertebrate Paleontology Memoir 14. Journal of Vertebrate Paleontology 34(6, Supplement).
Kirk, E. C., P. Lemelin, M. W. Hamrick, D. M. Boyer, and J. I. Bloch. 2008. Intrinsic hand proportions of euarchontans and other mammals: implications for the locomotor behavior of plesiadapiforms. Journal of Human Evolution 55:278–299.
Kitching, J. W., and M. A. Raath. 1984. Fossils from the Elliot and Clarens formations (Karoo Sequence) of the northeastern Cape, Orange Free State and Lesotho, and a suggested biozonation based on tetrapods. Palaeontologia africana 25:111–125.
Klima, M. 1973. Die Frühentwicklung des Schultergürtels und des Brustbeins bei den Monotremen (Mammalia: Prototheria). Advances in Anatomy, Embryology, and Cell Biology 47:1–80.
Klima, M. 1987. Early development of the shoulder girdle and sternum in marsupials (Mammalia: Metatheria). Advances in Anatomy, Embryology, and Cell Biology 109:1–91.
Krause, D. W. 2013. Gondwanatheria and ?Multituberculata (Mammalia) from the Late Cretaceous of Madagascar. Canadian Journal of Earth Sciences 50:324–340.
Krause, D. W. (ed.). 2014. *Vintana sertichi* (Mammalia, Gondwanatheria) from the Late Cretaceous of Madagascar. Society of Vertebrate Paleontology Memoir 14. Journal of Vertebrate Paleontology 34(6, Supplement), 222 pp.
Krause, D. W., and F. A. Jenkins Jr. 1983. The postcranial skeleton of North American multituberculates. Bulletin of the Museum of Comparative Zoology 150:199–246.
Krause, D. W., S. Hoffmann, and S. Werning. 2017. First postcranial remains of Multituberculata (Allotheria, Mammalia) from Gondwana. Cretaceous Research 80:91–100.
Krause, D. W., J. R. Groenke, S. Hoffmann, R. R. Rogers, and L. J. Rahantarisoa. 2020. Introduction to *Adalatherium hui* (Gondwanatheria, Mammalia) from the Late Cretaceous of Madagascar; pp. 4–18 in D. W. Krause and S. Hoffmann (eds.), *Adalatherium hui* (Mammalia, Gondwanatheria) from the Late Cretaceous of Madagascar. Society of Vertebrate Paleontology Memoir 21. Journal of Vertebrate Paleontology 40(2, Supplement).
Krause, D. W., R. R. Rogers, L. J. Rahantarisoa, J. R. Groenke, and H. Andriamialison. 2014a. Introduction, systematic paleontology, and geological context of *Vintana sertichi* (Mammalia, Gondwanatheria) from the Late Cretaceous of Madagascar; pp. 4–13 in D. W. Krause (ed.), *Vintana sertichi* (Mammalia, Gondwanatheria) from the Late Cretaceous of Madagascar.

Society of Vertebrate Paleontology Memoir 14. Journal of Vertebrate Paleontology 34(6, Supplement).
Krause, D. W., J. J. Sertich, P. M. O'Connor, K. C. Rogers, and R. R. Rogers. 2019. The Mesozoic biogeographic history of Gondwanan terrestrial vertebrates: insights from Madagascar's fossil record. Annual Review of Earth and Planetary Sciences 47:519–553.
Krause, D. W., S. Hoffmann, Y. Hu, J. R. Wible, G. W. Rougier, E. C. Kirk, J. R. Groenke, R. R. Rogers, J. B. Rossie, J. A. Schultz, A. R. Evans, W. von Koenigswald, and L. J. Rahantarisoa. 2020. Skeleton of Cretaceous mammal from Madagascar reflects long-term insularity. Nature 581:421–427.
Krause, D. W., S. Hoffmann, J. R. Wible, E. C. Kirk, J. A. Schultz, W. von Koenigswald, J. R. Groenke, J. B. Rossie, P. M. O'Connor, E. R. Seiffert, E. R. Dumont, W. L. Holloway, R. R. Rogers, L. J. Rahantarisoa, A. D. Kemp, and H. Andriamialison. 2014b. First cranial remains of a gondwanatherian mammal reveal remarkable mosaicism. Nature 515:512–517.
Krebs, B. 1991. Das Skelett von *Henkelotherium guimarotae* gen. et sp. nov. (Eupantotheria, Mammalia) aus dem Oberen Jura von Portugal. Berliner Geowissenschaftliche Abhandlungen A 133:1–110.
Kühne, W. G. 1956. The Liassic Therapsid *Oligokyphus*. British Museum (Natural History), London, U.K., 149 pp.
Lemelin, P. 1999. Morphological correlates of substrate use in didelphid marsupials: implications for primate origins. Journal of Zoology 247:165–175.
Lemelin, P., and B. W. Grafton. 1998. Grasping performance in *Saguinus midas* and the evolution of hand prehensility in primates; pp. 131–144 in E. Strasser, J. Fleagle, A. Rosenberger, and H. McHenry (eds.), Primate Locomotion: Recent Advances. Plenum Press, New York, New York.
Lessertisseur, J., and R. Saban. 1967. Squelette appendiculaire; pp. 709–1078 in P. P. Grassé (ed.), Traité de Zoologie 16 (1). Masson, Paris, France.
Lewis, O. J. 1962. The phylogeny of the crural and pedal flexor musculature. Proceedings of the Zoological Society of London 138:77–109.
Lewis, O. J. 1963. The monotreme cruro-pedal flexor musculature. Journal of Anatomy 97:55–63.
Lewis, O. J. 1964. The homologies of the mammalian tarsal bones. Journal of Anatomy 98:195–208.
Lewis, O. J. 1989. Functional Morphology of the Evolving Hand and Foot. Clarendon Press, Oxford, U.K., 359 pp.
Lewis, O. J., R. J. Hamshere, and T. M. Bucknill. 1970. The anatomy of the wrist joint. Journal of Anatomy 106:539–552.
Li, G., and Z.-X. Luo. 2006. A Cretaceous symmetrodont therian with some monotreme-like postcranial features. Nature 439:195–200.
Luo, Z.-X. 2015. Origin of the mammalian shoulder; pp. 167–187 in K. P. Dial, N. H. Shubin, and E. L. Brainerd (eds.), Great Transformations: Major Events in the History of Vertebrate Life. University of Chicago Press, Chicago, Illinois.
Luo, Z.-X., and Q. Ji. 2005. New study on dental and skeletal features of the Cretaceous "symmetrodontan" mammal *Zhangheotherium*. Journal of Mammalian Evolution 12:337–357.
Luo, Z.-X., and J. R. Wible. 2005. A Late Jurassic digging mammal and early mammalian diversification. Science 308:103–107.
Luo, Z.-X., Q. Ji, and C.-X. Yuan. 2007. Convergent dental adaptations in pseudo-tribosphenic and tribosphenic mammals. Nature 450:93–97.
Luo, Z.-X., Q. Ji, J. R. Wible, and C.-X. Yuan. 2003. An Early Cretaceous tribosphenic mammal and metatherian evolution. Science 302:1934–1939.
Luo, Z.-X., Q.-J. Meng, Y. G. Zhang, and C.-X. Yuan. 2016. Cruro-pedal structure of the paulchoffatiid *Rugosodon eurasiaticus* and evolution of the multituberculate ankle. Palaeontologica Polonica 67:149–169.
Luo, Z.-X., C.-X. Yuan, Q.-J. Meng, and Q. Ji. 2011. A Jurassic eutherian mammal and divergence of marsupials and placentals. Nature 476:442–445.
Luo, Z.-X., S. M. Gatesy, F. A. Jenkins Jr., W. W. Amaral, and N. H. Shubin. 2015a. Mandibular and dental characteristics of Late Triassic mammaliaform *Haramiyavia* and their ramifications for basal mammal evolution. Proceedings of the National Academy of Sciences of the United States of America 112:E7101–E7109.
Luo, Z.-X., Q.-J. Meng, Q. Ji, D. Liu, Y.-G. Zhang, and A. I. Neander. 2015b. Evolutionary development in basal mammaliaforms as revealed by a docodontan. Science 347:760–764.
Luo, Z.-X., Q.-J. Meng, D. M. Grossnickle, D. Liu, A. I. Neander, Y.-G. Zhang, and Q. Ji. 2017. New evidence for mammaliaform ear evolution and feeding adaptation in a Jurassic ecosystem. Nature 548:326–329.
Mao, F.-Y., and J. Meng. 2019. A new haramiyidan mammal from the Jurassic Yanliao Biota and comparisons with other haramiyidans. Zoological Journal of the Linnean Society 186:529–552.
Mao, F.-Y., Y. Wang, and J. Meng. 2016. New specimens of the multituberculate mammalian *Sphenopsalis* from the Paleocene of Inner Mongolia, China: implications for phylogeny and biology of taeniolabidoid multituberculates. Acta Palaeontologica Polonica 61:429–454.
Marshall, L. G., and D. Sigogneau-Russell. 1995. Part III: The postcranial skeleton; pp. 91–164 in L. G. Marshall, C. de Muizon, and D. Sigogneau-Russell (eds.), *Pucadelphys andinus* (Marsupialia, Mammalia) from the Early Paleocene of Bolivia. Mémoires du Muséum national d'Histoire naturelle, 165. Paris, France. University of Chicago Press, Chicago, Il.
Martin, T. 2005. Postcranial anatomy of *Haldanodon exspectatus* (Mammalia, Docodonta) from the Late Jurassic (Kimmeridgian) of Portugal and its bearing for mammalian evolution. Zoological Journal of the Linnean Society 145:219–248.
Martin, T. 2013. Mammalian postcranial bones from the Late Jurassic of Portugal and their implications for forelimb evolution. Journal of Vertebrate Paleontology 33:1432–1441.
Martin, T., J. Marugan-Lobon, R. Vullo, H. Martin-Abad, Z.-X. Luo, and A. D. Buscalioni. 2015. A Cretaceous eutriconodont and integument evolution in early mammals. Nature 526:380–384.
Meng, J. 2014. Mesozoic mammals of China: implications for phylogeny and early evolution of mammals. National Science Review 1:521–542.
Meng, J., Y. Wang, and C.-K. Li. 2011. Transitional mammalian middle ear from a new Cretaceous Jehol eutriconodont. Nature 472:181–185.
Meng, J., Y. Hu, Y. Wang, X. Wang, and C.-K. Li. 2006. A Mesozoic gliding mammal from northeastern China. Nature 444:889–893.
Meng, Q.-J., Q. Ji, Y.-G. Zhang, D. Liu, D. M. Grossnickle, and Z.-X. Luo. 2015. An arboreal docodont from the Jurassic and mammaliaform ecological diversification. Science 347:764–768.
Meng, Q.-J., D. M. Grossnickle, D. Liu, Y.-G. Zhang, A. I. Neander, Q. Ji, and Z.-X. Luo. 2017. New gliding mammaliaforms from the Jurassic. Nature 548:291–296.
Molinero, R. V. 2003. Comparative anatomy of *Henkelotherium guimarotae* (Holotheria), a Late Jurassic small mammal, and its relevance for the evolution of the mode of locomotion of modern mammals. Ph.D. dissertation, Freie Universität Berlin, Berlin, Germany, 125 pp.
Muizon, C. de. 1998. *Mayulestes ferox*, a borhyaenoid (Metatheria, Mammalia) from the early Palaeocene of Bolivia. Phylogenetic and palaeobiologic implications. Geodiversitas 20:19–142.
Narita, Y., and S. Kuratani. 2005. Evolution of the vertebral formulae in mammals: a perspective on developmental constraints. Journal of Experimental Zoology Part B: Molecular and Developmental Evolution 304B:91–106.
Novacek, M. J., G. W. Rougier, J. R. Wible, M. C. McKenna, D. Dashzeveg, and I. Horovitz. 1997. Epipubic bones in eutherian mammals from the Late Cretaceous of Mongolia. Nature 389:483–486.
O'Leary, M. A., J. I. Bloch, J. J. Flynn, T. J. Gaudin, A. Giallombardo, N. P. Giannini, S. L. Goldberg, B. P. Kraatz, Z.-X. Luo, J. Meng, X. Ni, M. J. Novacek, F. A. Perini, Z. S. Randall, G. W. Rougier, E. J. Sargis, M. T. Silcox, N. B. Simmons, M. Spaulding, P. M. Velazco, M. Weksler, J. R. Wible, and A. L. Cirranello. 2013. The placental mammal ancestor and the post-K-Pg radiation of placentals. Science 339:662–667.
Oliveira, T. V., and C. L. Schultz. 2015. Functional morphology and biomechanics of the cynodont *Trucidocynodon riograndensis* from the Triassic of southern Brazil: pectoral girdle and forelimb. Acta Palaeontologica Polonica 61:377–386.
Oliveira, T. V., M. B. Soares, and C. L. Schultz. 2010. *Trucidocynodon riograndensis* gen. nov. et sp. nov. (Eucynodontia), a new cynodont from the Brazilian Upper Triassic (Santa Maria Formation). Zootaxa 2382:1–71.
Pavanatto, A. E. B., R. T. Müller, Á. A. Stock Da-Rosa, and S. Dias-da-Silva. 2016. New information on the postcranial skeleton of *Massetognathus ochagaviae* Barberena, 1981 (Eucynodontia, Traversodontidae), from the Middle Triassic of southern Brazil. Historical Biology 28:978–989.
Pearson, K., and A. G. Davin. 1921. On the sesamoids of the knee-joint: part II. Evolution of the sesamoids. Biometrika 13:350–400.

Romer, A. S. 1966. Vertebrate Paleontology. University of Chicago Press, Chicago, Illinois, 468 pp.
Rougier, G. W. 1993. *Vincelestes neuquenianus* Bonaparte (Mammalia, Theria) un primitivo mamífero del Cretácico Inferior de la Cuenca Neuquina. Ph.D. dissertation, Universidad de Buenos Aires, Buenos Aires, Argentina, 720 pp.
Rougier, G. W., Q. Ji, and M. J. Novacek. 2003. A new symmetrodont mammal with fur impressions from the Mesozoic of China. Acta Geologica Sinica 77:7–14.
Rougier, G. W., J. R. Wible, and J. A. Hopson. 1992. Reconstruction of the cranial vessels in the Early Cretaceous mammal *Vincelestes neuquenianus*: implications for the evolution of the mammalian cranial vascular system. Journal of Vertebrate Paleontology 12:188–216.
Rougier, G. W., L. C. Gaetano, B. R. Drury, R. Colella, R. O. Gómez, and N. P. Arango. 2011. A review of the Mesozoic mammalian record of South America; pp. 195–214 in J. Calvo, J. Porfiri, B. G. Riga, and D. Dos Santos (eds.), Palaeontología y dinosaurios desde América Latina. Editorial de la Universidad Nacional de Cuyo, Mendoza, Argentina.
Sánchez-Villagra, M. R., Y. Narita, and S. Kuratani. 2007. Thoracolumbar vertebral number: the first skeletal synapomorphy for afrotherian mammals. Systematics and Biodiversity 5:1–7.
Schultz, A. H. 1961. Vertebral column and thorax; pp. 1–66 in H. Hofer, A. H. Schultz, and D. Starck (eds.), Primatologia, Handbuch der Primatenkunde. Karger, Basel, Switzerland.
Sereno, P. C. 2006. Shoulder girdle and forelimb in multituberculates: evolution of parasagittal forelimb posture in mammals; pp. 315–366 in M. T. Carrano, T. J. Gaudin, R. W. Blob, and J. R. Wible (eds.), Amniote Paleobiology: Perspectives on the Evolution of Mammals, Birds, and Reptiles. University of Chicago Press, Chicago, Illinois.
Sereno, P. C., and M. C. McKenna. 1995. Cretaceous multituberculate skeleton and the early evolution of the mammalian shoulder girdle. Nature 377:144–147.
Stafford, B. J., and R. W. Thorington. 1998. Carpal development and morphology in archontan mammals. Journal of Morphology 235:135–155.
Sun, A., and Y. Li. 1985. The postcranial skeleton of the late tritylodont *Bienotheroides*. Vertebrata PalAsiatica 23:135–150.
Szalay, F. S. 1993. Pedal evolution of mammals in the Mesozoic: tests for taxic relationships; pp. 108–128 in F. S. Szalay, M. J. Novacek, and M. C. McKenna (eds.), Mammal Phylogeny, Vol. 1: Mesozoic Differentiation, Multituberculates, Early Therians, and Marsupials. Springer, New York, New York.
Szalay, F. S. 1994. Evolutionary History of the Marsupials and Analysis of Osteological Characters. Cambridge University Press, New York, New York, 481 pp.
Szalay, F. S., and E. J. Sargis. 2001. Model-based analysis of postcranial osteology of marsupials from the Palaeocene of Itaboraí (Brazil) and the phylogenetics and biogeography of Metatheria. Geodiversitas 23:139–302.
Szalay, F. S., and B. A. Trofimov. 1996. The Mongolian Late Cretaceous *Asiatherium*, and the early phylogeny and paleobiogeography of Metatheria. Journal of Vertebrate Paleontology 16:474–509.
Trofimov, B. A., and F. S. Szalay. 1994. New Cretaceous marsupial from Mongolia and the early radiation of Metatheria. Proceedings of the National Academy of Sciences of the United States of America 91:12569–12573.
Vázquez-Molinero, R., T. Martin, M. S. Fischer, and R. Frey. 2001. Comparative anatomical investigations of the postcranial skeleton of *Henkelotherium guimarotae* Krebs, 1991 (Eupantotheria, Mammalia) and their implications for its locomotion. Zoosystematics and Evolution 77:207–216.
Vickaryous, M. K., and B. K. Hall. 2006. Homology of the reptilian coracoid and a reappraisal of the evolution and development of the amniote pectoral apparatus. Journal of Anatomy 208:263–285.
Vickaryous, M. K., and W. M. Olson. 2007. Sesamoids and ossicles in the appendicular skeleton; pp. 323–341 in B. K. Hall (ed.), Fins into Limbs: Evolution, Development, and Transformation. University of Chicago Press, Chicago, Illinois.
Wang, H., J. Meng, and Y. Wang. 2019. Cretaceous fossil reveals a new pattern in mammalian middle ear evolution. Nature 576:102–105.
Weisbecker, V., and S. Schmid. 2007. Autopodial skeletal diversity in hystricognath rodents: functional and phylogenetic aspects. Mammalian Biology 72:27–44.
Weisbecker, V., and D. I. Warton. 2006. Evidence at hand: diversity, functional implications, and locomotor prediction in intrinsic hand proportions of diprotodontian marsupials. Journal of Morphology 267:1469–1485.
Wible, J. R., and G. W. Rougier. 2000. Cranial anatomy of *Kryptobaatar dashzevegi* (Mammalia, Multituberculata), and its bearing on the evolution of mammalian characters. Bulletin of the American Museum of Natural History 247:1–120.
Xu, L., X. Zhang, H. Pu, S. Jia, J. Zhang, J. Lü, and J. Meng. 2015. Largest known Mesozoic multituberculate from Eurasia and implications for multituberculate evolution and biology. Scientific Reports 5:14950.
Yalden, D. W. 1966. A contribution to the functional morphology of the mammalian carpus. Ph.D. dissertation, The University of London, London, U.K., 229 pp.
Yuan, C.-X., Q. Ji, Q.-J. Meng, A. R. Tabrum, and Z.-X. Luo. 2013. Earliest evolution of multituberculate mammals revealed by a new Jurassic fossil. Science 341:779–783.
Zheng, X., S. Bi, X. Wang, and J. Meng. 2013. A new arboreal haramiyid shows the diversity of crown mammals in the Jurassic period. Nature 500:199–202.
Zhou, C.-F., S. Wu, T. Martin, and Z.-X. Luo. 2013. A Jurassic mammaliaform and the earliest mammalian evolutionary adaptations. Nature 500:163–167.
Zhou, C.-F., B.-A. S. Bhullar, A. I. Neander, T. Martin, and Z.-X. Luo. 2019. New Jurassic mammaliaform sheds light on early evolution of mammal-like hyoid bones. Science 365:276–279.

Submitted November 10, 2018; revisions received January 30, 2020; accepted May 30, 2020.
Memoir Editors: Lars Werdelin and Patrick O'Connor.